DISSERTATION

AXISYMMETRIC AND ASYMMETRIC PROCESSES CONTRIBUTING TO TROPICAL CYCLONE INTENSIFICATION AND EXPANSION

Submitted by

Jonathan Martinez

Department of Atmospheric Science

In partial fulfillment of the requirements

For the Degree of Doctor of Philosophy

Colorado State University

Fort Collins, Colorado

Summer 2020

Doctoral Committee:

Advisor: Michael M. Bell

Thomas Birner
Russ S. Schumacher
Christopher A. Davis
Georgiana Brooke Anderson

ABSTRACT

AXISYMMETRIC AND ASYMMETRIC PROCESSES CONTRIBUTING TO TROPICAL CYCLONE INTENSIFICATION AND EXPANSION

This dissertation endeavors to advance our understanding of tropical cyclones (TCs) by investigating axisymmetric and asymmetric processes contributing to TC intensification and expansion. Chapter 2 examines the extreme rapid intensification (RI) and subsequent rapid over-water weakening of eastern North Pacific Hurricane Patricia (2015). Spline-based analyses are created from high-resolution observations collected between 22–23 October during the Office of Naval Research Tropical Cyclone Intensity (TCI) experiment and the National Oceanic and Atmospheric Administration Intensity Forecasting Experiment (IFEX). The first full-tropospheric analysis of the dry, axisymmetric Ertel's potential vorticity (PV) in a TC is presented without relying on balance assumptions. Patricia's structural evolution is characterized by the formation of a "hollow tower" PV structure during RI that persists through maximum intensity and subsequently breaks down during rapid over-water weakening. Transforming the axisymmetric PV analyses from radius–height to potential radius–potential temperature coordinates reveals that Patricia's RI occurs "in-place"; eyewall heating remains fixed to the same absolute angular momentum surfaces as they contract in physical space, contributing to rapid PV concentration. Eddy mixing processes are inferred to concentrate PV radially inward of the symmetric heating maximum during RI and hypothesized to be a primary factor underlying the rearrangement of Patricia's PV distribution during rapid over-water weakening, diluting the PV tower while approximately conserving the absolute circulation.

Chapter 3 raises the question: do asymmetries facilitate or interfere with TC intensification? An idealized, high-resolution simulation of a rapidly intensifying TC is examined to assess asymmetric contributions to the intensification process. The inner-core asymmetric PV distribution remains on the same order of magnitude as the symmetric PV distribution throughout the intensification period. Scale-dependent contributions to the azimuthal-mean PV tendency are assessed by partitioning asymmetries into low-wavenumber (large-scale) and high-wavenumber (small-scale)

categories. Symmetric PV advection and generation are approximately twice larger than asymmetric contributions throughout the intensification period, but the two symmetric contributions largely oppose one another in the eyewall region. Low-wavenumber advection concentrates PV near the axis of rotation during the early and middle stages of RI and low-wavenumber heating concentrates PV in the hollow tower during the middle and late stages of RI. Therefore, asymmetric processes produce non-negligible contributions to TC intensification and may indeed facilitate the intensification process.

Chapter 4 investigates the contributions of incipient vortex circulation and environmental moisture to TC expansion with a set of idealized simulations. The incipient vortex circulation places the primary constraint on TC expansion and in part establishes the expansion rate. Increasing the mid-level moisture further promotes expansion but mostly expedites the intensification process. One of the more common findings related to TC expansion in the literature illustrates a proclivity for relatively small TCs to stay small and relatively large TCs to stay large. Findings reported herein suggest that an initially large vortex can expand more quickly than its relatively smaller counterpart; therefore, with all other factors contributing to expansion held constant, the contrast in size between the two vortices will *increase* with time. Varying the incipient vortex circulation is associated with subsequent variations in the amount and scale of outer-core convection. As the incipient vortex circulation decreases, outer-core convection is relatively scarce and characterized by small-scale, isolated convective elements. On the contrary, as the incipient vortex circulation increases, outer-core convection abounds and is characterized by relatively large rainbands and mesoscale convective systems. A combined increase in the amount and scale of outer-core convection permits an initially large vortex to converge a substantially larger amount of absolute angular momentum compared to its relatively smaller counterpart, resulting in distinct expansion rates.

ACKNOWLEDGMENTS

The research presented in this dissertation would not have been possible without the help and support of many extraordinary people. First and foremost, I sincerely thank my advisor Michael M. Bell. I'm truly grateful for all the opportunities you have presented me over the past six years. I thank you, as my mentor and a friend, for always entertaining my ideas and welcoming discussion. I appreciate your guidance, encouragement, and unwavering belief in my ability to succeed. I thank my committee members, Thomas Birner, Russ S. Schumacher, Chris A. Davis, and Georgiana Brooke Anderson for their guidance and support of my research endeavors. I thank my coauthors from the research project presented in chapter 2, Robert F. Rogers and James D. Doyle, for their contributions to the published manuscript. I further thank Rob for hosting my visit to the Hurricane Research Division in August 2019. I thank my fellow group member and coauthor from the research project presented in chapter 4, Chaehyeon Chelsea Nam, for all her contributions to the research project and for continuously encouraging and challenging my ideas. I thank George Bryan from the National Center for Atmospheric Research (NCAR) for providing the code to implement large-scale wind nudging in CM1 and for addressing my questions about CM1 on several occasions. I thank Bruno Melli for helping me debug multiple compiler issues and various other problems that arose on the Maui compute cluster. I thank all the faculty, staff, and students from the Colorado State University Department of Atmospheric Science for providing such an outstanding environment to engage in scientific inquiry.

I am indebted to the entire Bell research group and Chris Slocum for their incredible support as friends and colleagues. I thank my siblings, Sasha, Chris, and Nakita, and my mother Jocelyne for their continuous love, support, and encouragement. Thank you for the endless joy and laughter. I thank my amazing friends, Fred and Alyss, for helping me shape my visions and reminding me to never stop dreaming. I owe a tremendous amount of my success to the sincere loving kindness from my friends and family.

I thank all of my funding sources and travel sponsors during my graduate studies at Colorado State University. Research presented in this dissertation was funded by the National Science

Foundation (NSF) Bridge to the Doctorate (BD) Fellowship Award 004863-00003, the Office of Naval Research awards N000141613033 and N000141410118 under the Tropical Cyclone Intensity Departmental Research Initiative, and the NSF Grant AGS-1701225. High-performance computing support on Cheyenne (doi:10.5065/D6RX99HX) was provided by NCAR's Computational and Information Systems Laboratory, sponsored by the NSF. I thank the director of the BD Fellowship, Greg Florant, for all of his support, encouragement, and insight both during and beyond my time as a BD Fellow. I thank the Building Future Faculties (BFF) program at North Carolina State University for sponsoring my participation in March 2017. I also thank the professors from the Marine, Earth, and Atmospheric Sciences Department at NC State for their mentorship and hospitality during my visit as part of the BFF program. I thank the NCAR Advanced Study Program Summer Colloquium for funding my participation in June 2018. I thank the program coordinators of JuliaCon for providing me the opportunity to participate in JuliaCon 2018–London, United Kingdom. I also thank the Sloan and Moore foundations for generously funding my travel, housing, and event registration at JuliaCon 2018.

In closing, I thank the wonderful Significant Opportunities in Atmospheric Research and Science (SOARS) program at NCAR for providing me the first opportunity of my career as an atmospheric scientist.

DEDICATION

To my father, Edgar Osvaldo Antonio Martinez

Our journey is eternal

TABLE OF CONTENTS

LIST OF TABLES

LIST OF FIGURES

CHAPTER 1

Introduction

1.1 Motivation

Tropical cyclones (TCs) are among the deadliest and costliest natural phenomena occurring on Earth, producing significant hazards from storm-surge inundation, flash flooding, and severe winds. Landfalling TCs in the mainland United States (U.S.) alone were responsible for an estimated annual average of 43 direct deaths and 36 indirect deaths between 1963–2012 (Rappaport and Blanchard 2016). Recent analyses of community-wide excess mortality rates following Hurricane Maria (2017) suggest that the full impact of landfalling TCs could be substantially larger than estimates predicated on case-by-case assessments (Kishore et al. 2018; Santos-Burgoa et al. 2018; Santos-Lozada and Howard 2018; Cruz-Cano and Mead 2019). Landfalling TCs in the mainland U.S. also caused an annual average of $10 Billion in normalized damage between 1900–2005 (Pielke et al. 2008). As an illustrative example of the devastating impacts associated with landfalling TCs, the 2017 North Atlantic TC season produced major Hurricanes Harvey, Irma, and Maria that caused an overall estimated $265 billion in damages, resulting in the costliest U.S. TC season on record (NOAA 2018). Although the foregoing discussion pertains mostly to the mainland U.S., TCs pose significant threats to the well being of coastal populations and economies around the globe.

TC warning centers vary in their classifications of TC intensity and size but universally adhere to wind-related criteria when producing TC forecasts. For example, the National Hurricane Center (NHC) defines TC intensity in the North Atlantic and eastern North Pacific basins as the maximum 1-min sustained wind speed 10 m above the ocean surface. Although no single metric exists for TC size, NHC produces a set of wind radii forecasts that together quantify the lateral extent of a TC circulation. TC intensity and size are vital forecast metrics that inform the potential magnitude and extent of hazards associated with imminent landfalling TCs. Zhai and Jiang (2014) demonstrated that a damage potential index considering both TC intensity and size explains a larger fraction of variance in normalized damages compared to considering either metric in isolation. Klotzbach et al. (2020) demonstrated that the minimum sea-level pressure (MSLP) also explains

a larger fraction of variance in normalized damages compared to considering either intensity or size in isolation, partly because MSLP is an integrated metric of the entire TC wind field. Societal exposure to TC hazards has escalated among coastal communities in correspondence with continual population growth (Klotzbach et al. 2018). As the general trend in coastal population continues an upward trajectory, the number of lives and total property value threatened by landfalling TCs correspondingly increase. Therefore, continuously improving TC intensity and size forecasts is imperative to prevent casualties and mitigate economic losses. The following two sections provide brief compendiums of relevant scientific literature devoted to elucidating the processes associated with TC intensification and expansion. A brief synthesis of subject matter will follow, along with overarching scientific objectives that guide each chapter in the present dissertation.

1.2 Tropical cyclone intensification

Accurate predictions of TC intensification remain a central focus of the National Oceanic Atmospheric Administration (NOAA) Hurricane Forecast Improvement Project (Marks et al. 2019). Additionally, recommendations by the National Transportation Safety Board have emphasized that communicating accurate TC forecasts is fundamental "to assessing the strength, position, and potential movement of a hurricane; to conducting an effective risk analysis; and to improving mariners' safety" (Sumwalt et al. 2017). Notable operational forecasting challenges lie with predicting episodes of TC rapid intensification (RI), often defined when the one-minute maximum sustained winds increase between 25–35 knots in 24 h (Kaplan et al. 2010). Complex interactions among a vast range of atmospheric and oceanic processes in the vicinity of a TC contribute to large uncertainty in the precise timing and magnitude of RI. The current state of predicting RI episodes is largely dependent on probabilistic techniques that aid the intensity guidance provided by deterministic models. For example, the rapid intensification index (RII, Kaplan et al. 2010) employs large-scale environmental predictors from the Statistical Hurricane Intensity Prediction Scheme (SHIPS; DeMaria et al. 2005) to estimate the probability of RI. However, TC intensification rates are weakly dependent on large-scale environmental influences provided that the TC is embedded within a relatively favorable environment conducive for intensification (Hendricks et al. 2010). Forecast skill improvements have been made to SHIPS-RII by incorporating predictors that represent the

inner-core structure of a TC (Kaplan et al. 2015; Rozoff et al. 2015). Therefore, improving our understanding of processes internal to a TC can lead to more skillful RI forecasts.

A simplified framework often employed to understand TC intensification is predicated on the balanced vortex model and its associated transverse circulation equation formulated by Eliassen (1951). In the balanced vortex model framework, an axisymmetric vortex is assumed to continuously evolve in a state of gradient wind and hydrostatic balance. Thus, the streamfunction for radial and vertical motion (the transverse circulation) is determined by radial gradients of the diabatic heating, vertical gradients of the frictional torque, and three coefficients that represent the static stability, baroclinicity, and inertial stability (Eliassen 1951; Vigh and Schubert 2009; Schubert and McNoldy 2010). Within the balanced vortex framework, heating concentrated radially inward of the RMW in the region of high inertial stability favors TC intensification, which has been argued to result from increased heating efficiency (Schubert and Hack 1982; Hack and Schubert 1986; Pendergrass and Willoughby 2009; Vigh and Schubert 2009) and the convergence of lower-tropospheric angular momentum surfaces toward the heat source via a transverse circulation response (Smith and Montgomery 2016; Smith et al. 2018). Frictional forcing also plays a role in the balanced vortex model framework, but the evolution of a TC is primarily governed by sources of heating in the eyewall that drive the simultaneous development of a primary and secondary circulation. Central to the balanced vortex model framework is the inextricable evolution of the wind and mass fields, both inherent to the quantity known as Ertel's PV (e.g., Schubert and Hack 1983; Schubert and Alworth 1987. The "invertibility" principle states that through specification of a balanced state for the flow of interest (e.g., gradient wind and hydrostatic balance in a TC) and suitable boundary conditions, Ertel's PV can be inverted to recover the balanced mass and wind fields (Hoskins et al. 1985). Möller and Smith (1994) demonstrated that when a diabatic heating source is placed radially outward from the axis of rotation within the balanced vortex model framework, the emergent structure during intensification is characterized by high PV in the eyewall region and relatively low PV in the eye. Schubert et al. (1999) referred to this structure as resembling a "hollow tower of PV". It can be further shown in the axisymmetric steady state that the diabatic heating and PV

structures become "locked" with one another, providing a fundamental relationship between the TC primary and secondary circulations (Hausman et al. 2006).

Calculation of PV from observations is difficult as it requires dense sampling to derive both kinematic and thermodynamic gradients. Given sampling limitations, observational studies often use vertical vorticity as a proxy for PV. Doppler radar data and in situ measurements have been utilized in both composite and case studies to demonstrate that intensifying TCs are characterized by a ring-like structure of vorticity with a maximum displaced from the axis of rotation, radially inward of the RMW (Kossin and Eastin 2001; Rogers et al. 2013a, 2015; Martinez et al. 2017). Kossin and Eastin (2001) also demonstrated that intensifying TCs possess relatively lower angular velocity and equivalent potential temperature in the eye compared to the eyewall. The composite study of Rogers et al. (2013a) further noted that convective bursts (CBs) are preferentially located radially inward of the RMW for intensifying TCs compared to radially outward of the RMW for steady-state TCs; the former structure was observed in detail during the rapid intensification of Hurricane Earl (2010; Rogers et al. 2015). Martinez et al. (2017) noted that once a TC reaches major hurricane intensity (50 m s^{-1}), a ring of vorticity can be associated with further intensification or subsequent weakening, suggesting that additional processes may become important near the peak intensity of the strongest TCs. Collectively, observational studies have frequently documented axisymmetric vorticity structures that represent approximations to a more general hollow PV tower.

Previous studies have demonstrated that radial PV gradients near the TC eyewall can serve as waveguides for vortex Rossby waves (VRWs; Guinn and Schubert 1993; Montgomery and Kallenbach 1997). In the presence of a hollow PV tower, the sign reversal of the radial PV gradient satisfies the Rayleigh necessary condition for barotropic instability (Schubert et al. 1999), or more generally, the Charney–Stern necessary condition for combined barotropic-baroclinic instability (Montgomery and Shapiro 1995). Exponential instability arising from phase-locking and mutual amplification between counter-propagating VRWs can lead to a breakdown of the PV ring and mixing at the eye–eyewall interface (Schubert et al. 1999; Kossin and Schubert 2001; Hendricks et al. 2009; Hendricks and Schubert 2010). Barotropic modeling studies demonstrate that PV mixing associated with barotropic instability decreases both the central pressure and maximum

tangential winds (Schubert et al. 1999; Kossin and Schubert 2001; Hendricks et al. 2009). Although barotropic simulations of PV mixing produce an overall reduction in vortex intensity as measured by the maximum tangential winds, forced barotropic simulations reveal a "dual nature" to PV mixing. Asymmetric PV structures emerging from barotropic instability can induce a "transient intensification break" during symmetric intensification; however, the cumulative transport of high-PV air toward the axis of rotation via successive PV mixing events can result in the vortex attaining a higher intensity than it would have otherwise (Rozoff et al. 2009). Hendricks et al. (2014) found that barotropic instability in a forced shallow water model can result in the PV ring rolling up into convective (diabatic) mesovortices. Convectively modified mesovortices provide local sources of PV near the axis of rotation, thereby simultaneously reducing the minimum pressure and increasing the maximum tangential winds.

Möller and Montgomery (1999, 2000) proposed a "convective pulsing" intensification mechanism whereby inner-core PV asymmetries induced by repetitive convective bursts in the eyewall are axisymmetrized, spinning up the symmetric vortex. Asymmetric PV perturbations superposed onto a symmetric base-state vortex were considered the end product of a rapid adjustment process resulting from localized heat sources representing convective heating. Such an approximation of the evolution expected in nature was necessary within barotropic and balanced modeling frameworks. Nolan and Grasso (2003) expanded a generalized, three-dimensional linear model developed by Nolan and Montgomery (2002) to further investigate the response of a symmetric vortex to asymmetric perturbations. Rather than superposing PV perturbations onto a symmetric base-state vortex, instantaneous thermal perturbations were introduced to represent the rapid latent heat release in convective updrafts. Therefore, a more realistic evolution was captured by incorporating the full adjustment process to instantaneous thermal forcing. Nolan and Grasso concluded that the symmetric response of a vortex to asymmetric heating almost always results in the vortex weakening (i.e., asymmetries are a net-negative contribution to TC intensity). Nolan et al. (2007) further generalized the three-dimensional linear model to incorporate time varying heat sources and arrived at the same conclusion. A recent study by Bhalachandran et al. (2020) simulated the life cycles of TCs Phailin and Lehar from the 2013 Bay of Bengal cyclone season and Hurricane

Harvey (2017). In their fully nonlinear, moist simulations, Bhalachandran et al. found that the predominant growth and decay mechanisms associated with asymmetries were the baroclinic conversion of available potential energy to kinetic energy at the individual scale of asymmetries and through the exchange of kinetic energy between asymmetries of various azimuthal scales. That is, the growth and decay of asymmetries occurred largely independent from the symmetric vortex. The authors cast doubt that "eddies grow at the expense of the mean" and further demonstrate that asymmetries can contribute positively to symmetric TC intensification.

Conceptual models of TC intensification are often formulated in regards to "symmetric" and "asymmetric" modes corresponding to the various processes discussed throughout this section. At the foundation of most conceptual models for TC intensification is the evolution of PV amidst diabatic heating produced by convective processes. Observational limitations often preclude the calculation of PV absent balance assumptions and hence our conceptual models rely heavily on numerical simulations, theory, and approximating PV with vertical vorticity. Furthermore, it remains unclear if there is an optimal PV structure for RI and whether asymmetric processes facilitate or interfere with the development toward such a structure. This dissertation seeks to characterize the structural development of PV within rapidly intensifying TCs and elucidate the principal symmetric and asymmetric processes contributing to TC intensification.

1.3 Tropical cyclone expansion

Accurately forecasting the lateral extent of a TC wind field provides critical information to assess the potential scope of its wind, precipitation, and storm surge related hazards. Climatological studies have shown that TCs are characterized by an expansive range of scales (Merrill 1984; Chavas and Emanuel 2010; Chan and Chan 2012; Knaff et al. 2014); however, the processes contributing to variable TC sizes are not fully understood. Complex, multi-scale interactions occurring between a TC and its ambient environment underlie the difficulties associated with distinguishing the principal processes contributing to the lateral expansion of a TC's wind field.

In proceeding, it's worth noting that several metrics of "size" exist in the literature, each describing to varying degrees the lateral extent of a TC's circulation. Rather than elaborating the utility of each metric, a few among the more common employed in the literature are listed here

for reference: Radius of the outermost closed surface isobar (ROCI; Brand 1972; Merrill 1984; Kimball and Mulekar 2004), radius of hurricane-force winds (64 kt; Hill and Lackmann 2009), radius of damaging-force winds (50 kt; Kimball and Mulekar 2004; Xu and Wang 2010), and the equivalent radii of tropical storm-force and gale-force winds (34 kt; Chan and Chan 2012; Kilroy and Smith 2017). Operational forecasting agencies, such as the NHC and Joint Typhoon Warning Center, routinely produce wind radii forecasts for the radius of hurricane-force winds, damaging-force winds, and tropical storm-force winds (Knaff et al. 2017). Herein, TC size is defined as the maximum extent of the azimuthally averaged tangential velocity equal to the radius of gale-force winds (34 kt) 1 km above the ocean surface (henceforth, R_{gales})[1]. Furthermore, TC expansion is defined as the process whereby R_{gales} increases and conversely, contraction as the process whereby R_{gales} decreases. The definition of size chosen herein is located slightly above the frictional boundary layer where absolute angular momentum is approximately conserved and hence TC expansion can be directly related to absolute angular momentum convergence in the presence of various diabatic heating sources (e.g., Kilroy and Smith 2017).

The two tails of the global TC size distribution represent vastly different scales, demonstrating the potential for TCs to exhibit remarkable structural differences. Early studies provided evidence for weak typhoons with compact circulations, referred to as "midget" typhoons (Arakawa 1952; Harr et al. 1996). On the same tail of the TC size distribution are intense TCs with compact circulations, referred to as "micro-hurricanes" (Hawkins and Rubsam 1967) or "strong dwarfs" when depicted on an intensity–kinetic energy diagram (Musgrave et al. 2012). Exemplars of intense TCs with compact circulations include Hurricane Inez (1966; Hawkins and Rubsam 1967; Hawkins and Imbembo 1976 and Hurricane Patricia (2015; Rogers et al. 2017; Doyle et al. 2017; Martinez et al. 2019. The opposite tail of the TC size distribution is characterized by TCs such as Super Typhoon Tip (1979), which at its most intense stage possessed a maximum sustained wind speed of $\sim$85 m s^{-1} and a radius of gale-force winds exceeding 1100 km (Dunnavan and Diercks 1980). Together, the foregoing examples allude to the weak relationship between TC intensity and

[1]In practice, azimuthally averaged grid points 1 km above the ocean surface are searched for tangential velocity values between 17–19 m s^{-1} (33–37 kt) and the grid point that maximizes the radial extent of values within this range is defined as R_{gales}.

size (Merrill 1984; Weatherford and Gray 1988; Carrasco et al. 2014). Such profound differences in TC size further emphasize the difficulties in forecasting potential hazards as a TC approaches land, necessitating a better understanding of expansion at various stages during a TC's life cycle.

Inter-basin comparisons have demonstrated that TCs in the western North Pacific basin, on average, tend to be the largest (Merrill 1984; Knaff et al. 2014). Seasonal variations in TC size have been noted in the North Atlantic and western North Pacific basins, with average sizes exhibiting a relative minimum during mid-summer months and a relative maximum during the fall (Brand 1972; Merrill 1984; Liu and Chan 2002; Kimball and Mulekar 2004). Although basin and season alone do not necessarily provide physical information to describe TC size differences, inter-basin and seasonal variations in meso-synoptic scale precursor disturbances to cyclogenesis and environmental conditions, such as sea-surface temperatures and moisture, are certainly among the many factors underlying observed differences in TC size. For example, Knaff et al. (2014) concluded that small TCs are favored when vertical vorticity is supplied by the incipient vortex disturbance rather than the synoptic environment. Liu and Chan (2002) found that large TCs in the western North Pacific tend to be associated with a southwesterly surge of environmental flow into the vortex at 850 hPa, resulting from cross-equatorial monsoonal flow, whereas small TCs tend to be embedded within easterly flow. Congruous with the foregoing discussion, variance in TC size can be partly attributed to the scale of an incipient vortex and the ambient large-scale environment throughout a TC's life cycle.

Idealized modeling studies have sought to elucidate the most relevant processes governing TC expansion. Hill and Lackmann (2009) demonstrated that environmental humidity is an important factor contributing to TC size. Increasing the environmental humidity promotes a greater amount of PV generated by radially outward propagating spiral rainbands. PV generated by the spiral rainbands is then subsumed by the inner-core PV tower, increasing its lateral extent and spinning up the outer-core cyclonic wind field through a balanced response. Xu and Wang (2010) demonstrated that increasing the RMW of incipient vortices results in larger outer-core surface fluxes that promote stronger diabatic heating within spiral rainbands. Stronger diabatic heating within spiral rainbands promotes more boundary layer vorticity convergence that spins up the outer-core circulation,

which in turn increases the surface fluxes at increasingly larger radii. Xu and Wang (2010) also demonstrated that varying the RMW of incipient vortices has a larger influence on the final size of a TC compared to varying the environmental moisture. Chan and Chan (2014) demonstrated that TC size exhibits a dependency on both initial vortex size and planetary vorticity. They argued that when holding the initial vortex size constant, angular momentum fluxes imparted by the Coriolis torque increase when displacing a vortex further north, whereas radial fluxes of relative angular momentum decrease as a result of increased inertial stability. These competing effects on angular momentum fluxes were shown to be minimized at 25 N such that there may exist an "optimal" latitude for TC expansion. Chan and Chan (2015) demonstrated that expansion rates are not sensitive to the initial vortex intensity, but rather the outer-core wind profile radially outward of the RMW. Increasing the outer-core tangential winds produces larger absolute angular momentum that can be subsequently converged toward the TC center, thereby promoting larger expansion rates. Kilroy and Smith (2017) emphasized the importance of boundary layer dynamics in governing both the radial location of low-level ascent out of the boundary layer and the associated thermodynamic properties of this air. With the aid of a slab boundary layer model, they demonstrated that an initially large vortex concentrates relatively weak ascent over a broad radial region near the axis of rotation compared to an initially small vortex that instead concentrates relatively strong ascent closer to the axis of rotation. The organization of ascent occurs prior to the development of deep convection. A larger vortex will therefore develop a broader distribution of diabatic heating and stronger inflow at larger radii, which in the presence of a larger radial absolute angular momentum gradient contributes to a more rapid spin-up of the outer-core circulation. A reasonable conclusion drawn from idealized modeling studies in aggregate is that TC expansion is inextricably linked to convectively driven convergence of absolute angular momentum toward the TC center of circulation.

There are several internal and external factors that contribute to TC expansion; however, our understanding of how these factors evolve together and contribute to TC expansion remains limited. In nature, "internal" and "external" factors are interdependent, precluding definitive statements regarding the relative contributions of one factor in one category over the other. Furthermore, employing a combined framework that integrates both internal and external factors is challenging

and requires selecting from the numerous potential factors contributing to TC expansion in each respective category. Therefore, it is practical to limit the number of factors and investigate the underlying processes contributing to TC expansion associated with this reduced set of factors. Motivated by the foregoing discussion, this dissertation seeks to elucidate the contributions from incipient vortex circulation and environmental moisture to TC expansion.

1.4 Research objectives

The overarching scientific objective of this dissertation is to advance our understanding of the principal processes contributing to TC intensification and expansion. A locus of emphasis is placed on elucidating contributions from mesoscale processes. Toward attaining the overarching scientific objective, three projects were formulated to address the following three research questions:

(1) What is the observed symmetric and asymmetric potential vorticity structure of an intensifying tropical cyclone?
(2) Do asymmetric processes facilitate or interfere with TC intensification?
(3) How do variable incipient vortex circulations and environmental moisture profiles contribute to TC expansion?

The dissertation is structured such that individual chapters sequentially present findings from each project. Brief overviews are provided at the beginning of each chapter.

Chapter 2 investigates the structural evolution of eastern North Pacific Hurricane Patricia (2015) with high-resolution observations. Axisymmetric observational analyses are created and Patricia's structural evolution is elucidated during three key stages of development: rapid intensification, near maximum intensity, and rapid (over-water) weakening.

Chapter 3 builds upon the symmetric Hurricane Patricia analyses by explicitly accounting for asymmetric contributions to TC intensification. An idealized, high-resolution (1-km horizontal grid spacing) simulation of a TC undergoing rapid intensification is examined in detail. Symmetric and asymmetric structures are quantified throughout the intensification period and contributions from both symmetric and asymmetric processes to TC intensification are analyzed with a scale-dependent, azimuthal-mean PV budget analysis.

Chapter 4 investigates the contributions of incipient vortex circulation and environmental moisture to TC expansion. The amount and scale of outer-core convection are quantified for a set of idealized numerical simulations and related to variable expansion rates through examination of the circulation equation.

Chapter 5 presents a synthesis of the principal findings reported throughout the dissertation. Concluding remarks, remaining questions, and avenues for future work are discussed.

CHAPTER 2

Axisymmetric potential vorticity evolution of Hurricane Patricia (2015)[2]

2.1 Overview

The origins of Hurricane Patricia can be traced back to a gap wind event that occurred over the Gulf of Tehuantepec in association with a variety of multi-scale processes culminating in the formation of a tropical depression at 0600 UTC 20 October 2015 (Kimberlain et al. 2016). Over the next 24 h, Patricia gradually strengthened to a relatively compact tropical storm and operational intensity guidance predicted modest development from that point forward. As Patricia began to traverse an environment characterized by sea-surface temperatures exceeding 30° C, nearly zero deep-layer vertical wind shear, and abundant mid-tropospheric moisture, a remarkable development began. Hurricane Patricia intensified 105 knots in 24 hours despite modest intensity guidance from both global and mesoscale models (Rogers et al. 2017; their Fig. 1), resulting in a 48-h intensity forecast error of 105 knots (Kimberlain et al. 2016). Six hours later, Patricia attained a maximum lifetime intensity of 185 kts ($\sim$95 m s^{-1}) with a minimum central pressure of 872 hPa. Both the extreme rapid intensification and maximum lifetime intensity of Patricia were unprecedented in global observations, placing it in the "tropical record books" [see Table 2 of Rogers et al. (2017)]. Prior to making landfall in the Mexican state of Jalisco, Patricia experienced an equally noteworthy rapid over-water weakening of 50 knots in 5 h that is unprecedented in the western Hemisphere "tropical record books" Rogers et al. (2017).

In this chapter, high-resolution observations collected during the Office of Naval Research (ONR) Tropical Cyclone Intensity experiment (TCI, Doyle et al. 2017) and the National Oceanic and Atmospheric Administration (NOAA) Intensity Forecasting Experiment (IFEX, Rogers et al. 2006, 2013b) are examined to understand Hurricane Patricia's structural evolution during its record-breaking rapid intensification and over-water weakening. Combining new observational capabilities

[2]Research presented in Chapter 2 has been previously published in the *Journal of the Atmospheric Sciences* by the American Meteorological Society. Modifications were made to the text and two figures were added. The complete bibliographic citation of the original source follows: Martinez, J., M. M. Bell, R. F. Rogers, and J. D. Doyle, 2019: Axisymmetric potential vorticity evolution of Hurricane Patricia (2015). *J. Atmos. Sci.*, **76**, 2043–2063, doi: 10.1175/JAS-D-18-0373.1.

from high-density dropsondes and airborne Doppler radar data, the full-tropospheric, dry axisymmetric Ertel's potential vorticity (PV; Ertel 1942) is calculated within the inner-core region of Patricia without relying on balance assumptions. Unprecedented observations of PV are analyzed to elucidate the mesoscale processes contributing to Patricia's rapid intensity changes and to better understand the evolution of the strongest TC observed to date in the Western Hemisphere (Rogers et al. 2017).

Section 2.2 describes the intensive observing periods when Patricia was sampled. Section 2.3 describes the various observing platforms, the quality control processes for the observations, and the variational analysis technique to synthesize the observations. Section 2.4 presents the axisymmetric inner-core PV structure and evolution of Patricia during its rapid intensification, near maximum intensity, and rapid weakening phases. Section 2.5 presents a discussion of the processes contributing to Patricia's rapid intensity changes along with conclusions from the analyses and avenues for future work.

2.2 Intensive observing periods

High-resolution observations gathered in Patricia's inner-core region during both TCI and IFEX provide the unique opportunity to explore the processes contributing to Patricia's remarkable intensity changes. Coordinated flight missions between the National Aeronautics and Space Administration (NASA) B-57 (hereafter B-57) and the NOAA WP-3D (hereafter P-3) aircraft were executed from 21 to 23 October. For the sake of organization, an intensive observing period (IOP) is defined for each time period that observations were collected in Patricia by both the P-3 and B-57. The time window for each IOP is defined with respect to the time Patricia was sampled by the P-3 tail Doppler radar. Table 2.1 provides a brief summary of the three IOPs analyzed in this study and their corresponding time windows. An earlier IOP took place on 21 October 2015 as Patricia began the early stages of its intensification and it was not analyzed in this study. Future work will investigate the structure of Patricia during the earlier stages of organization and rapid development.

Table 2.1. The name of each intensive observing period (IOP) for Hurricane Patricia (2015) analyzed in this study and its corresponding time window.

IOP	Analysis Time
Rapid Intensification (RI)	22 Oct 1715–1915 UTC
Near Maximum Intensity (MI)	23 Oct 1710–1800 UTC
Rapid Weakening (RW)	23 Oct 2015–2100 UTC

Observations collected on 22 October between 1715–1915 UTC as Patricia was in the midst of its record-breaking rapid intensification (Fig. 2.1a) constitute the "rapid intensification" (RI) IOP. Microwave imagery nearest in time to the RI IOP shows deep convection in the eyewall wrapping around a compact center of circulation as Patricia had just achieved category 4 status (Fig. 2.2a). Both the P-3 and B-57 executed figure-4 patterns as they sampled Patricia during the RI IOP; the P-3 flew the 700-hPa flight level (blue path shown in Fig. 2.1b) and the B-57 flew at $\sim$18-km altitude.

On 23 October, the P-3 encountered severe turbulence while traversing Patricia's inner core at the 700-hPa flight level, forcing the crew to loiter and recover on the southeastern side of Patricia for $\sim$2 h before completing the second center pass (Rogers et al. 2017). Therefore, observations are divided into a "near maximum intensity" (MI) IOP between 1710–1800 UTC and a "rapid weakening" (RW) IOP between 2015–2100 UTC. The P-3 flight tracks for the MI and RW IOPs are shown by the green and orange paths in Fig. 2.1b, respectively. A single B-57 overpass at 18-km altitude coincided with the RW IOP (second P-3 center pass on 23 October). Microwave imagery approximately 4 h before the first P-3 center pass on 23 October highlights Patricia's remarkably compact eyewall and corresponding deep convection, along with a pronounced principal rainband (Fig. 2.2b). A dramatic change is observed $\sim$5 h later in the microwave imagery as Patricia approached the coast of Mexico, showing the development of a concentric eyewall structure (Fig. 2.2c). A detailed description of each observing platform is given in the following section along with the method of creating the observational analyses for each IOP.

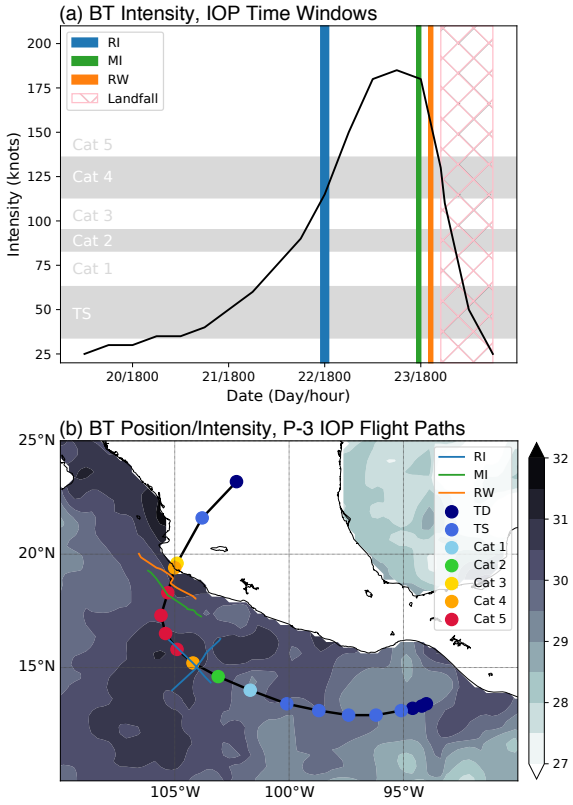

Fig. 2.1. (a) National Hurricane Center (NHC) Best Track (BT) intensity (knots) for Hurricane Patricia (2015). Colored lines denote the time windows for each intensive observing period (IOP) as follows: Rapid intensification (RI): 1715–1915 UTC 22 October, maximum intensity (MI): 1710–1800 UTC 23 October, and rapid weakening (RW): 2015–2100 UTC 23 October. (b) BT position (black curve) and Saffir-Simpson scale intensity (colored dots) throughout Patricia's life cycle are overlaid on the sea-surface temperatures (shaded, K) valid 19 October from the Optimum Interpolation Sea Surface Temperature (OISST) database (Banzon et al. 2016). The colored lines denote the P-3 flight paths corresponding to the IOPs listed above.

2.3 Datasets and analysis methodology

The B-57 was equipped with the High Definition Sounding System (HDSS) designed to simultaneously receive data from multiple dropsondes. As the B-57 flew above Patricia's inner core at approximately 18-km altitude, eXpendable Digital Dropsondes (XDDs) were released in a "rapid-fire" sequence that resulted in a spatial interval of ∼4 km between each XDD. The XDDs are Global Positioning System (GPS) dropsondes designed without a parachute, containing grooves etched into the polystyrene plastic-printed circuit board to provide stability during rapid descent (Black et al. 2017). Pressure, temperature, and relative humidity (PTH) are recorded along the XDD trajectories with a 2-Hz sampling frequency, and horizontal velocity measurements are recorded with a 4-Hz sampling frequency. The HDSS has been successfully tested and evaluated on multiple platforms

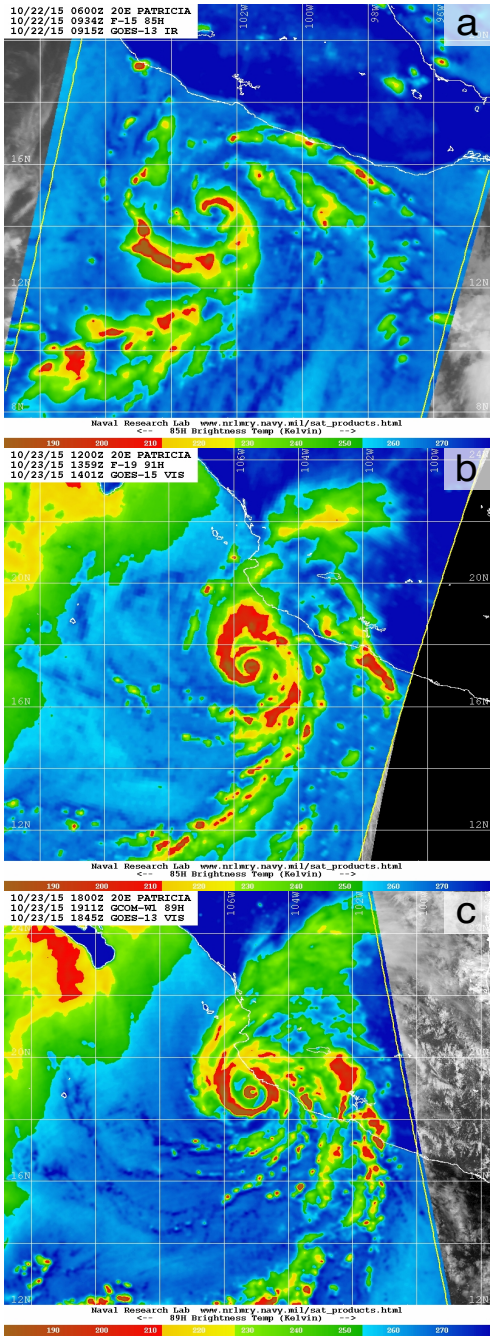

Fig. 2.2. Horizontal-polarized microwave (85–91 GHz) brightness temperature structure of Hurricane Patricia from 22–23 October as observed by the Defense Meteorological Satellite Program (DMSP) and *Global Change Observation Mission - Water "Shizuku" (GCOM-W)* polar orbiting satellites. The microwave imagery is from (a) the Special Sensor Microwave Imager (SSM/I) aboard DMSP *F-15* at 0934 UTC 22 October, (b) the SSMIS aboard DMSP *F-19* at 1359 UTC 23 October, and (c) the Advanced Microwave Scanning Radiometer 2 (AMSR2) aboard *GCOM-W1* at 1911 UTC 23 October. Source: Naval Research Laboratory.

and in different environments prior to its implementation during TCI, showing robust results and strong agreement with measurements made by Vaisala RD94 GPS dropsondes (Black et al. 2017). Pressure, temperature, relative humidity, and horizontal velocity errors are reported as 1.5 hPa, 0.14° C, 1.8%, and 0.1 m s^{-1}, respectively (Bell et al. 2016; Black et al. 2017). Each sounding gathered during TCI was subject to a combined objective-subjective quality control procedure, described in detail by Bell et al. (2016), to ensure reliable data quality for the final product.

The P-3 tail Doppler radar is an X-band ($\sim$3-cm wavelength) radar with two antennas, one scanning fore and the other scanning aft, both positioned at an $\sim$20° offset from the aircraft's longitudinal axis. The $\sim$40° separation between radar beams permits a dual-Doppler synthesis of the observed Doppler velocities from both the fore and aft scanning radars. The radar data are corrected for navigational errors using the method described by Cai et al. (2018) and subject to an automated quality control process following the "medium-threshold" algorithm described by Bell et al. (2013). Additional quality control of the radar observations is carried out manually to remove ocean returns, radar side-lobes, and second-trip echoes.

The HDSS and tail Doppler radar observations constitute the majority of the data used in the analyses presented herein; additional datasets that are used in the analyses are described below. The P-3 released several of the Vaisala RD94 GPS dropsondes during its eyewall penetrations. The RD94 dropsondes provide PTH and velocity observations along a trajectory as they fall from the aircraft with a 2-Hz sampling frequency, resulting in a vertical resolution of approximately 5 m. RD94 dropsondes are quality controlled with the Atmospheric Sounding Processing Environment (ASPEN) software. In situ (flight-level) kinematic and thermodynamic observations are collected by the P-3 instrumentation with a 1-Hz sampling frequency. A correction is applied to both the temperature and dewpoint temperature observations to account for potential instrument wetting events following the method outlined by Zipser et al. (1981) and discussed in detail by Eastin et al. (2002). Atmospheric Motion Vectors (AMVs) derived from feature tracking in satellite imagery through a combination of water vapor and infrared channels are obtained from the Cooperative Institute for Meteorological Satellite Studies (CIMSS) and also included in the analyses (Velden et al. 1997, 2005).

Observations are synthesized for each IOP with a two-dimensional (axisymmetric) variational analysis technique that is termed SAMURAI: Spline Analysis at Mesoscale Utilizing Radar and Aircraft Instrumentation (Bell et al. 2012; Foerster et al. 2014; Foerster and Bell 2017). Given a set of observations and associated error estimates, the SAMURAI technique yields the maximum likelihood estimate of the atmosphere through a minimization of a variational cost function. Unique characteristics of the SAMURAI technique include the ability to perform the analysis directly in an axisymmetric cylindrical coordinate system and the absence of any imposed balance or physical constraints other than mass continuity. The SAMURAI technique uses a finite element approach that employs second-order continuous cubic B-splines as a set of basis functions (Ooyama 2002), providing high numerical precision for derived quantities.

Axisymmetric SAMURAI analyses are created for each respective IOP. The center of circulation is identified as the point that maximizes the tangential circulation within the RMW (Marks et al. 1992). The 2–8 km layer-averaged circulation center is specified as the center of circulation for each IOP analysis, and an f-plane approximation is assumed with the Coriolis parameter calculated at the center of circulation. Figure 2.3 shows the data distribution for each IOP in both polar and axisymmetric coordinates with the radar reflectivity overlaid in cyan contours for the axisymmetric analyses. All axisymmetric cross-sections presented in this chapter are scaled to preserve the true aspect ratio. The Doppler radar observations provide dense coverage throughout the analysis domain, giving high confidence in the retrieved kinematic fields apart from the 5-km region nearest to the axis of rotation due to a lack of hydrometeors in the eye. A soft $w = 0$ (vertical velocity) variational constraint is applied in clear air with a standard deviation of 0.5 m s^{-1} to reduce numerically spurious vertical velocities at small radii. As a result, the magnitude of downdrafts in Patricia's eye may be underestimated. XDDs released by the B-57 (red dots in Fig. 2.3) extend throughout the full depth of the troposphere and provide extensive radial coverage except near the RMW where a few sondes failed before reaching the surface.

Given the different sampling resolutions of the dropsondes and Doppler radar, separate analyses are created for the thermodynamic and kinematic fields. SAMURAI uses a spline-cutoff (Ooyama 2002) and recursive Gaussian filter (Purser et al. 2003) to smooth the analyses and spread both

thermodynamic and kinematic information across the analysis domain. Tests with different spatial resolutions and filter lengths indicate trade-offs between the level of detail, the magnitude of resolved gradients, and potential analysis artifacts resulting from the different sampling resolutions. The thermodynamic analyses presented herein limit resolved scales to 6 km along the radial dimension and 0.5 km along the vertical dimension. The kinematic analyses limit resolved scales to 1.5 km along the radial dimension and 0.5 km along the vertical dimension. Since several of the XDDs failed in the upper troposphere near the eyewall, spatial filters interpolate the observations in this region across an approximately 10–20 km data gap for the thermodynamic analysis of each IOP. A higher resolution is preserved in the kinematic analyses given the dense Doppler radar sampling. Lastly, note that the B-57 overpass on 23 October coincided with the RW IOP (second center pass of the P-3) and not the MI IOP, and this is evidenced by the lack of dropsondes in the data distribution for the MI IOP (Figs. 2.3c,d). To resolve the lack of thermodynamic observations during the MI IOP, the axisymmetric thermodynamic structure is assumed to evolve on a slow enough timescale to warrant using the same thermodynamic analysis for both the MI and RW IOPs. This assumption will be further examined in the discussion and conclusions section.

2.4 Axisymmetric structural evolution

2.4.1 Rapid intensification

On 22 October, Hurricane Patricia entered an environment characterized by sea-surface temperatures exceeding 30° C (Fig. 2.1b) and weak deep-layer (850–200 hPa) environmental vertical wind shear (not shown).[3] These favorable environmental conditions facilitated Patricia's rapid intensification from a tropical storm ($\sim$30 m s^{-1}) at 0000 UTC to a category 4 major hurricane ($\sim$60 m s^{-1}) at 1800 UTC, at which point it was sampled by both the P-3 and B-57 (see Fig. 2.1).

The axisymmetric kinematic and thermodynamic structure of Patricia for the RI IOP (1715–1915 UTC 22 October) is shown in Fig. 2.4. At this stage, Patricia is characterized by a remarkably compact circulation with an RMW at 2-km altitude of 15 km. Deep convection (shown by the cyan

[3]All references to the deep-layer (850–200 hPa) environmental vertical wind shear magnitude and direction are obtained from the Statistical Hurricane Intensity Prediction Scheme (SHIPS) predictors labeled "SHDC" and "SDDC". SHDC and SDDC represent the 850–200 hPa vertical wind shear magnitude and direction, respectively, averaged between 0–500 km radius from the vortex center after removing the vortex circulation. These variables are obtained from the operational Global Forecast System (GFS) analyses.

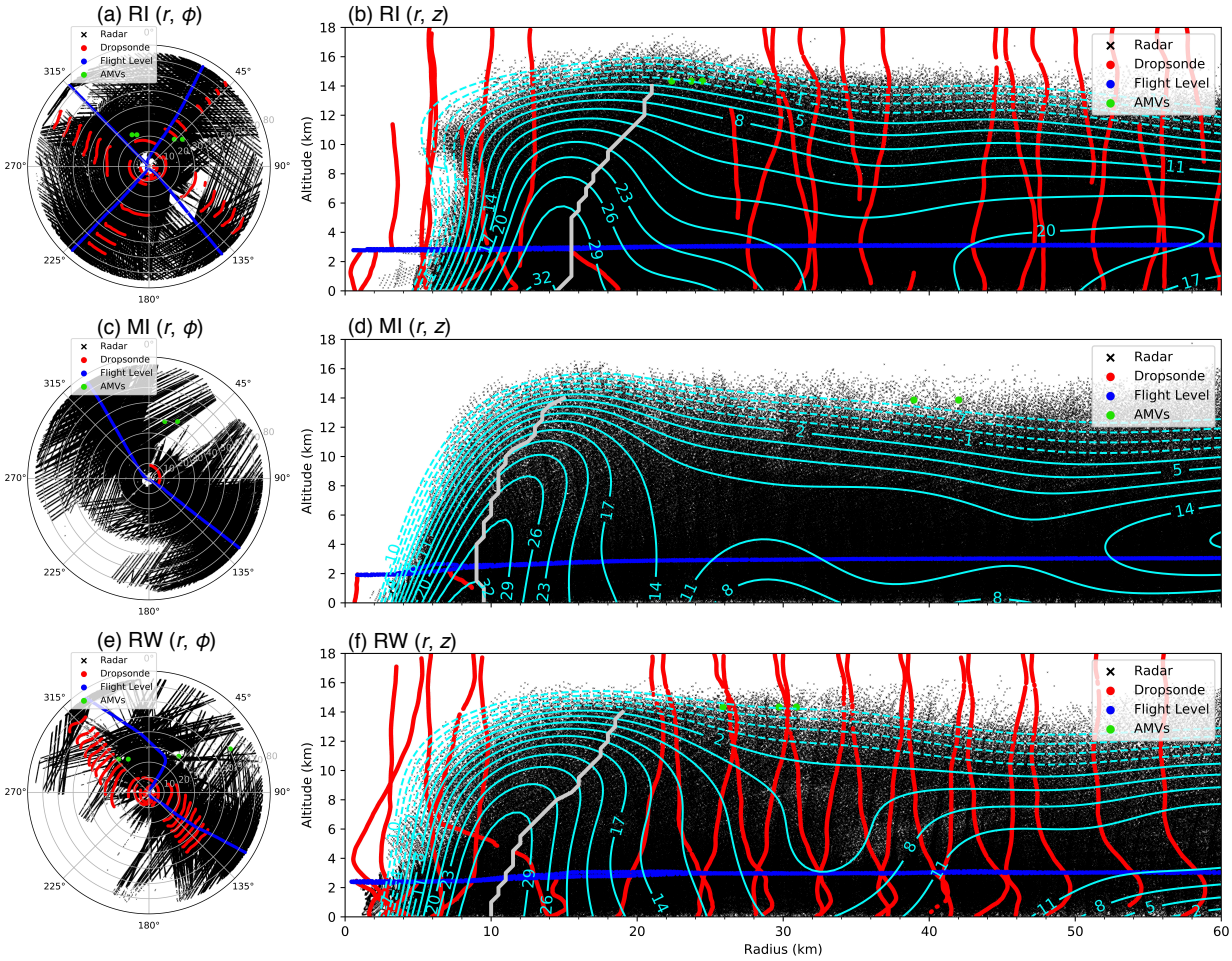

Fig. 2.3. Storm-relative data distributions for each intensive observing period (IOP) in (a), (c), (e) the radius–azimuth (r, ϕ) plane and (b), (d), (f) the radius–height (r, z) plane. Dropsonde trajectories (XDDs and RD94 sondes) are shown in red, in situ measurements from the P-3 in blue, atmospheric motion vectors (AMVs) in green, and P-3 tail Doppler radar observation points in black. Radar reflectivity (cyan, contoured every 3 dBZ) and the radius of maximum tangential winds (RMW, gray) from each respective SAMURAI analysis are overlaid in (b), (d), and (f).

contours representing radar reflectivity) is concentrated radially inward of the RMW, which is a configuration commonly observed with intensifying TCs (e.g., Rogers et al. 2013a). A secondary reflectivity maximum is apparent at a radius of ∼45 km and is associated with a pronounced principal rainband evident at this stage in Patricia's development (Fig. 2.2a). The deep, cyclonic primary circulation near the eyewall is characterized by tangential velocities exceeding 30 m s^{-1} at 12-km altitude and a relatively small slope between 2–8 km altitude (Fig. 2.4a). The secondary circulation is characterized by a shallow inflow layer that penetrates radially inward of the RMW,

accelerates upward in the eyewall updraft, and then turns radially outward to a strong outflow (>10 m s^{-1}) between 12–16 km altitude.

Figure 2.4b shows Patricia's potential temperature structure during the RI IOP overlaid with absolute angular momentum surfaces given by $M = rv + 1/2fr^2$, where f is the Coriolis parameter and v the axisymmetric tangential velocity. The $M = 0.8 \times 10^6$ m^2 s^{-1} contour is shown in bold to emphasize the evolution of M near the RMW throughout the three IOPs. Isentropes descend near the axis of rotation as Patricia's warm core develops during RI, and the M surfaces are tightly packed radially inward of the RMW, contributing to an intense vorticity tower (Fig. 2.5a). The axisymmetric absolute vertical vorticity is given by $\eta = f + \partial(rv)/r\partial r$. Patricia's compact primary circulation contributes to both strong curvature (v/r) and radial shearing ($\partial v/\partial r$) components of vorticity, with η values between 5–10 $\times 10^{-3}$ s^{-1} found along the inner edge of the RMW.

In addition to absolute vorticity, Fig. 2.5a shows contours of the vertical gradient of potential temperature (θ), which is related to the static stability. Patricia's thermodynamic structure is characterized by a local static stability maximum in the eye at approximately 2-km altitude where a low-level inversion is often observed, separating the dry subsiding air aloft from relatively cooler and moister air below (Jordan 1961; Franklin et al. 1988; Willoughby 1998). The high-altitude flight level of the B-57 provided thermodynamic observations in the upper-troposphere–lower-stratosphere (UTLS) region of Patricia, showing strong stratification between 16–18-km altitude and a vertical gradient of θ exceeding 25 K km^{-1}.

Together, the kinematic and thermodynamic analyses allow for calculation of the full-tropospheric, axisymmetric PV in Patricia without the use of balance assumptions. Ertel's PV[4] is given in geometric, axisymmetric cylindrical coordinates as

$$P = \frac{1}{\rho}\left\{-\frac{\partial v}{\partial z}\frac{\partial \theta}{\partial r} + \left[f + \frac{\partial (rv)}{r\partial r}\right]\frac{\partial \theta}{\partial z}\right\}, \tag{2.1}$$

where ρ is the dry air density and the remaining variables assume their aforementioned definitions. Figure 2.5b shows the axisymmetric PV structure of Patricia during RI overlaid with the transverse

[4]In this study, the original, dry formulation of PV with potential temperature serving as the relevant thermodynamic variable is analyzed. A PV principle valid for a moist, precipitating atmosphere has been derived (Schubert et al. 2001; Schubert 2004), but given uncertainties in the measured humidity and quantitative similarity between the moist and dry PV, the dry PV definition is chosen herein.

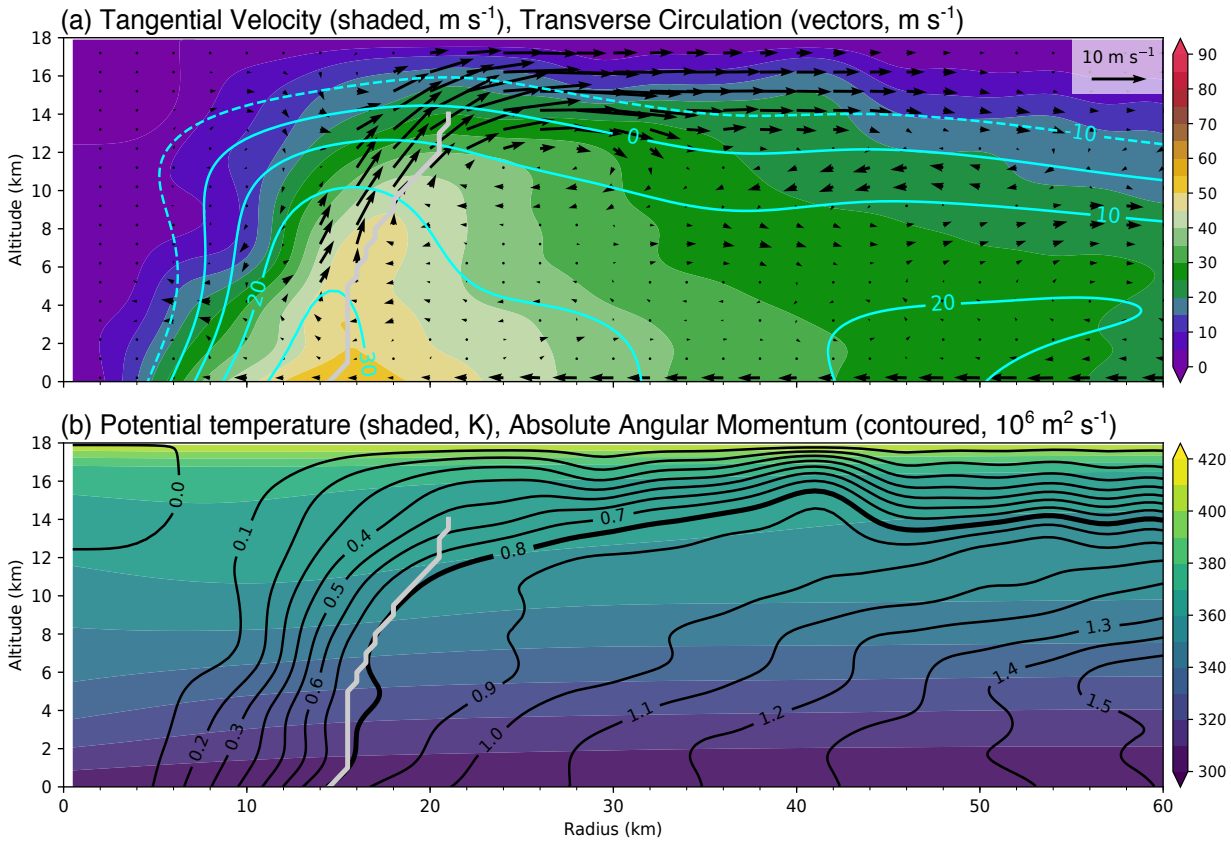

Fig. 2.4. Axisymmetric SAMURAI analysis for the rapid intensification (RI) intensive observing period (IOP) in Hurricane Patricia (1715–1915 UTC 22 Oct. 2015). (a) Tangential velocity (shaded, m s^{-1}) is overlaid with the transverse circulation (vectors, m s^{-1}) and radar reflectivity (cyan, contoured every 10 dBZ). (b) Potential temperature (shaded, K) is overlaid with absolute angular momentum (black, contoured every 10^6 m^2 s^{-1}). The angular momentum surface given by 0.8×10^6 m^2 s^{-1} is shown in bold. In both panels, the radius of maximum tangential winds (RMW) is shown in gray.

circulation vectors. Patricia possesses a hollow tower PV structure with a mid-level PV maximum located in the eyewall exceeding 100 PV units (PVU; 1 PVU $= 10^{-6}$ K kg^{-1} m^2 s^{-1}). A second local maximum of ∼60 PVU is evident in the low-level eye, collocated with the local maximum in static stability (Fig. 2.5a). In the UTLS region, high static stability contributes to several PV "rings" with maxima on the order of 200 PVU. Given that observations in the UTLS are sparse, there is a high degree of uncertainty in the magnitude of these PV rings. However, given both the strong rotation and static stability in the UTLS, the analyzed PV rings are believed to be at least qualitatively realistic.

An estimate for Patricia's diabatic heating $\dot{\theta}$ is calculated under an approximate steady-state assumption where diabatic heating is exactly offset by adiabatic cooling (e.g., Roux et al. 1993).

The local tendency of potential temperature ($\partial\theta/\partial t$) in the eyewall region is expected to be a small residual between latent heating and adiabatic cooling that is less than $\sim$2 K hr^{-1} (Zhang et al. 2002; Stern and Zhang 2013). If the local tendency is assumed to be exactly zero, the diabatic heating can be estimated as $\dot{\theta} = u\partial\theta/\partial r + w\partial\theta/\partial z$, where u represents the radial velocity and w the vertical velocity. Note that heating from eddy sources and additional diabatic processes such as radiation are not included in this heating estimate. The absolute uncertainty in the calculated heating magnitude is difficult to estimate given uncertainties in the analysis and unresolved processes, such that the interpretation of the heating field is limited to a qualitative discussion about the location and relative magnitudes of the heating in each IOP. During the RI period, heating is maximized at mid-levels radially inward of the RMW and slightly outward of the PV maximum (Fig. 2.5b). As will be discussed in the following sections, subsequent changes to the heating and PV fields have a close correspondence.

2.4.2 Maximum intensity

Hurricane Patricia continued to intensify beyond the RI IOP and reached its lifetime maximum intensity of 95 m s^{-1} at 1200 UTC on 23 October. Patricia remained in an environment with sea-surface temperatures exceeding 30° C (Fig. 2.1b); however, it began to encounter weak-to-moderate deep-layer vertical wind shear between $\sim$4–5 m s^{-1} from the south-southwest (not shown). The MI IOP took place on 23 October between 1710–1800 UTC, approximately 6 h after Patricia reached its maximum lifetime intensity. Patricia maintained category 5 major hurricane status during the MI IOP with an intensity of $\sim$93 m s^{-1}. Figure 2.6 shows the axisymmetric kinematic and thermodynamic structure of Patricia for the MI IOP. In the 24-h time window separating RI and MI, Patricia's RMW contracted to 9 km at 2-km altitude and the slope of the RMW between 2–8 km altitude decreased. A decreased slope of the RMW with altitude in correspondence with an overall contraction of the RMW is consistent with previous findings (Stern and Nolan 2009; Stern et al. 2014). Deep convection has persisted in the primary eyewall and a secondary reflectivity maximum is apparent near a radius of 60 km (Fig. 2.3d), likely associated with deep convection in the principal rainband wrapping around Patricia's circulation (Fig. 2.2b). Although the RMW is

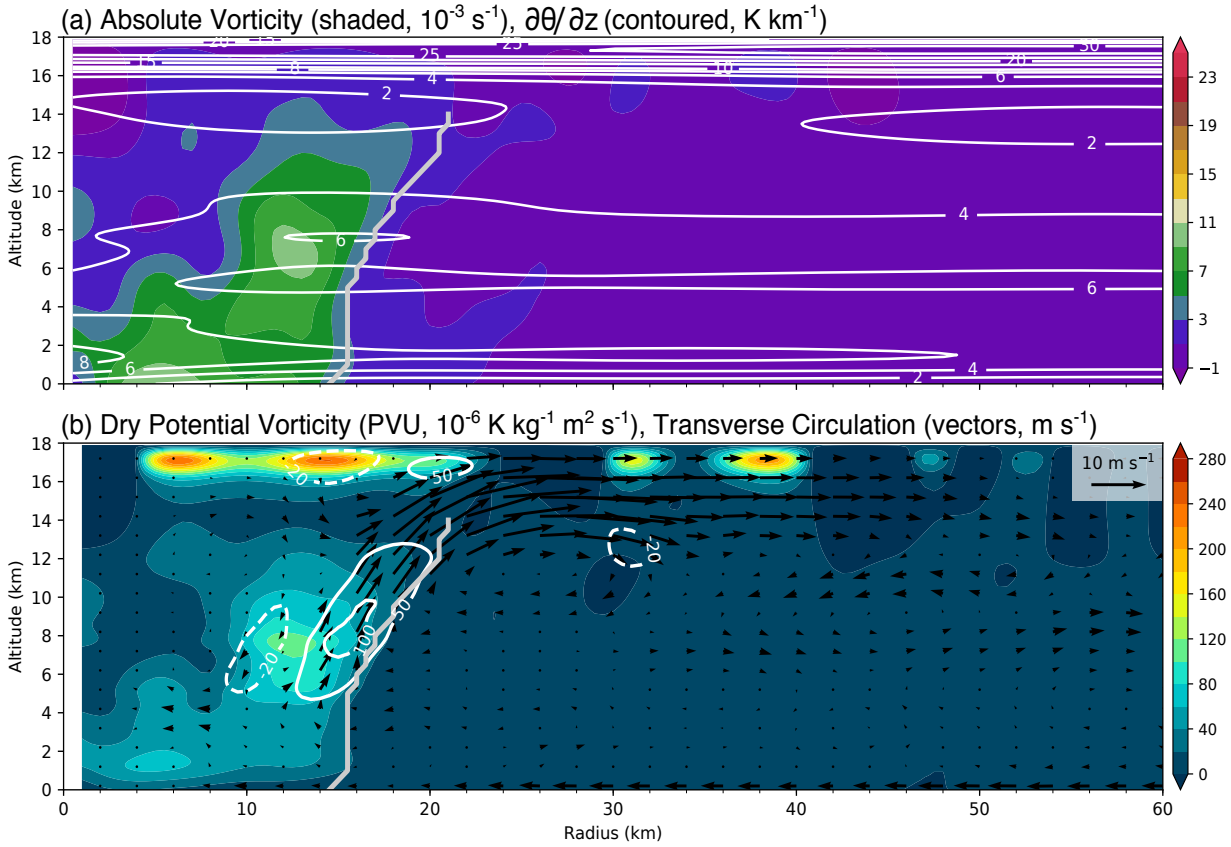

Fig. 2.5. Rapid intensification (RI) axisymmetric SAMURAI analysis (continued) in Hurricane Patricia (1715–1915 UTC 22 Oct. 2015). (a) Absolute vertical vorticity (η; shaded, 10^{-3} s^{-1}) is overlaid with the vertical gradient of potential temperature (white, contoured every 2 K km^{-1} between 0–10 K km^{-1} and every 5 K km^{-1} between 10–30 K km^{-1}). (b) Dry Ertel's PV (shaded, PVU; 1 PVU = 10^{-6} K kg^{-1} m^2 s^{-1}) is overlaid with the transverse circulation (vectors, m s^{-1}) and the diabatic heating ($\dot{\theta}$) estimate (white, contoured at -20, 50, 100, 150, and 200 K h^{-1}). In both figures, the radius of maximum tangential winds (RMW) is shown in gray.

nearly vertically aligned, convection in the primary eyewall possesses a larger slope such that its reflectivity core is displaced radially outward of the RMW above 4-km altitude (Fig. 2.6a).

Patricia's kinematic structure during MI is characterized by a deep, intense primary circulation with tangential velocities exceeding 60 m s^{-1} at 12-km altitude. The inflow layer deepened and intensified compared to the RI IOP and penetrates radially inward of the RMW where strong convergence is located at the base of the eyewall. A mid-level inflow layer has developed near the eyewall between ∼2- and 4-km altitudes, appearing to be somewhat separated from the near-surface inflow layer. Updrafts concentrated along the RMW approach magnitudes of 20 m s^{-1} near 8-km altitude, turning radially outward to an outflow that exceeds 15 m s^{-1} between 14–16 km altitude.

As described in section 2.3, the thermodynamic structure from the B-57 pass three hours after MI (during the RW IOP) is used to analyze the MI IOP. Figure 2.6b shows Patricia's potential temperature structure evaluated for the MI and RW IOPs along with the M surfaces unique to the MI IOP. Although the warm core has intensified during the ∼24 h between RI and RW, the static stability structure remains largely the same (cf. Figs. 2.5a and 2.7a). The $M = 0.8 \times 10^6$ m^2 s^{-1} contour has migrated radially inward, remaining mostly aligned with the RMW from the surface up to nearly 14-km altitude, and the radial gradient of the M surfaces has increased inward of the RMW. Figure 2.7a shows Patricia's remarkable vorticity structure resulting from its intensification and contraction between RI and MI. The radial shear of the tangential velocity approaches values of 9 m s^{-1} km^{-1} between the axis of rotation and RMW (Fig. 2.6a), contributing to η exceeding 25×10^{-3} s^{-1} radially inward of the RMW.

A local static stability maximum remains in the low-level eye during MI with a similar magnitude to that observed during RI, and the upper portion of the outflow layer in the UTLS remains highly stratified (Fig. 2.7a). Figure 2.7b shows that a significant structural evolution has occurred from RI to MI; the hollow PV tower has further concentrated into an intense, vertically coherent tower. The hollow PV tower is characterized by maximum PV values approaching 250 PVU along the inner edge of the RMW and extending from near the surface up to 12-km altitude. Local PV maxima are again noted in the UTLS region with amplitudes exceeding 250 PVU near the eyewall and ∼160 PVU radially outward of the RMW. A UTLS PV ring at approximately $r = 45$ km is located in the region where Patricia's secondary eyewall eventually develops, but it is unclear whether this is coincidental or dynamically relevant, especially given uncertainties in the magnitude of PV in the UTLS region.

2.4.3 Rapid weakening

Approximately 3 h after MI, the P-3 flew its second center pass through Patricia on 23 October between 2015–2100 UTC, denoted herein as the RW IOP. Patricia remained in a region with warm sea-surface temperatures, exceeding 31° C. The magnitude of the deep-layer vertical wind shear was increasing from ∼5 m s^{-1} at 1800 UTC 23 October to ∼13 m s^{-1} at 0000 UTC 24 October. Figure 2.8a shows the axisymmetric kinematic and thermodynamic structure of Patricia for the RW

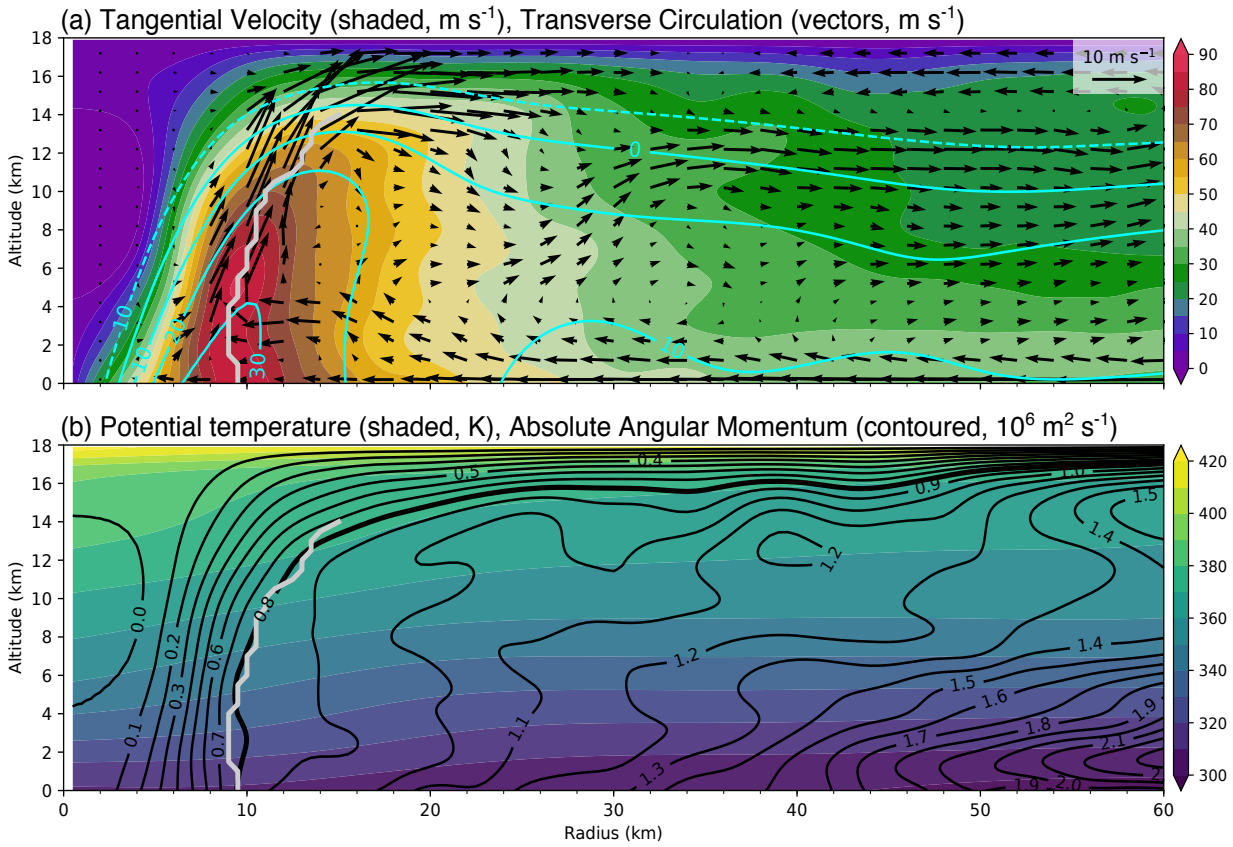

Fig. 2.6. Axisymmetric SAMURAI analysis for the near maximum intensity (MI) intensive observing period (IOP) in Hurricane Patricia (1710–1800 UTC 23 Oct. 2015). (a) Tangential velocity (shaded, m s^{-1}) is overlaid with the transverse circulation (vectors, m s^{-1}) and radar reflectivity (cyan, contoured every 10 dBZ). (b) Potential temperature (shaded, K) is overlaid with absolute angular momentum (black, contoured every 10^6 m^2 s^{-1}). The angular momentum surface given by 0.8×10^6 m^2 s^{-1} is shown in bold. In both panels, the radius of maximum tangential winds (RMW) is shown in gray. Note that the thermodynamic analysis for the MI IOP was created using data that coincided with the rapid weakening (RW) IOP.

IOP. Although MI and RW are separated by only 3 h, a dramatic structural change is evident in the analyses. Deep convection is concentrated along the RMW, but now a pronounced secondary reflectivity maximum is located between a radius of 45–60 km, associated with a developing secondary eyewall. The two eyewalls are separated by a region of relatively low reflectivity values known as the "moat" (Houze et al. 2007).

The slope of the RMW has increased significantly and the tangential velocity maximum is now located near 5-km altitude (Fig. 2.8a). The secondary eyewall is apparent in both the primary and secondary circulations with an overall shallower structure compared to the primary eyewall. The near-surface inflow spiraling into the primary eyewall appears to have been impeded by the

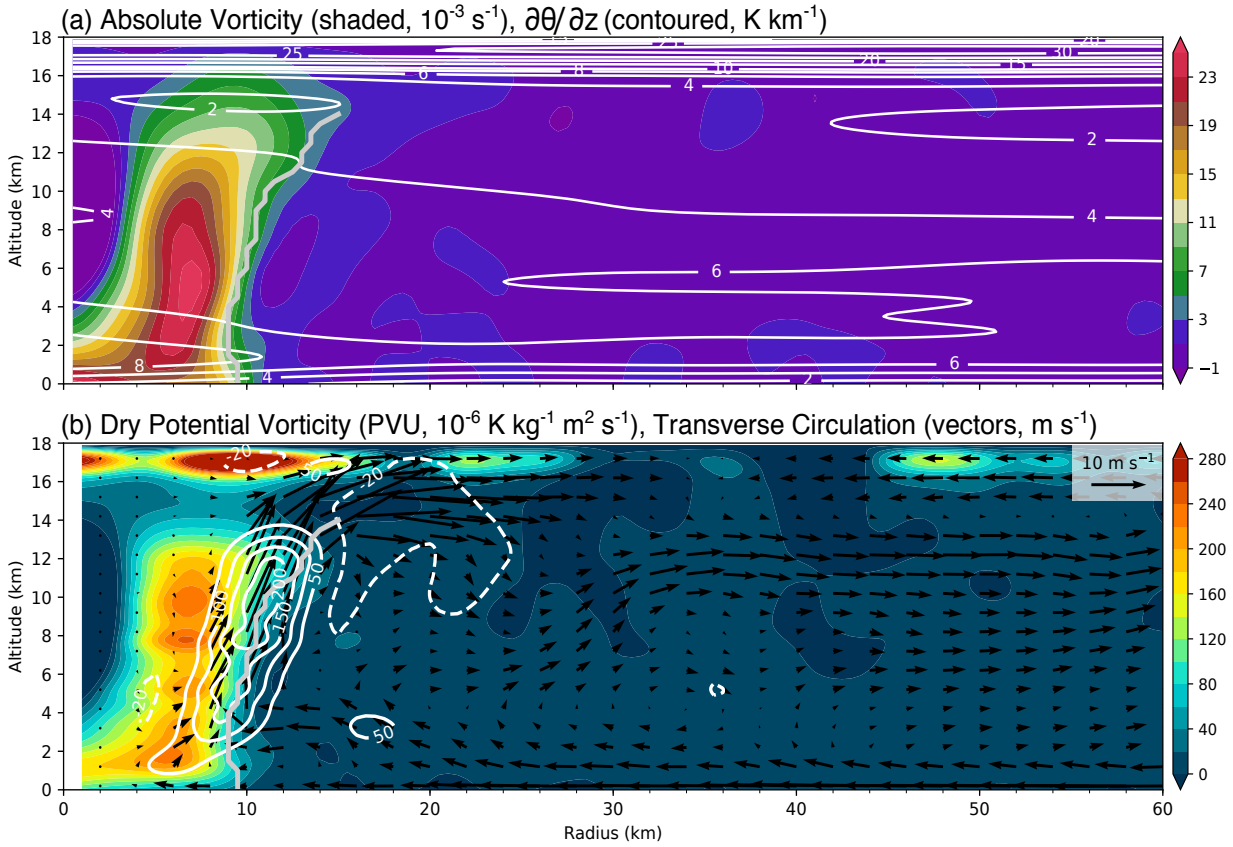

Fig. 2.7. Near maximum intensity (MI) axisymmetric SAMURAI analysis (continued) in Hurricane Patricia (1710–1800 UTC 23 Oct. 2015). (a) Absolute vertical vorticity (η; shaded, 10^{-3} s^{-1}) is overlaid with the vertical gradient of potential temperature (white, contoured every 2 K km^{-1} between 0–10 K km^{-1} and every 5 K km^{-1} between 10–30 K km^{-1}). (b) Dry Ertel's PV (shaded, PVU; 1 PVU = 10^{-6} K kg^{-1} m^2 s^{-1}) is overlaid with the transverse circulation (vectors, m s^{-1}) and the diabatic heating ($\dot{\theta}$) estimate (white, contoured at -20, 50, 100, 150, and 200 K h^{-1}). In both figures, the radius of maximum tangential winds (RMW) is shown in gray. Note that the thermodynamic analysis for the MI IOP was created using data that coincided with the rapid weakening (RW) IOP.

formation of the secondary eyewall, and the mid-level inflow has developed a toroidal circulation around 5-km altitude. Note that this toroidal circulation is vertically centered near the freezing level, suggesting it may be related to strong diabatic heating at this altitude. The magnitude of the updrafts in the primary and secondary eyewalls are comparable with maximum values of ~5 m s^{-1}. The outflow associated with the primary eyewall has weakened to ~10 m s^{-1} and the outflow associated with the secondary eyewall has a maximum of ~5 m s^{-1}.

In addition to an increased slope of the RMW, the radial shear of tangential velocity between the axis of rotation and the RMW has substantially decreased. The radial M gradient has weakened in the primary eyewall, especially below 4-km altitude where the inflow has been reduced (Fig. 2.8b).

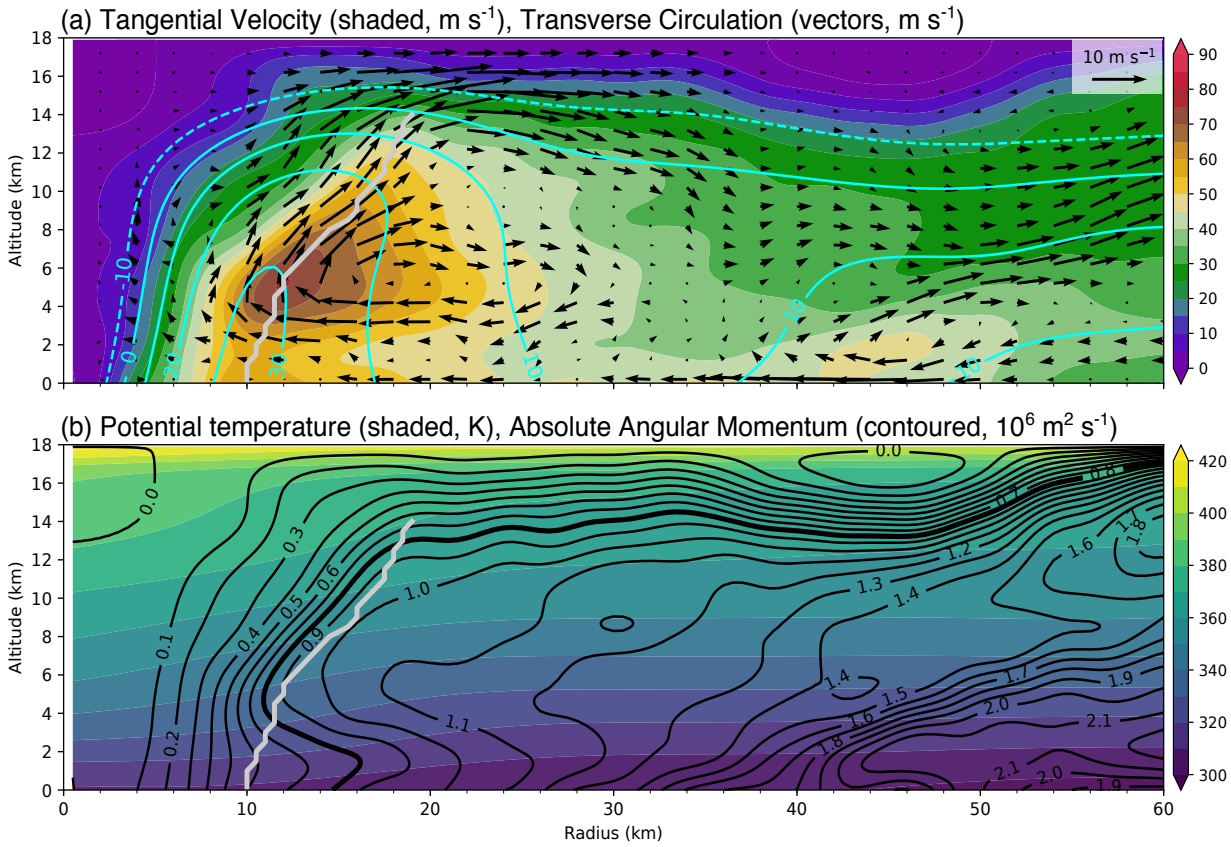

Fig. 2.8. Axisymmetric SAMURAI analysis for the rapid weakening (RW) intensive observing period (IOP) in Hurricane Patricia (2015–2100 UTC 23 Oct. 2015). (a) Tangential velocity (shaded, m s^{-1}) is overlaid with the transverse circulation (vectors, m s^{-1}) and radar reflectivity (cyan, contoured every 10 dBZ). (b) Potential temperature (shaded, K) is overlaid with absolute angular momentum (black, contoured every 10^6 m^2 s^{-1}). The angular momentum surface given by 0.8×10^6 m^2 s^{-1} is shown in bold. In both panels, the radius of maximum tangential winds (RMW) is shown in gray.

In contrast, the M surfaces have radially converged near the developing secondary eyewall. The aforementioned changes to tangential velocity and absolute angular momentum are manifested in the absolute vertical vorticity structure as an overall decrease in the magnitude of vorticity within the primary eyewall, with maximum values on the order of 15×10^{-3} s^{-1} (Fig. 2.9a). The PV structure during RW no longer resembles a pronounced hollow PV tower but rather a more diffuse, vertically sloping structure with two separate mid-level maxima (Fig. 2.9b). PV is no longer confined to the inner edge of the RMW and maximum values have decreased to ∼120 PVU. The tropospheric PV maximum is now collocated with the static stability maximum in the low-level eye. Collectively, the PV structure during RW suggests that substantial mixing has occurred between the eye–eyewall interface, which will be discussed further in the following section. It is worth emphasizing that

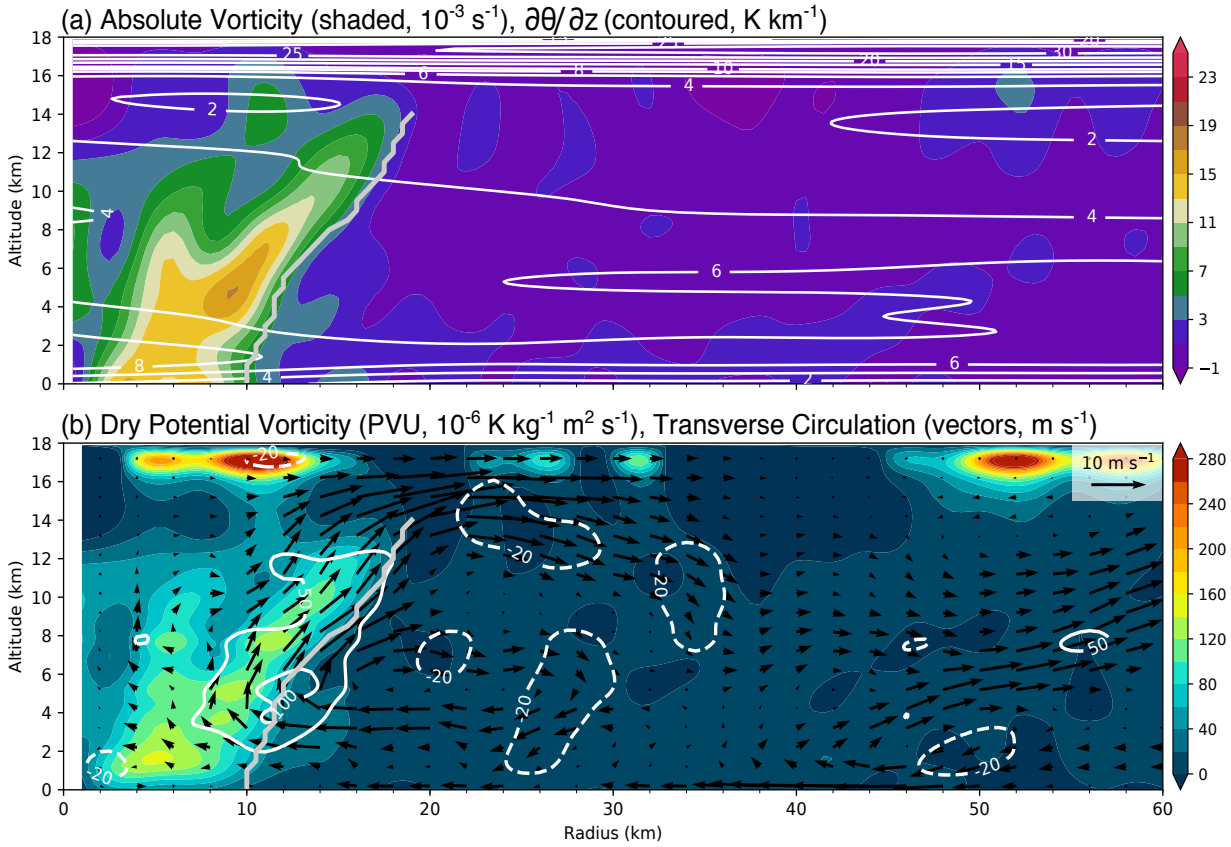

Fig. 2.9. Rapid weakening (RW) axisymmetric SAMURAI analysis (continued) in Hurricane Patricia (2015–2100 UTC 23 Oct. 2015). (a) Absolute vertical vorticity (η; shaded, 10^{-3} s^{-1}) is overlaid with the vertical gradient of potential temperature (white, contoured every 2 K km^{-1} between 0–10 K km^{-1} and every 5 K km^{-1} between 10–30 K km^{-1}). (b) Dry Ertel's PV (shaded, PVU; 1 PVU = 10^{-6} K kg^{-1} m^2 s^{-1}) is overlaid with the transverse circulation (vectors, m s^{-1}) and the diabatic heating ($\dot{\theta}$) estimate (white, contoured at -20, 50, 100, 150, and 200 K h^{-1}). In both figures, the radius of maximum tangential winds (RMW) is shown in gray.

these dramatic inner-core structural changes took place on a short time scale of approximately three hours.

2.5 Potential vorticity evolution

To gain further insight into Patricia's rapid intensification and weakening, the evolution of axisymmetric PV is analyzed in more detail. Note that the estimates of PV presented herein are limited in their quantitative accuracy given observational uncertainties, under-sampling, and spatiotemporal filtering. Furthermore, the axisymmetric thermodynamic analysis valid for the RW IOP is used to calculate PV in the MI IOP under the assumption that the axisymmetric thermodynamic structure evolves on a slower timescale than the axisymmetric wind field. Figs. 2.7b

and 2.9b demonstrate that Patricia experienced a dramatic PV structural evolution in the 3 h separating the MI and RW IOPs. However, given the remarkably similar vertical gradients of potential temperature between the RI and RW IOPs (Figs. 2.5a and 2.9a), Patricia's PV evolution between MI and RW is posited to be largely dominated by vorticity evolution with changes in the mass field contributing to a lesser degree. Despite the aforementioned limitations and assumptions, high-resolution analyses from the TCI observations yield quantitative estimates of the PV evolution that provide a useful framework for understanding Patricia's rapid intensification and weakening.

2.5.1 Coordinate transformation

Seminal work by Schubert and Hack (1983) introduced the transformed Eliassen balanced vortex model wherein absolute angular momentum served as an independent variable, simplifying the transverse circulation equation and providing a useful way to obtain dynamical insight into the evolution of TCs. The potential radius R is defined for an inertially stable vortex as $(1/2)fR^2 = rv + (1/2)fr^2 \equiv M$ and represents the radius to which a parcel must be displaced (conserving absolute angular momentum) in order for its tangential velocity (v) to become zero. The Lagrangian evolution of R is therefore related to sources and sinks of M, and is given by

$$f R\dot{R} = \dot{M} = -\overline{u'\frac{\partial M'}{\partial r}} - \overline{w'\frac{\partial M'}{\partial z}}, \tag{2.2}$$

where $\dot{R} = DR/Dt$, $\dot{M} = DM/Dt$, and the material derivative operator is given by $D/Dt = \partial/\partial t + u\partial/\partial r + w\partial/\partial z$. The terms on the right hand side of Eq. (2.2) denote the eddy sources and sinks of absolute angular momentum (torques), which can arise from frictional fluid stresses and asymmetric processes.

A notable advantage of the potential radius framework is the natural coordinate stretching it provides in regions where the vertical vorticity exceeds the planetary vorticity (see Eqs. 8 and 10 of Schubert and Hack 1983). Schubert and Alworth (1987) took an additional step toward simplifying the transformed Eliassen balanced vortex model by simultaneously using potential radius and isentropic (potential temperature) coordinates. Following the derivation provided in

section 2c of Schubert and Alworth (1987) and section 4 of Hausman et al. (2006), the Lagrangian PV equation for a dry axisymmetric vortex can be written in the (R,θ) coordinate space as

$$\frac{DP}{Dt} = P\left[\frac{\partial(R\dot{R})}{R\partial R} + \frac{\partial\dot{\theta}}{\partial\theta}\right], \tag{2.3}$$

where the material derivative operator is given by

$$\frac{D}{Dt} = \frac{\partial}{\partial\tau} + \dot{R}\frac{\partial}{\partial R} + \dot{\theta}\frac{\partial}{\partial\theta}. \tag{2.4}$$

In the transformed coordinate space, τ is equivalent to time t, but $\partial/\partial\tau$ implies fixed (R,θ) compared to a fixed (r,z) position given by $\partial/\partial t$. Adopting the (R,θ) coordinate space permits analyzing Patricia's PV structure from a dynamically relevant perspective in which "movement" arises from sources and sinks of absolute angular momentum and diabatic processes, which can concentrate or dilute PV within isentropic layers (Haynes and McIntyre 1987). In the (R,θ) coordinate space, radial movement across R surfaces is associated with material changes in the absolute angular momentum of an air parcel through eddy torques ($\dot{R}$; see Eq. 2.2), and vertical movement across θ surfaces is associated with material changes in the potential temperature of an air parcel through diabatic processes ($\dot{\theta}$). The material variance of PV is then associated with gradients in both $\dot{R}$ and $\dot{\theta}$, or "acceleration" across M and θ surfaces in the transformed coordinate space given by the two terms on the right hand side of Eq. (2.3), respectively. Fig. 2.10 shows Patricia's combined potential radius and potential temperature evolution in axisymmetric cylindrical coordinates. The $R = 200$ km surface is located between $r = 10$–20 km for each IOP; therefore, the coordinate transformation from $r \rightarrow R$ produces an approximately 10–20-fold stretching in Patricia's eyewall region.

2.5.2 Patricia's evolution in (R,θ) space

Figure 2.11 shows Patricia's PV structure for each IOP within the transformed (R,θ) coordinate framework. A bilinear interpolation is carried out for the transformation from (r,z) space to (R,θ) space. In the (R,θ) coordinate space, a strong link between the diabatic heating field and the PV structure is apparent. The PV maxima are located radially inward of regions with heating maxima and evolve in concert with the changing structure and magnitude of the heating.

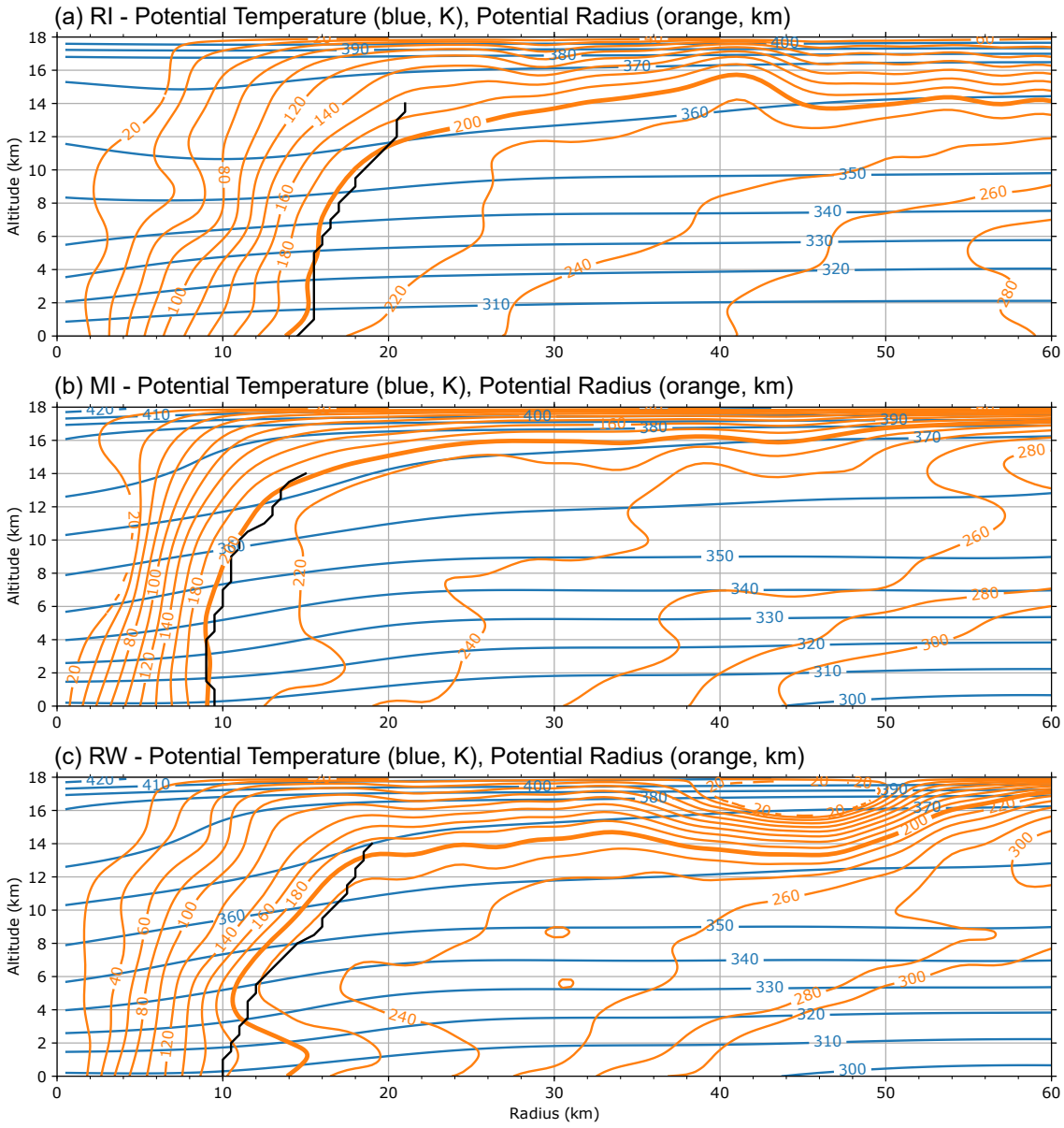

Fig. 2.10. Potential radius (orange, km) and potential temperature (blue, K) are shown for the (a) rapid intensification (RI), (b) near maximum intensity (MI), and (c) rapid weakening (RW) intensive observing periods (IOPs) in Hurricane Patricia. In each panel, the 200-km potential radius surface is shown in bold orange and the radius of maximum tangential winds (RMW) is shown in black.

There is an approximately twofold increase in the maximum value of diabatic heating between RI and MI, followed by a corresponding decrease during RW. The increase in both magnitude and depth of the diabatic heating in the eyewall between RI and MI is accompanied by an approximate 100 PVU amplification of the hollow PV tower as Patricia reached its maximum intensity. It is also noted that although the physical RMW contracted between RI and MI, in the (R, θ) space, the PV

essentially concentrated "in-place" (along the same R surfaces) with the maximum PV remaining near $R = 125$ km (cf. Figs. 2.11a and 2.11b). The spatial evolution of the $M = 0.8 \times 10^6$ m^2 s^{-1} surface was shown earlier to approximately follow the RMW and corresponds to the $R = 188$ km surface.

Eq. (2.3) can be rearranged using (2.4) to yield the Eulerian PV equation in (R, θ) space, and with an application of the quotient rule, the terms can be combined to yield

$$\frac{\partial P}{\partial \tau} = P^2 \left[\frac{\partial}{R \partial R} \left(\frac{R\dot{R}}{P} \right) + \frac{\partial}{\partial \theta} \left(\frac{\dot{\theta}}{P} \right) \right]. \tag{2.5}$$

The two terms on the right hand side of Eq. (2.5) demonstrate that the evolution of PV at a fixed (R, θ) position depends on how the ratio of $\dot{R}/P$ changes radially along a fixed θ surface and how the ratio of $\dot{\theta}/P$ changes vertically along a fixed R surface. The local tendency of PV is then scaled by the square of preexisting PV at a given location in (R, θ) space. A conceptual model depicting Patrica's rapid development of a hollow PV tower can now be developed within the (R, θ) coordinate framework. As air parcels rise out of the boundary layer along an R surface, a positive P tendency requires the vertical gradient of $\dot{\theta}/P$ to be positive. Below the heating and P maxima (which are vertically collocated; see Fig. 2.11a), a positive P tendency occurs when the diabatic source of P exceeds the vertical advection of smaller P from below. Conversely, above the heating and P maxima, a positive P tendency occurs when the vertical advection of larger P from below exceeds the diabatic sink of P. The local tendency resulting from these processes scales with P^2, supporting a rapid increase of P in the presence of sustained vertical mass flux and heating.

In the absence of eddy torques, a steady state is achieved when the vertical gradients of $\dot{\theta}$ and P become identical, and the PV field becomes "locked" to the heating field (Hausman et al. 2006). In the steady state and above the frictional boundary layer, the PV maximum is concentrated along the same R surfaces and at the same isentropic level as the heating maximum. However, the analyses presented herein indicate that the heating maximum is located radially outward of the PV maximum and remains nearly fixed to the same R surfaces ($\sim R = 180$ km) as they contract in physical space (see Figs. 2.5 and 2.7).

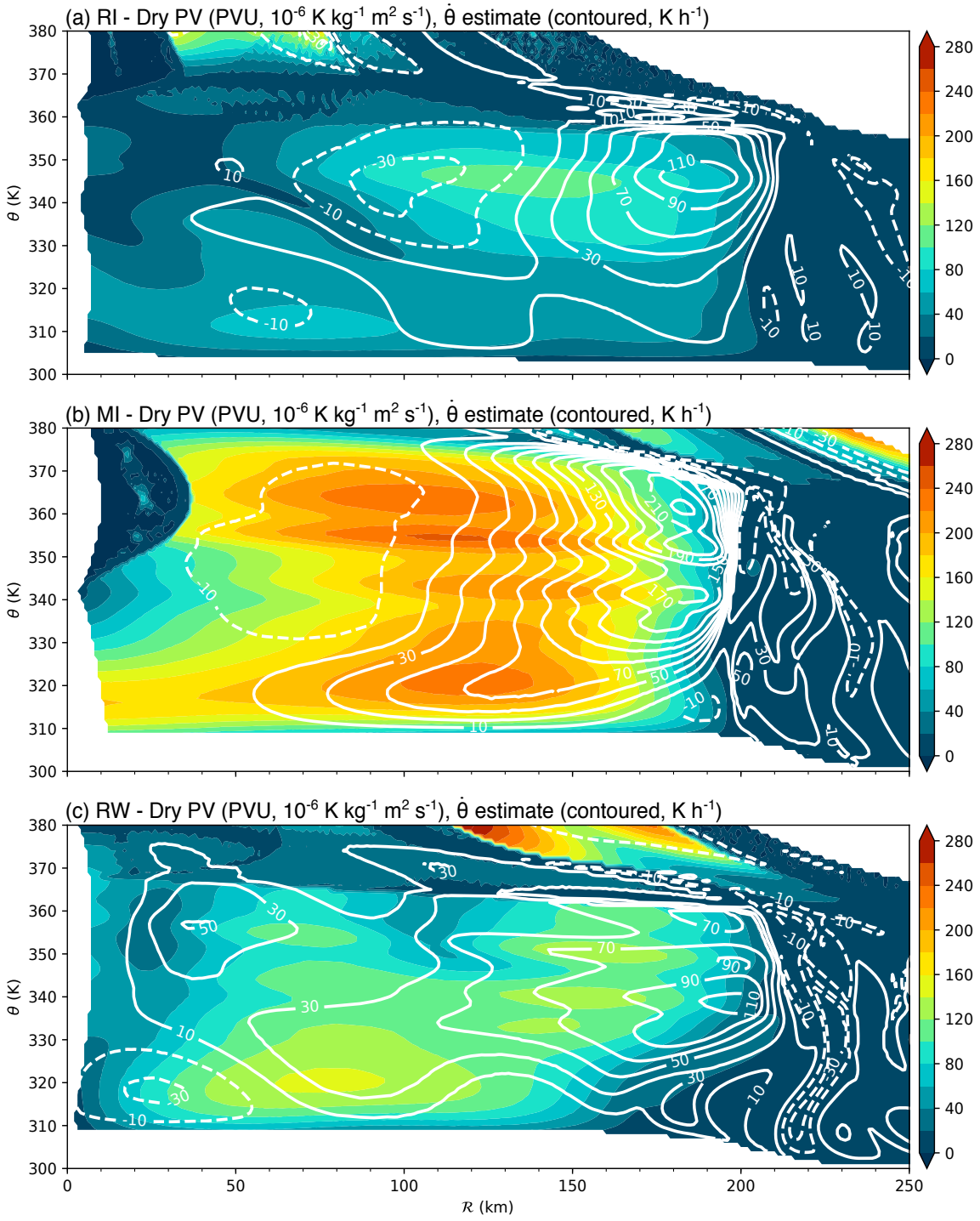

Fig. 2.11. Dry Ertel's PV (shading, PVU; 1 PVU $= 10^{-6}$ K kg^{-1} m^2 s^{-1}) and the diabatic heating ($\dot{\theta}$) estimate (white, contoured at -20, 50, 100, 150, and 200 K h^{-1}) are shown in potential radius and potential temperature (R, θ) space for (a) the rapid intensification (RI), (b) maximum intensity (MI), and (c) rapid weakening (RW) intensive observing periods (IOPs) in Hurricane Patricia.

Figure 2.12 shows the diabatic heating estimate overlaid on Patricia's potential radius and potential temperature structure for each IOP. The heating maximum remains nearly fixed to the same R surfaces (between $R = 180$–200 km) as they contract in physical space. Furthermore, the heating maximum is persistently located radially outward of the PV maximum (see Figs. 2.5 and 2.7). Patricia's structural evolution during rapid intensification can be understood via two processes. The axisymmetric generation of PV from diabatic processes results from projecting radial and vertical gradients of heating on to the absolute vorticity vector. Since the vorticity vector in the eyewall region is oriented radially outward and vertically upward, the generation of PV should occur both radially inward and beneath the diabatic heating maximum. However, the slope of the vorticity vector and heating distribution in the eyewall leads to a partial cancellation between these two individual terms. Therefore, eddy processes are inferred to concentrate the hollow PV tower radially inward of the heating maximum.

The first term on the right hand side of (2.5) includes the effects of eddy torques (Eq. 2.2) on the evolution of PV at a fixed (R, θ) position. Although the eddy terms cannot be calculated from the current analyses, inferences can be drawn to their role in the observed development of Patricia's hollow tower PV structure. Above the frictional boundary layer, it is reasonable to assume a first order local eddy viscosity turbulence closure that implies $\dot{R}$ would be maximized where the M surfaces have the largest radial gradient in physical space, near the eye–eyewall interface (Fig. 2.12). Although eddy sources of momentum can also possess counter-gradient characteristics in TCs (Persing et al. 2013), here it is assumed that the dominant effect of eddy mixing is diffusive and down-gradient. The concentration of the hollow PV tower near $R = 125$ km is consistent with Eq. 2.5 and the idea that diffusive eddy mixing provides a source of P radially inward of the $\dot{R}$ maximum and a sink of P radially outward of the maximum. The location of the $\dot{R}$ maximum moves radially inward in physical space as Patricia intensifies, but remains approximately fixed in potential radius space near $R = 140$ km.

Collectively, the aforementioned heating and eddy processes can explain the observed "in-place" concentration of PV within the (R, θ) framework during RI and MI. Diabatic heating $\dot{\theta}$ concentrates PV near the same R surfaces from RI to MI through vertical gradients of latent heating

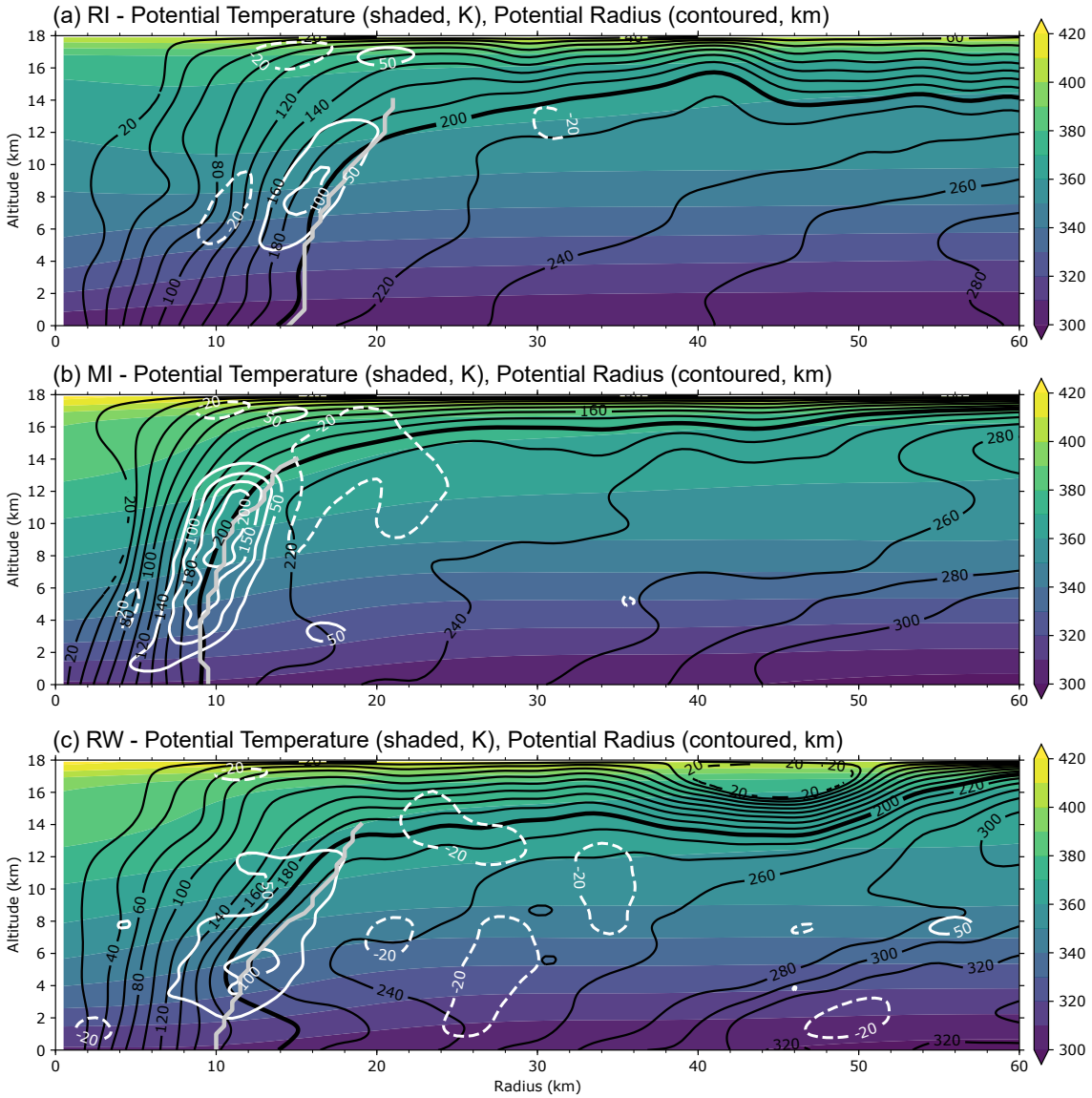

Fig. 2.12. Potential temperature (shaded, K) is overlaid with the potential radius (black, contoured every 20 km) and the diabatic heating ($\dot{\theta}$) estimate (white, contoured at -20, 50, 100, 150, and 200 K h^{-1}) for the (a) rapid intensification (RI), (b) near maximum intensity (MI), and (c) rapid weakening (RW) intensive observing periods (IOPs) in Hurricane Patricia. In each panel, the 200-km potential radius surface is shown in bold and the radius of maximum tangential winds (RMW) is shown in gray.

in the eyewall, with a positive feedback of local tendency as P^2 increases. Eddy torques $\dot{R}$ are maximized radially inward of the heating maximum in the eyewall, thereby concentrating PV near the eye–eyewall interface where the radial gradient of $\dot{R}$ is positive and diluting PV in the eyewall where the radial gradient of $\dot{R}$ is negative. During RW, the PV tower became diluted and expanded radially across R, suggesting that eddy mixing was occurring over a broader region as the eyewall

broke down and asymmetries amplified. Despite the more complicated PV structure during RW, a strong correspondence with the diabatic heating field is still apparent (Fig. 2.11c).

As discussed in section 1.2, the sign reversal of the radial PV gradient satisfies the Rayleigh necessary condition for barotropic instability, which may result in the development of mesovortices and enhanced PV mixing between the eye–eyewall interface. PV mixing associated with barotropic or combined barotropic–baroclinic instability is argued to have potentially played an important role Patricia's observed rapid weakening and vortex breakdown prior to landfall. To provide evidence supporting this argument, 3-D Cartesian SAMURAI analyses are created for both the MI and RW IOPs. Using the same data as the axisymmetric analyses (see Fig. 2.3), the Cartesian analyses are created on a grid with 1-km horizontal spacing and 0.5-km vertical spacing. Figure 2.13 shows the evolution of absolute vertical vorticity in Cartesian coordinates ($\hat{\eta} = f + \partial v/\partial x - \partial u/\partial y$) between MI and RW at both 2- and 6-km altitude as a proxy for PV. The analysis captures an evolution consistent with rapid vorticity mixing; the vorticity "ring" apparent during MI evolved into a structure more closely resembling a "monopole" during RW. Furthermore, through Stokes' theorem, the absolute circulation can be calculated as the area-integrated absolute vorticity within the domain bounded by each analysis shown in Fig. 2.13. In doing so, the absolute circulation at each respective vertical level changes no more than 5% between MI and RW. The approximately conserved absolute circulation in the eye–eyewall region is consistent with the evolution expected from vorticity mixing associated with barotropic instability (Schubert et al. 1999).

In the case of Patricia's evolution, the effects of vertical wind shear and formation of a secondary eyewall may have introduced potential pathways for barotropic instability to ensue. The effects of vertical wind shear likely played a role in reducing Patricia's vertical alignment, tilting the vortex between MI and RW and enhancing asymmetries (see Fig. 20 in Rogers et al. 2017). The developing secondary eyewall disrupts near-surface inflow to the primary eyewall and is accompanied by a significant reduction in diabatic heating within the primary eyewall (cf. Figs. 2.7 and 2.9), Therefore, the formation of a secondary eyewall may have substantially reduced the forcing acting to concentrate PV along the inner edge of the eyewall. Another potential negative factor may have been the introduction of dry air advected from land into Patricia's circulation as it approached

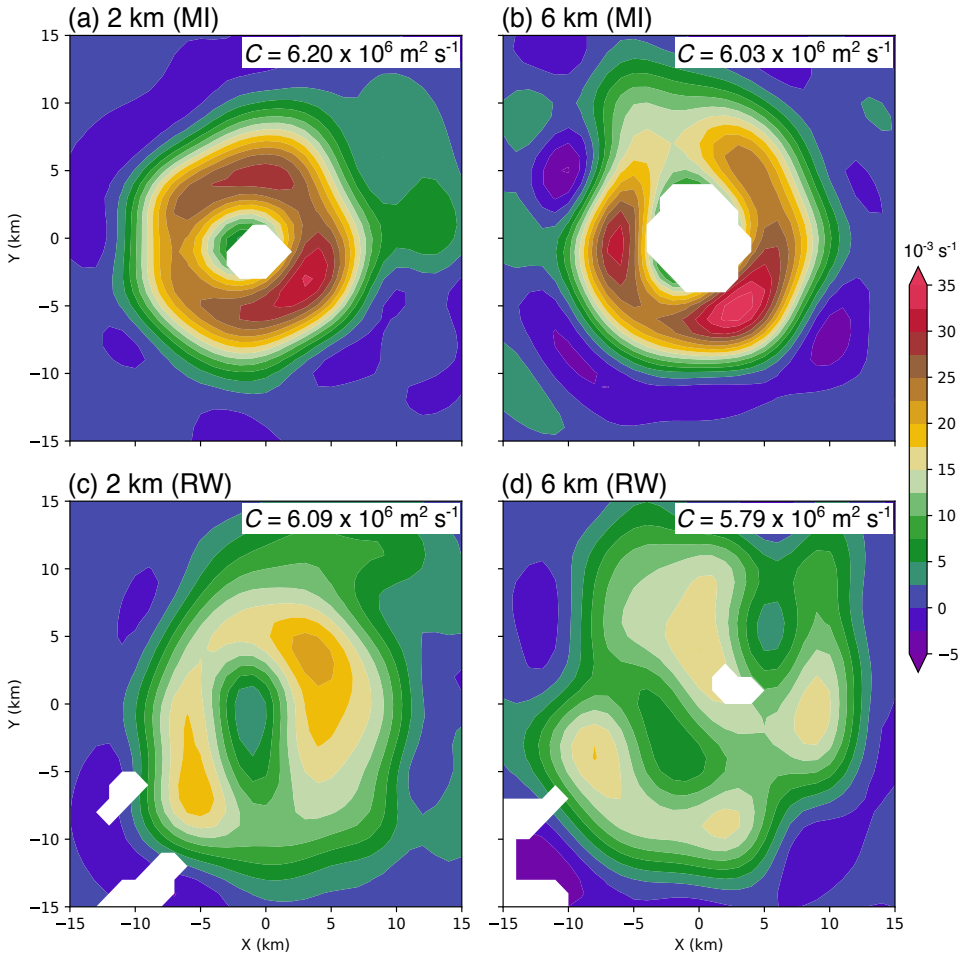

Fig. 2.13. Cartesian SAMURAI analysis for the maximum intensity (MI) and rapid weakening (RW) intensive observing periods (IOPs) in Hurricane Patricia. Absolute vertical vorticity is shown at (a,b) 2- and 6-km altitude for MI and (c,d) 2- and 6-km altitude for RW, respectively. The absolute circulation calculated within the horizontal domain bounded by the figures is shown in the upper right corner of each respective panel.

the coast of Mexico. Although the present observational analysis precludes a detailed diagnosis of the relative importance of the various aforementioned factors, Patricia's observed structural change collectively suggests that multiple processes contributed rapid weakening. It is difficult to explicitly calculate the most unstable modes and growth rates from the observations because of their strong sensitivity to resolved gradients and spatial filtering. A combination of internal and external factors is hypothesized to have sufficiently disrupted the diabatic forcing within Patricia's primary eyewall, facilitating instabilities to rapidly breakdown the symmetric PV ring and contributing to enhanced mixing between the eye–eyewall interface. Further confirmation of this proposed evolution for rapid weakening may require high-resolution numerical modeling.

2.5.3 Comparisons to earlier observations

Comparisons to the observed PV structure of other TCs are limited because of the difficulties in resolving thermodynamic gradients required to calculate PV from observations. A mid-level PV maximum was noted in a western North Pacific composite analysis of typhoons (Schubert and Hack 1983; their Fig. 4) and in Hurricane Gloria of 1985 (Shapiro and Franklin 1995; their Fig. 11). Bell and Montgomery (2008) highlighted a low-level PV maximum in the eye of Hurricane Isabel (2003), which is similar to that seen in Hurricane Patricia. This "PV bridge" structure has been attributed to preferential PV mixing at low levels where both the shear and curvature vorticity are maximized, leading to a rapid growth of the most unstable modes (Hendricks and Schubert 2010). Hendricks and Schubert (2010) also attributed the low-level PV bridge structure to the enhanced stratification found near the subsidence inversion in the eye. Recent studies have shown that high PV transported from the eyewall into the eye at low levels can contribute to increased stratification, suggesting that the low-level inversion itself may in part be dynamically driven through PV mixing (Rozoff et al. 2009; Hendricks and Schubert 2010).

As Patricia reached its maximum intensity, the magnitude of PV concentrated within the hollow tower was approximately 3–4 times greater than that observed in Gloria (Shapiro and Franklin 1995; Shapiro 1996) and Isabel (Bell and Montgomery 2008). A similar structure was documented by Hausman et al. (2006); the authors used an axisymmetric model to simulate a TC that developed a hollow PV tower with maximum values of $\sim$275 PVU. The compact RMW, the vertically coherent PV tower with a mid-level PV maximum, and the intense wind speed in the simulated TC from Hausman et al. are remarkably similar to Patricia and suggest that axisymmetric processes can provide a reasonable first order approximation to explain Patricia's rapid intensification. However, the idealized TC in Hausman et al. (2006) does not weaken after achieving maximum intensity. As was hypothesized above, a combination of internal asymmetric processes and external environmental forcing is necessary to explain Patricia's observed rapid weakening.

Earlier studies that attempted to calculate PV in a TC had to rely on determining the mass field via a balance assumption whereby the observed winds are used to calculate the mass field given

an imposed balance condition (e.g., Schubert and Hack 1983; Shapiro and Franklin 1995; Shapiro 1996). To examine the validity of a balance assumption, PV is calculated using the mass fields that would be in gradient wind and hydrostatic balance with the observed wind fields for both the RI and RW analyses[5] following the method described by Smith (2006) and Foerster and Bell (2017). During RI, PV calculated using the balanced mass field is qualitatively similar to the analyzed PV maximum in the mid-troposphere, but shows distinct quantitative differences, especially in the lower troposphere and outflow layer where the "balanced" PV is much lower (Fig. 2.14a). Differences are largest in the regions where gradient wind balance is a poor approximation for the observed winds. Calculating PV from the balanced mass field is particularly problematic during the RW period (Fig. 2.14b) given that the tangential velocity increases with height up to its maximum near 5-km altitude (Fig. 2.8a), requiring that the isentropes slope upward approaching the axis of rotation via thermal wind balance (i.e., a cold-core cyclone). Compounding errors result when calculating the gradients of unrealistic isentropic structures necessary to calculate PV (not shown). Similar issues resulting from calculating PV using a balance assumption were noted by Shapiro and Franklin (1995). Therefore, the balance assumption is concluded to be a reasonable first-order approximation above the boundary layer and below the outflow layer during the RI analysis, but the balance assumption is largely invalid during the RW analysis because of large regions with unbalanced flow. These results suggest that the high-resolution thermodynamic observations obtained from the XDDs are crucial in permitting the calculations of PV presented herein.

2.6 Discussion and conclusions

A new observational dataset created from the Tropical Cyclone Intensity experiment (TCI; Doyle et al. 2017) and the Intensity Forecasting Experiment (IFEX; Rogers et al. 2006, 2013a) field campaigns provided an opportunity to investigate the record-breaking evolution of Hurricane Patricia (2015). Dropsondes released with high spatial resolution from approximately 18-km altitude allowed for an unprecedented full-tropospheric analysis of a TC experiencing rapid intensity

[5]Since the MI analysis used the thermodynamic analysis valid during RW, a comparison to the mass field calculated using a balance assumption during MI would be indirect.

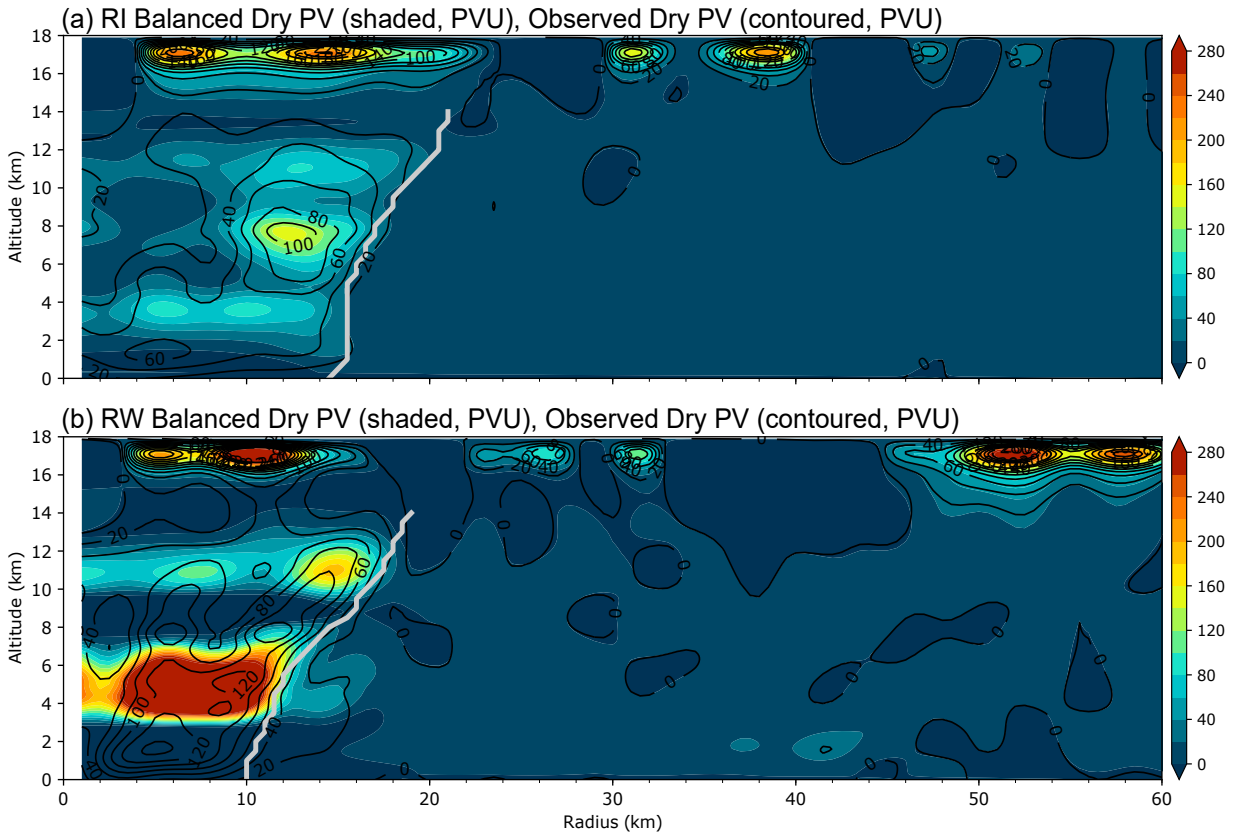

Fig. 2.14. "Balanced" potential vorticity comparison for (a) the rapid intensification (RI) and (b) rapid weakening (RW) intensive observing periods (IOPs). PV calculated from the balance assumption (shaded, PVU; 1 PVU $= 10^{-6}$ K kg^{-1} m^2 s^{-1}) is overlaid with PV calculated from each respective SAMURAI analysis (contoured, PVU) using the same 20 PVU contour interval. See section 2.5.3 for additional details.

changes. The analyses presented herein provide the first full-tropospheric, axisymmetric calculations of Ertel's potential vorticity (PV) within the inner-core of a TC, derived from observations without the use of balance assumptions. Observations gathered during three intensive observing periods (IOPs) by the NOAA P-3 and NASA B-57 aircraft provided information at three critical stages during Patricia's life cycle: rapid intensification (RI), near maximum intensity (MI), and rapid weakening (RW).

During the rapid intensification phase, Patricia's structure was characterized by a hollow tower PV structure concentrated along the inner edge of the radius of maximum tangential winds (RMW). The low-level eye (beneath ∼3-km altitude) exhibited a secondary PV maximum that was related to both the subsidence inversion and mixing between the eye–eyewall interface. The present analysis confirms the co-existence of a PV bridge at low levels and a hollow tower PV structure with a

mid-level maximum during rapid intensification. Near maximum intensity, the hollow PV tower extended throughout the depth of the troposphere with peak values exceeding 250 PVU. To the author's knowledge, Patricia's hollow PV tower possesses the largest tropospheric PV documented from observations in the literature to date.

Discrete PV maxima were also noted in the upper-troposphere–lower-stratosphere (UTLS) region in association with strong static stability. These discrete upper-level PV "rings" have been noted in past numerical simulations (e.g., Kieu and Zhang 2010), but their role in Patricia's intensity change is currently unclear and warrants further investigation. It is worth noting that during each IOP, the UTLS PV rings located between $r = 40$–50 km were accompanied by anticyclonic PV anomalies radial outward of their location (visible in Fig. 2.5b despite the color scale saturating at 0 PV but located beyond the 60-km domain shown in Figs 2.7b and 2.9b). The radial pattern of cyclonic and anticyclonic UTLS PV anomalies is congruous with the structure of mesoscale "PV dipoles" discussed by Hitchman and Rowe (2019). It is possible that deep convection associated with Patricia's principal rainband and secondary eyewall provided a pathway for the development of a PV dipole; tilting of horizontal vorticity concomitant with the vertical transport of anomalous cyclonic momentum into the UTLS region would result in the formation of a PV dipole with an anticyclonic PV anomaly positioned radially outward of a cyclonic PV anomaly. Additional analyses would be necessary to substantiate the formation of PV dipoles in Hurricane Patricia as described by Hitchman and Rowe (2019).

The hollow tower PV structure observed in Patricia's eyewall supported the Charney–Stern necessary condition for combined barotropic–baroclinic instability. Patricia's rapid weakening over a 3-h period was influenced by increasing vertical wind shear, a secondary eyewall, and possibly by dry air from the nearby landmass; together, these factors contributed to reducing the symmetric heating in Patricia's eyewall. Evidence of vorticity mixing between the eye–eyewall interface and an approximate conservation of absolute circulation in this region suggest that barotropic or combined barotropic–baroclinic instability may have played an important role during Patricia's rapid weakening. Collectively, the aforementioned influences from both internal and external processes resulted in a broader, weaker PV tower with maximum values of $\sim$160 PVU.

Additional insight into Patricia's evolution was obtained by transforming the PV analyses to potential radius–potential temperature (R, θ) coordinates. The rapid development of Patricia's hollow PV tower within the (R, θ) framework essentially occurred "in-place" along the same absolute angular momentum surfaces as they contracted in physical space. The Eulerian PV tendency equation in (R, θ) coordinates indicates that PV is concentrated more quickly in regions with preexisting large values of PV, suggesting that the rapid vertical development of the PV tower resulted from sustained vertical mass flux and heating in the eyewall region. The location of the PV maximum radially inward of the heating maximum was inferred to result from eddy mixing near the eye–eyewall interface. The rapid breakdown of Patricia's hollow PV tower during the transition from MI to RW can be explained within the (R, θ) framework as resulting from increased eddy mixing over a broad radial region, but a strong correspondence of the PV field with the symmetric heating distribution is still evident during Patricia's rapid weakening. The absolute circulation was shown to be approximately conserved during the rapid weakening, substantiating the evolution expected from eddy-driven vortex breakdown put forth in earlier idealized work (e.g., Schubert et al. 1999).

The observational analyses presented herein illustrate the evolution of Hurricane Patricia within an axisymmetric framework and provide some validation of the PV conceptual model to provide insight into rapid TC intensity changes. However, the present axisymmetric PV analyses are fundamentally limited in their representation of Patricia's full 3-D evolution, both temporally and spatially. Although the calculation of 3-D Ertel's PV from observations is difficult, it may be possible with a combination of high-resolution dropsondes and Doppler radar data in future observational analyses of TCs and can help provide further insight into TC evolution. Along with observations, high-resolution numerical simulations are necessary to examine the key processes contributing to rapid intensity changes and to better predict TC intensity prior to landfall. Future work will further investigate the role of asymmetric processes during Patricia's evolution and compare the observed features presented herein with other TCs to further explore the utility of a PV framework for understanding TC structure and intensity change.

CHAPTER 3

On the nature and evolution of asymmetric structures during tropical cyclone rapid intensification

3.1 Overview

Conceptual models of tropical cyclone (TC) evolution are often established in the context of axial symmetry and deviations from axial symmetry, designated as asymmetries or eddies. Satellite and radar imagery of numerous TCs depict a variety of asymmetric structures during all stages in the TC life cycle, with some of the more salient asymmetric features arising from contrasts in the nature of convection embedded within the TC circulation. Previous studies have documented bouts of asymmetric convection during the rapid development phase of a TC that aid in moistening the incipient vortex and concentrating potential vorticity (PV) near its core (Hendricks et al. 2004; Montgomery et al. 2006). Following the developmental phase, low-wavenumber PV asymmetries near the TC core persist throughout the rapid intensification phase and are often accompanied by continued bouts of asymmetric convection prior to the TC achieving its maximum intensity (e.g., Nguyen et al. 2008).

Asymmetric structures comprise various scales in a TC circulation, including but not limited to: turbulent eddies, vortical hot towers, vortex Rossby waves, mesovortices, and spiral rainbands. Conceptual models of TC intensification often depict a structural evolution where "eddies grow at the expense of the mean"; that is, the entire spectrum of eddies is often considered to produce a net-negative contribution to TC intensification (e.g., Nolan and Montgomery 2002; Nolan and Grasso 2003; Nolan et al. 2007). Within this conceptual model, it can be argued that either

(1) in the absence of eddies, a purely symmetric TC would have reached a relatively higher intensity, or similarly,

(2) in the absence of eddies, a purely symmetric TC would have intensified more quickly[6].

[6]Of course, a trivial counterargument would posit that a purely symmetric TC is inconceivable and therefore the entire subject is dispensable; a concern rectified by framing 1) and 2) with gradations of symmetry rather than pure symmetry.

Although it may be difficult to argue against maximizing the "symmetric mode" as a pathway toward maximizing intensification rates, it is unclear that the presence of vortex asymmetries necessarily entails a reduction in the symmetric mode. It would indeed be the case if one presupposes that eddies grow at the expense of the mean; however, one can just as easily conceive a scenario where eddy interactions instead contribute positively to the symmetric mode. Therefore, the role of asymmetries must come under further scrutiny.

In this chapter, an idealized, high-resolution (1-km horizontal grid spacing) simulation of a TC undergoing rapid intensification is examined in detail to begin clarifying the role of asymmetries throughout the intensification process. Section 3.2 describes the initial conditions for the idealized TC simulation and provides context for establishing the initial vortex structure. Section 3.3 describes the numerical modeling framework. Section 3.4 quantifies the bulk magnitude and azimuthal scales of inner-core asymmetries throughout the intensification period. Section 3.5 discusses the overall structural evolution of the simulated TC for three time slices representing the approximate intensification period quartiles prior to the TC attaining its maximum intensity. Sections 3.6–3.8 present the framework for categorizing the scale of asymmetries, and scale-dependent contributions to TC intensification are assessed with the azimuthal-mean PV budget. Section 3.9 compares the evolution of the simulated TC in potential radius–potential temperature space to Hurricane Patricia. Section 3.10 presents a discussion of the principal findings and avenues toward further understanding asymmetric contributions to TC intensification.

3.2 Initial environment and vortex structure

The idealized simulation is initialized with a horizontally homogeneous environment that is characteristic of the climatological average atmospheric conditions observed in the Caribbean and North Atlantic basin during the July–October hurricane season (Dunion 2011). The environmental sounding is commonly referred to as the "Dunion moist-tropical" sounding and its thermodynamic characteristics are shown in Fig. 3.1. A weak, cyclonic vortex representing a tropical depression is superposed on the initial environment to facilitate the development of a TC. Although extensive 3-D observations of tropical depressions are limited, the initial vortex is constructed in light of available information. Precursor disturbances to cyclogenesis are often characterized by a broad cyclonic

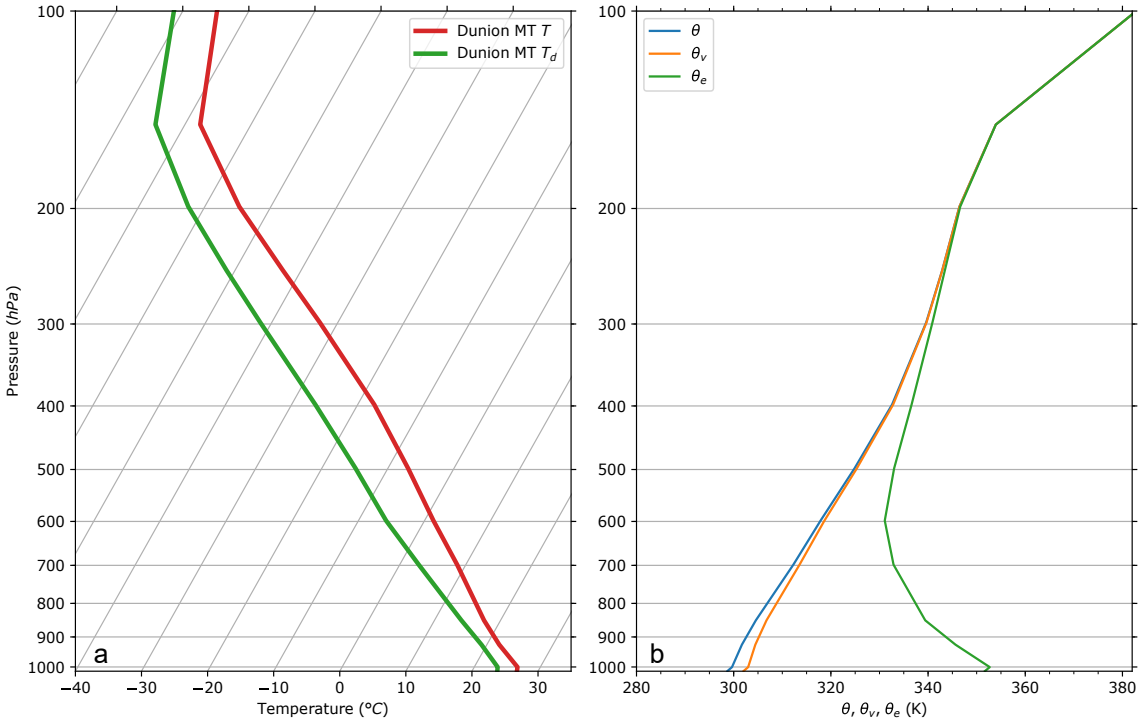

Fig. 3.1. (a) Temperature (red, °C) and dewpoint temperature (green, °C) are shown as a function of log-pressure for the Dunion moist-tropical sounding. (b) Potential temperature (blue, K), virtual potential temperature (orange, K), and equivalent potential temperature (green, K) are shown as a function of log-pressure for the Dunion moist-tropical sounding.

circulation comprising a mid-level vortex (e.g., McBride and Zehr 1981; Bister and Emanuel 1997; Gray 1998; Raymond et al. 2011). The cyclonic PV anomaly that accompanies a mid-level vortex is balanced by a relatively warm potential temperature anomaly above its circulation and a relatively cool potential temperature anomaly below (Raymond and Jiang 1990; Raymond et al. 2014).

Collectively, information gathered from the aforementioned studies suggest that an initial vortex representing a tropical depression should possess a broad cyclonic circulation with maximum winds displaced above the surface. The radial structure of tangential velocity is prescribed via a modified Rankine vortex of the form

$$v(r) = \begin{cases} v_{max}\left(\frac{r}{r_{max}}\right) & 0 \leq r < r_{max} \\ v_{max}\left(\frac{r}{r_{max}}\right)^{-\alpha} & r \geq r_{max}, \end{cases} \tag{3.1}$$

where $v_{max} = 15$ m s^{-1} is the maximum tangential velocity, $r_{max} = 135$ km is the radius of maximum tangential winds (RMW), and $\alpha = 0.3$ is the decay of tangential velocity radially outward of the

RMW. Ritchie and Holland (1999) constructed a similar initial vortex for their idealized simulations based on the composite observations of tropical depressions from McBride and Zehr (1981)[7]. After the radial structure of the initial vortex is prescribed, a decay function is applied radially outward of the RMW following Nolan (2007) to ensure that the total circulation within the doubly periodic model domain is zero. The radial decay function is given by

$$v(r) = v_0(r) \exp\left(-\frac{r}{R}\right), \tag{3.2}$$

where $v_0(r)$ denotes the initial modified Rankine vortex profile given by (3.1), r is the radius, and R is set to 600 km.

The initial vortex is then extended in the vertical following Nolan (2007) such that the initial axisymmetric vortex structure is given by

$$v(r,z) = v(r) \exp\left(-\frac{|z - z_{max}|^{\beta}}{\beta L_z^{\beta}}\right), \tag{3.3}$$

where $v(r)$ is the initial modified Rankine vortex profile after the radial decay function has been applied, z the altitude, z_{max} the altitude of maximum tangential velocity, L_z the depth of an approximately barotropic region of the vortex, and β the vertical decay of tangential velocity above and below the barotropic region. To construct a tropical depression with maximum tangential velocity displaced above the surface, z_{max} is set to 1.5 km, L_z is set to 2.5 km and 3.5 km above and below z_{max}, respectively, and β is set to 1.8. The initial axisymmetric vortex structure is shown in Fig. 3.2 and is characterized by a maximum surface tangential velocity of $\sim$12 m s^{-1}. Additionally, the initial axisymmetric vortex is characterized by an $\sim$3 K warm potential temperature anomaly above 1.5-km altitude and an $\sim$3 K cool potential temperature anomaly below 1.5-km altitude. Axisymmetric potential temperature anomalies are defined relative to the height-dependent average between $r = 500$–600 km.

[7]Rios-Berrios (2020) identified the motivation in creating this common initial vortex structure for idealized TC simulations.

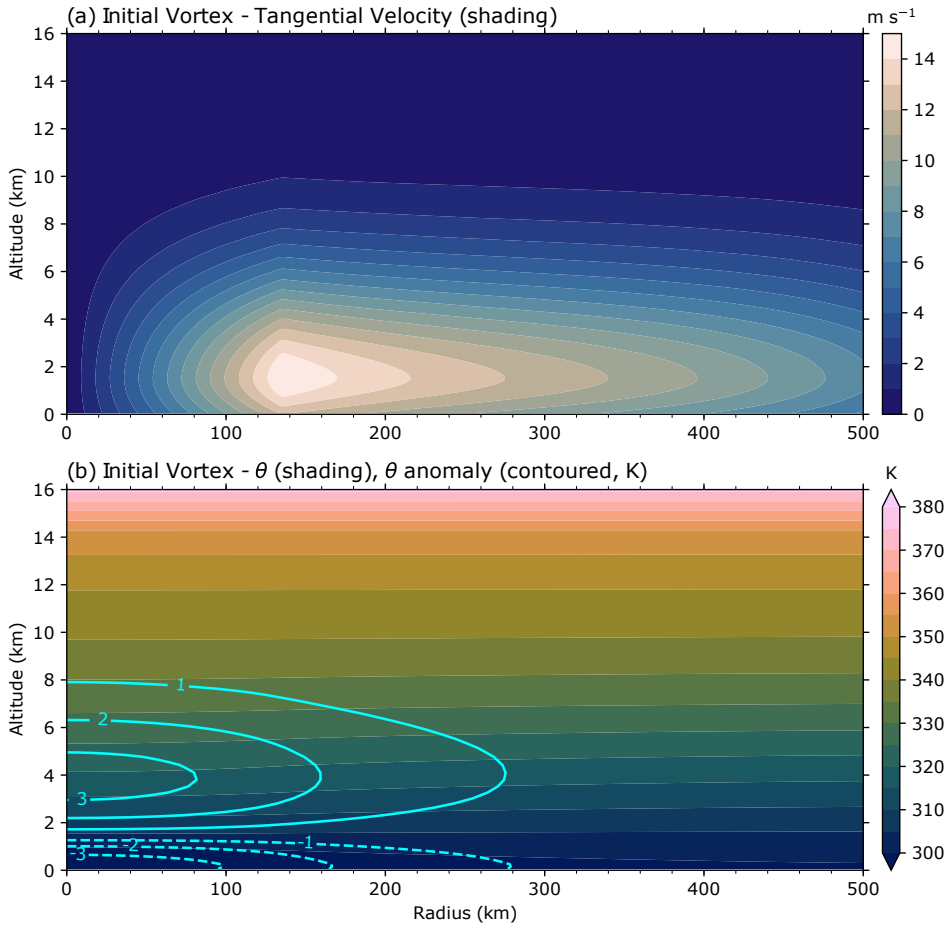

Fig. 3.2. The initial axisymmetric vortex structure is shown for the idealized tropical cyclone simulation. (a) The axisymmetric tangential velocity is shown in shading and (b) the axisymmetric potential temperature (shading) is overlaid with the axisymmetric potential temperature anomaly (contoured, K) relative to the height-dependent average between $r = 500$–600 km.

3.3 Numerical model setup

The idealized TC is simulated with the nonhydrostatic, fully compressible Cloud Model 1 (CM1) version 19.7 (Bryan and Fritsch 2002). The horizontal grid spans 2670×2670 km and is defined with a uniform 1-km grid spacing in the innermost 800 km that gradually stretches to 10-km spacing at the domain boundaries. There is a total of 1140×1140 grid points contained within a doubly period domain. The vertical grid spans 26 km in altitude. The vertical grid is defined with 100-m grid spacing in the lowest 2-km altitude that gradually stretches to 500-m spacing at 8-km altitude and is constant 500-m spacing above 8-km altitude. There is a total of 76 vertical grid

points. A Rayleigh damping layer is applied above 22-km altitude to aid in mitigating the reflection of internal gravity waves.

The TC simulation is integrated for seven days on an f-plane corresponding to $\sim$15 N with underlying sea-surface temperatures fixed at 28°C. Radiative processes are approximated via a simple 2 K day^{-1} Newtonian relaxation to the base-state temperature profile (Rotunno and Emanuel 1987). Microphysical processes are parameterized with the Morrison double-moment scheme and graupel is selected as the large ice category (Bryan and Morrison 2012). Sub-grid scale turbulent processes are parameterized with a first-order local closure commonly referred to as the "Louis PBL scheme" (Louis 1979; Kepert 2012; Bryan et al. 2017). The horizontal and vertical eddy viscosities are separately determined given the local flow deformation and the moist Brunt-Väisälä frequency. The heat diffusivity is taken as identical to the momentum diffusivity such that the Prandtl number is unity. This turbulence parameterization requires specifying the horizontal and vertical mixing length scales, chosen herein as $l_h = 1000$ m and $l_v = 100$ m, respectively.

Rather than placing the incipient vortex in a quiescent environment, a 5 m s^{-1} uniform easterly flow is imposed throughout the domain following a methodology similar to the time-varying point-downscaling (TVPDS) technique (Onderlinde and Nolan 2017). The uniform flow is introduced by adding a Newtonian relaxation term to the horizontal momentum equations, given by

$$\frac{\partial u}{\partial t} = \ldots - \frac{\langle u \rangle - u_{ref}}{\tau_n}, \tag{3.4}$$

and

$$\frac{\partial v}{\partial t} = \ldots - \frac{\langle v \rangle - v_{ref}}{\tau_n}, \tag{3.5}$$

where $\langle u \rangle(z)$ and $\langle v \rangle(z)$ denote the domain-averaged zonal and meridional wind velocities, respectively, $u_{ref}(z,t)$ and $v_{ref}(z,t)$ denote the reference zonal and meridional wind profiles to nudge toward, respectively, and τ_n is the nudging time scale. Thus, domain-averaged winds at each vertical level are nudged toward a specified reference profile that is a function of height and time, avoiding the introduction of a net circulation into the domain. The nudging time scale τ_n sets the rate at which the domain-averaged winds are nudged toward the reference wind profiles. The incipient vortex is permitted 12 h to develop deep, moist convection within a quiescent environment prior

to introducing the 5 m s^{-1} uniform easterly flow with a 6 h nudging timescale. A time-varying translational domain is updated each hour in the simulation to track the minimum of a smoothed surface-pressure field that represents the approximate vortex center, and the domain translation velocity vector is subtracted from the total wind to produce grid-relative winds.

The center location is further refined by locating the point that maximizes the tangential circulation within a 5-km annulus centered on the RMW using a simplex algorithm (Marks et al. 1992; Lee and Marks 2000). Following the summary provided in section 2 of Bell and Lee (2012), a set of nine "center guesses" is specified for each vertical level between 1–10 km altitude; all of the sets comprising nine center guesses are centered on the smoothed surface-pressure minimum. The first-guess RMW at each vertical level is determined in accordance with the smoothed surface-pressure minimum center location, and then a set of 11 circuits (radius rings) is constructed in increments of 1-km radius, centered on the first-guess RMW. The centroid of a 2-simplex (triangle) is placed at each of the nine center guess locations for each of the radius rings, yielding 99 independent simplexes for a given vertical level.

The azimuthal-mean tangential velocity within a 5-km annulus centered on a given radius ring is calculated at the vertices of the simplexes. The optimization procedure for an individual simplex ensues via four potential operations to locate a new point in the (x, y) plane that maximizes the azimuthal-mean tangential velocity: reflection, expansion, contraction, and shrink[8]. The number of iterations for a sequence of operations is limited to 30 for each simplex and the tolerance for convergence of the algorithm is specified as 10^{-4} km. The parameters corresponding to the distance for each potential operation listed above and the initial simplex size are given by the default options described in Julia's Optim package (Mogensen et al. 2020). Once the simplex algorithm has either converged or reached the maximum number of iterations, there remain nine "preliminary" center locations for a given radius ring. The mean and standard deviation of the center locations are computed for each radius ring and outliers located beyond one standard deviation of the mean center location are removed, forming a set of "converging centers". The mean of the converging center locations is computed for each radius ring and the "optimal" center location corresponds

[8]See section 3 of Lee and Marks (2000) for a detailed description of the simplex algorithm procedure.

to the radius ring that maximizes the azimuthal-mean tangential velocity (i.e., the RMW). The analysis center for each time step is then defined by layer-averaging the optimal center locations identified between 1–10 km altitude.

3.4 Vortex intensification and symmetricity

The maximum azimuthally averaged wind speed at the lowest model level (25 m), the corresponding RMW, and the minimum sea-level pressure are shown as a function of time in Fig. 3.3. The initiation of rapid intensification (RI) is defined following a method similar to that used by Judt and Chen (2016) and Rios-Berrios et al. (2018), which is motivated by the approximate 95th percentile of 24-h over-water TC intensification rates in the North Atlantic basin (Kaplan et al. 2010). The initiation of RI is specified as the first (hourly) time step where the subsequent 24-h intensification rate exceeds 15.4 m s^{-1} and each consecutive 6-h intensification rate within the 24-h time window exceeds 3.8 m s^{-1}. The black dots in Fig. 3.3 denote the initiation of RI occurring at $t = 71$ h and maximum intensity occurring at $t = 143$ h in the simulation. The time scale of interest for this study occurs between the initiation of RI and maximum intensity, henceforth defined as the intensification period. During the 72-h intensification period, the TC intensifies 70 m s^{-1}, deepens 100 hPa, and the RMW contracts approximately 30 km.

Here, the definition of Ertel's PV (Ertel 1942) is introduced to facilitate the following discussion. Let ρ denote the dry air density, $\mathbf{\Omega}$ the Earth's angular velocity vector, $\mathbf{u}$ the three-dimensional velocity vector, $\eta = 2\mathbf{\Omega} + \nabla \times \mathbf{u}$ the absolute vorticity vector, and θ the potential temperature. Then, the dry Ertel's PV is given by

$$P = \frac{1}{\rho} \eta \cdot \nabla \theta. \tag{3.6}$$

Henceforth, references to "PV" are given by Eq. 3.6.

To assess the bulk evolution of asymmetric structures during the intensification period, the magnitude of inner-core asymmetries are first examined. In a cylindrical coordinate framework, an arbitrary scalar ψ (or vector) can be partitioned into components representing axial symmetry and deviations from axial symmetry such that

$$\psi(r, \phi, z, t) = \bar{\psi}(r, z, t) + \psi'(r, \phi, z, t), \tag{3.7}$$

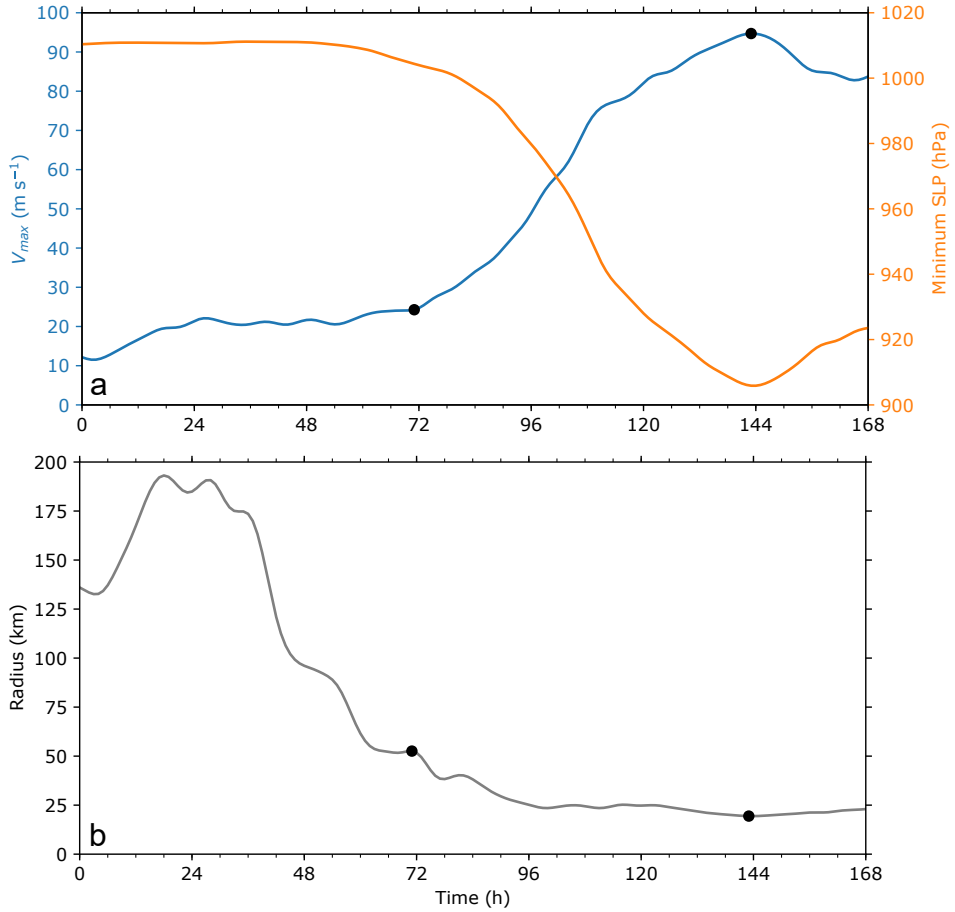

Fig. 3.3. (a) The maximum azimuthally averaged wind speed at the lowest model level (25 m) and the minimum sea-level pressure are shown as a function of time for the idealized tropical cyclone simulation. The domain translation velocity is included in the wind speed calculation. (b) The azimuthally averaged radius of maximum tangential winds (RMW) at the lowest model level is shown as a function of time. Each time series is smoothed using a 12-h low-pass Lanczos filter with nine weights.

where r denotes the radial axis, ϕ the azimuthal axis, z the vertical axis, t the time, $\bar{\psi}$ the component representing axial symmetry, and ψ' the component representing deviations from axial symmetry (henceforth, asymmetries). The magnitude of symmetry can then be quantified for ψ by

$$S_{\psi} = \frac{|\bar{\psi}|}{|\bar{\psi}| + \frac{1}{2\pi}\int_0^{2\pi} |\psi'| \, \partial\phi}. \tag{3.8}$$

Thus, S_{ψ} quantifies the absolute deviation from axial symmetry in contrast to the squared deviation (Miyamoto and Takemi 2013; Miyamoto and Nolan 2018). S_{ψ} is defined between 0–1 with 0 denoting an entirely asymmetric structure and 1 denoting an entirely symmetric[9] structure.

[9]The adjective "symmetric" refers to axial symmetry and is interchangeable with "axisymmetric".

The magnitude of symmetry, often referred to as symmetricity, is computed for the mass-weighted PV and heating/cooling from microphysical processes $\dot{\theta}$ between two layers: 1–3 km altitude (low) and 5–8 km altitude (high). Hence, the symmetricity is reduced to a function of radius and time. Symmetricity is then area-averaged between the axis of rotation and $1.5 \times RMW_{z=2km}(t)$ for the low layer and $1.5 \times RMW_{z=6km}(t)$ for the high layer. Figure 3.4 shows time series for the low- and high-layer symmetricity corresponding to the intensification period. Note that the azimuthal distributions of both PV and $\dot{\theta}$ are never fully symmetric during the intensification period. Rather, the azimuthal PV distribution fluctuates between ∼40–70% symmetricity while the azimuthal $\dot{\theta}$ distribution generally progresses toward larger symmetricity throughout the intensification period.

To further investigate the scales of PV asymmetries during the intensification period, the low- and high-layer PV are represented as Fourier series along the azimuthal dimension, given by

$$P_m(r,t) = \sum_{j=0}^{J-1} P(r,j,t)\left[cos(2\pi mj/J) + isin(2\pi mj/J)\right], \tag{3.9}$$

where $P(r,j,t)$ is the layer-averaged PV, m the azimuthal wavenumber ($m = 0,1,2,\ldots,180$), r the radius, j the azimuth angle in degrees ($j = 0,1,2,\ldots,J = 360$), and t the time. The Fourier coefficient for each azimuthal wavenumber is given by $P_m(r,t)$. Then, the power for each azimuthal wavenumber is given by

$$\mathcal{P}_m(r,t) = \frac{1}{J^2}|P_m(r,t)|^2, \tag{3.10}$$

and the normalized power for each azimuthal wavenumber is given by

$$\hat{\mathcal{P}}_m(r,t) = \frac{\mathcal{P}_m(r,t)}{\sum_m \mathcal{P}_m(r,t)}. \tag{3.11}$$

The normalized power spectra (3.11) for each layer are computed for individual radius circuits within the inner-core region following the same method as the symmetricity analysis and then area-averaged for each hourly time step.

Figure 3.5 shows the normalized power spectra for each layer as a function of time during the intensification period and truncated at azimuthal wavenumber $m = 12$. During the first 25 h

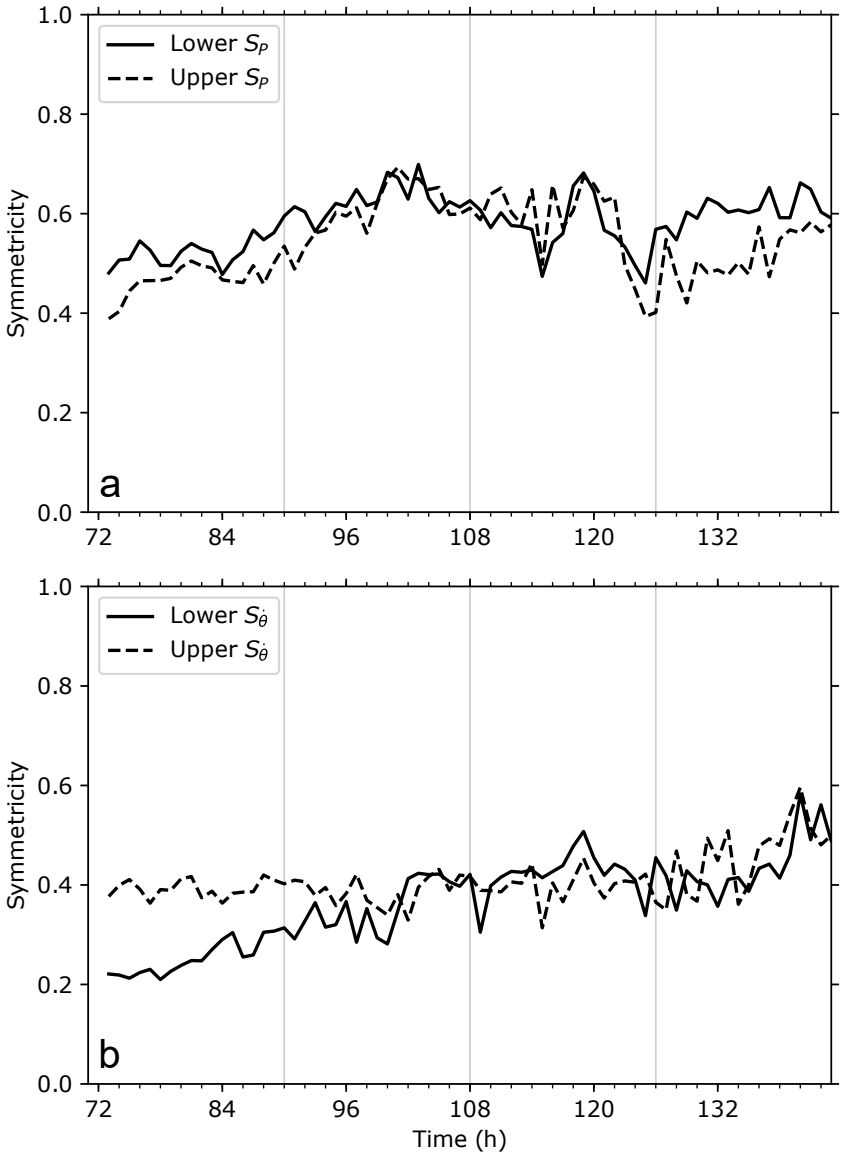

Fig. 3.4. Time series are shown for the low-layer (1–3 km altitude) and high-layer (5–8 km altitude) (a) potential vorticity (PV) symmetricity and (b) heating ($\dot{\theta}$) symmetricity during the intensification period. Vertical gray lines are overlaid at 18-h intervals, denoting the approximate intensification period quartiles beginning at $t = 90$, 108, and 126 h. See section 3.4 for details on how the symmetricity is defined.

of intensification, the inner-core asymmetric PV is distributed across a broad range of azimuthal scales. As intensification continues, the low-layer azimuthal PV distribution becomes increasingly concentrated among lower wavenumbers (i.e., asymmetries with larger azimuthal scales). Although the low and high layers are nearly equivalent in PV symmetricity throughout the intensification period, Fig. 3.5 demonstrates that the high-layer PV is distributed across a broader range of azimuthal scales compared to the low-layer PV.

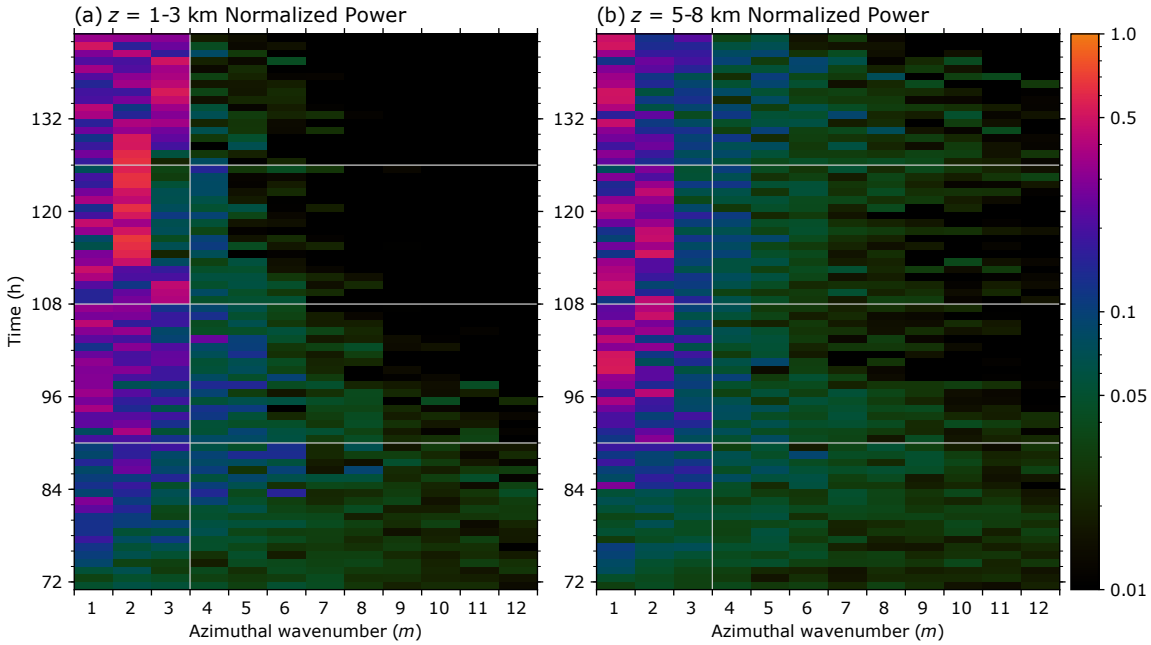

Fig. 3.5. The inner-core potential vorticity (PV) normalized power spectra are shown as a function of azimuthal wavenumber m and time for the (a) low layer (1–3 km altitude) and (b) high layer (5–8 km altitude). Horizontal gray lines are overlaid at 18-h intervals, denoting the approximate intensification period quartiles beginning at $t = 90$, 108, and 126 h. The vertical gray line separates the low-wavenumber PV (azimuthal wavenumbers $m = 1$–3) from the high-wavenumber PV truncated at azimuthal wavenumber $m = 12$. See section 3.4 for details on how the normalized power spectra are constructed.

Figure 3.6 shows the normalized power spectra cumulatively summed over each azimuthal wavenumber. Beginning with the low-layer PV asymmetries, 90% of the power becomes concentrated within azimuthal wavenumbers $m = 1$–3 near the midway point of the intensification period ($t = 108$ h). Note that this time corresponds to a slight reduction in the intensification and deepening rates (see Fig. 3.3). Transitioning to the high-layer PV asymmetries, 90% of the power becomes concentrated within azimuthal wavenumbers $m = 4$–12 near $t = 96$ h, but fluctuates more thereafter in comparison to the low-layer PV asymmetries. Therefore, the high-layer asymmetric PV is distributed among a broader range of smaller azimuthal scales compared to the low layer.

Results discussed up to this point have demonstrated that the inner-core azimuthal distributions of PV and $\dot{\theta}$ are never fully symmetric during the intensification period, further stimulating the primary question raised in this chapter: do asymmetries facilitate or interfere with TC intensification? Toward addressing this question, the following sections will elucidate the evolution of symmetric and asymmetric structures during the RI period.

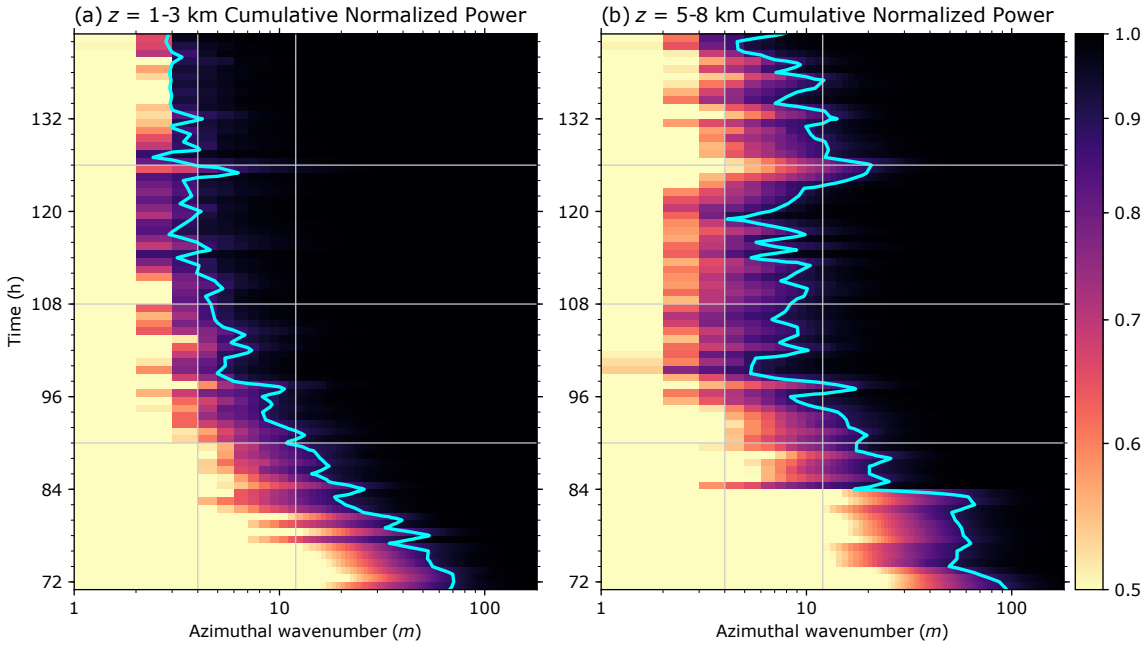

Fig. 3.6. The inner-core potential vorticity (PV) cumulative normalized power spectra are shown as a function of azimuthal wavenumber (m) and time for the (a) low layer (1–3 km altitude) and (b) high layer (5–8 km altitude). The cyan contour denotes 90% of the cumulative power at each respective hourly time step. Horizontal gray lines are overlaid at 18-h intervals, denoting the approximate intensification period quartiles beginning at $t = 90$, 108, and 126 h. Vertical gray lines are overlaid at the boundaries separating azimuthal wavenumbers $m = 3,4$ and $m = 12,13$. Note that axes are left-aligned such that the cumulative normalized power for azimuthal wavenumber $m = 1$ is shaded between $m = 1$–2 on the abscissa and likewise for time on the ordinate. See section 3.4 for details on how the cumulative normalized power spectra are constructed.

3.5 Structural evolution during intensification

Asymmetries are partitioned into low and high azimuthal wavenumbers for all scalar and vector quantities, representing relatively large and small azimuthal scales, respectively. Spectral binning into categories of low and high wavenumbers is somewhat arbitrary and therefore no precise definition exists in the literature. Herein, low-wavenumber asymmetric structures are defined by azimuthal wavenumbers $m =$ 1–3 and high-wavenumber asymmetric structures by azimuthal wavenumbers $m =$ 4–180[10]. The definition is largely predicated on the low-layer PV spectral analysis that demonstrates 90% of the power becomes concentrated within azimuthal wavenumbers $m =$ 1–3 near the midway point of the intensification period (Fig. 3.6). Limitations associated with the low- and high-wavenumber categorization include: 1) the low- and high-layer PV are distributed differently across azimuthal scales throughout the intensification period (Fig. 3.5), and

[10]The azimuth dimension is defined for the interval $[0, 2\pi)$ in increments of $\pi/180$, giving 360 azimuthal grid points. Therefore, $m = 180$ is the Nyquist wavenumber.

2) the azimuthal scale of asymmetries for a given wavenumber increases as a function of radius in a cylindrical coordinate framework. Despite these limitations, the low- and high-wavenumber categorization provides a useful conceptual framework to distinguish scale-dependent contributions from asymmetries to TC intensification. The low-wavenumber category as defined herein falls in between the azimuthal wavenumber $m = 1$–2 definition from Bhalachandran et al. (2020) and the $m = 1$–4 definition from Reasor et al. (2009).

The spatial distribution of asymmetric structures embedded within the TC circulation is examined via radius–azimuth (horizontal) and azimuth–height (vertical) cross-sections. Horizontal cross-sections are created at 1- and 5-km altitude, corresponding to the first vertical level within the low- and high-layer analyses presented in Figs. 3.4–3.6. Vertical cross-sections are created via radial averaging near the TC eyewall. Several averaging methods and regions were tested to produce azimuth–height depictions that captured the dynamically relevant vertical structure of asymmetries during the intensification period. Rather than averaging over a vertically oriented annulus (i.e., averaging between constant radius surfaces throughout the troposphere), a slanted annulus accounting for the RMW slope is constructed. Given large radial variations in the RMW exist throughout the troposphere, a linear approximation to the RMW is calculated from the average RMW slope between the surface and 12-km altitude. The radial location of the "linear" RMW is calculated as a function of altitude and time via the linear relationship given by

$$RMW_{linear}(z,t) = \mu z + RMW_{surface}(t), \tag{3.12}$$

where μ denotes the average RMW slope between the surface and 12-km altitude and $RMW_{surface}(t)$ is the RMW at the surface. The slanted averaging annulus boundaries are then constructed by applying scaling factors to the linear RMW. The innermost boundary is given by $0.4 \times RMW_{linear}(z,t)$ and the outermost boundary is given by $1.2 \times RMW_{linear}(z,t)$. Several scaling factors were tested and these were chosen as a set that consistently captures the bulk hollow PV tower region.

Symmetric and asymmetric structures are examined at three time slices during the rapid intensification period: early RI ($t = 90$ h), middle (mid) RI ($t = 108$ h), and late RI ($t = 126$ h). The time slices represent the approximate intensification period quartiles prior to the TC attaining

its maximum intensity (i.e., the 25th, 50th, and 75th percentiles for the intensification time scale; see gray lines in Figs. 3.4–3.6 for reference). Figure 3.7 shows the inner-core structure at 1- and 5-km altitude for each of the time slices. During the early RI time slice, the TC is characterized by an asymmetric distribution of PV located radially inward of reflectivity maxima in the eyewall region. At 1-km altitude, the asymmetric wind vectors demonstrate that air is exchanged between the eye–eyewall interface in regions of relatively low reflectivity (i.e., weaker convection). Transitioning from the early RI time slice to the mid RI time slice, the azimuthal distributions of PV and convection have become increasingly symmetric; however, there remains a predominant $m = 3$ asymmetry and polygonal eyewall structure. Furthermore, asymmetric wind circulations associated with PV anomalies embedded in vertices of the polygonal eyewall provide a pathway for air to be exchanged between the eye–eyewall interface. Transitioning from the mid RI time slice to the late RI time slice, the azimuthal distributions of PV and convection have become concentrated in a highly asymmetric elliptical eyewall structure. At 1-km altitude, the asymmetric wind vectors depict a strong deformation zone in the eye–eyewall region with an axis of dilitation oriented slightly (azimuthally) upwind of the ellipse vertices and an axis of contraction oriented slightly downwind of the ellipse vertices. Consistent with the inner-core PV spectral analysis, the asymmetries are concentrated among higher wavenumbers (smaller azimuthal scales) with increasing altitude for each of the time slices. In general, Fig. 3.7 demonstrates that the TC transitions from a high-wavenumber asymmetric structure to a low-wavenumber asymmetric structure during the intensification period. The following sections will further analyze the symmetric and asymmetric vortex structure during each of the time slices.

3.5.1 Early rapid intensification

During the early RI time slice ($t = 108$ h), the overall vortex structure is comprised of a relatively weak-amplitude hollow PV tower superposed by convectively generated cyclonic PV anomalies. The tangential (primary) circulation exhibits an $\sim$35 m s^{-1} near-surface maximum and a rapidly decaying vertical structure (Fig. 3.8a). A transverse (secondary) circulation has developed with boundary layer inflow exceeding 5 m s^{-1} near the surface and upper-tropospheric radial outflow

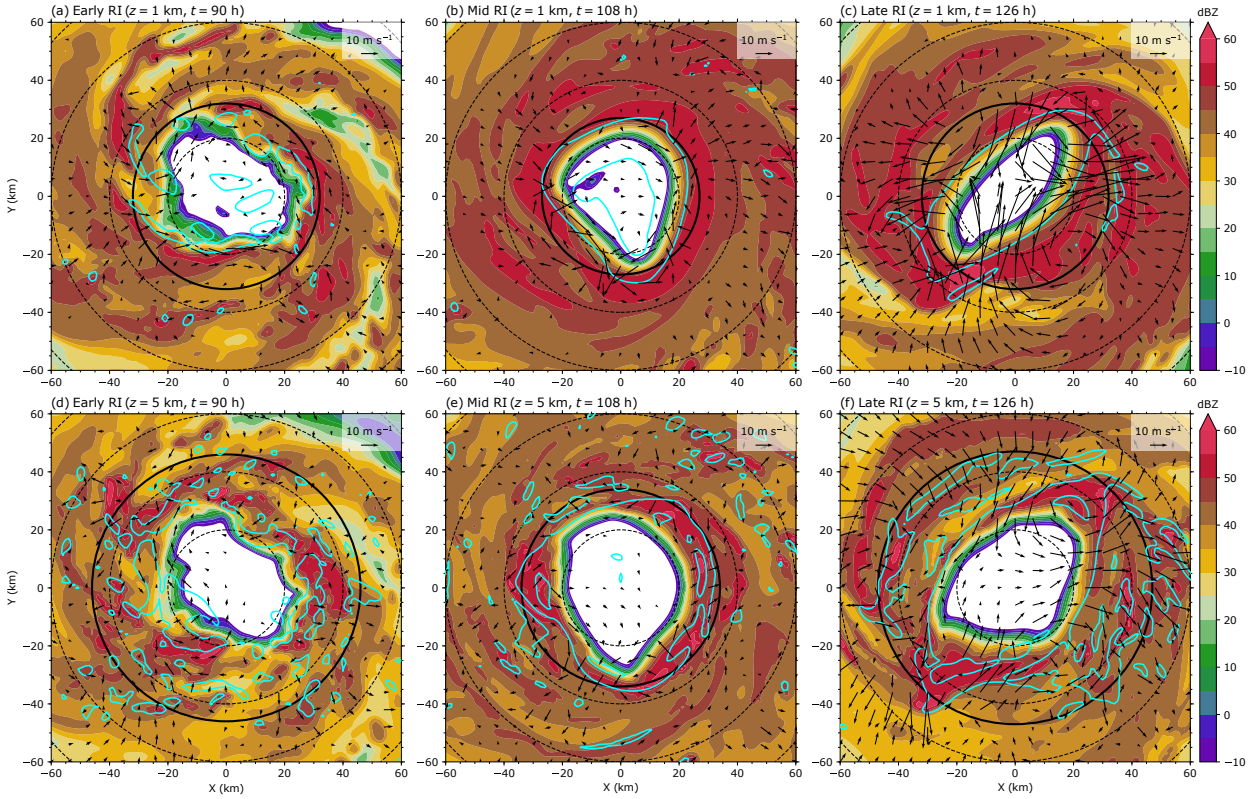

Fig. 3.7. The inner-core structure of the simulated TC is shown at (top) ∼1-km altitude and (bottom) ∼5-km altitude for (a, d) the early rapid intensification (RI) time slice ($t = 90$ h), (b, e) the mid RI time slice ($t = 108$ h), and (c, f) the late RI time slice ($t = 126$ h). Radar reflectivity (shaded, dBZ) is overlaid with the asymmetric wind vectors (m s^{-1}) and the 20 potential vorticity unit (PVU) contour (cyan). The solid black ring denotes the azimuthally averaged radius of maximum tangential winds (RMW) and dashed-black radius rings are shown in increments of 20 km from the center.

exceeding 10 m s^{-1} above 12-km altitude[11]. The RMW is located at 30-km radius near the surface, sloping radially outward with increasing altitude and located between the $M = 0.8$–1.0×10^{-6} m^2 s^{-1} absolute angular momentum surfaces (Fig. 3.8b). Additionally, the maximum symmetric heating exceeds 20 K h^{-1} and is concentrated along the inner-edge of the RMW between 3–8 km altitude. A hollow PV tower structure has begun to emerge with maximum values of ∼20 PVU concentrated radially inward of the maximum symmetric heating (Fig. 3.8c). Furthermore, PV "bridge" structures are evident below 2-km altitude and between 4–8 km altitude where relatively high PV air extends radially inward from the developing eyewall into the eye. Note that the orange

[11]Radial outflow in the upper-tropospheric outflow layer increases with radius beyond the 60-km domain shown in the axisymmetric analyses.

lines in Fig. 3.8c denote the slanted annulus averaging boundaries for the early RI azimuth–height analyses.

Figure 3.9 shows the presence of small-scale, convectively generated cyclonic PV asymmetries embedded within the vortex circulation. The horizontal asymmetric PV distribution is characterized by low-wavenumber PV asymmetries comprising high-wavenumber structures. Consistent with the inner-core PV spectral analysis, PV asymmetries are concentrated among higher-wavenumbers (smaller azimuthal scales) with increasing altitude. The azimuth–height analysis depicts $m = 2$ radial and tangential velocity structures below ∼2-km altitude with cyclonic velocity anomalies located azimuthally downwind of radial inflow anomalies (Fig. 3.10a). The upper-tropospheric outflow layer is primarily concentrated within a local jet positioned in the NE quadrant of the circulation, upwind of the strongest BL inflow maximum positioned in the SW quadrant. Furthermore, small-scale heating and PV maxima extend from the boundary layer up to ∼10-km altitude (Fig. 3.10b). Congruous with the radius–azimuth analysis, the combined vertical structure of asymmetric heating and PV is concentrated within low-wavenumber asymmetries comprising high-wavenumber structures. In summation, the TC eyewall is largely asymmetric during the early RI time slice and the overall structure is best characterized by low-wavenumber PV asymmetries that comprise high-wavenumber PV structures.

3.5.2 Mid rapid intensification

During the mid RI time slice, 18 h after early RI, the overall vortex structure is comprised of a strong-amplitude hollow PV tower superposed by a predominant $m = 3$ PV asymmetry. The primary circulation has strengthened throughout the troposphere with an ∼70 m s^{-1} near-surface maximum and tangential velocities exceeding 45 m s^{-1} throughout 10-km altitude along the RMW (Fig. 3.11a). The transverse circulation has strengthened with maximum boundary layer inflow exceeding 20 m s^{-1}, penetrating 5–10 km radially inward of the RMW, and upper-tropospheric radial outflow exceeding 15 m s^{-1}. The RMW has contracted to 25-km near the surface and slopes radially outward with increasing altitude, approximately in alignment with the $M = 1.8 \times 10^{-6}$ m^2 s^{-1} absolute angular momentum surface (Fig. 3.11b). The maximum symmetric heating now exceeds 80 K h^{-1} and remains concentrated along the inner-edge of the RMW, located between 5–8

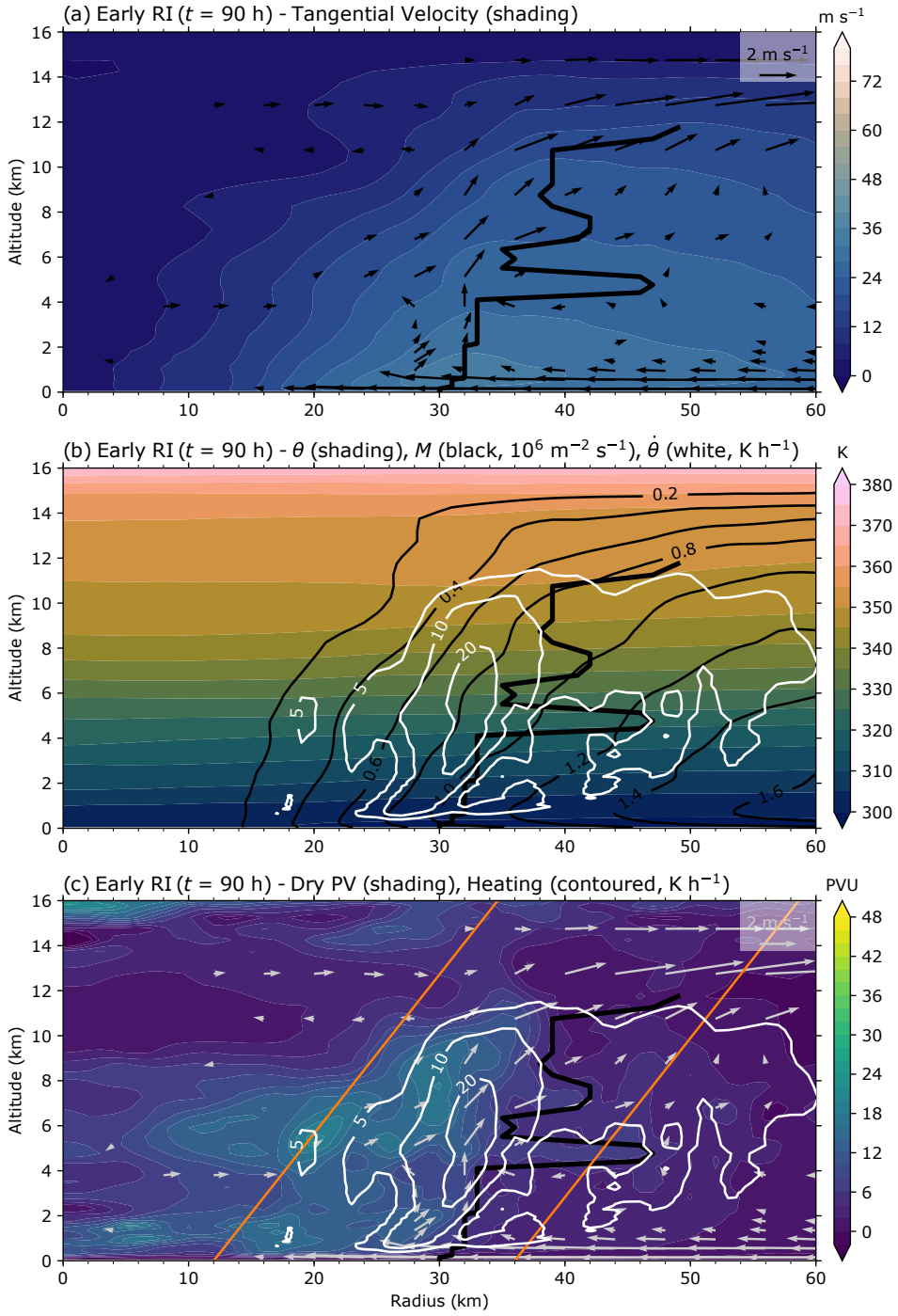

Fig. 3.8. The axisymmetric vortex structure is shown for the early rapid intensification time slice ($t = 90$ h). (a) Tangential velocity (shaded, m s^{-1}) is overlaid with the transverse circulation (vectors, m s^{-1}). (b) Potential temperature (shaded, K) is overlaid with absolute angular momentum surfaces (black, contoured every 0.2×10^6 m^2 s^{-1}) and heating from microphysical processes (white, contours at 5, 10, 20, 40, 60, and 80 K h^{-1}). (c) The dry Ertel's potential vorticity (PV; shaded, PVU) is overlaid with the transverse circulation (vectors, m s^{-1}) and heating from microphysical processes (contoured, white). The orange lines denote the slanted annulus averaging boundaries for the azimuth–height analyses. In (a) and (c), vectors that do not exceed a 0.5 m s^{-1} transverse circulation wind speed magnitude are excluded (i.e., $\sqrt{u^2+w^2} < 0.5$, where u is the radial velocity and w the vertical velocity). The black line in each panel denotes the radius of maximum tangential winds (RMW).

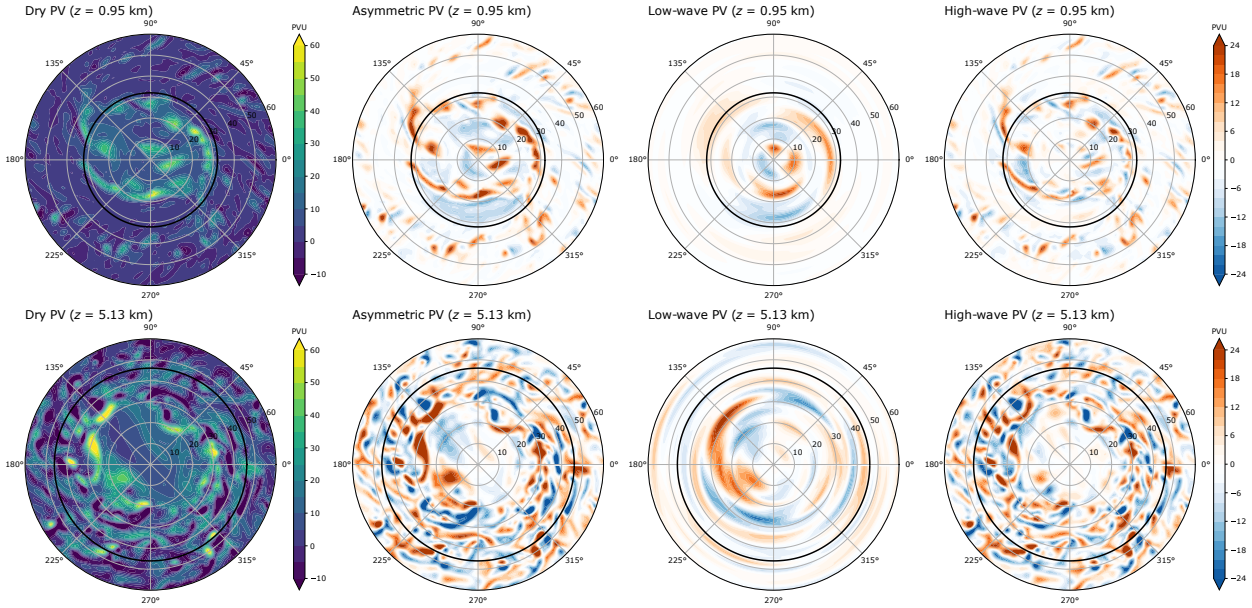

Fig. 3.9. The dry Ertel's potential vorticity (PV) structure is shown at (top) ∼1-km altitude and (bottom) ∼5-km altitude for the early rapid intensification time slice ($t = 90$ h). From left to right: The dry Ertel's PV, the asymmetric PV, the low-wavenumber PV ($m = 1$–3), and the high-wavenumber PV ($m = 4$–180). The solid black ring in each panel denotes the azimuthally averaged radius of maximum tangential winds (RMW) at each respective vertical level.

km altitude; however, it is worth noting that the maximum symmetric heating is not concentrated along the same M surfaces from the early RI period (see Fig. 3.8b). From the early to mid RI time slices, M surfaces have continued to converge toward the axis of rotation, but the RMW has contracted a relatively small radial distance of ∼5 km. This evolution is distinct from the observed RI of Hurricane Patricia (2015) in chapter 2 where the maximum symmetric heating remained fixed to the same M surfaces as they contracted in physical space. The hollow PV tower has also strengthened with three distinct maxima: a primary low-level maximum exceeding 60 PVU located between 1–2 km altitude along the PV bridge, a secondary mid-level maximum exceeding 50 PVU, and a tertiary upper-troposphere–lower-stratosphere (UTLS) maximum exceeding 45 PVU above the eyewall between 14–16 km altitude (Fig. 3.11c) Furthermore, the hollow PV tower structure remains concentrated radially inward of the maximum symmetric heating. Note that the orange lines in Fig. 3.11c denote the slanted annulus averaging boundaries for the mid RI azimuth–height analyses.

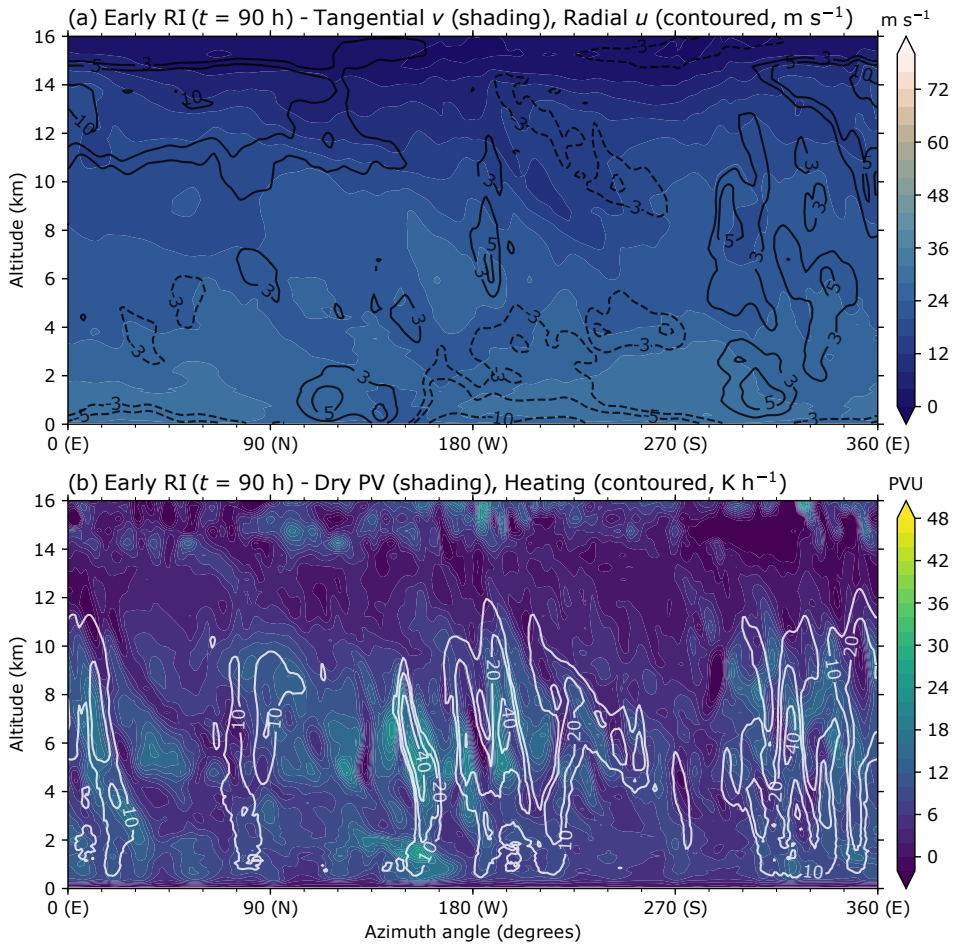

Fig. 3.10. The azimuth–height structure in the eyewall region is shown for the early rapid intensification time slice ($t = 90$ h). (a) The tangential velocity (shaded, m s^{-1}) is overlaid with the radial velocity (black, contours at 3, 5, 10, 15, 20, and 25 m s^{-1} with dashed contours denoting radial inflow and solid contours radial outflow). (b) The dry Ertel's potential vorticity (PV; shading, PVU) is overlaid with the heating from microphysical processes (white, contours at 10, 20, 40, 60, 80, 100, and 120 K h^{-1}). See section 3.5 for details on how the eyewall region is defined and radially averaged to create the azimuth–height analyses.

Figure 3.12 shows the presence of PV ring structures at both 1- and 5-km altitudes, but a more hollow structure at 1-km altitude (i.e., the ratio of eyewall PV to inner-core PV is larger at 1-km altitude). Similar to the early RI time slice, the predominant low-wavenumber $m = 3$ asymmetry comprises small-scale (high-wavenumber) PV asymmetries. At 1-km altitude, there is a thin "moat" of relatively low PV separating the primary PV ring from a secondary PV ring displaced radially inward, and the secondary PV ring also comprises high-wavenumber asymmetries. The source and relevance of this double PV ring structure remain unclear, but it is noted at various times during the intensification period (not shown). The azimuth–height analysis highlights the

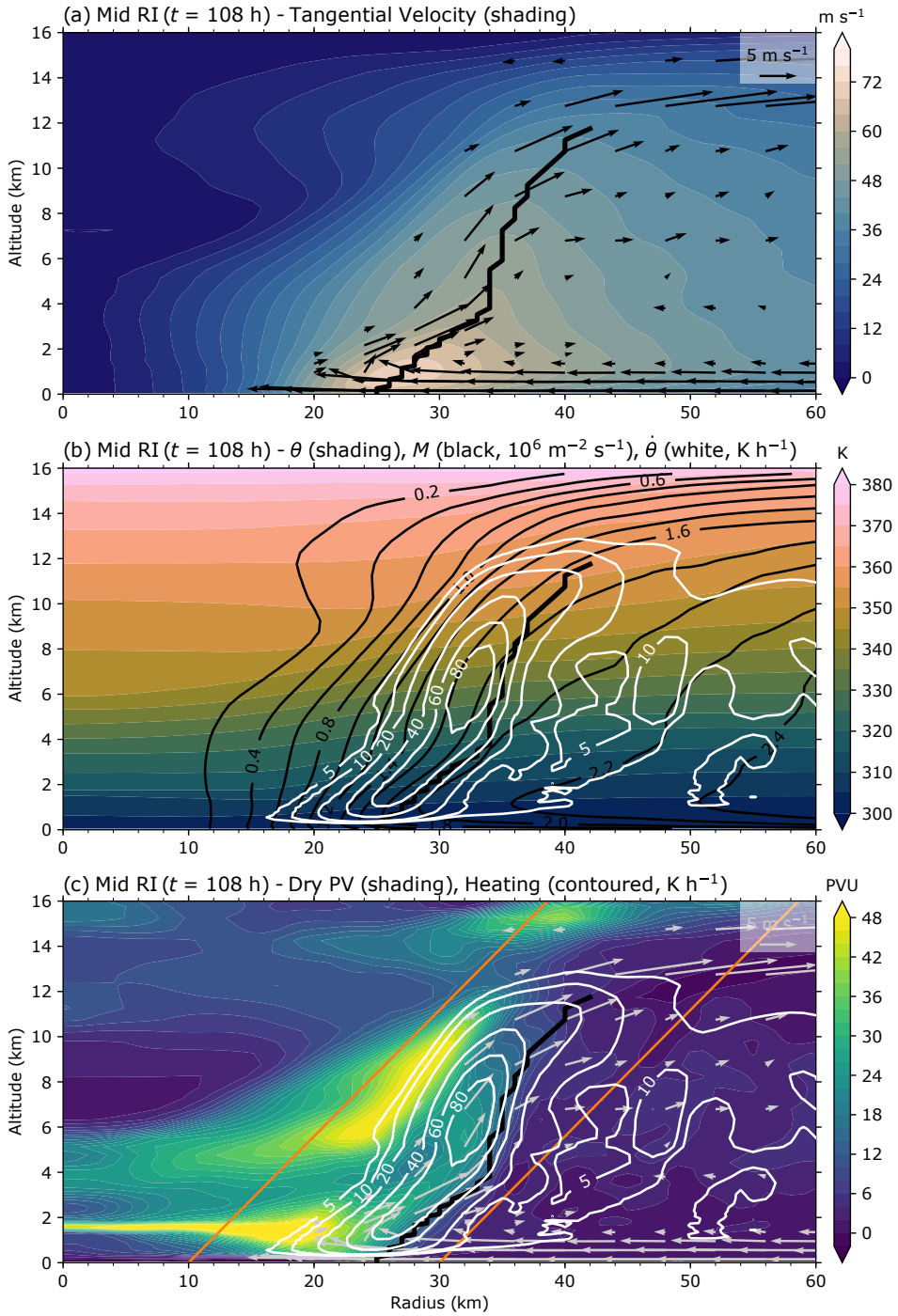

Fig. 3.11. The axisymmetric vortex structure is shown for the middle rapid intensification time slice ($t = 108$ h). (a) Tangential velocity (shaded, m s^{-1}) is overlaid with the transverse circulation (vectors, m s^{-1}). (b) Potential temperature (shaded, K) is overlaid with absolute angular momentum surfaces (black, contoured every 0.2×10^6 m^2 s^{-1}) and heating from microphysical processes (white, contours at 5, 10, 20, 40, 60, and 80 K h^{-1}). (c) The dry Ertel's potential vorticity (PV; shaded, PVU) is overlaid with the transverse circulation (vectors, m s^{-1}) and heating from microphysical processes (contoured, white). The orange lines denote the slanted annulus averaging boundaries for the azimuth–height analyses. In (a) and (c), vectors that do not exceed a 1 m s^{-1} transverse circulation wind speed magnitude are excluded (i.e., $\sqrt{u^2+w^2} < 1$, where u is the radial velocity and w the vertical velocity). The black line in each panel denotes the radius of maximum tangential winds (RMW).

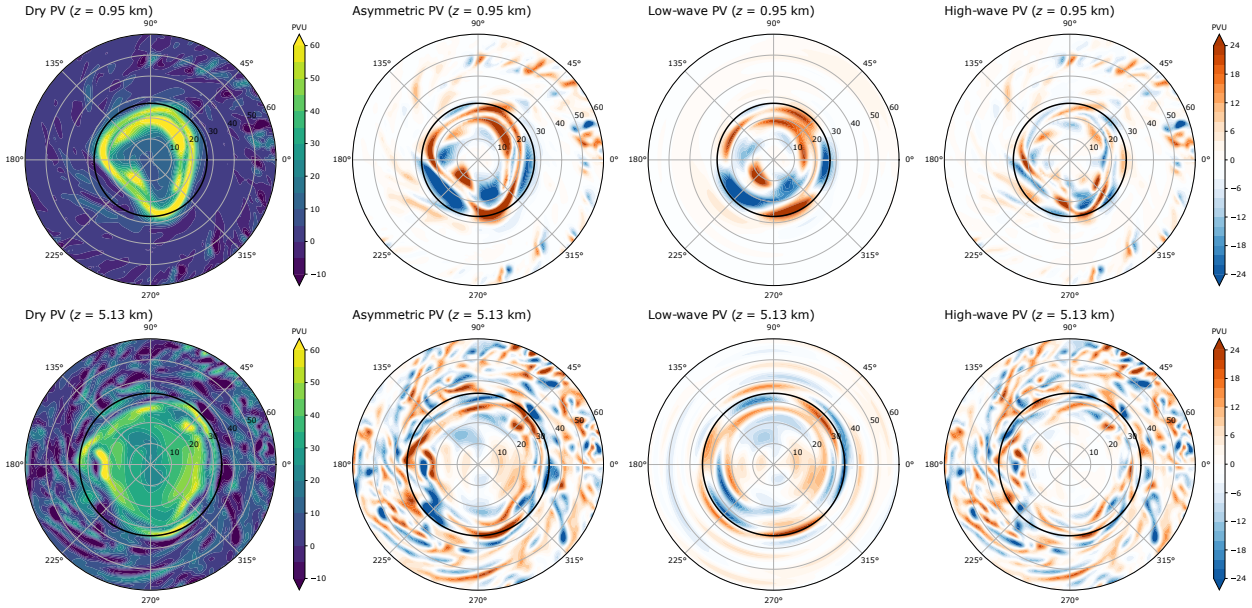

Fig. 3.12. The dry Ertel's potential vorticity (PV) structure is shown at (top) ∼1-km altitude and (bottom) ∼5-km altitude for the middle rapid intensification time slice ($t = 108$ h). From left to right: The dry Ertel's PV, the asymmetric PV, the low-wavenumber PV ($m = 1$–3), and the high-wavenumber PV ($m = 4$–180). The solid black ring in each panel denotes the azimuthally averaged radius of maximum tangential winds (RMW) at each respective vertical level.

predominant $m = 3$ asymmetric structure and further reveals that the asymmetries possess a large degree of vertical coherence, extending from near the surface through 8-km altitude. Similar to the early RI time slice, cyclonic velocity anomalies are located azimuthally downwind of radial inflow anomalies (Fig. 3.13a). The upper-tropospheric outflow layer is now fully encompassed by at least 5 m s^{-1} radial outflow between 12–14 km altitude. Upper-tropospheric outflow maxima are located almost directly above the boundary layer outflow maxima. The heating and PV asymmetries are predominantly $m = 3$ below 3-km altitude, but also comprise high-wavenumber asymmetries above 3-km altitude (Fig. 3.13b). In summation, the symmetric PV structure has amplified significantly between the early and mid RI time slices with maximum values approximately tripling in the hollow PV tower. Furthermore, relatively high-amplitude heating and PV asymmetries have persisted in the eyewall and are on the same order of magnitude as the symmetric PV component.

3.5.3 Late rapid intensification

During the late RI time slice, 18 h after mid RI and 36 h after early RI, the overall vortex structure is comprised of a more diffuse hollow PV tower compared to the mid RI time slice and

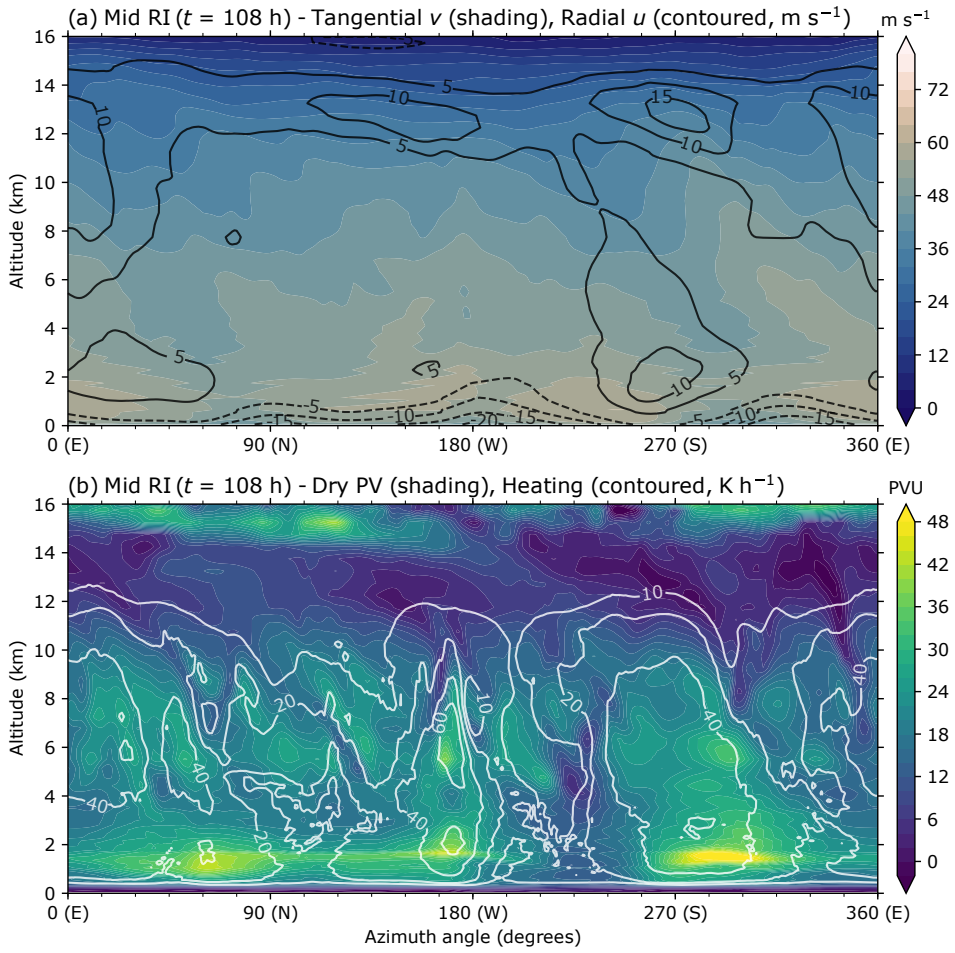

Fig. 3.13. The azimuth–height structure in the eyewall region is shown for the middle rapid intensification time slice ($t = 108$ h). (a) The tangential velocity (shaded, m s^{-1}) is overlaid with the radial velocity (black, contours at 5, 10, 15, 20, and 25 m s^{-1} with dashed contours denoting radial inflow and solid contours radial outflow). Note that the 3 m s^{-1} contour is excluded for clarity in comparison to Fig. 3.10a. (b) The dry Ertel's potential vorticity (PV; shading, PVU) is overlaid with the heating from microphysical processes (white, contours at 10, 20, 40, 60, 80, 100, and 120 K h^{-1}). See section 3.5 for details on how the eyewall region is defined and radially averaged to create the azimuth–height analyses.

a highly asymmetric elliptical eyewall. The primary circulation enveloping the eyewall region has radially broadened and the maximum tangential velocity is displaced from the surface near ∼800-m altitude, exceeding 70 m s^{-1} (Fig. 3.14a). The radial branches of the transverse circulation have continued to strengthen with maximum boundary layer inflow values exceeding 25 m s^{-1} and upper-tropospheric radial outflow exceeding 18 m s^{-1}. In general, the primary circulation near the eyewall possesses a much larger radially outward slope compared to the mid RI time slice, and the RMW slope substantially fluctuates between the surface and 12-km altitude. Additionally, the cyclonic tangential velocity tower appears to have been radially and vertically severed; a local

tangential velocity maximum is located between $r = 28$–32 km on the inner edge of the RMW below 4-km altitude and another maximum is located between $r = 44$–50 km on the inner edge of the RMW between 4–7 km altitude (Fig. 3.14a). The M surfaces are not as compact in the eyewall region compared to the mid RI time slice, but larger M surfaces have continued converging toward the axis of rotation (Fig. 3.14b). The maximum symmetric heating remains concentrated along the inner edge of the RMW near 6-km altitude, exceeding 80 K h^{-1}; however, the symmetric heating structure has also become more radially diffuse in contrast to the mid RI time slice. Furthermore, the hollow PV tower has become more radially diffuse with two discrete mid-level PV maxima located radially inward of the aforementioned discrete tangential velocity maxima (Fig. 3.14c). The maximum symmetric PV is concentrated between 1–3 km altitude, exceeding 200 PVU near the axis of rotation where substantial mixing appears to be taking place between the eye–eyewall interface. Note that the orange lines in Fig. 3.14c denote the slanted annulus averaging boundaries for the late RI azimuth–height analyses.

Figure 3.15 shows the presence of a pronounced elliptical eyewall structure at both 1- and 5-km altitude. In association with the elliptical eyewall, a high-amplitude $m = 2$ PV asymmetry is present at 1- and 5-km altitude, but the asymmetric PV is dispersed among relatively higher wavenumbers at 5-km altitude. High-wavenumber cyclonic PV anomalies are also superposed on vertices of the $m = 2$ ellipse. The azimuth–height analysis demonstrates that the $m = 2$ asymmetries exhibit vertically coherent structures between the surface and 8–10 km altitude. The $m = 2$ cyclonic tangential velocity maxima exceed 60 m s^{-1} and extend from the surface up to approximately 8-km altitude, located azimuthally downwind of $m = 2$ boundary layer radial inflow jets exceeding 30 m s^{-1} (Fig. 3.16a). Additionally, $m = 2$ boundary layer outflow jets exceeding 20 m s^{-1} are located slightly downwind of the cyclonic tangential velocity maxima. The upper-tropospheric outflow layer is now characterized by an $m = 2$ asymmetry with outflow jets azimuthally collocated with the boundary layer outflow jets. The PV and heating asymmetries exhibit predominant $m = 2$ structures but also comprise high-wavenumber asymmetries (Fig. 3.16b). In summation, the symmetric PV structure has become radially diffuse during the late RI time slice. A significant

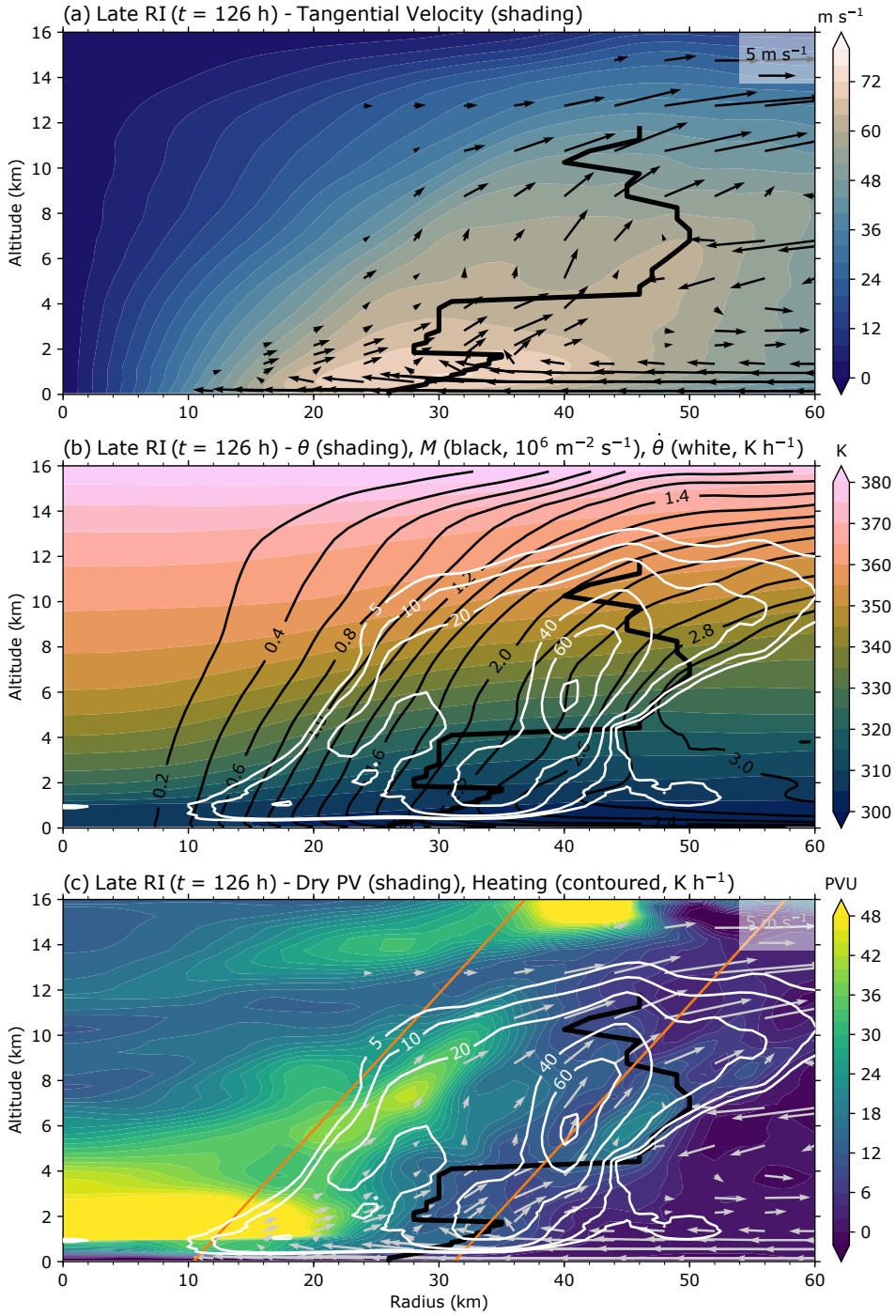

Fig. 3.14. The axisymmetric vortex structure is shown for the late rapid intensification time slice (t = 126 h). (a) Tangential velocity (shaded, m s^{-1}) is overlaid with the transverse circulation (vectors, m s^{-1}). (b) Potential temperature (shaded, K) is overlaid with absolute angular momentum surfaces (black, contoured every 0.2×10^6 m^2 s^{-1}) and heating from microphysical processes (white, contours at 5, 10, 20, 40, 60, and 80 K h^{-1}). (c) The dry Ertel's potential vorticity (PV; shaded, PVU) is overlaid with the transverse circulation (vectors, m s^{-1}) and heating from microphysical processes (contoured, white). The orange lines denote the slanted annulus averaging boundaries for the azimuth–height analyses. In (a) and (c), vectors that do not exceed a 1 m s^{-1} transverse circulation wind speed magnitude are excluded (i.e., $\sqrt{u^2+w^2} < 1$, where u is the radial velocity and w the vertical velocity). The black line in each panel denotes the radius of maximum tangential winds (RMW).

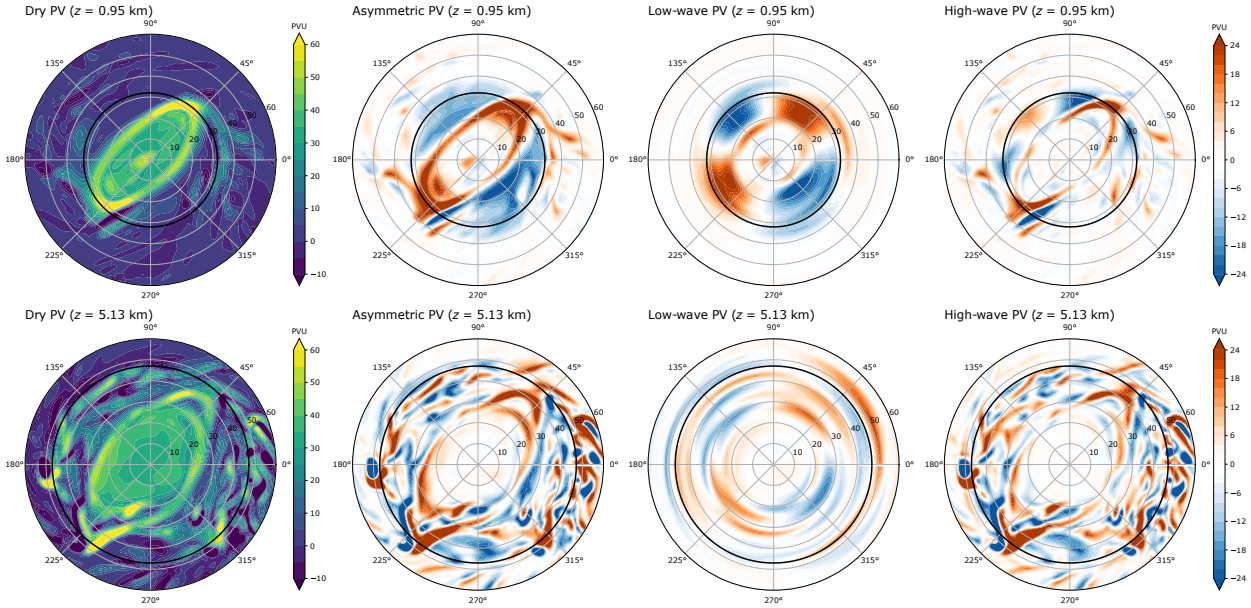

Fig. 3.15. The dry Ertel's potential vorticity (PV) structure is shown at (top) ∼1-km altitude and (bottom) ∼5-km altitude for the late rapid intensification time slice ($t = 126$ h). From left to right: The dry Ertel's PV, the asymmetric PV, the low-wavenumber PV ($m = 1$–3), and the high-wavenumber PV ($m = 4$–180). The solid black ring in each panel denotes the azimuthally averaged radius of maximum tangential winds (RMW) at each respective vertical level.

amount of high-PV air has been mixed into the eye in association with the formation of a highly asymmetric $m = 2$ elliptical eyewall structure.

3.6 Scale-dependent interactions

The preceding analysis has demonstrated that the TC eyewall is comprised of both low- and high-wavenumber asymmetries at all stages of the intensification period. Furthermore, the PV asymmetries are persistently on the same order of magnitude as the symmetric PV structure. To quantitatively assess asymmetric contributions during the intensification period, the azimuthal-mean PV equation is examined in light of the low- and high-wavenumber categories. The following sections present the analysis methodology and formulation of the azimuthal-mean PV equation.

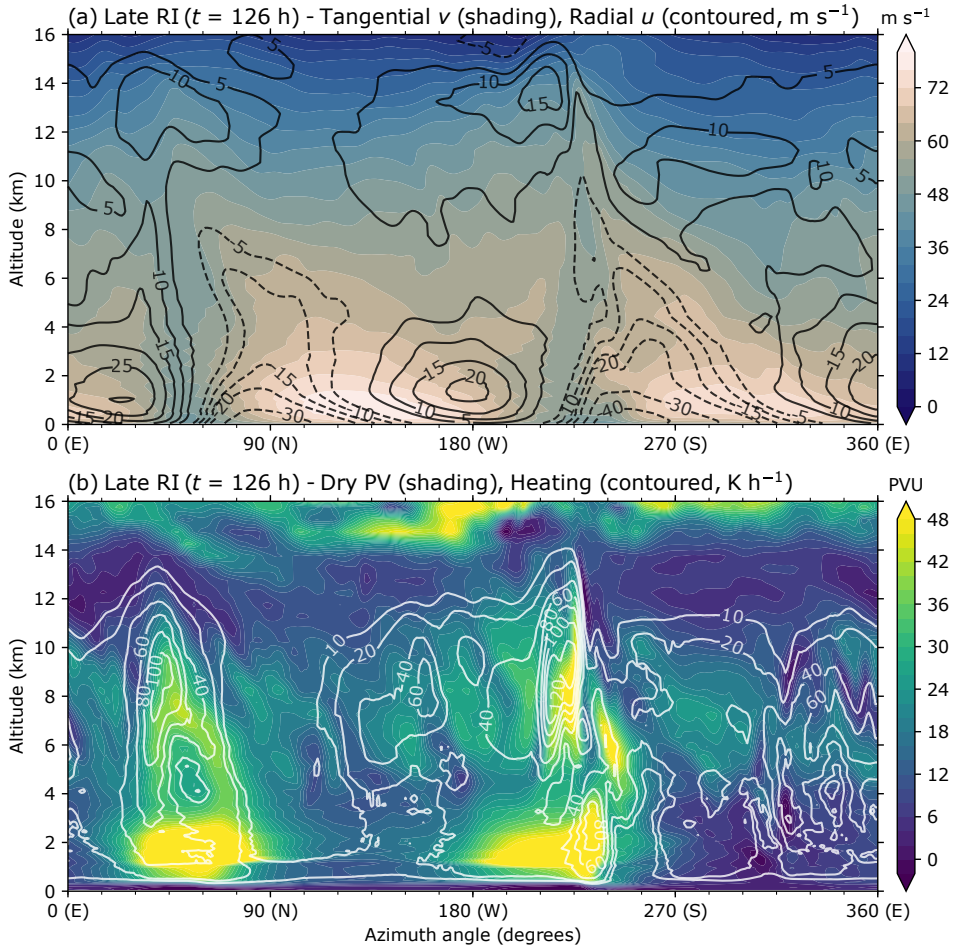

Fig. 3.16. The azimuth–height structure in the eyewall region is shown for the late rapid intensification time slice ($t = 126$ h). (a) The tangential velocity (shaded, m s^{-1}) is overlaid with the radial velocity (black, contours at 5, 10, 15, 20, and 25 m s^{-1} with dashed contours denoting radial inflow and solid contours radial outflow). Note that the 3 m s^{-1} contour is excluded for clarity in comparison to Fig. 3.10a. (b) The dry Ertel's potential vorticity (PV; shading, PVU) is overlaid with the heating from microphysical processes (white, contours at 10, 20, 40, 60, 80, 100, and 120 K h^{-1}). See section 3.5 for details on how the eyewall region is defined and radially averaged to create the azimuth–height analyses.

3.6.1 Spectral truncation and Reynolds averaging

As discussed in section 3.4, an arbitrary scalar ψ (or vector) can be partitioned into components representing axial symmetry and deviations from axial symmetry (asymmetries). The azimuthal dimension of ψ can be represented as a Fourier series, given by

$$\psi_m(r,z,t) = \sum_{j=0}^{J-1} \psi(r,j,z,t)\,[cos(2\pi mj/J) + isin(2\pi mj/J)], \text{ for } m = 0,1,2,\ldots,180, \qquad (3.13)$$

where $\psi(r,j,z,t)$ is the arbitrary quantity of interest in cylindrical coordinates, m the azimuthal wavenumber, r the radius, j the azimuth angle in degrees ($j = 0,1,2,\ldots,J = 360$), z the altitude, and t the time. Thus, the symmetric component is given by the Fourier coefficient ψ_0 and the full spectrum of asymmetries is given by the Fourier coefficient ψ_m for $m = 1,2,3,\ldots,180$.

Recall that low-wavenumber asymmetric structures are defined by azimuthal wavenumbers $m =$ 1–3 and high-wavenumber asymmetric structures by azimuthal wavenumbers $m =$ 4–180. Therefore, the Fourier series is spectrally truncated to produce low- and high-wavenumber categories as follows:

$$\psi_{m,l} = \begin{cases} \psi_m, & \text{for } m = 1,2,3 \\ 0+0i, & \text{otherwise} \end{cases} \tag{3.14}$$

and

$$\psi_{m,h} = \begin{cases} \psi_m, & \text{for } m = 4,5,6,\ldots,180 \\ 0+0i, & \text{otherwise,} \end{cases} \tag{3.15}$$

where the subscripts l and h denote the low- and high-wavenumber categories, respectively. Then, ψ can be reconstructed for the low- and high-wavenumber asymmetries by applying the inverse Fourier transform to Eqs. 3.14 and 3.15, such that

$$\psi'_l(r,\phi,z,t) = F^{-1}\left\{\psi_{m,l}\right\} \tag{3.16}$$

and

$$\psi'_h(r,\phi,z,t) = F^{-1}\left\{\psi_{m,h}\right\}, \tag{3.17}$$

where F^{-1} denotes the inverse Fourier transform operator, ψ'_l the low-wavenumber asymmetries, and ψ'_h the high-wavenumber asymmetries. In applying the spectral truncation, ψ (Eq. 3.7) is now given by

$$\psi(r,\phi,z,t) = \bar{\psi}(r,z,t) + \psi'_l(r,\phi,z,t) + \psi'_h(r,\phi,z,t). \tag{3.18}$$

In accordance with Reynolds averaging, the average product of two partitioned quantities ψ_1 and ψ_2 is given by

$$\overline{\psi_1\psi_2} = \overline{(\bar{\psi}_1 + \psi'_{1,l} + \psi'_{1,h})(\bar{\psi}_2 + \psi'_{2,l} + \psi'_{2,h})} = \bar{\psi}_1\bar{\psi}_2 + \overline{\psi'_{1,l}\psi'_{2,l}} + \overline{\psi'_{1,h}\psi'_{2,h}}. \tag{3.19}$$

3.6.2 *The potential vorticity equation*

Recall that the definition of Ertel's dry PV is given by $P = \rho^{-1}\eta \cdot \nabla\theta$. The flux form of the PV equation can be obtained directly by forming the scalar product of the absolute vorticity equation with $\nabla\theta$ (Haynes and McIntyre 1987). The flux form of the PV equation, formulated in Cartesian coordinates for the Earth's rotating (non-inertial) reference frame, is given by

$$\frac{\partial(\rho P)}{\partial t} = -\nabla \cdot (\rho P\mathbf{u} - \dot{\theta}\eta - \mathbf{F} \times \nabla\theta), \tag{3.20}$$

where ρ is the dry air density, $\mathbf{u}$ the three-dimensional velocity vector, $\dot{\theta} = D\theta/Dt$ the diabatic heating rate (material tendency of potential temperature θ), η the absolute vorticity vector, and $\mathbf{F}$ the three-dimensional friction force vector. Haynes and McIntyre (1987) elucidated the analogy between PV and chemical tracers via the flux form of the PV equation, where the amount of PV per unit volume of physical space ρP denotes a notional "PV-substance" (PVS[12]) with mixing ratio P. The advective form of the PV equation can be recovered from Eq. 3.20 by noting that mass conservation requires

$$\frac{\partial\rho}{\partial t} + \nabla \cdot (\rho\mathbf{u}) = 0. \tag{3.21}$$

Hence, the advective form of the PV equation is given by

$$\frac{\partial P}{\partial t} = -\mathbf{u} \cdot \nabla P + \frac{1}{\rho}(\eta \cdot \nabla\dot{\theta}) + \frac{1}{\rho}(\nabla\theta \cdot \nabla \times \mathbf{F}). \tag{3.22}$$

Tory et al. (2012) discussed in detail the inherent limitations associated with PV equations of the forms listed above. The primary issue arises from a large cancellation between the vertical advection of PV and the diabatic source of PV and likewise a large cancellation between the vertical flux of PVS and the diabatic source of PVS. Tory et al. noted that the "adiabatic/diabatic cancellation problem" will be present for any PV or PVS equation in which the vertical PV advection or PVS flux can transport the diabatic PV or PVS source away from the source region. The adiabatic/diabatic cancellation is problematic in regions where the two terms have a different sign, resulting in a small residual between two opposing terms with relatively large magnitudes. Hence,

[12]The PV-substance terminology was later introduced by Haynes and McIntyre (1990) to elucidate the distinction between a notional tracer substance ρP and its mixing ratio P.

the residual is prone to numerical roundoff errors associated with successive finite differencing required to compute terms in the PV and PVS equations. In an isentropic coordinate framework, the adiabatic/diabatic cancellation problem vanishes. There is an exact cancellation between the "cross-isentropic advective flux" and "the cross-isentropic component of a flux whose divergence represents σ [the isentropic mass density] times the diabatic material rate of change of PV" (Haynes and McIntyre 1987). The exact cancellation in isentropic coordinates underlies some of the physical insights obtained when viewing PVS as a chemical tracer (Haynes and McIntyre 1987, 1990).

Tory et al. introduced alternative formulations of the PV and PVS equations in geometric coordinates that remain exact for nonhydrostatic flows and are not burdened by the adiabatic/diabatic cancellation problem. Additionally, their alternative formulations reduce to the isentropic PV and PVS equations when the vertical axis in the geometric coordinate framework is rotated in the direction of $\nabla\theta$ (see their section 3). Both the absence of potential adiabatic/diabatic cancellations and equivalences to isentropic PV and PVS equations are desirable features from the alternative formulations of the PV equations put forth in Tory et al. (2012); however, the utility of their alternative formulations is partly obscured by their complexity. To illustrate, the advective form of their alternative PV equation is reformulated here in a geometric cylindrical coordinate framework (cf. their Eq. 21):

$$\begin{aligned}\frac{\partial P}{\partial t} = &-\frac{1}{\rho}\left\{\nabla\theta\cdot\left[\frac{\partial}{r\partial\phi}(v\eta_r)+\frac{\partial}{\partial z}(w\eta_r),\ \frac{\partial}{\partial r}(u\eta_\phi)+\frac{\partial}{\partial z}(w\eta_\phi),\frac{\partial}{\partial r}(u\eta_z)+\frac{\partial}{r\partial\phi}(v\eta_z)\right]\right\}\\ &+\frac{1}{\rho}\left\{\nabla\theta\cdot\left[\frac{\partial}{r\partial\phi}(u\eta_\phi)+\frac{\partial}{\partial z}(u\eta_z),\frac{\partial}{\partial r}(v\eta_r)+\frac{\partial}{\partial z}(v\eta_z),\frac{\partial}{\partial r}(w\eta_r)+\frac{\partial}{r\partial\phi}(w\eta_\phi)\right]\right\}\\ &+\frac{P}{\rho}\nabla\cdot(\rho\mathbf{u})+\frac{1}{\rho}\left(\eta\cdot\nabla\frac{\partial\theta}{\partial t}\right)+\frac{1}{\rho}(\nabla\theta\cdot\nabla\times\mathbf{F}),\end{aligned} \tag{3.23}$$

where η_r, η_ϕ, and η_z denote the radial, azimuthal, and vertical components of the absolute vorticity vector η, respectively, and the remaining variables assume their aforementioned definitions. The first term encapsulated by curly braces represents the isentrope-parallel flux of isentrope-perpendicular vorticity; the second term encapsulated by curly braces represents the isentrope-perpendicular flux of isentrope-parallel vorticity; the first two terms on the bottom line represent

contributions to the PV tendency associated with changes in the mass field; and the last term represents contributions to the PV tendency associated with frictional processes.

Assessing the azimuthal-mean tendency of PV requires partitioning Eq. 3.23 into symmetric and asymmetric components. Ignoring azimuthal variations in density, the isentrope-parallel and isentrope-perpendicular fluxes will require Reynolds averaging combinations of at least three terms (triplets). If distinctions are made between low- and high-wavenumber asymmetries, each triplet will produce nine partitioned terms. Attempting to interpret results from analyses comprising over 20 terms would surely entail a convoluted endeavor. A scale analysis might reveal leading order terms and warrant the exclusion of small-order terms, thereby reducing the complexity; however, this pursuit is reserved for future work and instead the simpler advective form of the PV equation (3.22) is examined while acknowledging its potential limitations discussed above. The ramifications of this choice will be further examined in section 3.10.

Ignoring azimuthal variations in density, the advective form of the azimuthal-mean PV equation is given by

$$\begin{aligned}
\frac{\partial \bar{P}}{\partial t} = &-\left(\bar{u}\frac{\partial \bar{P}}{\partial r}+\bar{w}\frac{\partial \bar{P}}{\partial z}\right)-\left(\overline{u'_l\frac{\partial P'_l}{\partial r}}+\overline{u'_h\frac{\partial P'_h}{\partial r}}+\overline{v'_l\frac{\partial P'_l}{r\partial \phi}}+\overline{v'_h\frac{\partial P'_h}{r\partial \phi}}+\overline{w'_l\frac{\partial P'_l}{\partial z}}+\overline{w'_h\frac{\partial P'_h}{\partial z}}\right)\\
&+\frac{1}{\bar{\rho}}\left(\bar{\eta}_r\frac{\partial \bar{\dot{\theta}}}{\partial r}+\bar{\eta}_z\frac{\partial \bar{\dot{\theta}}}{\partial z}\right)+\frac{1}{\bar{\rho}}\left(\overline{\eta'_{r,l}\frac{\partial \dot{\theta}'_l}{\partial r}}+\overline{\eta'_{r,h}\frac{\partial \dot{\theta}'_h}{\partial r}}+\overline{\eta'_{\phi,l}\frac{\partial \dot{\theta}'_l}{r\partial \phi}}+\overline{\eta'_{\phi,h}\frac{\partial \dot{\theta}'_h}{r\partial \phi}}+\overline{\eta'_{z,l}\frac{\partial \dot{\theta}'_l}{\partial z}}+\overline{\eta'_{z,h}\frac{\partial \dot{\theta}'_h}{\partial z}}\right)\\
&+\frac{1}{\bar{\rho}}\left(\bar{\mathcal{F}}_r\frac{\partial \bar{\theta}}{\partial r}+\bar{\mathcal{F}}_z\frac{\partial \bar{\theta}}{\partial z}\right)+\frac{1}{\bar{\rho}}\left(\overline{\mathcal{F}'_{r,l}\frac{\partial \theta'_l}{\partial r}}+\overline{\mathcal{F}'_{r,h}\frac{\partial \theta'_h}{\partial r}}+\overline{\mathcal{F}'_{\phi,l}\frac{\partial \theta'_l}{r\partial \phi}}+\overline{\mathcal{F}'_{\phi,h}\frac{\partial \theta'_h}{r\partial \phi}}+\overline{\mathcal{F}'_{z,l}\frac{\partial \theta'_l}{\partial z}}+\overline{\mathcal{F}'_{z,h}\frac{\partial \theta'_h}{\partial z}}\right).
\end{aligned} \tag{3.24}$$

Overbars represent the symmetric components and primes the asymmetric components; low wavenumbers are denoted by the subscript l and high wavenumbers by the subscript h. The radial, azimuthal, and vertical components of the force-curl vector $\nabla \times \mathbf{F}$ in Eq. 3.22 are given by $\mathcal{F}_r$, $\mathcal{F}_\phi$, and $\mathcal{F}_z$, respectively. Eq. 3.24 is structured to emphasize contributions from symmetric and asymmetric processes. Beginning on the first line of Eq. 3.24 and moving from left to right, terms encapsulated in parentheses represent contributions to the azimuthal-mean PV tendency from: 1) symmetric PV advection, 2) asymmetric PV advection, 3) PV generation via symmetric heating,

4) PV generation via asymmetric heating, 5) PV generation via symmetric friction, and 6) PV generation via asymmetric friction. Note that the use of "heating" is more appropriately replaced by "diabatic heating or cooling". The generation terms correspond to material (Lagrangian) sources and sinks of PV and are therefore described with respect to the processes that bring about material PV variance: heating and friction. A more precise description of "PV generation via symmetric and asymmetric heating" would be PV generation via the projection of symmetric and asymmetric heating gradients onto the symmetric and asymmetric absolute vorticity vector, respectively. Likewise, a more precise description of "PV generation via symmetric or asymmetric friction" would be PV generation via the projection of symmetric or asymmetric potential temperature gradients onto the symmetric or asymmetric force-curl vector, respectively. More concise descriptions are chosen to facilitate the general discussion. Note that "asymmetric" processes described above comprise contributions from both low- and high-wavenumber asymmetries. Henceforth, results from the azimuthal-mean PV budget will be categorized by symmetric, low-wavenumber, and high-wavenumber processes. For example, references to the low-wavenumber PV advection are given by the sum of terms 1, 3, and 5 within the asymmetric PV advection term listed above.

3.7 Azimuthal-mean PV evolution during intensification

The contributions from symmetric, low-wavenumber, and high-wavenumber processes to the azimuthal-mean PV evolution are analyzed for the three time slices during intensification. The simulation is restarted beginning at each of the time slices and model output is stored every five minutes for the proceeding 3-h time period. Terms on the right-hand side of Eq. 3.24 are calculated with 5-min model output and integrated over the 3-h time period beginning at each of the time slices.

Time-integrated contributions to the azimuthal-mean PV change for the early RI time slice ($t =$ 90 h), mid RI time slice ($t = 108$ h), and late RI time slice ($t = 126$ h) are shown in Figs. 3.17, 3.18, and 3.19, respectively. Contributions to the azimuthal-mean PV change from symmetric and asymmetric friction are excluded from Figs. 3.17–3.19 because of their relatively small magnitude compared to the other terms (not shown). It is worth noting that in the preceding analyses, the diabatic heating $\dot{\theta}$ was restricted to microphysical processes to elucidate relationships between the

PV and convective-driven heating. The full diabatic heating $\dot{\theta}$ in CM1 includes contributions from diffusion, turbulent processes, moisture convergence, Newtonian cooling, and dissipative heating. The full diabatic heating $\dot{\theta}$ is incorporated into calculations for the azimuthal-mean PV budget.

To provide context for the spatial contributions from each time-integrated term to the azimuthal-mean PV structure, the azimuthal-mean PV is averaged over the respective 3-h integration time periods and shown in gray contours for each analysis. Additionally, the transverse circulation is averaged over the respective 3-h integration time periods and overlaid on the symmetric contributions to the azimuthal-mean PV change (top panels in Figs. 3.17–3.19). Results are presented in the following section for time-integrated contributions to the azimuthal-mean PV change over each 3-h time period corresponding to the early RI, mid RI, and late RI time slices.

3.7.1 Early rapid intensification

Figure 3.17 shows the time-integrated contributions to the azimuthal-mean PV change beginning at the early RI time slice ($t = 90$ h). Recall that the overall vortex structure during early RI is characterized by a relatively weak-amplitude hollow PV tower superposed by low-wavenumber PV asymmetries comprising high-wavenumber structures (see section 3.5.1). The symmetric PV advection and PV generation via symmetric heating are largely opposed radially inward of the RMW between 9–13 km altitude; a region where the magnitude of symmetric heating decreases rapidly with increasing altitude (Fig. 3.8). The low- and high-wavenumber PV advection contribute positively toward the development of a hollow PV tower structure during early RI (i.e., a positive azimuthal-mean PV tendency in the eyewall region radially inward of the RMW). Contributions from the low-wavenumber PV advection are mostly positive between $r = 25$–30 km and throughout 12-km altitude. Furthermore, the low-wavenumber PV advection is contributing to an increase of PV near the axis of rotation from the surface up to 8-km altitude. Contributions from the high-wavenumber PV advection are negative between $r = 25$–30 km and below $\sim$4-km altitude but positive in the same radial region between 4–8 km altitude. On the contrary, PV generation via both low- and high-wavenumber heating mostly contributes negatively toward the development of a hollow tower PV structure. Collectively, the results suggest that asymmetric PV advection from low-wavenumber PV asymmetries comprising high-wavenumber structures contributes positively

to developing the hollow PV tower and increasing PV near the axis of rotation. However, PV generation via asymmetric heating processes, such as convective PV generation, opposes the contributions from asymmetric PV advection and extracts from the hollow PV tower.

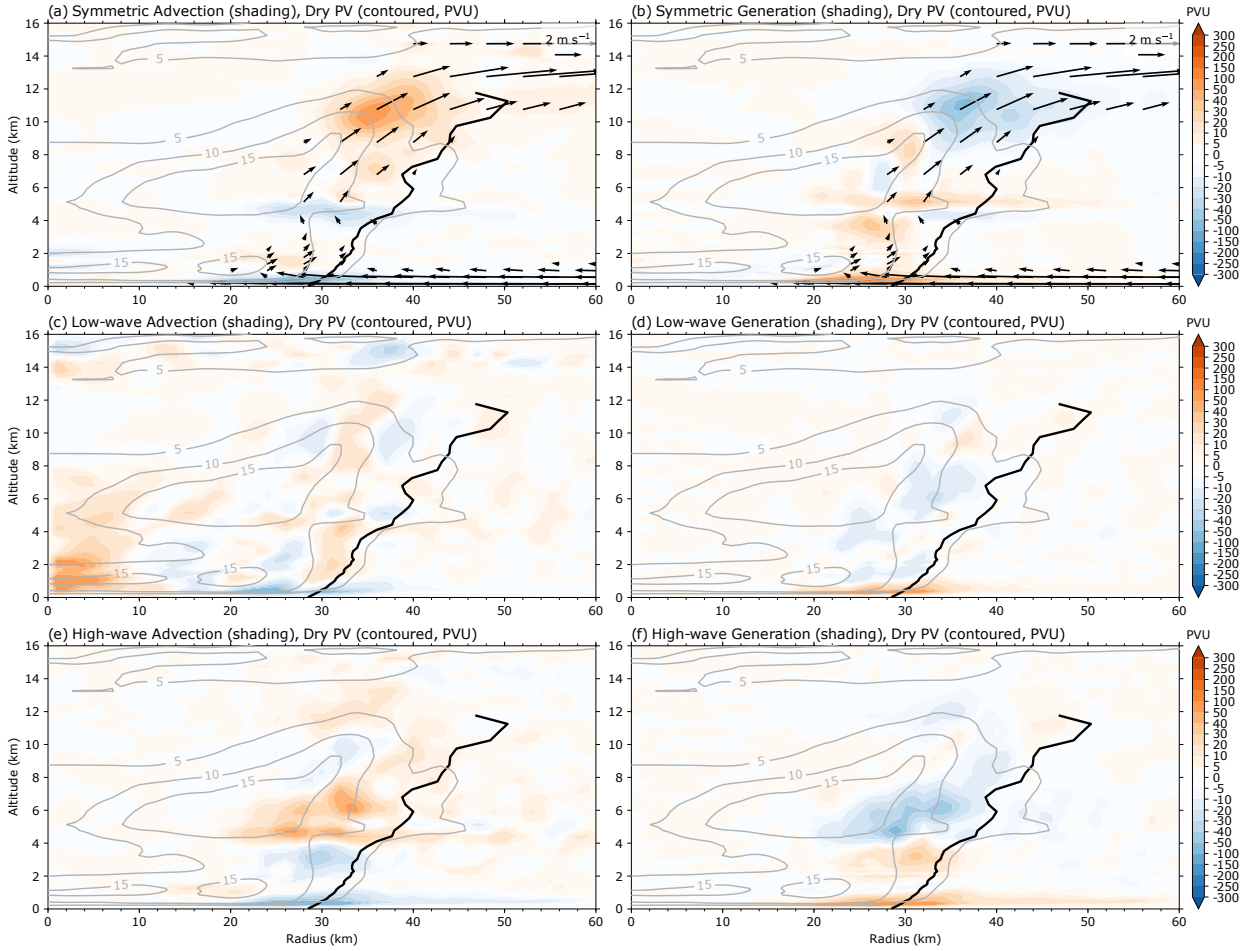

Fig. 3.17. Contributions to the azimuthal-mean PV change (3.24) from (left) advection and (right) generation are shown for the 3-h integration time period beginning at the early rapid intensification time slice ($t = 90$ h). Individual panels display in shading the time-integrated contributions from: (a) symmetric PV advection, (b) PV generation via symmetric heating, (c) low-wavenumber PV advection, (d) PV generation via low-wavenumber heating, (e) high-wavenumber PV advection, and (f) PV generation via high-wavenumber heating (all in PVU). Note that the color scale is not linear. Time-integrated contributions to the azimuthal-mean PV budget in (a) and (b) are overlaid with the following quantities averaged over the 3-h integration time period: the transverse circulation vectors (m s^{-1}), the dry PV (contoured every 5 PVU), and the radius of maximum tangential winds (black). In (a) and (b), vectors that do not exceed a 0.5 m s^{-1} transverse circulation wind speed magnitude are excluded (i.e., $\sqrt{u^2+w^2} < 1$, where u is the radial velocity and w the vertical velocity).

3.7.2 Mid rapid intensification

Figure 3.18 shows the time-integrated contributions to the azimuthal-mean PV change beginning at the mid RI time slice ($t = 108$ h). Recall that the overall vortex structure during the

mid-RI time slice is comprised of a strong-amplitude hollow PV tower superposed by a predominant low-wavenumber $m = 3$ PV asymmetry (see section 3.5.2). Similar to the early RI time slice, the symmetric PV advection and PV generation via symmetric heating are largely opposed radially inward of the RMW between 8–14 km altitude. Furthermore, the cancellation between PV advection and generation terms is evident in the low- and high-wavenumber contributions. The low-wavenumber PV advection continues to contribute positively toward increasing PV near the axis of rotation. In contrast to the early RI time slice, PV generation via low-wavenumber heating contributes positively toward strengthening the hollow PV tower; a thin strip of positive azimuthal-mean PV tendency is located radially inward of a negative azimuthal-mean PV tendency, suggesting contributions to both strengthening and contraction of the hollow PV tower (Fig. 3.18d). The high-wavenumber PV advection and generation terms approximately cancel one another radially inward of the RMW, but both contribute to a net increase of the azimuthal-mean PV radially outward of the RMW between ∼6–12 km altitude. Comparing the vertical structure of symmetric and asymmetric contributions reveals that the centroids of maximum azimuthal-mean PV tendency persistently occur at higher altitudes in the eyewall region for symmetric contributions. For example, the maximum positive contribution from symmetric PV advection occurs between 10–12 km altitude whereas the maximum positive contributions from low- and high-wavenumber PV advection occur between 6–8 km altitude (Figs. 3.18a,c,e). The same relationship holds true when comparing the symmetric and asymmetric PV generation terms (Figs. 3.18b,d,f). Contrasting the symmetric and azimuth–height analyses reveals that the vertical extent of asymmetric PV structures in the eyewall region are shallower compared to the symmetric PV structure (see Figs. 3.11 and 3.13).

3.7.3 Late rapid intensification

Figure 3.19 shows the time-integrated contributions to the azimuthal-mean PV change beginning at the late RI time slice ($t = 126$ h). Recall that the overall vortex structure during the late RI time slice is comprised of a more diffuse hollow PV tower compared to the mid RI time slice and a highly asymmetric elliptical eyewall (see section 3.5.3). Similar to the early and mid RI time slices, the symmetric PV advection and PV generation via symmetric heating are largely opposed radially

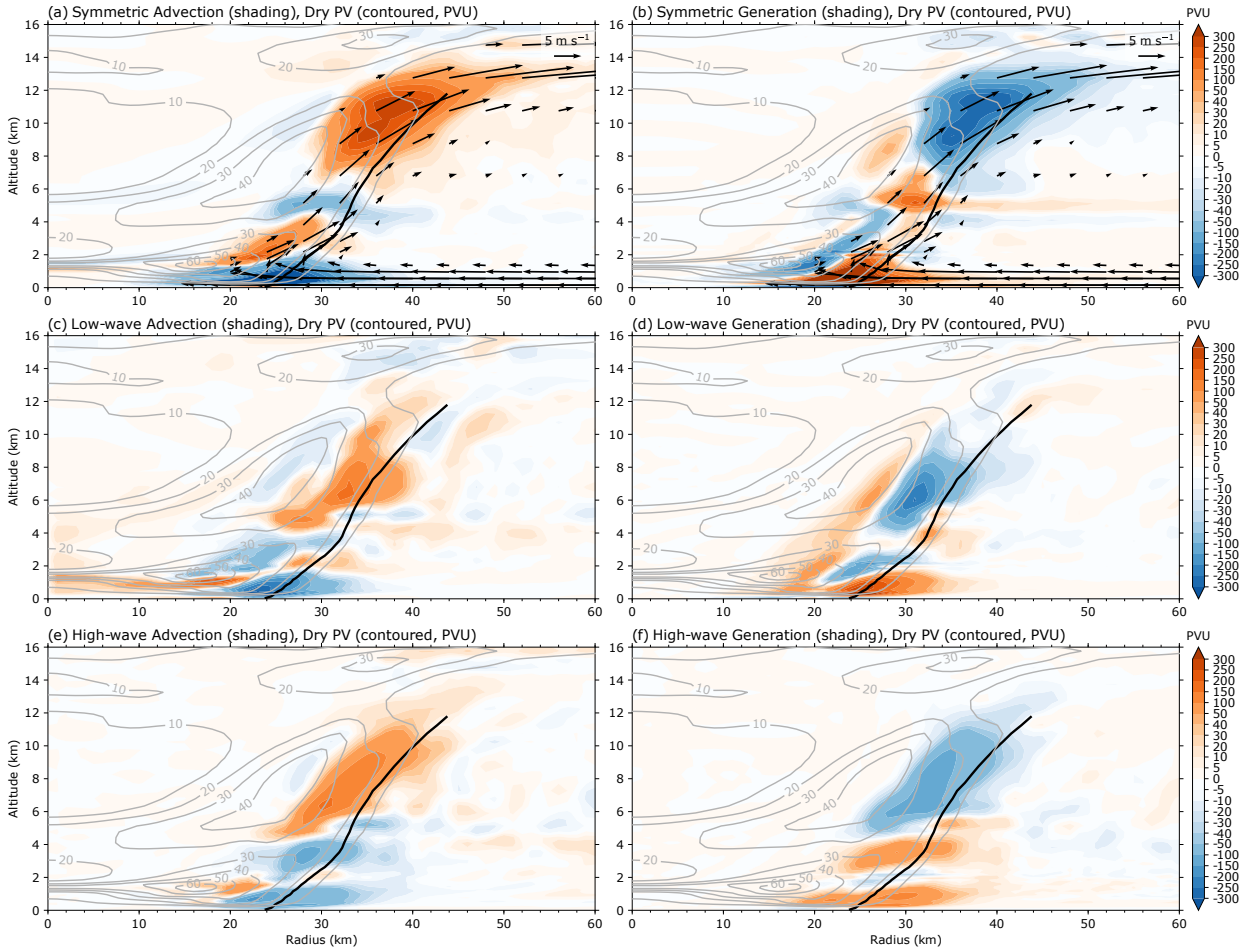

Fig. 3.18. Contributions to the azimuthal-mean PV change (3.24) from (left) advection and (right) generation are shown for the 3-h integration time period beginning at the mid rapid intensification time slice ($t = 108$ h). Individual panels display in shading the time-integrated contributions from: (a) symmetric PV advection, (b) PV generation via symmetric heating, (c) low-wavenumber PV advection, (d) PV generation via low-wavenumber heating, (e) high-wavenumber PV advection, and (f) PV generation via high-wavenumber heating (all in PVU). Note that the color scale is not linear. Time-integrated contributions to the azimuthal-mean PV budget in (a) and (b) are overlaid with the following quantities averaged over the 3-h integration time period: the transverse circulation vectors (m s^{-1}), the dry PV (contoured every 5 PVU), and the radius of maximum tangential winds (black). In (a) and (c), vectors that do not exceed a 1 m s^{-1} transverse circulation wind speed magnitude are excluded (i.e., $\sqrt{u^2+w^2} < 1$, where u is the radial velocity and w the vertical velocity). Note that the vector magnitude in the legend corresponds to 5 m s^{-1} rather than 2 m s^{-1} as in Fig. 3.17.

inward of the RMW between 8–14 km altitude; however, the region of negative contributions from symmetric PV advection between 4–7 km altitude is maximized (in magnitude) approximately 1-km below the corresponding region of maximum positive contributions from symmetric PV generation between 5–8 km altitude. The cancellation between PV advection and generation contributions is also evident in the low- and high-wavenumber contributions. As in both the early and mid RI time slices, low-wavenumber PV advection contributes positively toward increasing PV near

the axis of rotation. Low-wavenumber PV advection contributions radially inward of $r = 20$ km are negative between ∼1.5–3 km altitude and positive between ∼4–8 km altitude. Furthermore, PV generation via low-wavenumber heating remains a positive contribution along a thin radial strip coincident with the hollow PV tower between ∼7–11 km altitude. The high-wavenumber PV advection and generation terms largely cancel one another throughout the eyewall region, but the PV generation via high-wavenumber heating contributes positively to the azimuthal-mean PV located radially outward of the RMW. Similar to the early and mid RI time slices, the centroids of maximum azimuthal-mean PV tendency persistently occur at higher altitudes in the eyewall region for symmetric contributions compared to asymmetric contributions; however, the vertical extent of asymmetric PV structures in the eyewall region are deeper compared to the symmetric PV structure during late RI (see Figs. 3.14 and 3.16).

3.8 Residual analysis

To assess the reliability of results presented in the previous section, a residual analysis is carried out for each of the time-integrated PV budgets. The net azimuthal-mean PV change is calculated by differencing the end-time (t_1) and start-time (t_0) azimuthal-mean PV for each 3-h integration time period, given by $\Delta P = P(t_1) - P(t_0)$. Then, the residual $\mathcal{R}$ is defined as the difference between ΔP and the sum of time-integrated terms on the right-hand side of Eq. 3.24. That is,

$$\mathcal{R} = \Delta P - \int_{t_0}^{t_1} \frac{\partial P}{\partial t} \partial t. \tag{3.25}$$

The friction terms in Eq. 3.24 are included in the sum of contributions on the right hand side of Eq. 3.25. Figures 3.20–3.22 show the residual analysis for each of the time-integrated azimuthal-mean PV budgets. In general, the sum of contributions produces an azimuthal-mean PV change that is too large in magnitude compared to the net azimuthal-mean PV change for each of the time slices. Furthermore, the spatial variance in the sum of contributions is too large. There are radial and vertical dipoles in the sum of contributions that are not present in the net azimuthal-mean PV change, resulting in the presence of residual dipoles. Given the residual has a comparable

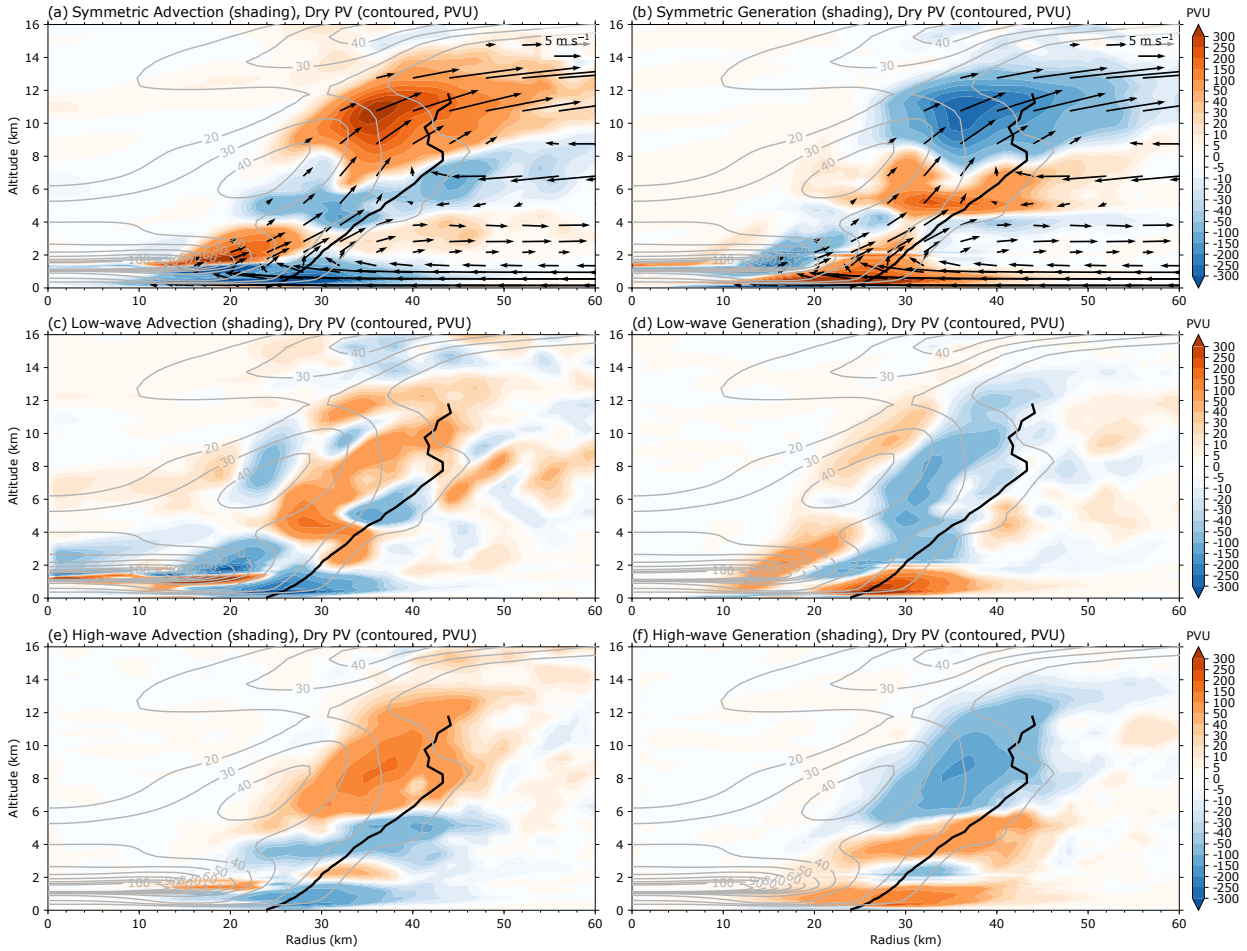

Fig. 3.19. Contributions to the azimuthal-mean PV change (3.24) from (left) advection and (right) generation are shown for the 3-h integration time period beginning at the late rapid intensification time slice ($t = 126$ h). Individual panels display in shading the time-integrated contributions from: (a) symmetric PV advection, (b) PV generation via symmetric heating, (c) low-wavenumber PV advection, (d) PV generation via low-wavenumber heating, (e) high-wavenumber PV advection, and (f) PV generation via high-wavenumber heating (all in PVU). Note that the color scale is not linear. Time-integrated contributions to the azimuthal-mean PV budget in (a) and (b) are overlaid with the following quantities averaged over the 3-h integration time period: the transverse circulation vectors (m s^{-1}), the dry PV (contoured every 5 PVU), and the radius of maximum tangential winds (black). In (a) and (c), vectors that do not exceed a 1 m s^{-1} transverse circulation wind speed magnitude are excluded (i.e., $\sqrt{u^2+w^2} < 1$, where u is the radial velocity and w the vertical velocity). Note that the vector magnitude in the legend corresponds to 5 m s^{-1} rather than 2 m s^{-1} as in Fig. 3.17.

magnitude to the net azimuthal-mean PV change, it is difficult to deduce a tenable conclusion from results presented in the previous section.

There may be several factors exacerbating the residual magnitude and complicating a clear interpretation of the azimuthal-mean PV budget results. First and foremost, the aforementioned adiabatic/diabatic cancellation noted by Tory et al. (2012) appears to be problematic. The adiabatic/diabatic cancellation problem is noticeably pronounced in the symmetric contributions to the

azimuthal-mean PV budget where the symmetric PV advection is almost exactly counterbalanced by the PV generation via symmetric heating (see panels (a) and (b) in Figs. 3.17–3.19). Given that symmetric contributions to the azimuthal-mean PV change are approximately twice the magnitude of low- and high-wavenumber contributions, there is a higher potential for errors arising from symmetric adiabatic/diabatic cancellations; however, there are also large cancellations among the low- and high-wavenumber contributions during the mid and late RI time slices (see Figs. 3.18 and 3.19). As noted earlier, the residual is prone to numerical roundoff errors associated with successive finite differencing required to compute terms in the azimuthal-mean PV budget. In addition to numerical roundoff errors associated with successive finite differencing, the azimuthal-mean PV budget requires first interpolating variables from the Cartesian grid to a cylindrical grid. Errors inherent to interpolation approximations are therefore carried into the finite difference approximations, producing a potential pathway for compounding numerical errors. The Cartesian to cylindrical transformation is approximated with a bilinear interpolation and finite differences are computed with a 3-point stencil that is second-order accurate for stretched grids. Future work will investigate the impacts of increasing the order of accuracy for both the interpolation and finite differencing. Additional considerations for error sources in the azimuthal-mean PV budget analysis include neglecting azimuthal density variations and potential center misplacement errors. Additional analyses are required to isolate the primary error sources and substantiate the principal findings described in the previous section.

3.9 Vortex evolution in (R, θ) space

As noted earlier, the structural evolution during RI for the simulated TC presented in this chapter is distinct from the structural evolution during the observed RI of Hurricane Patricia (2015) presented in chapter 2. Specifically, the symmetric diabatic heating maximum in the eyewall region did not remain fixed to the same absolute angular momentum (M) surfaces during RI. Instead, M surfaces continued to converge toward the axis of rotation throughout RI while the symmetric diabatic heating maximum remained approximately fixed in physical space slightly inward of the RMW (see Figs. 3.8b, 3.11b, and 3.14b). On the contrary, during Patricia's RI, the symmetric

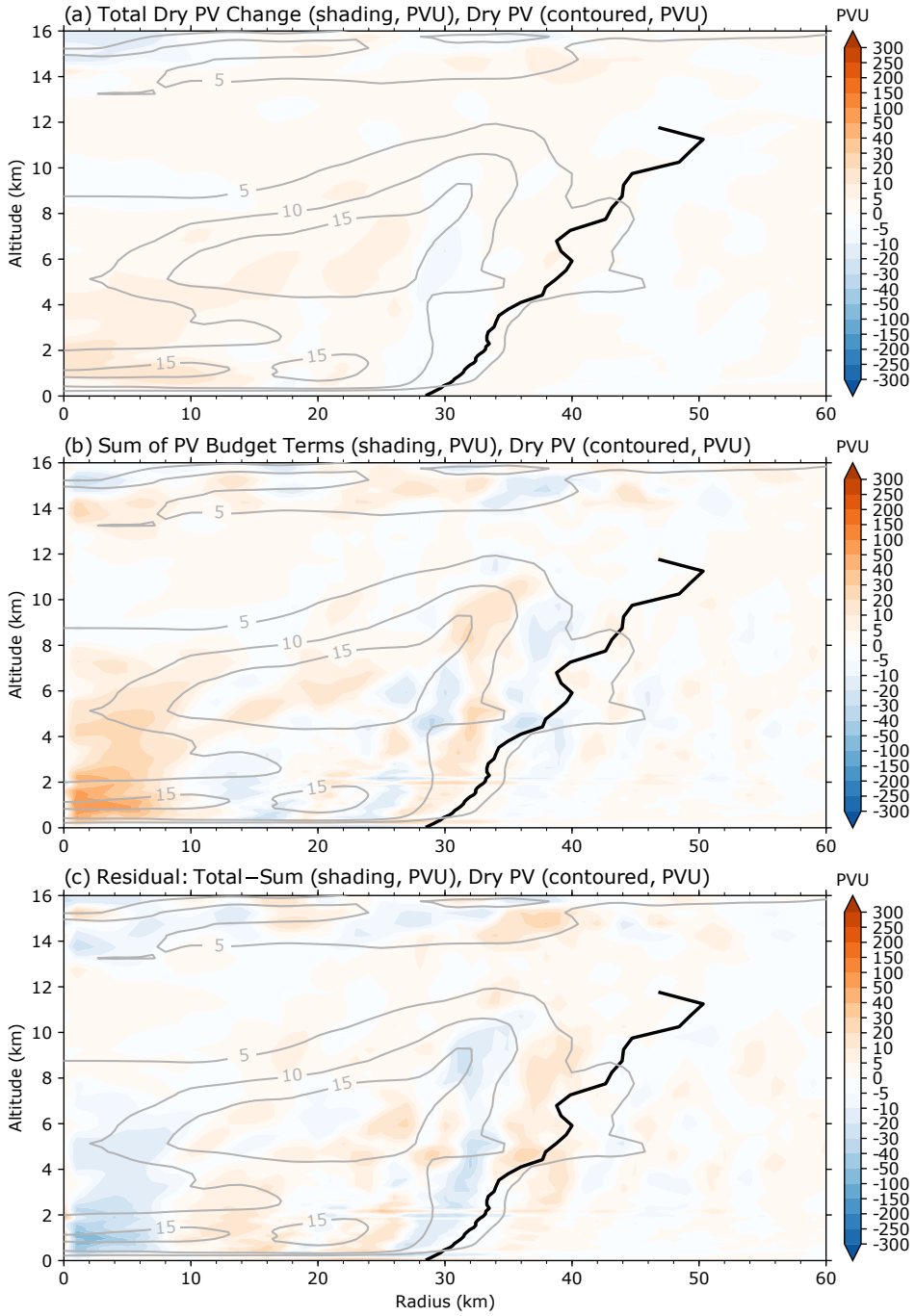

Fig. 3.20. (a) The net azimuthal-mean potential vorticity (PV) change (ΔP) is shown for the 3-h integration time period beginning at the early rapid intensification time-slice ($t = 90$ h). (b) The sum of all time-integrated contributions to the azimuthal-mean PV change. (c) The residual between the net azimuthal-mean PV change and the sum of all time-integrated contributions [(a) minus (b)]. Note that the color scale is not linear. Each panel is overlaid with the following quantities averaged over the 3-h integration time period: the dry PV (contoured every 5 PVU) and the radius of maximum tangential winds (black).

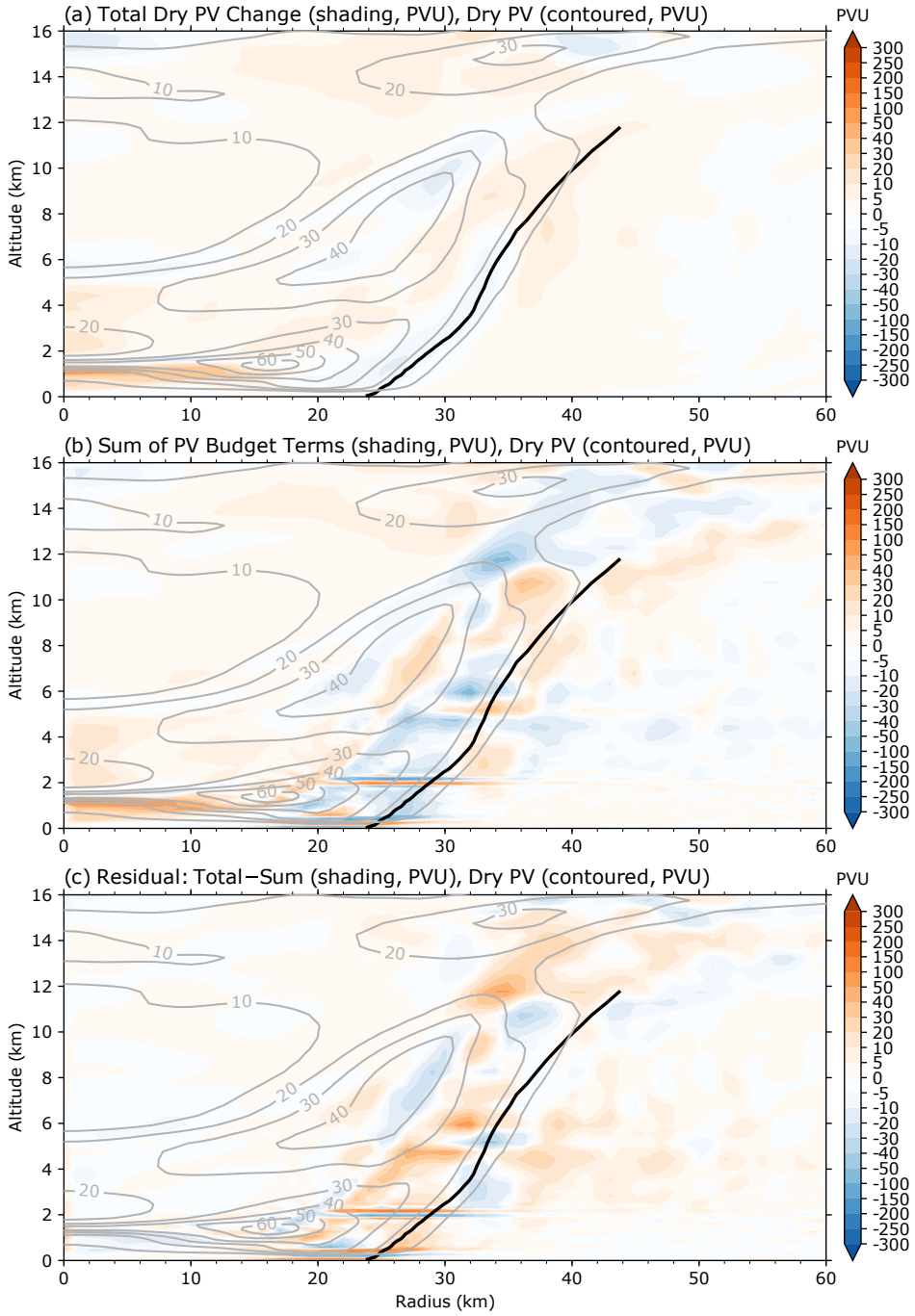

Fig. 3.21. (a) The net azimuthal-mean potential vorticity (PV) change (ΔP) is shown for the 3-h integration time period beginning at the mid rapid intensification time-slice ($t = 108$ h). (b) The sum of all time-integrated contributions to the azimuthal-mean PV change. (c) The residual between the net azimuthal-mean PV change and the sum of all time-integrated contributions [(a) minus (b)]. Note that the color scale is not linear. Each panel is overlaid with the following quantities averaged over the 3-h integration time period: the dry PV (contoured every 5 PVU) and the radius of maximum tangential winds (black).

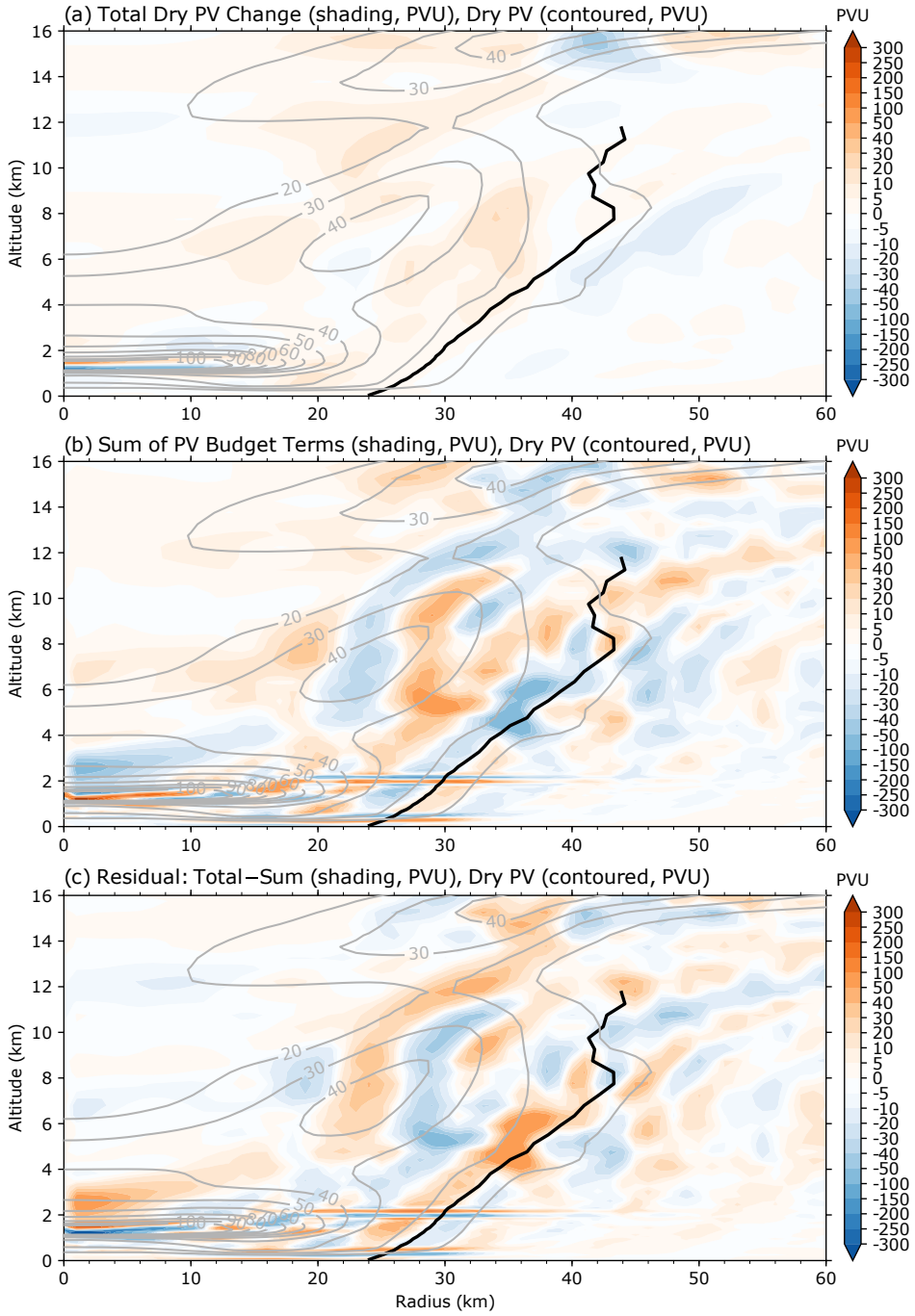

Fig. 3.22. (a) The net azimuthal-mean potential vorticity (PV) change (ΔP) is shown for the 3-h integration time period beginning at the late rapid intensification time-slice ($t = 126$ h). (b) The sum of all time-integrated contributions to the azimuthal-mean PV change. (c) The residual between the net azimuthal-mean PV change and the sum of all time-integrated contributions [(a) minus (b)]. Note that the color scale is not linear. Each panel is overlaid with the following quantities averaged over the 3-h integration time period: the dry PV (contoured every 5 PVU) and the radius of maximum tangential winds (black).

diabatic heating maximum in the eyewall region remained nearly fixed to the same M surfaces as they contracted in physical space (see Fig 2.12).

To further contrast the simulated TC to Hurricane Patricia, Fig. 3.23 shows the axisymmetric PV structure for each of the time slices in the potential radius–potential temperature (R, θ) coordinate space. The hollow PV tower begins to emerge during the early RI time slice with maximum values concentrated between $R = 125$–200 km and located radially inward of the symmetric diabatic heating maximum. As RI continues throughout the mid and late RI time slices, the hollow PV tower and symmetric diabatic heating maximum gradually shift outward to increasingly larger potential radius. Furthermore, the mid-level PV maximum becomes increasingly displaced from the symmetric diabatic heating maximum. Together, the structural evolution of the simulated TC and Hurricane Patricia may exemplify two different "modes" of intensification; PV is concentrated "in-place" for the simulated TC in physical space and PV is concentrated "in-place" for Hurricane Patricia in the (R, θ) coordinate space. Underlying the two different modes of intensification may be differences in the incipient vortex circulation between the simulated TC and Hurricane Patricia.

It is also worth noting in the (R, θ) coordinate space that the PV structure becomes largely dominated by the low-level PV bridge during the late RI time slice (Fig. 3.23c). The maximum PV found along the low-level PV bridge exceeds 200 PVU near the axis of rotation, which is approximately four times larger than the maximum PV found in the hollow tower. Hurricane Patricia also exhibited a low-level PV bridge structure during the near maximum intensity and rapid weakening intensive observing periods; however, the maximum PV found along Patricia's low-level PV bridge remained nearly the same as the maximum PV found in the hollow tower, even during rapid weakening (Fig. 2.11c). To this point, results in the (R, θ) coordinate space have primarily been discussed in context of the horizontal stretching that occurs in regions of large radial M gradients, but vertical stretching also occurs in regions of large vertical θ gradients (i.e., regions of high stratification). The PV bridge structure is associated with both a large M gradient radially inward of the RMW and enhanced stratification in the eye region (see Fig. 3.14b) that together produce a "dynamically large" region of PV in the (R, θ) coordinate space. The azimuthal-mean PV budget indicates that contributions to the PV bridge structure primarily arise from

low-wavenumber PV advection during the mid and late RI time slices (see Figs. 3.18c and 3.19c), suggesting that substantial PV mixing is occurring between the eye–eyewall interface. Future work will examine the Eulerian PV budget in the (R, θ) coordinate space (Eq. 2.5) to further assess asymmetric contributions to TC intensification and potentially alleviate issues arising from the adiabatic/diabatic cancellation problem.

3.10 Discussion and conclusions

The nature and evolution of asymmetric structures are examined during tropical cyclone (TC) intensification with an idealized, high-resolution simulation. The primary question raised in this chapter was: do asymmetries facilitate or interfere with tropical cyclone rapid intensification? To begin addressing this question, several metrics to quantify the magnitude of symmetry within the TC inner-core region are analyzed. A locus of emphasis is placed on quantifying the various scales of potential vorticity (PV) asymmetries that develop throughout the TC intensification period. The bulk evolution of PV asymmetries during the intensification period is summarized as follows:

- The low-layer (1–3 km altitude) and high-layer (5–8 km altitude) azimuthal distributions of PV and diabatic heating are never fully symmetric during the intensification period. Instead, the azimuthal PV distribution fluctuates between 40–70% symmetricity while the azimuthal diabatic heating distribution generally progresses toward larger symmetricity throughout the intensification period, attaining approximately 50–60% symmetricity at maximum intensity (Fig. 3.4).
- The low- and high-layer symmetricity for both PV and diabatic heating remain within $\sim$20% of one another throughout the intensification period.
- The low-layer azimuthal PV distribution becomes increasingly concentrated within lower wavenumbers (i.e., asymmetries with larger azimuthal scales) throughout the intensification period (Figs. 3.5a, 3.6a).
- In contrast to the low-layer azimuthal PV distribution, the high-layer PV remains distributed over a relatively broader range of azimuthal scales throughout the intensification period (Figs. 3.5b, 3.6b).

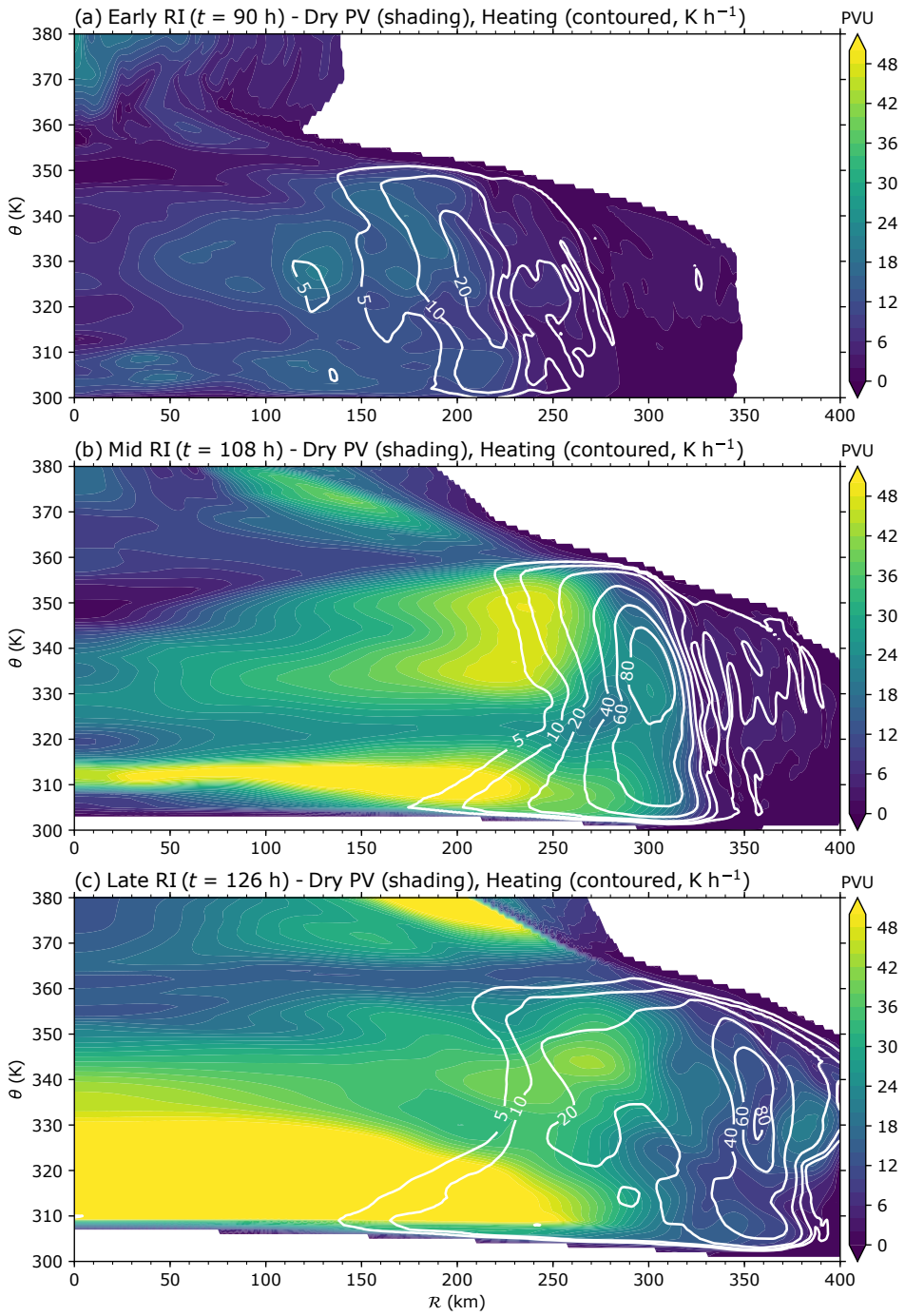

Fig. 3.23. The dry Ertel's potential vorticity (PV; shading, PVU) is overlaid with diabatic heating from microphysical processes (white, contours at 5, 10, 20, 40, 60, and 80 K h^{-1}) in the potential radius–potential temperature (R, θ) coordinate space for (a) the early rapid intensification (RI) time slice ($t = 90$ h), (b) the mid RI time slice ($t = 108$ h), and (c) the late RI time slice ($t = 126$ h).

The three-dimensional kinematic and thermodynamic structure of asymmetries are examined at three time slices during the intensification period: early RI ($t = 90$ h), middle (mid) RI ($t = 108$ h),

and late RI ($t = 126$ h). The time slices represent the approximate intensification period quartiles prior to the TC attaining its maximum intensity (i.e., the 25th, 50th, and 75th percentiles for the intensification time scale). To further investigate the inner-core structural evolution during intensification, asymmetries are partitioned into low azimuthal wavenumbers ($m = 1$–3) and high azimuthal wavenumbers ($m = 4$–180), representing relatively large and small azimuthal scales, respectively. The inner-core vortex structure varies significantly throughout the intensification period, transitioning from: 1) a weak-amplitude hollow PV tower superposed by low-wavenumber PV asymmetries comprising high-wavenumber structures, to 2) a strong-amplitude hollow PV tower superposed by a predominant $m = 3$ PV asymmetry, to 3) a relatively diffuse hollow PV tower and a highly asymmetric elliptical eyewall. Azimuth–height analyses averaged over the bulk hollow PV tower region demonstrate that asymmetries possess a large degree of vertical coherence (Figs. 3.10, 3.13, and 3.16). As intensification progresses and the asymmetries become concentrated among smaller azimuthal wavenumbers (larger scales), the degree of vertical coherence increases. At no time during the intensification period is the TC entirely symmetric. In fact, the asymmetric PV distribution remains on the same order of magnitude as the symmetric PV distribution at all stages of the intensification period analyzed herein (Figs. 3.9, 3.12, and 3.15).

Scale-dependent contributions to TC intensification are examined by partitioning the advective form of the azimuthal-mean PV equation into components representing symmetric, low-wavenumber, and high-wavenumber processes. The scale-dependent azimuthal-mean PV budget demonstrates that low- and high-wavenumber contributions are persistently on the same order of magnitude as symmetric contributions throughout the intensification period. Persistent features are noted in the azimuthal-mean PV budget analysis during the intensification period. Low-wavenumber PV advection contributes to an enhancement of PV near the axis of rotation from near the surface through 8-km altitude during both the early and mid RI time slices (Figs. 3.17c, 3.18c). The analyses suggest that low-wavenumber asymmetries are transporting PV between the eye–eyewall interface, resulting in a net-positive increase of azimuthal-mean PV near the axis of rotation (in the eye). Previous studies have demonstrated that asymmetric PV mixing events flux high-PV air from the eyewall toward the axis of rotation, inducing a decrease in central pressure (deepening;

Schubert et al. 1999; Kossin and Schubert 2001; Hendricks et al. 2009; Hendricks and Schubert 2010). The asymmetric PV mixing events from the aforementioned studies arise from combined barotropic–baroclinic instability. Although the release of a combined barotropic–baroclinic instability is not examined herein, the principal dynamics that induce deepening concomitant with high-PV transport toward the axis of rotation may be relevant in the present analysis. A recent study has attributed asymmetric PV mixing as a principal deepening mechanism prior to and during the early stages of RI (Tsujino and Kuo 2020). Additional analyses are required to delineate the potential relationship between low-wavenumber PV transport toward the axis of rotation and TC intensification.

Another persistent feature noted in the azimuthal-mean PV budget arises from PV generation via low-wavenumber heating, contributing to a concentration of PV along a thin radial strip during both the mid and late RI time slices (Figs. 3.18d, 3.19d). Low-wavenumber asymmetries may therefore have a non-negligible contribution to both the strengthening and thinning of the hollow PV tower during intensification. In chapter 2, asymmetric (eddy) torques were hypothesized to concentrate PV radially inward of the eyewall diabatic heating maximum during Hurricane Patricia's RI. Contributions to PV generation via asymmetric heating were acknowledged as another unresolved process in the axisymmetric Patricia analyses, but were not discussed in light of concentrating PV radially inward of the symmetric diabatic heating maximum. Furthermore, Nolan and Grasso (2003) and Nolan et al. (2007) demonstrated that asymmetric heating can result in a contraction of the RMW via asymmetric fluxes of high-PV air. The findings reported herein instead suggest a direct pathway toward both the strengthening and thinning of the hollow PV tower during intensification accomplished through PV generation via low-wavenumber heating. Additional analyses are required to substantiate potential contributions from asymmetric PV fluxes to the strengthening and thinning of the hollow PV tower.

A residual budget analysis is constructed by comparing the net azimuthal-mean PV change over a three hour time beginning at each of the time slices to the time-integrated sum of contributions to the azimuthal-mean PV change (Figs. 3.20–3.22). In general, the sum of contributions produces an azimuthal-mean PV change that is too large in magnitude compared to the net azimuthal-mean PV

change for each of the time slices. Furthermore, the spatial variance in the sum of contributions is too large. Given the residual has a comparable magnitude to the net azimuthal-mean PV change, it is difficult to deduce tenable conclusions from the azimuthal-mean PV budget analysis. Therefore, an emphasis is placed on the aforementioned persistent features noted in the azimuthal-mean PV budget analysis.

In summation, low-wavenumber PV advection near the axis of rotation and contributions from PV generation via low-wavenumber heating to the development of a hollow PV tower appear as persistent features that may facilitate TC intensification. Although additional analyses are required to accept or reject this hypothesis, it is evident that asymmetric contributions to TC intensification are dynamic and predicated on the asymmetry scale and structure. The analyses presented herein depict a single facet of asymmetric contributions to TC intensification: the direct contribution from low- and high-wavenumber asymmetries to the azimuthal-mean PV structure. Indirect contributions from asymmetries are left unaccounted but may constitute an important facet of TC intensification. Can asymmetries indirectly contribute to TC intensification via structural modifications to the vortex that further stimulate the intensification process? And is it possible to disentangle indirect from direct contributions to TC intensification? Future work will be directed toward understanding the precise direct and indirect contributions from asymmetric structures to TC intensification. Approximately 100,000 passive parcels have been released at the start of each time slice analyzed herein. A Lagrangian analysis will be used to quantify the characteristics of parcels that traverse asymmetric structures in the TC eyewall. An asymmetric PV budget will be constructed to investigate the growth and decay processes of asymmetric structures discussed herein. Furthermore, an axisymmetric PV budget will be constructed in the potential radius–potential temperature coordinate space to elucidate the principal dynamics associated with the formation of a hollow PV tower and asymmetric contributions to TC intensification.

CHAPTER 4

On the contributions of incipient vortex circulation and environmental moisture to tropical cyclone expansion

4.1 Overview

To provide an illustrative example of the vastly different scales represented by the two tails of the global TC size distribution, Fig. 4.1 provides a comparison between the synoptic weather charts for Hurricane Inez (1966; Hawkins and Rubsam 1967; Hawkins and Imbembo 1976) and Super Typhoon Tip (1979; Dunnavan and Diercks 1980). The entire circulation of Inez can fit within what might be approximated as Super Typhoon Tip's inner-core circulation, and yet both TCs possessed nearly identical minimum sea-level pressures ($\sim$925 hPa) at the times shown. Together, Hurricane Inez and Super Typhoon Tip raise a compelling question: what are the principal processes that contribute to such large variability in TC sizes? As noted in chapter 1, there are several factors contributing to TC expansion and it's likely that a combination of several factors produced the dramatic size difference noted between Inez and Tip.

Previous studies have highlighted a proclivity for relatively small TCs to stay small and relatively large TCs to stay large, suggesting that TCs possess a sort of "memory" with respect to their incipient circulation (e.g., Merrill 1984; Knaff et al. 2014; Kilroy and Smith 2017; Tao et al. 2020). In addition to the incipient vortex circulation, previous studies often note environmental moisture as an important factor contributing to variable TC sizes (e.g., Hill and Lackmann 2009; Xu and Wang 2010; Knaff et al. 2017). Motivated by the prevailing findings reported in previous studies, this chapter further investigates the contributions of incipient vortex circulation and environmental moisture to TC expansion within an idealized modeling framework. Section 4.2 discusses the methods to create variable incipient vortex circulations and environmental moisture profiles within the idealized numerical modeling framework. Section 4.3 describes the overall structural evolution for each simulated TC and associated contributions to expansion rates. Section 4.4 relates the structural progression of each simulated TC to variable expansion rates by examining the absolute

circulation evolution. Section 4.5 discusses the principal findings underlying TC expansion along with concluding remarks and avenues for future work.

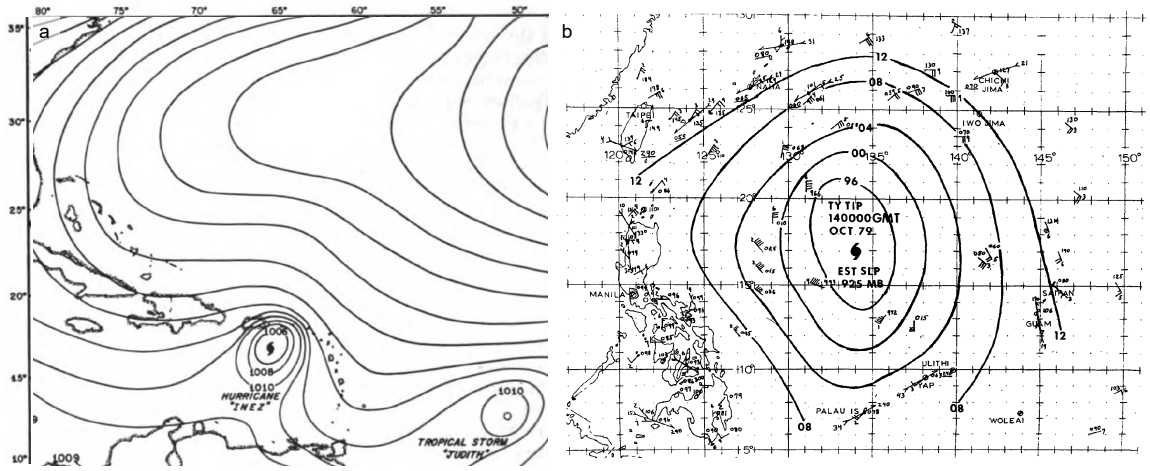

Fig. 4.1. Surface weather maps are shown for (a) Hurricane Inez (1966) at 1200 UTC on 28 September and (b) Super Typhoon Tip (1979) at 0000 UTC on 14 October. (a) Contours denote the surface pressure (hPa). (b) Contours denote the surface pressure truncated to the first two digits for values below 1000 hPa and truncated to the last two digits for values $\geq$ 1000 hPa. Wind barbs denote the surface wind speed (knots). Adapted from Fig. 3 in Hawkins and Rubsam (1967) and Fig. 8 in Dunnavan and Diercks (1980).

4.2 Experimental design and numerical model setup

Previous studies investigating the contributions of initial vortex size to TC expansion within an idealized modeling framework begin by prescribing an axisymmetric vortex profile with a fixed tangential velocity maximum. A subset of vortices with different sizes is created by either varying the radius of maximum tangential winds (RMW; e.g., Xu and Wang 2010; Kilroy and Smith 2017; Xu and Wang 2018) or fixing the RMW and varying the radial vortex shape outward of the RMW (e.g., Chan and Chan 2014, 2015; Xu and Wang 2018). Although the two methods vary a different element of the incipient vortex circulation, and thus likely differ in producing variable TC expansion rates, both methods more generally vary the incipient vortex circulation strength. That is, either increasing the RMW or decreasing the radial decay of tangential velocity outward of the RMW is tantamount to increasing the incipient vortex circulation strength.

Herein, the initial tangential velocity maximum and RMW are fixed while varying the radial decay of tangential velocity outward of the RMW to produce a set of incipient vortices. The radial structure of tangential velocity is prescribed via a modified Rankine vortex of the form

$$v(r) = \begin{cases} v_{max}\left(\frac{r}{r_{max}}\right) & 0 \leq r < r_{max} \\ v_{max}\left(\frac{r}{r_{max}}\right)^{-\alpha} & r \geq r_{max}, \end{cases} \tag{4.1}$$

where $v_{max} = 15$ m s^{-1} is the maximum tangential velocity, r_{max} = 50 km is the RMW, and α is the decay parameter. After the radial structure of the incipient vortices is prescribed, a radial decay function is applied following Nolan (2007) to ensure that the total circulation is zero in the doubly periodic model domain for 3-D simulations. The radial decay function is given by

$$v(r) = v_0(r)\exp\left(-\frac{r}{R}\right), \tag{4.2}$$

where $v_0(r)$ denotes the initial modified Rankine vortex profile given by (4.1), r is the radius, and R is chosen as 600 km. Figure 4.2 shows the axisymmetric tangential velocity and vorticity profiles after applying the radial decay function. Then, a linear vertical decay function is applied that reduces the tangential velocity to zero at an altitude of 20 km. Values of α are chosen as 0.3, 0.5, and 0.7, in accordance with observations of North Atlantic basin TCs (Mallen et al. 2005). It is unlikely that a tropical storm is characterized by as steep a radial decay of tangential velocity given by the $\alpha = 0.7$ vortex, but this subset of vortices is examined to elucidate the contributions of incipient vortex circulation to TC expansion. The $\alpha = 0.7$ and $\alpha = 0.3$ vortices will henceforth be referred to as small and large, respectively.

The degree to which environmental moisture modulates TC expansion will largely depend on its horizontal and vertical variations throughout the atmosphere. Previous studies investigating the contributions of environmental moisture to TC expansion often designate a sounding representative of the tropics, fix the temperature profile, and vary the mixing ratio; this method preserves the temperature while varying the relative humidity. For example, Hill and Lackmann (2009) placed their vortices in a moist envelope where the environmental humidity was held constant within 100 km of the incipient vortex center, linearly reduced between 100–150 km, and constant beyond 150-km

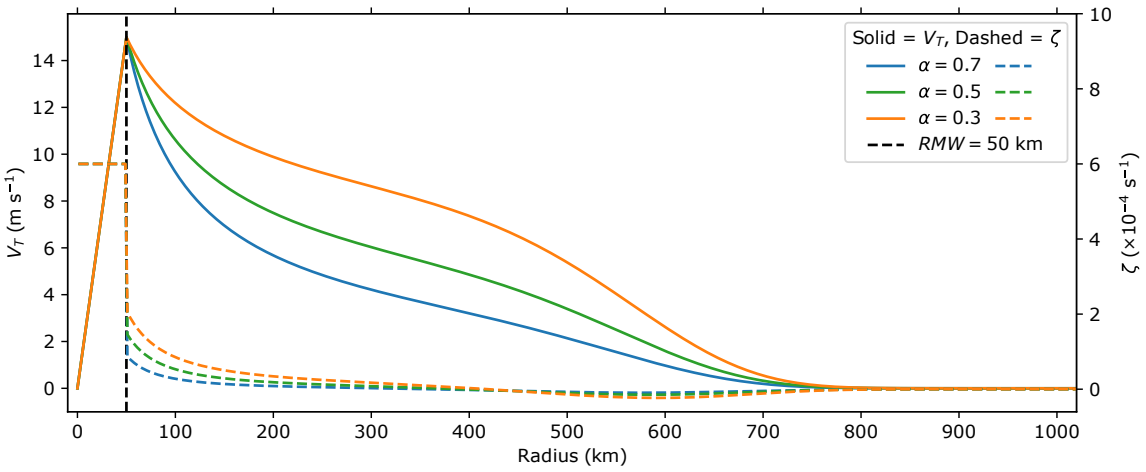

Fig. 4.2. Axisymmetric radial profiles of tangential velocity (solid) and vertical vorticity (dashed) are shown for each of the incipient vortices. The decay parameter used for each modified Rankine vortex is given in the legend by α. A radial decay function (4.2) is applied to each of the tangential velocity profiles to ensure that the circulation is zero at the doubly-periodic boundaries of 3-D simulations.

radius. The environmental moisture reduction factor was applied uniformly in the vertical (i.e., no variations in the vertical were introduced beyond those given in the original sounding). Xu and Wang (2010) also applied a uniform reduction factor in the vertical to create variable initial environments. Herein, a methodology is adopted that is motivated by climatological studies demonstrating that tropical moisture variance is maximized near the mid troposphere (e.g., Holloway and Neelin 2009; Dunion 2011). Furthermore, relatively high mid-tropospheric moisture content within tropical waves has been shown to be an important factor contributing to cyclogenesis (Davis and Ahijevych 2013; Komaromi 2013).

Beginning with the Dunion moist-tropical sounding (Dunion 2011), the temperature profile is fixed and the vertical structure of moisture is systematically varied to produce a set of three soundings. The Dunion moist-tropical sounding is first interpolated to 40-m vertical intervals between the surface and 10-km altitude. This 10-km region is smoothed using a 3-km low-pass Lanczos filter with 35 weights. Variations to the smoothed moisture profile are then introduced by applying a Hanning window with a multiplicative factor such that the relative humidity ($\mathcal{H}$) is set to 20%, 40%, or 60% at 4960-m altitude (~560 hPa; Fig. 4.3a). The dewpoint temperature profiles are reconstructed with these variations and shown on a skew-t log-p diagram in Fig. 4.3b, along with the original Dunion moist-tropical sounding for reference. The $\mathcal{H} = 60\%$ sounding is nearly

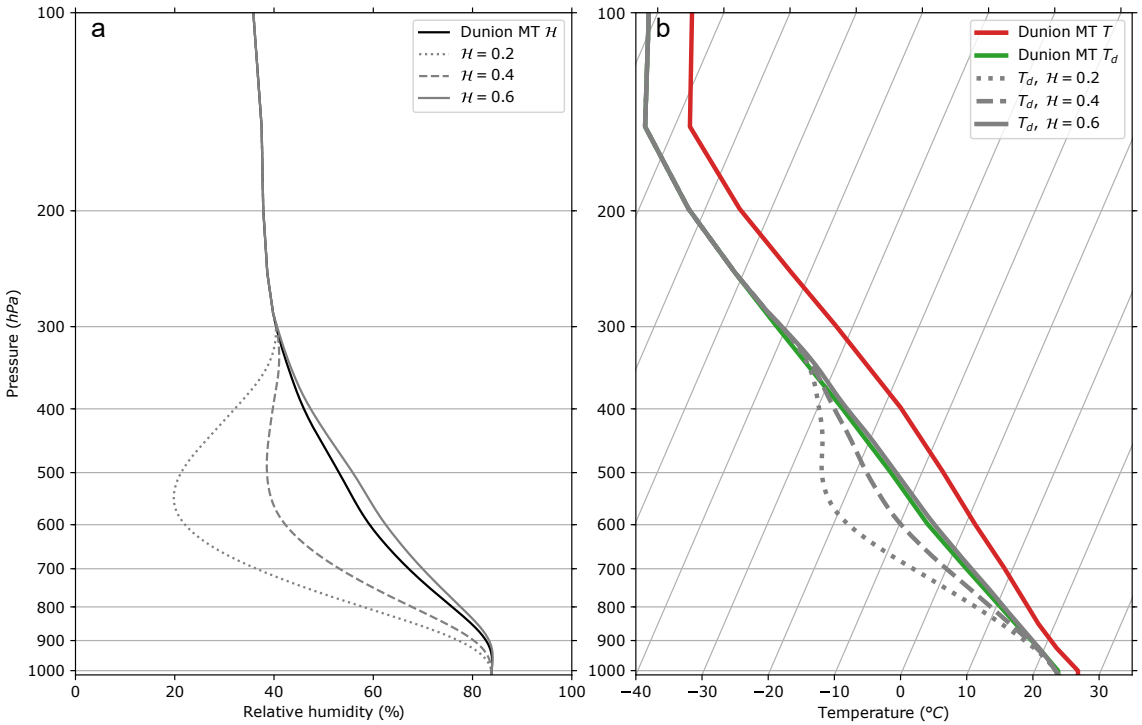

Fig. 4.3. (a) Relative humidity ($\mathcal{H}$) is shown as a function of log-pressure for the Dunion moist-tropical sounding (black) and each of the environmental moisture profiles (gray). (b) Temperature and dewpoint temperature are shown as a function of log-pressure for the Dunion moist-tropical sounding (red and green, respectively), along with dewpoint temperature for each of the environmental moisture profiles (gray).

identical to the Dunion moist-tropical sounding, and the $\mathcal{H} = 20\%$ sounding resembles the mid-level moisture content observed during a Saharan air layer event in the North Atlantic basin (Dunion 2011). Initial horizontal moisture variations are neglected aside from those required to satisfy thermal wind balance when superposing an axisymmetric vortex circulation onto a horizontally homogeneous environment. This method is limited in its representation of nature where TCs often develop in asymmetric distributions of moisture; however, it is fruitful to examine the expansion of TCs in a simplified framework that can be generalized to represent a larger set of environments in future studies. The $\mathcal{H} = 20\%$ and $\mathcal{H} = 60\%$ environments will henceforth be referred to as dry and moist, respectively.

Numerical simulations are carried out with the nonhydrostatic, fully compressible Cloud Model 1 (CM1) version 19.7 (Bryan and Fritsch 2002). As described above, the incipient vortex circulation and environmental moisture are varied to create three different initial conditions for each parameter, resulting in nine experiments. Each of the nine experiments are simulated with the axisymmetric

configuration of CM1, and the four experiments representing the small/large incipient vortices and the dry/moist environments are simulated with the full, three-dimensional configuration of CM1. Axisymmetric simulations are computationally inexpensive, and therefore an ensemble of ten axisymmetric simulations is produced for each of the nine experiments in the original set. The 3-D experimental design is chosen to aid in delineating the underlying processes contributing to TC expansion in three dimensions by selecting the extrema of initial conditions. Following Nguyen et al. (2008), random moisture perturbations with an amplitude of $\pm$ 0.5 g kg^{-1} are introduced to the lowest 500 m of the axisymmetric simulation domains. This method is chosen to examine the sensitivity of TC expansion, and the processes discussed herein, to stochastic processes such as deep, moist convection.

The axisymmetric grid spans 3050 km in radius and is defined with a uniform 1-km radial grid spacing in the innermost 300 km that gradually stretches to 10-km spacing at the domain boundary. There are 800 radial grid points in total. The vertical grid spans 28 km in altitude and is defined with a grid spacing that stretches from 50- to 500-m in the lowest 5.5 km and is a uniform 500-m above 5.5 km. There are 65 vertical grid points in total, with 12 lying in the lowest 2-km altitude. A Rayleigh damping layer is applied 100 km from the outer horizontal boundary and above 22-km altitude to aid in mitigating the reflection of internal gravity waves.

The 3-D grid spans 2040$\times$2040 km in the horizontal and is defined with a uniform 2.5-km grid spacing in the innermost 1200 km that gradually stretches to 11.5-km spacing at the domain boundaries. There are 600×600 horizontal grid points in total. The vertical grid and Rayleigh damping layer applied above 22-km altitude are identical to those used in the axisymmetric simulations. Note that the radial grid spacing in the axisymmetric domain is not identical to the horizontal grid spacing in the 3-D domain. The principal findings in this study are not sensitive to the choice of axisymmetric grid spacing (not shown), and therefore results from the axisymmetric simulations with a finer 1-km radial grid spacing are presented.

Rather than placing the 3-D vortices in a quiescent environment, a 5 m s^{-1} uniform westerly flow is gradually imposed throughout the domain following a methodology similar to the time-varying point-downscaling (TVPDS) technique (Onderlinde and Nolan 2017). The uniform flow

is introduced by adding a Newtonian relaxation term to the horizontal momentum equations, given by

$$\frac{\partial u}{\partial t} = \ldots - \frac{\langle u \rangle - u_{ref}}{\tau_n}, \tag{4.3}$$

and

$$\frac{\partial v}{\partial t} = \ldots - \frac{\langle v \rangle - v_{ref}}{\tau_n}, \tag{4.4}$$

where $\langle u \rangle(z)$ and $\langle v \rangle(z)$ denote the domain-averaged zonal and meridional wind velocities, respectively, $u_{ref}(z,t)$ and $v_{ref}(z,t)$ denote the reference zonal and meridional wind profiles to nudge toward, respectively, and τ_n is the nudging time scale. Thus, domain-averaged winds at each vertical level are nudged toward a specified reference profile that is a function of height and time, avoiding the introduction of a net circulation into the domain. The nudging time scale τ_n sets the rate at which the domain-averaged winds are nudged toward the reference wind profile. Each of the vortices is permitted to develop deep, moist convection for 24 h prior to introducing the 5 m s^{-1} uniform westerly flow with a 6-h nudging time scale. A time-varying translational domain is updated each hour in the simulation to track the minimum of a smoothed pressure field that represents the approximate center of each vortex, and the domain translation velocity vector is subtracted from the total wind to produce grid-relative winds. The center location is further refined by selecting the 2–8 km layer-averaged pressure centroid following the method described by Nguyen et al. (2014).

All simulations are integrated for eight days on an f-plane corresponding to $\sim$16 °N latitude with underlying sea-surface temperatures fixed at 29° C. Radiative processes are approximated via a simple 2 K day^{-1} Newtonian relaxation to the base-state temperature profile (Rotunno and Emanuel 1987). Microphysical processes are parameterized using the Morrison double-moment scheme with graupel selected as the large ice category (Bryan and Morrison 2012). Sub-grid-scale turbulent processes are parameterized using a first-order local closure, commonly referred to as the "Louis PBL scheme" (Louis 1979; Kepert 2012; Bryan et al. 2017). The horizontal and vertical eddy viscosities are separately determined given the local flow deformation and the moist Brunt-Väisälä frequency. The heat diffusivity is taken as identical to the momentum diffusivity such that the Prandtl number is unity. This turbulence parameterization requires specifying the horizontal

and vertical mixing length scales, chosen herein as $l_h = 1000$ m and $l_v = 100$ m, respectively for both the axisymmetric and 3-D simulations.

4.3 Structural evolution during expansion

4.3.1 Intensity and initiation of rapid intensification

The intensity of each simulated TC is shown as a function of time in Fig. 4.4, where intensity is approximated as the maximum azimuthally averaged wind speed at the lowest model level (25 m). There are no discernible intensity relationships as a function of either incipient vortex circulation or environmental moisture for the axisymmetric ensemble averages, whereas an initially larger incipient vortex circulation and larger environmental moisture produce slightly higher-intensity TCs for the 3-D simulations. Discrepancies in the timing to begin rapid intensification (RI) are noted among the axisymmetric ensemble averages and the 3-D simulations. Consistent with previous studies, larger tropospheric moisture content expedites the development phase and initiation of RI as the incipient vortex is more quickly moistened, thereby promoting deep convection (e.g., Tao and Zhang 2014; Kilroy and Smith 2017). The initiation of RI is defined following a method similar to that used by Judt and Chen (2016) and Rios-Berrios et al. (2018), which is motivated by the approximate 95th percentile of 24-h over-water TC intensification rates in the North Atlantic basin (Kaplan et al. 2010). The initiation of RI is specified as the first (hourly) time step where the subsequent 24-h intensification rate exceeds 15.4 m s^{-1} and each consecutive 6-h intensification rate within the 24-h time window exceeds 3.8 m s^{-1}. Black dots in Fig. 4.4 denote the initiation of RI for each simulation following this definition. To account for timing discrepancies in the initiation of RI and provide a more consistent comparison of TC evolution, the time when RI begins is subtracted off from each simulation unless otherwise specified. Furthermore, to facilitate the discussion of results as a function of incipient vortex circulation and environmental moisture, references to each simulation are abbreviated as follows: small (*S*), large (*L*), dry (*D*), and moist (*M*). For example, the simulation with a decay parameter of $\alpha = 0.7$ and mid-level environmental moisture of $\mathcal{H} = 20\%$ is referred to as the *SD* simulation.

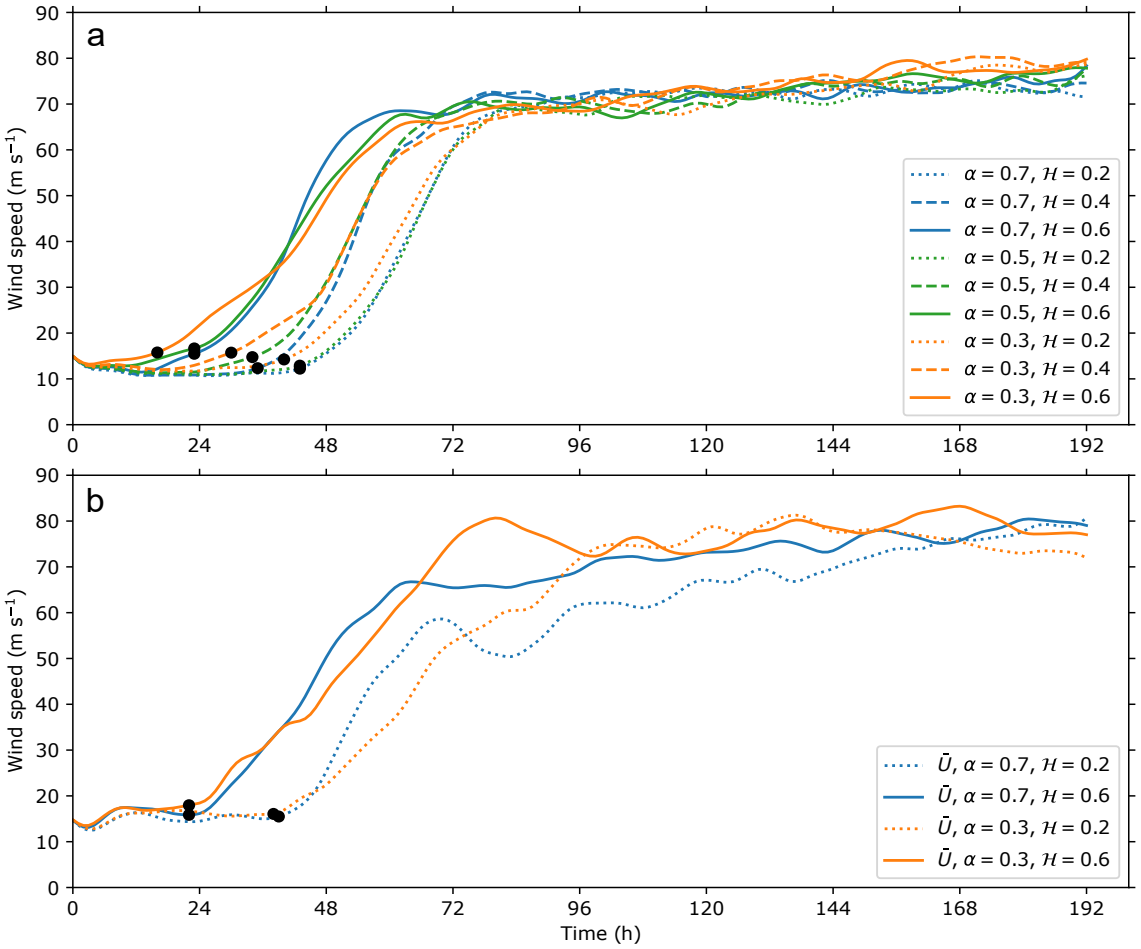

Fig. 4.4. The maximum azimuthally averaged wind speed at the lowest model level (25 m) is shown as a function of time for (a) the nine axisymmetric ensemble averages (10 ensemble members each) and (b) the four 3-D simulations. Simulations are distinguished by the modified Rankine vortex decay parameter (α, color) and by the mid-level environmental relative humidity ($\mathcal{H}$, line style). $\bar{U}$ denotes the presence of a uniform 5 m s^{-1} westerly flow for 3-D simulations (see section 4.2 for details). Black dots denote the initiation of rapid intensification for each respective simulation. Each time series is smoothed using a 12-h low-pass Lanczos filter with nine weights.

4.3.2 RMW and R_{gales} evolution

Time series of the azimuthally averaged RMW at the lowest model level and R_{gales} are shown for all simulations in Fig. 4.5. In each of the axisymmetric ensemble averages, the RMW contracts to approximately 10-km radius during the intensification phase and subsequently expands for the remainder of the simulation. 3-D simulations exhibit a similar contraction of the RMW during intensification; however, the RMW does not expand subsequent to the intensification phase for the small TCs. Both sets of axisymmetric and 3-D simulations show that for a given environmental

moisture, as the incipient vortex circulation increases, the resulting RMW is larger at all times during the TC life cycle. Furthermore, the axisymmetric ensemble averages show that for a given incipient vortex circulation, TCs embedded in environments with larger moisture content attain a larger RMW; however, this relationship is not present for small TCs in the 3-D simulations.

Figure 4.5 elucidates the principal finding of this study; the incipient vortex circulation places the primary constraint on TC expansion, and in part establishes the expansion rate. An initially large vortex ($\alpha = 0.3$) expands more quickly than its relatively smaller counterpart ($\alpha = 0.7$); therefore, with all other factors contributing to expansion held constant, the contrast in size between the two vortices *increases* with time. Increasing the environmental moisture produces larger TCs when the timing to rapid intensification is left unaccounted; however, a more consistent comparison accounting for the timing to RI reveals that the expansion rate is only slightly modulated by increasing the environmental moisture. The axisymmetric ensemble averages show a slightly larger expansion rate as the environmental moisture is increased for a given incipient vortex circulation. The degree to which varying the environmental moisture modulates the expansion rate in the 3-D simulations is dependent on the incipient vortex circulation. Increasing the environmental moisture does not influence the expansion rate for initially small vortices, whereas increasing the environmental moisture results in larger expansion rates for initially large vortices. Furthermore, Fig. 4.5 shows that as the RMW begins to expand for the large 3-D vortices, the expansion rate increases. Henceforth, results will only be discussed for the 3-D simulations.

As noted in chapter 1, TC expansion is inextricably linked to convectively driven convergence of absolute angular momentum (M) toward the TC center of circulation. To illustrate this relationship, Fig. 4.6 shows the azimuthally averaged evolution of M for each TC at 1-km altitude. Overlaid in orange is the M surface corresponding to 3.0×10^6 m^2 s^{-1} (for simplicity, the $M = 3.0$ surface) for each respective TC. The large TCs begin with larger outer-core M compared to the small TCs and subsequently converge a substantially larger amount of M throughout their life cycles. Furthermore, the extent of radial inflow is a function of incipient vortex circulation, such that the small TCs do not have radial inflow exceeding 3 m s^{-1} beyond 100-km radius. Collectively, this evolution is captured by the $M = 3.0$ surface beginning at approximately 300-km radius for the small TCs and

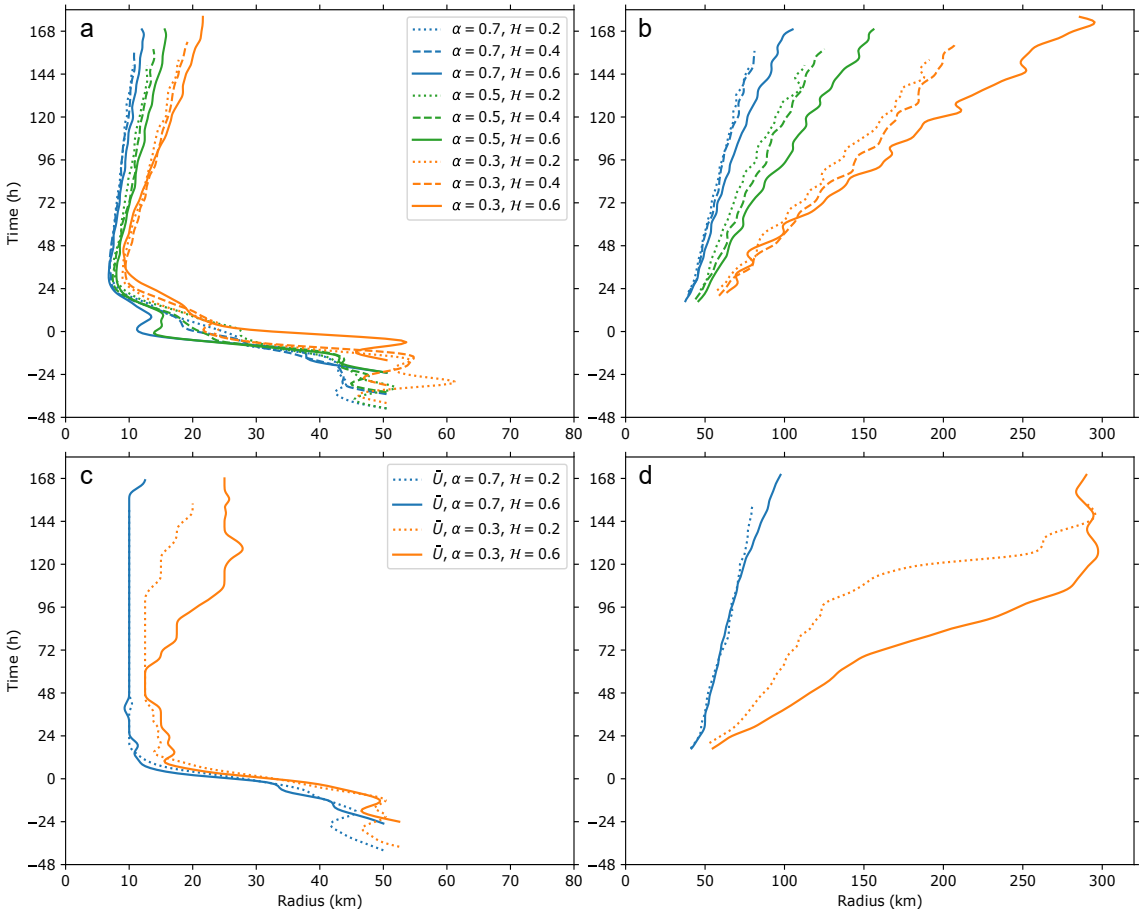

Fig. 4.5. The radius of maximum tangential winds (RMW) and the radius of gale force winds (R_{gales}) are shown as a function of time with respect to the initiation of rapid intensification for (a, b) the nine axisymmetric ensemble averages and (c, d) the four 3-D simulations, respectively. Simulations are distinguished by the modified Rankine vortex decay parameter (α, color) and mid-level environmental relative humidity ($\mathcal{H}$, line style). $\bar{U}$ denotes the presence of a uniform 5 m s^{-1} westerly flow for 3-D simulations (see section 4.2 for details). Each time series is smoothed using a 12-h low-pass Lanczos filter with nine weights.

contracting ∼50–75 km, whereas the $M = 3.0$ surface begins at approximately 230-km radius for the large TCs and contracts over 200 km; the $M = 3.0$ surface is eventually subsumed into the inner-core circulation of the *LM* TC (Fig. 4.6d). A combination of initially larger outer-core M and a broader extent of radial inflow contributes to the large TCs converging a substantially larger amount of M throughout their life cycles compared to the small TCs. The following sections will demonstrate that this finding is primarily related to the areal distribution and nature of convection found in the outer-core region.

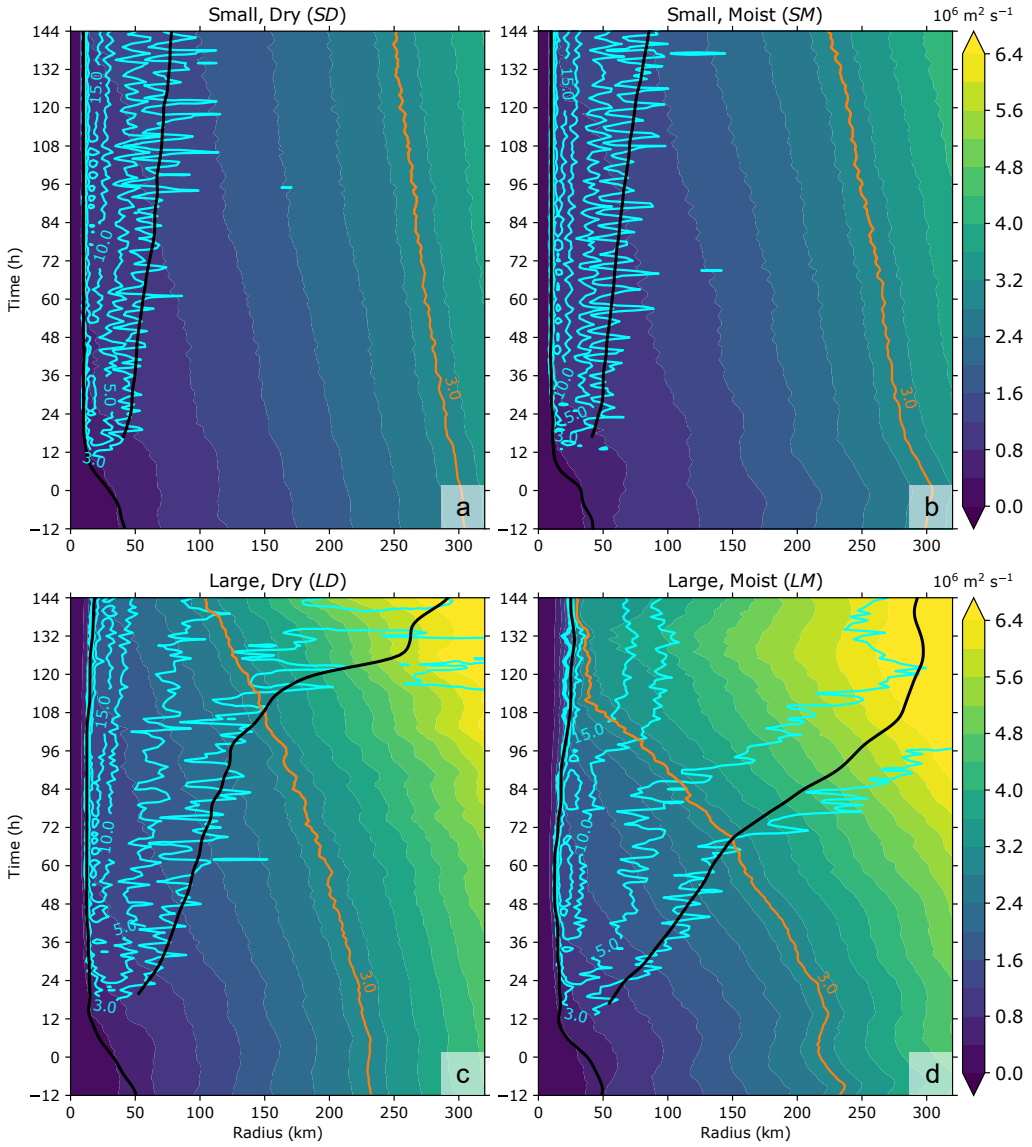

Fig. 4.6. Azimuthally averaged absolute angular momentum at 1-km altitude (shaded), 0–1 km altitude layer-averaged radial inflow magnitude (cyan contours at 3, 5, 10, and 15 m s^{-1}), and the absolute angular momentum surface corresponding to 3.0×10^6 m^2 s^{-1} (orange) are shown as a function of time relative to the initiation of rapid intensification for the 3-D simulations: (a) *SD*, (b) *SM*, (c) *LD*, and (d) *LM*. The innermost black curve in each panel is the radius of maximum tangential winds (RMW) and the outermost black curve is the radius of gale-force winds (R_{gales}).

4.3.3 Convective evolution

The evolution of convection for each 3-D simulation is shown by azimuthally averaged radar reflectivity (dBZ) in Fig. 4.7. Each simulated TC is characterized by vigorous eyewall convection near the RMW, denoted by reflectivity values exceeding 50 dBZ. Notable differences are found radially outward of the RMW, where decreasing the incipient vortex circulation strength or environmental

moisture generally corresponds to less convection. Figures 4.7c,d show that the aforementioned expanding RMW in the large TCs is accompanied by radially propagating convection that contributes to an expansion of the eyewall in both simulations. Animations of radar reflectivity and potential vorticity (PV) show an increase in the amount of spiral rainband convection and a subsequent growth of the eye region during the time period that the RMW expands for the large TCs (not shown). The animations suggest that the eyewall may have expanded via PV mixing near the eye–eyewall interface or an eyewall replacement cycle. A thorough analysis of the processes contributing to eyewall expansion in the large TCs is reserved for future work.

Cartesian snapshots of radar reflectivity at 2-km altitude, 72 h after the initiation of RI, are shown for each simulation in Fig. 4.8. As the incipient vortex circulation is decreased, outer-core convection is relatively scarce and characterized by small-scale, isolated convective elements. On the contrary, as the incipient vortex circulation is increased, outer-core convection abounds and is characterized by relatively large-scale rainbands and mesoscale convective systems. Varying the environmental moisture slightly increases the areal coverage of convection, but does not appear to have a significant influence on the spatial scale of outer-core convection.

The relationship between incipient vortex circulation and the scale of outer-core convection is quantified by representing the reflectivity at 2-km altitude, given by $Z(r,j,t)$, as a Fourier series along the azimuthal dimension

$$Z_m(r,t) = \sum_{j=0}^{J-1} Z(r,j,t)\left[cos(2\pi mj/J) + isin(2\pi mj/J)\right], \tag{4.5}$$

where m is the azimuthal wavenumber ($m = 0,1,2,\ldots,180$), r the radius, j the azimuth angle in degrees ($j = 0,1,2,\ldots,J = 360$), and t the time. The Fourier coefficient for each azimuthal wavenumber is given by $Z_m(r,t)$. Then, the power spectrum for each azimuthal wavenumber is given by

$$\mathcal{Z}_m(r,t) = \frac{1}{J^2}|Z_m(r,t)|^2, \tag{4.6}$$

and the normalized power spectrum for each azimuthal wavenumber is given by

$$\hat{\mathcal{Z}}_m(r,t) = \frac{\mathcal{Z}_m(r,t)}{\sum_m \mathcal{Z}_m(r,t)}. \tag{4.7}$$

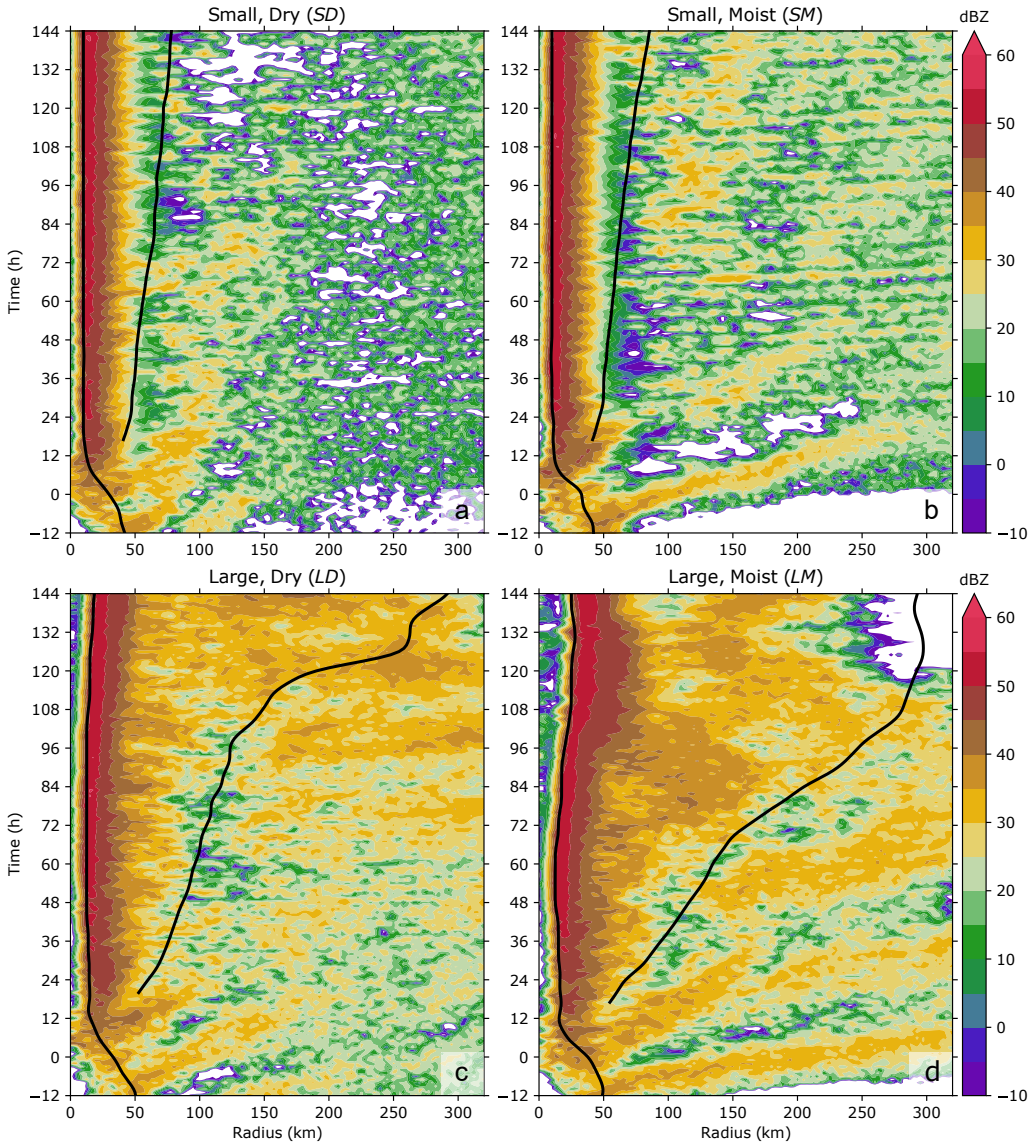

Fig. 4.7. Radar reflectivity (dBZ) at 2-km altitude is shown as a function of radius and time relative to the initiation of rapid intensification for the 3-D simulations: (a) *SD*, (b) *SM*, (c) *LD*, and (d) *LM*. The innermost black curve in each panel is the radius of maximum tangential winds (RMW) and the outermost black curve is the radius of gale-force winds (R_{gales}).

The normalized power spectrum (4.7) is computed for reflectivity at 2-km altitude between 100–300 km radius and for each hourly time step. Normalized power spectra are then area-averaged between 100–300 km radius and cumulatively summed over all wavenumbers for each hourly time step.

Figure 4.9 shows the cumulative normalized power spectra at 48 h and 72 h after the initiation of RI for each simulation. The median cumulative power of outer-core reflectivity occurs between azimuthal wavenumbers 4–8 for the large TCs and above azimuthal wavenumber 9 for the small TCs.

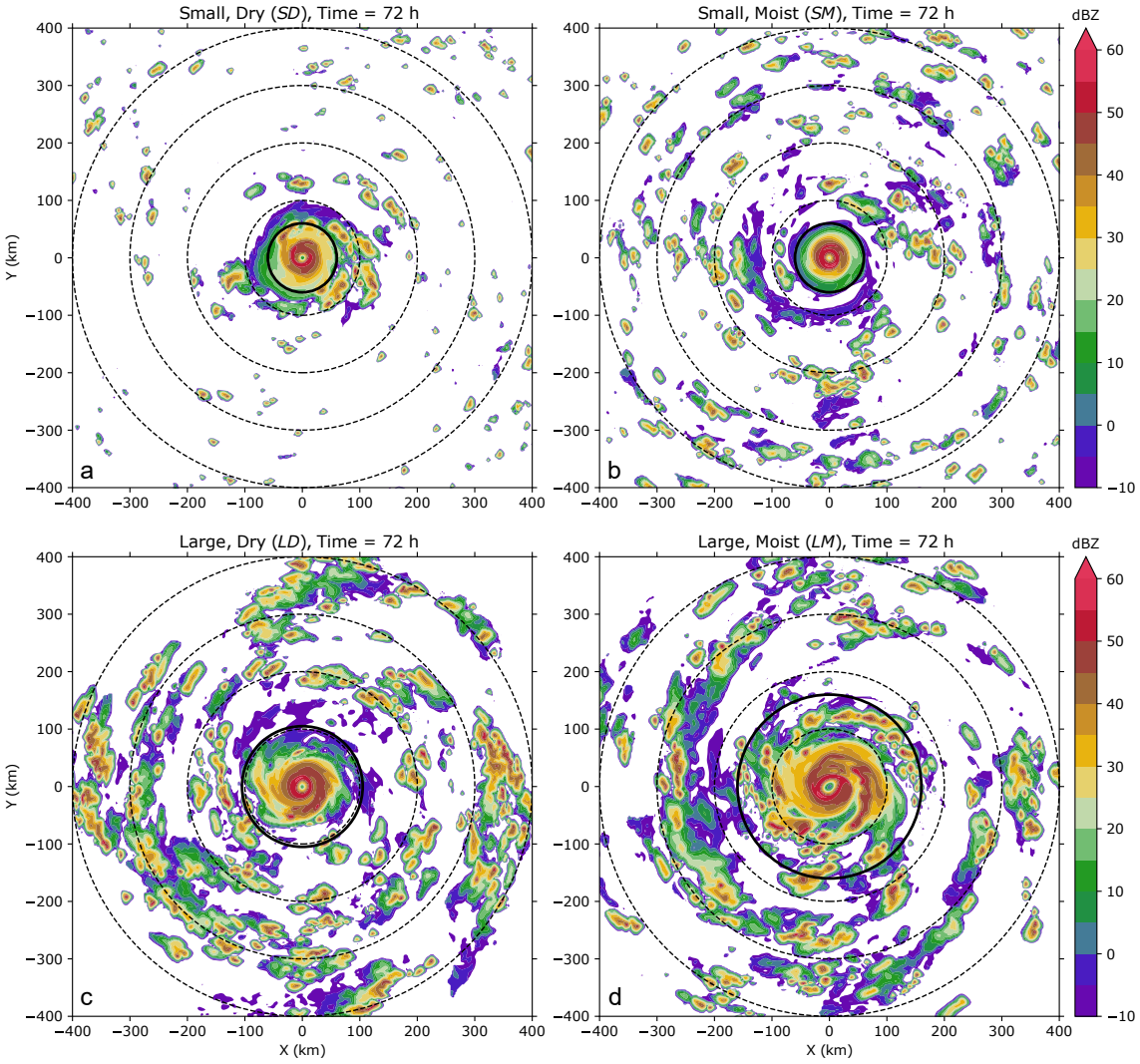

Fig. 4.8. Cartesian snapshots of radar reflectivity (dBZ) at 2-km altitude, 72 h after the initiation of rapid intensification, are shown for the (a) *SD*, (b) *SM*, (c) *LD*, and (d) *LM* simulations. Radius rings in increments of 100 km from the center of each TC are given by the dashed-black lines and the radius of gale-force winds (R_{gales}) for each respective TC is given by the solid black line.

Therefore, the median distribution of convection is shifted toward larger scales as the incipient vortex circulation is increased. In general, the large TCs have a propensity to develop relatively large-scale convection in the outer-core region throughout their life cycle, regardless of environmental moisture. The outer-core convection for the small TCs exhibits a slightly greater scale-dependence on environmental moisture compared to the large TCs, with the moist environment producing larger scales of convection; however, Fig. 4.5d suggests that differences in the scales of convection between the *SM* and *SD* TCs have a negligible influence on the their expansion rates. This may

be partly due to the longevity of convection that develops in the outer-core region or the relative scarcity of outer-core convection for the *SD* TC. The following section will further investigate differences in the nature of convection among the simulated TCs to elucidate the differences in expansion rates.

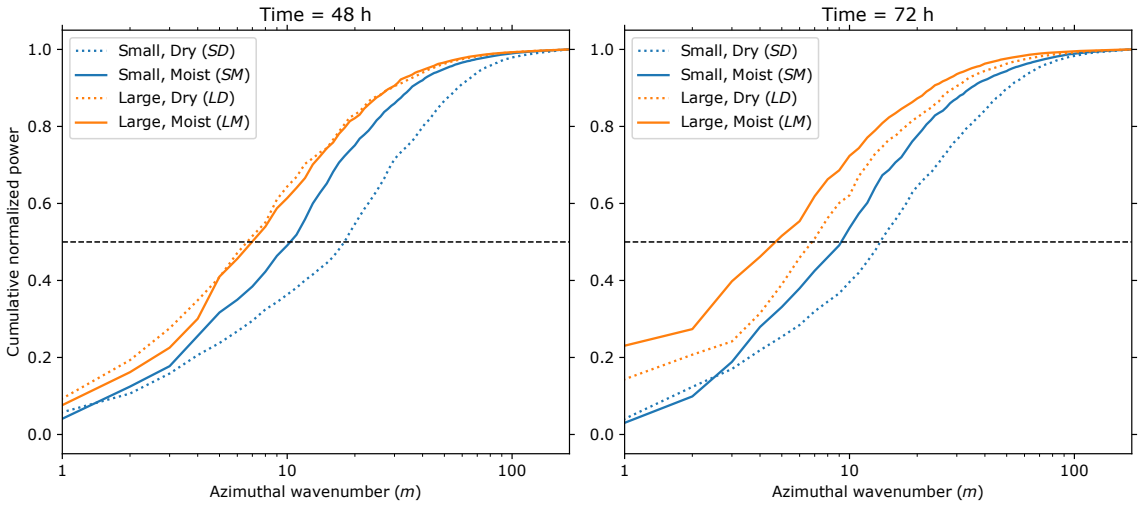

Fig. 4.9. Cumulative normalized power spectra of outer-core (r = 100–300 km) radar reflectivity at 2-km altitude are shown as a function of azimuthal wavenumber m for each simulation at (left) 48 h and (right) 72 h after the initiation of rapid intensification. The dashed-black line denotes the median cumulative normalized power. See section 4.3.3 for details on how the cumulative normalized power spectra are constructed.

4.3.4 Vertical mass flux distributions

The nature of convection is compared between the simulated TCs via frequency distributions of vertical mass flux within the inner- and outer-core regions. The inner-core region is defined as the area enclosed by $r \leq 50$ km; this definition is chosen to capture the evolution of convection confined by the initial RMW for each TC ($r = 50$ km), including the eyewall, principal, and secondary rainbands (Houze 2010). The outer-core region is defined as the area enclosed by $100 \leq r \leq 300$ km; this definition is chosen to capture the evolution of convection beyond twice the initial RMW for each TC, including principal and secondary rainbands that propagate from the inner- to outer-core region and distant rainbands (Houze 2010). Several definitions for the inner- and outer-core regions were tested, including dynamic boundaries that follow the RMW (e.g., Hence and Houze 2012). The aforementioned static boundaries are chosen when distinguishing between the inner- and outer-core regions to preserve the same number of grid points compared between

each TC and to avoid issues with boundaries that account for the RMW given that the RMW flares radially outward at upper levels in the TC circulation. Results remain qualitatively similar when using a definition that accounts for the RMW. Furthermore, inner- and outer-core vertical mass flux frequency distributions are created as a function of altitude for various time windows and the results remain largely consistent regardless of the initial window time or length (not shown). Therefore, the vertical mass flux frequency distributions are shown during the 12-h time window beginning 48-h after the initiation of RI for each TC. This time window captures the evolution of convection in each TC subsequent to its bulk intensification phase (see Fig. 4.4) and coincides with the previous reflectivity spectral analysis (Fig. 4.9a).

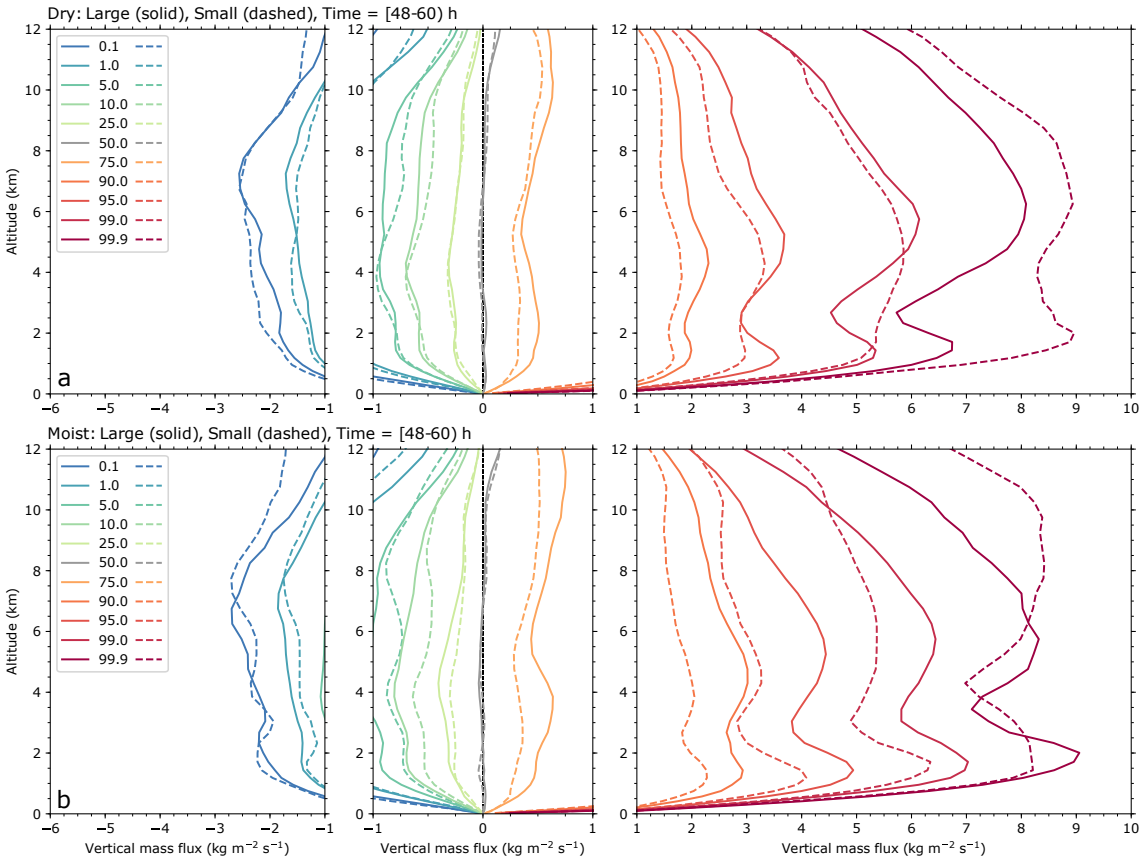

Fig. 4.10. Individual quantiles (colors) from the inner-core ($r \leq 50$ km) vertical mass flux distribution are shown as a function of altitude for each TC between 48–60 h after the initiation of rapid intensification. (a) Vertical mass flux quantiles are shown for the (solid) large, dry (*LD*) TC and the (dashed) small, dry (*SD*) TC. (b) Vertical mass flux quantiles are shown for the (solid) large, moist (*LM*) TC and the (dashed) small, moist (*SM*) TC. The middle panel is horizontally stretched to twice the spacing between vertical mass flux values compared to the left and right panels.

Figure 4.10 shows individual quantiles from the inner-core ($r \leq 50$ km) vertical mass flux distribution for each TC between 48–60 h after the initiation of RI. Vertical mass flux quantiles are shown separately for TCs in the dry and moist environments to facilitate comparisons between the small and large TCs. Beginning with the dry environment (Fig. 4.10a), the *LD* TC is characterized by a higher frequency of modest-to-large inner-core updraft mass flux throughout 12-km altitude compared to the *SD* TC; however, the *SD* TC has a higher frequency of the largest inner-core updraft mass flux values. This result is demonstrated by the 75%, 90%, 95%, and 99% updraft mass flux quantiles occurring at larger values for the *LD* TC but the 99.9% updraft mass flux quantile occurring at larger values for the *SD* TC. Furthermore, the *LD* TC is characterized by a higher frequency of modest-to-large inner-core downdraft mass flux between ∼4–10 km altitude compared to the *SD* TC, but the *SD* TC has a higher frequency of the largest inner-core downdraft mass flux values.

Transitioning to the moist environment (Fig. 4.11b), note that differences between the *LM* and *SM* TCs are largely similar to those found in the dry environment. One noticeable difference is that a higher frequency of the largest updraft mass flux values for the *SM* TC is only found above 8-km altitude rather than throughout 12-km altitude as in the dry environment. It is also worth noting that differences in the inner-core vertical mass flux distributions between the small and large TCs are more pronounced in the moist environment compared to the dry environment. In general, the vertical mass flux distributions shown in Fig. 4.10 demonstrate that subsequent to the bulk intensification phase, an initially large vortex is characterized by a higher frequency of modest-to-large inner-core vertical mass fluxes compared to its relatively smaller counterpart that is characterized by a higher frequency of the largest inner-core vertical mass fluxes.

Figure 4.11 shows individual quantiles from the outer-core ($100 \leq r \leq 300$ km) vertical mass flux distribution for each TC between 48–60 h after the initiation of rapid intensification. The general results are consistent when comparing the small and large TCs for both the dry and moist environments; the large TCs are characterized by larger outer-core updraft and downdraft mass fluxes compared to the small TCs. In contrast to the inner-core vertical mass flux analysis, large TCs exhibit a higher frequency of outer-core updraft and downdraft mass fluxes for all quantiles.

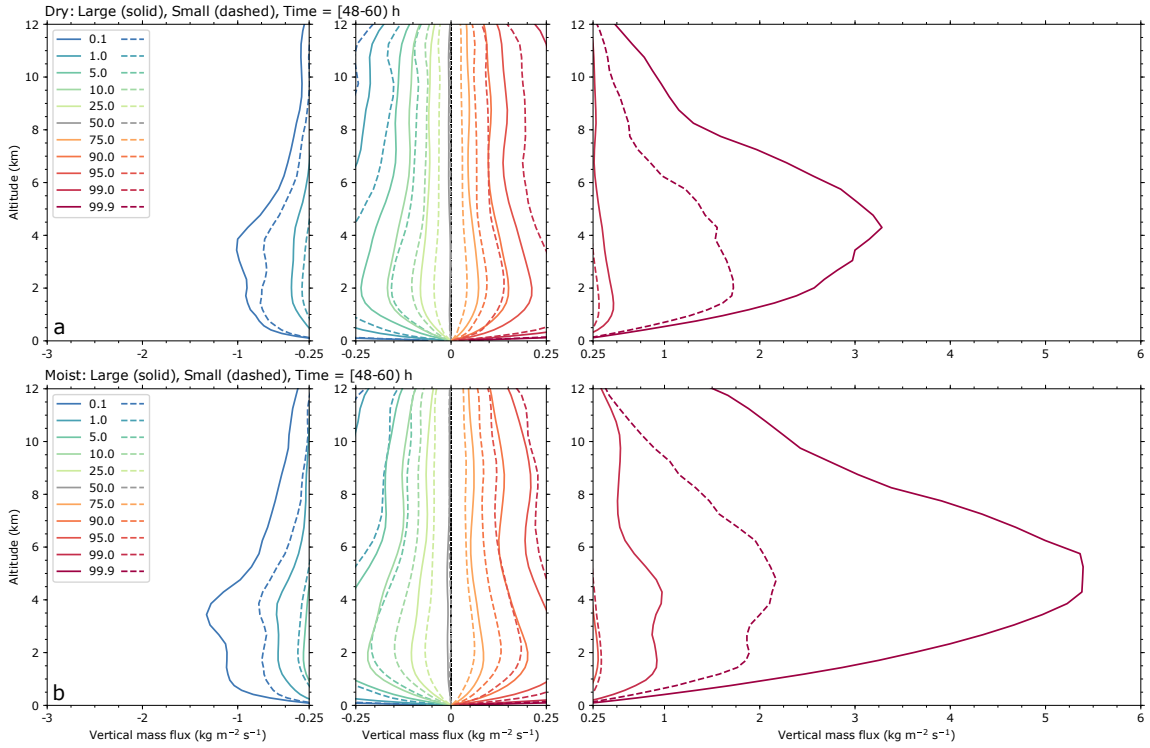

Fig. 4.11. Individual quantiles (colors) from the outer-core ($100 \leq r \leq 300$ km) vertical mass flux distribution are shown as a function of altitude for each TC between 48–60 h after the initiation of rapid intensification. (a) Vertical mass flux quantiles are shown for the (solid) large, dry (*LD*) TC and the (dashed) small, dry (*SD*) TC. (b) Vertical mass flux quantiles are shown for the (solid) large, moist (*LM*) TC and the (dashed) small, moist (*SM*) TC. The middle panel is horizontally stretched to four times the spacing between vertical mass flux values compared to the left and right panels.

A higher frequency of larger updraft and downdraft mass fluxes for all quantiles corresponds with the greater amount of outer-core convection previously noted for large TCs (see Figs. 4.7 and 4.8). Additionally, larger magnitudes of vertical mass flux correspond to relatively stronger outer-core convection for the large TCs. Collectively, Fig. 4.11 demonstrates that for a given environment, the large TCs are distinguished from their relatively smaller counterparts by a greater amount of stronger outer-core convection.

4.4 Absolute circulation evolution

Results discussed up to this point have demonstrated that large TCs are primarily distinguished from their relatively smaller counterparts by more abundant outer-core convection that occurs at a larger scale and transports a greater amount of mass throughout the troposphere. The relationships between the characteristics of outer-core convection and TC expansion rates are examined via

the absolute circulation equation. Following the discussion in section 2 of Davis and Galarneau (2009) and section 1 of Raymond et al. (2011), the absolute circulation equation is formulated in a geometric cylindrical coordinate framework as

$$\frac{\partial C}{\partial t} = -\overline{\eta}_z \widetilde{\delta} A - \oint \eta_z' \mathbf{V}_h' \cdot \hat{\mathbf{n}} dl + \oint w \eta_h \cdot \hat{\mathbf{n}} dl - \oint (\hat{\mathbf{k}} \times \mathbf{F}) \cdot \hat{\mathbf{n}} dl, \tag{4.8}$$

where C is the absolute circulation, t the time, η_z the absolute vertical vorticity, $\widetilde{\delta}$ the area-averaged horizontal divergence within the area (A) bounded by the integration circuit, $\mathbf{V}_h$ the horizontal velocity vector comprising the radial (u) and tangential (v) velocity components, w the vertical velocity, η_h the horizontal vorticity vector, and $\mathbf{F}$ the three-dimensional friction force vector. In a geometric cylindrical coordinate framework, the integration of terms on the right hand side of Eq. (4.8) occurs along a circuit of constant radius and altitude, where $\hat{\mathbf{n}}$ is the unit vector that lies in the horizontal plane normal to the circuit, $\hat{\mathbf{k}}$ the vertical unit vector, and dl the incremental length along the circuit path. An overbar denotes the azimuthal mean (i.e., average along the circuit) and primes denote deviations from the azimuthal mean (i.e., asymmetries). Eq. (4.8) can be further simplified by noting that in a geometric cylindrical coordinate framework, the radial vector is parallel to the unit normal vector and the azimuthal vector is parallel to the direction of integration along the circuit path (i.e., counterclockwise). Therefore, Eq. (4.8) becomes

$$\frac{\partial C}{\partial t} = -\overline{\eta}_z \widetilde{\delta} A - \oint \eta_z' u' dl - \oint w \frac{\partial v}{\partial z} dl + \oint F_t dl, \tag{4.9}$$

where F_t denotes friction opposing the tangential circulation (i.e., flow along the circuit). The terms on the right hand side of Eq. (4.9) represent 1) the product of area-integrated horizontal divergence within the circuit and azimuthal-mean absolute vorticity along the circuit, 2) asymmetric fluxes of absolute vertical vorticity across the circuit, 3) the flux of absolute vertical vorticity across the circuit arising from tilting horizontal vorticity normal to the circuit, and 4) the flux of absolute vertical vorticity across the circuit associated with friction that opposes the tangential circulation. For simplicity, the contributions are henceforth referred to as stretching, eddy fluxes, tilting, and friction, respectively. Similar to Rios-Berrios et al. (2016) Eq. (4.9) is normalized by the area of

the circuit and integrated forward in time from t_0 to t_1, yielding the area-averaged absolute vorticity change

$$\widetilde{\eta}_z(t_1) - \widetilde{\eta}_z(t_0) = -\int_{t_0}^{t_1} \overline{\eta}_z \widetilde{\delta} dt - \frac{1}{A}\int_{t_0}^{t_1} \oint \eta'_z u' dl dt - \frac{1}{A}\int_{t_0}^{t_1} \oint w \frac{\partial v}{\partial z} dl dt + \frac{1}{A}\int_{t_0}^{t_1} \oint F_t dl dt.$$

The area-averaged absolute vorticity change (henceforth, area-averaged vorticity change for simplicity) is evaluated for each TC with a 48-h integration time window. Toward the later integration time windows for the *LM* TC (e.g., beginning 72-h after the initiation of RI), the magnitude of stretching begins to decrease rapidly as the TC stops expanding (see Figs. 4.5d and 4.6d). The processes contributing to the structural evolution of the *LM* TC during this time period has not been thoroughly examined and is reserved for future work. Results beginning 48 h after the initiation of RI are chosen to capture the evolution of each TC during the time periods shown in the reflectivity spectral analysis (Fig. 4.9) and the vertical mass flux analyses (Figs. 4.10 and 4.11). Additionally, the bulk intensification has completed for each TC 48 h after the initiation of RI (Fig. 4.4b) such that the area-averaged vorticity change is primarily comprised of contributions associated with strengthening and expansion (e.g., Merrill 1984). All 48-h integration time windows beginning 24 h after the initiation of RI are examined and the principal results remain largely consistent (not shown).

The 300-km radius circuit is chosen to capture contributions from both the inner- and outer-core convection to the area-averaged vorticity change. In contrast to perturbing the center of a square integration domain and producing an ensemble-averaged circulation budget (Davis and Galarneau 2009; Rios-Berrios et al. 2016), the radial extent of the circular integration domain is perturbed $\pm$12.5 km to produce an area-weighted, ensemble-averaged budget. The ensemble-average approach is designed to mitigate biases introduced by convective activity concentrated along the integration circuit. Terms on the right hand side of Eq. 4.10 are then integrated for the 48-h time window using hourly model output. The sum of terms on the right hand side of Eq. 4.10 is compared to the net area-averaged vorticity change over the 48-h integration time window on the left hand side. Note that hourly model output reasonably captures the quantitative area-averaged

vorticity change for each TC (Fig. 4.12), providing confidence in the assessment of individual terms in the budget and comparisons between the TCs.

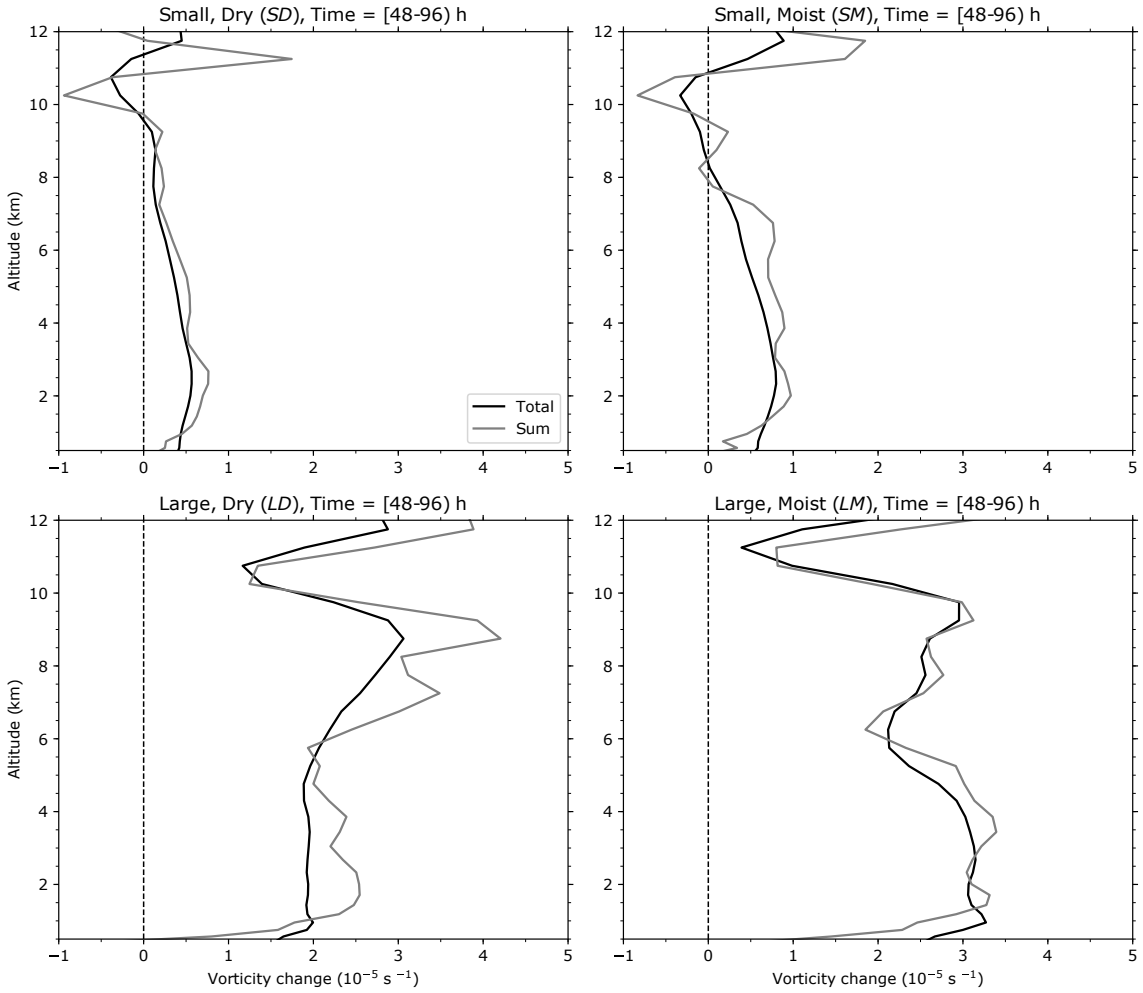

Fig. 4.12. The net area-averaged vorticity change [left hand side of Eq. 4.10] over a 48-h time window beginning 48-h after the initiation of rapid intensification is shown as a function of altitude for each TC in black. The sum of individual contributions to the net area-averaged vorticity change [right hand side of Eq. 4.10] is shown for each respective TC in gray. See section 4.4 for additional details on the analysis method.

Figure 4.13 shows the individual contributions on the right hand side of Eq. 4.10 to the area-averaged vorticity change. In general, as the incipient vortex circulation or environmental moisture increases, the stretching contribution to the net area-averaged vorticity change increases. Contributions from stretching substantiate the statement made earlier that varying the environmental moisture has a larger influence on expansion rates for the large TCs. When comparing the small TCs, increasing the environmental moisture produces a slight increase in stretching throughout 9-km altitude. In contrast, when comparing the large TCs, increasing the environmental moisture

results in approximately twice the stretching throughout 9-km altitude. For a given environmental moisture, the large TCs are characterized by a relative abundance of outer-core convection that occurs at a larger scale compared to their relatively smaller counterparts (see Figs. 4.8 and 4.9), resulting in approximately 2–4 times more stretching throughout 9-km altitude.

As the incipient vortex circulation increases, the tilting contribution to the net area-averaged vorticity change also increases. Differences in tilting primarily arise from differences in the amount of convection located near the 300-km radius circuit; large TCs have a greater amount of outer-core convection and therefore larger tilting contributions to the net area-averaged vorticity change. Differences in tilting are smaller between TCs in the moist environment compared to TCs in the dry environment. When comparing the *SM* and *LM* TCs, the *SM* TC is characterized by less outer-core convection compared to the *LM* TC, but differences in the amount of convection are not as large compared to those between the *SD* and *LD* TCs (see Fig. 4.8). Additionally, differences in the scale of outer-core convection between the *SM* and *LM* TCs are smaller than those between the *SD* and *LD* TCs (Fig. 4.9). Therefore, the tilting contribution is approximately 2–3 times larger for the *LM* TC compared to the *SM* TC, and approximately 2–4 times larger for the *LD* TC compared to the *SD* TC. The differences in tilting contributions to the net area-averaged vorticity change between the large and small TCs generally increases with altitude. Fig. 4.11 demonstrates that the large TCs have a greater amount of outer-core updraft mass flux at all vertical levels throughout 12-km altitude compared to the small TCs. Given that the large TCs are characterized by an initially larger amount of horizontal vorticity compared to the small TCs, a combination of more upper-level updraft mass flux that tilts stronger horizontal vorticity into the vertical results in a larger upper-level tilting contribution.

In general, the eddy vorticity fluxes provide a negative contribution to the net area-averaged vorticity change throughout a deep layer of the troposphere. Negative contributions from eddy vorticity fluxes indicate that cyclonic vorticity produced by outer-core convection is exported across the circuit, or equivalently, that anticyclonic vorticity is imported across the circuit. Differences in the eddy vorticity fluxes between TCs are relatively small below $\sim$4-km altitude and primarily increase with increasing incipient vortex circulation above 4-km altitude, with large TCs exhibiting

a greater (negative) eddy vorticity flux compared to the small TCs. Similar to the differences noted in the tilting contributions between the large and small TCs, a greater amount of upper-level updraft mass flux for the large TCs produces a greater amount of vorticity that can be transported across the circuit, and hence the differences in eddy vorticity flux contributions between the large and small TCs increase with altitude. Finally, larger TCs are characterized by a stronger outer-core tangential circulation compared to the small TCs, and therefore possess a slightly greater (negative) contribution from the friction term in the boundary layer.

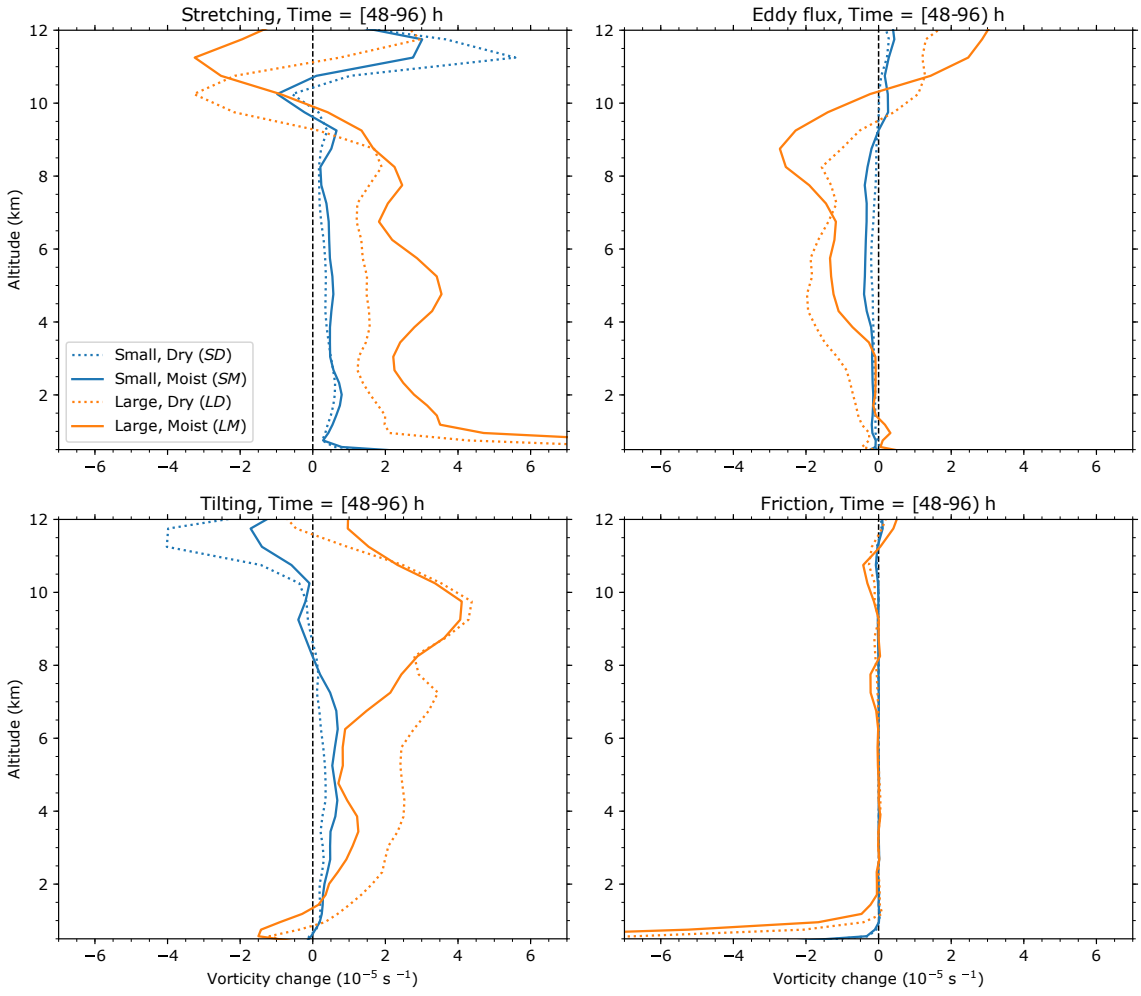

Fig. 4.13. Individual contributions to the area-averaged vorticity change [right hand side of Eq. (4.10)] are shown as a function of altitude for each TC, distinguished by incipient vortex circulation (color) and mid-level environmental humidity (line style).

4.5 Discussion and conclusions

The contributions of incipient vortex circulation and environmental moisture to tropical cyclone (TC) expansion have been examined with a set of idealized numerical simulations. The incipient vortex circulation strength is varied by fixing the radius of maximum tangential winds (RMW) and modifying the decay of tangential velocity radially outward of the RMW in accordance with observations of North Atlantic basin TCs (Mallen et al. 2005). The environmental moisture is varied by imposing a vertical decay function that largely preserves moisture content within the boundary layer (below $\sim$850 hPa) and maximizes the mid-level moisture variance in accordance with climatological observations of tropical environments (Holloway and Neelin 2009; Dunion 2011) and observations of tropical wave disturbances preceding cyclogenesis (Komaromi 2013; Davis and Ahijevych 2013).

As discussed in chapter 1, several past studies have employed similar idealized numerical simulation frameworks to investigate the processes contributing to TC expansion. Hill and Lackmann (2009) posited two potential feedback mechanisms associated with increasing the environmental moisture and producing larger TC expansion rates. Their second feedback mechanism is pertinent to the discussion of results presented herein and the mechanism is recapitulated below. Increasing the environmental moisture of TCs promotes a greater amount of PV generated by radially outward propagating spiral rainbands. PV generated by the spiral rainbands is subsumed by the inner-core PV tower, resulting in a broader PV distribution, and the cyclonic wind field expands in balance with the broader inner-core PV tower. As the cyclonic wind field expands, subsequent heating in spiral rainbands will generate a larger amount of PV given that the diabatic PV tendency is proportional to the magnitude of the absolute vorticity vector. Therefore, an expanding cyclonic wind field promotes a larger amount of PV generation via outward propagating spiral rainbands, which in turn promote an expanding cyclonic wind field, and hence a positive feedback emerges. Although Hill and Lackmann posited this feedback mechanism in association with increasing the environmental moisture, the fundamental processes underlying its premise appear in previous studies that vary the incipient vortex circulation while fixing the environmental moisture (Xu and Wang 2010; Chan and Chan 2015; Kilroy and Smith 2017). Each of these studies emphasize to a varying degree the

relationship between the areal distribution of diabatic heating and the magnitude of the absolute vorticity vector and hence their combined influence on TC expansion rates. The findings reported herein are predicated on the same fundamental processes, and thus to a large extent are congruous with the aforementioned studies.

In addition to reproducing findings reported in the aforementioned studies with an independent modeling framework, it is further demonstrated that varying the incipient vortex circulation is associated with a scale-dependent response of outer-core convection. Specifically, as the incipient vortex circulation increases, the scale of outer-core convection increases. Increasing the environmental moisture produces a greater amount of outer-core convection, but appears to have a relatively minor influence on its scale in the idealized modeling setup employed herein. Therefore, the principal findings reported in this study are primarily attributed to the scale-dependent response of outer-core convection to varying the incipient vortex circulation. Large TCs are distinguished from their relatively smaller counterparts by a relative abundance of outer-core convection occurring at a larger scale that cumulatively spins up the outer-core TC circulation at a quicker rate via combined stretching and tilting; therefore, with all other factors contributing to expansion held constant, the contrast in size between the two TCs will *increase* with time.

Increasing the environmental moisture further promotes convection, thereby modulating the expansion rates; however, in the absence of additional factors contributing to expansion other than incipient vortex circulation, varying the environmental moisture mostly acts to delay or expedite the intensification process. Increasing the environmental moisture for small TCs produces more outer-core convection that occurs at a slightly larger scale, but the overall nature of outer-core convection remains best characterized by isolated convective elements. Therefore, increasing the environmental moisture for small TCs produces a negligible contribution to their expansion rates. On the contrary, increasing the environmental moisture for large TCs produces more outer-core convection at a slightly larger scale. In both moist and dry environments, the nature of outer-core convection for the large TCs is best characterized by spiral rainbands and mesoscale convective systems; however, the large TC in the moist environment benefits from a greater amount of large-scale outer-core convection. Therefore, increasing the environmental moisture for large

TCs produces a relatively larger contribution to their expansion rates compared to the small TCs. Together, increasing both the incipient vortex circulation and environmental moisture produces a nonlinear increase in TC expansion rates.

Schenkel et al. (2018a) demonstrated that TCs in the western North Pacific basin experience larger expansion rates compared to TCs in the North Atlantic basin (their Fig. 6). Given that TCs developing in the western North Pacific are on average larger than their North Atlantic counterparts, it is hypothesized that the results presented by Schenkel et al. provide evidence to support the principal finding that an initially larger vortex can expand more quickly than its relatively smaller counterpart; however, western North Pacific typhoons also develop in environments characterized by larger moisture content and higher sea-surface temperatures compared to North Atlantic hurricanes (e.g., Gray 1968; Dai 2006), obscuring statements regarding a direct connection or attribution of either variable in isolation. Additionally, the incipient vortex circulation and environmental moisture are interdependent in nature, further obscuring statements regarding the contributions of either variable in isolation. Therefore, the extent to which the principal finding is manifested within the results presented by Schenkel et al. (2018a) cannot be estimated, but the parallel between our two studies warrants further investigation.

Previous studies have demonstrated that TCs possess a sort of "memory" with respect to their incipient circulation (Rotunno and Emanuel 1987; Knaff et al. 2014), which underlies the statement that large TCs stay large and small TCs stay small. Synthesizing the results presented herein, it is further demonstrated that a cumulatively larger convergence of angular momentum over time permits an initially large vortex to expand more quickly than its relatively smaller counterpart. Therefore, memory of the incipient vortex circulation is imparted upon TC size through variable expansion rates. Schenkel et al. (2018a) demonstrate that this memory is largely preserved prior to TCs attaining their lifetime maximum size, but is attenuated afterwards as TCs begin contracting. Therefore, the principal findings reported herein may only be valid prior to TCs attaining their lifetime maximum size.

There may be several processes contributing to the noted differences in the scale of outer-core convection that warrant further investigation. For example, how do variations to the incipient

vortex circulation and environmental moisture have an influence on the upscale growth of outer-core convection? Furthermore, the duration of outer-core convection has not been examined given difficulties arising from tracking individual convective elements with hourly model output. It is surmised that the scale and duration of outer-core convection are interdependent; thus, their combined influence may in part account for the variable expansion rates noted herein. That is, relatively large-scale convection with a long duration is expected to have a stronger influence on the net area-averaged vorticity change, and hence expansion rate, compared to relatively small-scale convection with a short duration. Additional work is required to elucidate potential relationships between the duration of convection and TC expansion.

The idealized numerical simulations analyzed herein contain simplifying assumptions that may limit the extent to which the principal results are found in nature. For example, the simulations analyzed herein begin with an axisymmetric incipient vortex circulation and horizontally homogeneous environmental conditions, but precursor disturbances are intrinsically asymmetric and embedded within spatially inhomogeneous environments (McTaggart-Cowan et al. 2008, 2013; Chang et al. 2017). The analysis is limited by excluding contributions from cloud-radiative forcing which have been shown to aid the expansion of TC wind fields by producing weak, sustained ascent in the outer-core region that promotes and enhances convective activity (Bu et al. 2014; Fovell et al. 2016). Furthermore, the analysis is limited by imposing a uniform flow throughout the simulation domain instead of introducing vertical shear flow. Previous studies have demonstrated that a low-level flow vector oriented along the upshear-right quadrant of a TC embedded in vertical shear flow favors larger expansion rates (Chen et al. 2018, 2019). Future work will expand upon the results presented in our study by incorporating the aforementioned considerations into experiments with additional numerical simulations and by comparing the idealized numerical simulations to analyses that combine reanalysis products and satellite observations.

Results gathered from this study can further aid the development of statistical–dynamical wind radii forecasts (e.g., Knaff et al. 2017). Furthermore, the results may have implications for understanding how the TC size distribution might shift amidst Earth's warming climate system. Dynamical downscaling projections of TC activity have demonstrated that TC size distributions will

shift toward larger TCs in a future, warmer climate among all ocean basins except the western North Pacific (Knutson et al. 2015). Schenkel et al. (2018b) found that the global TC size distribution will shift toward larger TCs in a future, warmer climate but that TC size at the time of genesis remains unchanged. The results presented herein motivate additional investigations into how the wind structure of precursor disturbances might vary in a future, warmer climate and associated implications for TC expansion rates among individual ocean basins.

CHAPTER 5

Synthesis and future work

In this dissertation, tropical cyclone (TC) intensity and size are posited as vital forecast metrics that can inform the potential magnitude and extent of hazards associated with landfalling TCs. A wealth of literature has been devoted toward understanding the principal processes contributing to TC intensification and expansion. Although remarkable strides have been made toward such ends, many questions remain unanswered. This dissertation endeavors to advance our scientific understanding of TCs by investigating the mesoscale processes contributing to TC intensification and expansion. Although findings reported herein have made progress toward this goal, several questions remain and several have emerged. The principal findings reported throughout this dissertation are recapitulated below along with potential avenues for future work.

Chapter 2

In chapter 2, observations from the remarkable rapid intensification (RI) and subsequent rapid weakening of Hurricane Patricia (2015) are analyzed to better understand the structural evolution of a TC experiencing rapid intensity changes. The predominant structure during Patricia's rapid intensification is characterized by a high-amplitude, hollow potential vorticity (PV) tower. Patricia's structural evolution raises the question: are hollow PV towers ubiquitous features among intensifying TCs? Several past observational studies have documented a similar structure during TC intensification (e.g., Kossin and Eastin 2001; Rogers et al. 2013a; Martinez et al. 2017). It also remains unclear if a hollow PV tower structure can further lend the TC to intensification or if a hollow PV tower is solely a manifestation of TC intensification. Future work should further examine the ubiquity of hollow PV towers in ensemble simulations of TC intensification and explore the potential for hollow PV towers to facilitate intensification.

Transforming the observational analyses from radius–height to potential radius–potential temperature coordinates reveals that Patricia's hollow PV tower is persistently collocated with the same

absolute angular momentum surfaces as they contract in physical space. Therefore, within the (R, θ) framework, Patricia's extreme RI occurs "in-place" with a close correspondence between the diabatic heating and absolute angular momentum surfaces. Unresolved eddy processes in the form of asymmetries and frictional fluid stresses are hypothesized to aid in concentrating the hollow PV tower radially inward of the heating maximum. Patricia's intensification "in-place" raises a few questions. Could asymmetric processes contribute to the contraction of a TC eyewall during rapid intensification? Previous studies provide evidence that inner-core PV asymmetries can flux high-PV air from the eyewall into the eye, resulting in a contraction of the RMW (Nolan and Grasso 2003; Nolan et al. 2007). Additional work should investigate the relationship between asymmetric processes and eyewall contraction in full-physics simulations of TC intensification. More generally, does Patricia's structural evolution typify the progression of a rapidly intensifying TC? Or are there variable structural pathways for TCs undergoing RI? The (R, θ) framework demonstrates that heating concentrated along the same absolute angular momentum surfaces corresponds to a nonlinear (quadratic) amplification of preexisting PV, thereby providing a pathway toward rapid PV development. However, it remains unclear if this pathway is common among other TCs undergoing RI. Future work should examine the structural evolution of TCs undergoing RI with variable intensification rates.

The dilution of Patricia's hollow PV tower during the rapid weakening phase is associated with PV mixing between the eye–eyewall interface. Cartesian analyses reveal that absolute vorticity is mixed from the eyewall into the eye while conserving the absolute circulation. Consistent with previous studies, this finding suggests that there may have been a release of combined barotropic–baroclinic instability (e.g., Schubert et al. 1999). Future work should investigate if the release of combined barotropic–baroclinic instability is a precursor for rapid weakening events.

Chapter 3

In chapter 3, a high-resolution, three-dimensional TC is simulated to begin addressing the question: do asymmetries facilitate or interfere with TC intensification? The azimuthal distributions of

PV and diabatic heating within the TC inner core remain asymmetric throughout the intensification period. At no time during TC intensification does the inner core become entirely symmetric. Additionally, the asymmetric PV distribution remains on the same order of magnitude as the symmetric PV throughout the intensification period. The low-layer (1–3 km altitude) and high-layer (5–8 km altitude) PV symmetricity remain approximately equivalent throughout the intensification period; however, the high-layer asymmetric PV is distributed among a broader range of smaller azimuthal scales compared to the low layer. Recall that the idealized TC simulation included a uniform easterly flow, but no vertical shear flow. Collectively, the foregoing discussion raises the question: how does the distribution of asymmetric PV vary among TCs embedded in vertical shear flow? Future work should quantify the evolution of asymmetric structures among an ensemble of TC simulations embedded in variable environments to confirm the results presented herein.

Persistent features are noted during the intensification period and require additional research to elucidate their contributions to TC intensification. Specifically, low-wavenumber PV advection contributes to an enhancement of azimuthal-mean PV near the axis of rotation during the early RI time slice ($t = 90$ h) and mid RI time slice ($t = 108$ h). Additionally, PV generation via low-wavenumber heating contributes to concentrating PV along a thin radial strip coincident with the hollow PV tower during both the mid RI time slice and late RI time slice ($t = 126$ h). Additional work will be directed toward improving the azimuthal-mean PV budget analysis presented herein and assessing the precise contributions from asymmetries throughout the intensification period. Returning to the discussion from chapter 1: do asymmetric modes of TC intensification exist in nature? That is, can asymmetries provide net-positive contributions toward symmetric TC intensification? Bhalachandran et al. (2020) recently demonstrated that asymmetries can grow and decay largely independent of the symmetric circulation and furthermore, asymmetries can contribute positively to symmetric TC intensification at various stages. The authors noted discrepancies between their results and earlier studies utilizing linear modeling frameworks that concluded eddies grow at the expense of the mean (Nolan and Montgomery 2002; Nolan and Grasso 2003; Nolan et al. 2007); nonlinear interactions provide an important pathway for the growth and decay of asymmetries independent from the symmetric TC circulation. Persing et al. (2013) demonstrated that

asymmetric fluxes of momentum can exhibit counter-gradient characteristics and simultaneously contribute to eyewall contraction and symmetric TC intensification. Future work will extend the analysis framework presented herein to an ensemble of TC simulations and identify the salient asymmetric contributions to symmetric TC intensification among a larger set of cases.

The foregoing discussion has primarily considered "direct" asymmetric contributions to TC intensification. Can "indirect" asymmetric contributions to TC intensification be quantified? And might they provide an important missing link toward further understanding TC intensification? Addressing these questions will require a thorough analysis of nonlinear interactions during TC intensification. It's worth noting that the quantification of asymmetric contributions to the symmetric structure does not necessarily reveal a causal link between asymmetric processes and TC intensification. Future work should consider methods to identify both linear and nonlinear causal relationships between asymmetric processes and TC intensification.

Analyzing the structural evolution during RI in the potential radius–potential temperature (R, θ) framework reveals that the hollow PV tower and symmetric diabatic heating maximum gradually shift outward to increasingly larger potential radius between the early and late RI time slices. Therefore, PV is concentrated "in-place" when analyzed in physical space, but PV is concentrated at increasingly larger potential radius when analyzed in (R, θ) space. The structural evolution was contrasted to Hurricane Patricia where PV is concentrated "in-place" when analyzed in the (R, θ) framework during RI. At the end of section 3.9, the structural evolution of the simulated TC and Hurricane Patricia were considered to potentially exemplify two different "modes" of intensification arising from differences in the incipient vortex circulation. Results from chapter 4 may provide an underlying link between the two different modes of intensification. An initially large vortex converges a substantially larger amount of absolute angular momentum (M) compared to its relatively smaller counterpart, resulting in distinct expansion rates and potentially facilitating a pathway for larger M to be converged into the inner-core region during the intensification process. Although both the initially large and small vortices undergo RI, the large TCs displace a significantly larger amount of M compared to their relatively smaller counterparts. The simulated TC from chapter 3 is thus akin to the "large, moist (LM)" TC from chapter 4 in that the two TCs displace a substantial

amount of M. In the (R, θ) framework, differences in the amount of inner-core M convergence could manifest as the difference between PV concentration "in-place" for initially small TCs and PV concentration at increasingly larger potential radius for initially large TCs. Therefore, the evolution of PV in light of the incipient vortex structure may provide an important link between TC intensification and expansion. Future work will continue investigating the relationship between incipient vortex circulation, TC intensification, and TC expansion within the (R, θ) framework.

Chapter 4

In chapter 4, a set of idealized TC simulations is constructed to better understand the contributions of incipient vortex circulation and environmental moisture to TC expansion. The incipient vortex circulation strength places the primary constraint on TC expansion, and in part establishes the expansion rate. Increasing the mid-level moisture further promotes expansion, thereby modulating the expansion rate; however, in the absence of additional factors contributing to expansion other than incipient vortex circulation, varying the mid-level moisture mostly acts to delay or expedite the intensification process. The principal finding demonstrates that an initially large vortex can expand more quickly than its relatively smaller counterpart; therefore, with all other factors contributing to expansion held constant, the contrast in size between the two vortices will *increase* with time. Varying the incipient vortex circulation is associated with subsequent variations in the amount and scale of outer-core convection. Increasing the incipient vortex circulation subsequently results in a greater amount of convection occurring at a larger scale. The combined increase in the amount and scale of outer-core convection permits an initially large vortex to converge a substantially larger amount of absolute angular momentum compared to its relatively smaller counterpart. An important question arising from the principal findings reported herein is to what extent does the relationship between incipient vortex circulation and the scale of convection appear in the evolution of TCs embedded in vertical shear flow? Future work should further test the strength of the relationship between incipient vortex circulation and the scale of outer-core convection with an ensemble of idealized simulations.

Similar to findings reported in previous studies, TCs analyzed herein possess a sort of "memory" with respect to their incipient circulation (e.g., Merrill 1984; Knaff et al. 2014; Kilroy and Smith 2017). Future work should continue investigating the extent to which incipient vortex circulations impart memory to subsequent TC expansion. This relationship may have important implications toward understanding how the TC size distribution might change amidst Earth's warming climate system. For example, will the scale and structure of precursor disturbances change as Earth's climate system continues warming? And how might variations in the scale and structure of precursor disturbances influence the global TC size distribution?

Collectively, the principal findings reported in this dissertation and associated remaining questions motivate additional research on the processes underlying TC intensification and expansion. Furthermore, the principal findings reported in this dissertation motivate additional research on how TC intensity and size distributions might change amidst Earth's warming climate system.

REFERENCES

Arakawa, H., 1952: Mame-Taifu or midget typhoon (small storms of typhoon intensity). *Geophys. Mag.*, **24**, 463–474.

Banzon, V., T. M. Smith, T. M. Chin, C. Liu, and W. Hankins, 2016: A long-term record of blended satellite and in situ sea-surface temperature for climate monitoring, modeling and environmental studies. *Earth Sys. Sci. Data*, **8**, 165–176, doi: 10.5194/essd-8-165-2016.

Bell, M. M., and W.-C. Lee, 2012: Objective tropical cyclone center tracking using single-Doppler radar. *J. Appl. Meteor. Climatol.*, **51**, 878–896, doi: 10.1175/JAMC-D-11-0167.1.

Bell, M. M., W.-C. Lee, C. A. Wolff, and H. Cai, 2013: A solo-based automated quality control algorithm for airborne tail doppler radar data. *J. Appl. Meteor. Climatol.*, **52**, 2509–2528, doi: 10.1175/JAMC-D-12-0283.1.

Bell, M. M., and M. T. Montgomery, 2008: Observed structure, evolution, and potential intensity of Category 5 Hurriane Isabel (2003) from 12 to 14 September. *Mon. Wea. Rev.*, **136**, 2023–2046, doi: doi.org/10.1175/2007MWR1858.1.

Bell, M. M., M. T. Montgomery, and K. A. Emanuel, 2012: Air–sea enthalpy and momentum exchange at major hurricane wind speeds observed during CBLAST. *J. Atmos. Sci.*, **69**, 3197–3122, doi: 10.1175/JAS-D-11-0276.1.

Bell, M. M., and Coauthors, 2016: ONR Tropical Cyclone Intensity 2015 NASA WB-57 Dropsonde Data. Version 1.0. UCAR/NCAR - Earth Observing Laboratory, accessed 23 January 2017, doi: 10.5065/D6KW5D8M.

Bhalachandran, S., D. R. Chavas, F. D. Marks, Jr., S. Dubey, A. Shreevastava, and T. N. Krishnamurti, 2020: Characterizing the energetics of vortex-scale and sub-vortex-scale asymmetries during tropical cyclone rapid intensity changes. *J. Atmos. Sci.*, **77**, 315–336, doi: 10.1175/JAS-D-19-0067.1.

Bister, M., and K. A. Emanuel, 1997: The genesis of Hurricane Guillermo: TEXMEX analyses and a modeling study. *Mon. Wea. Rev.*, **125**, 2662–2682, doi: 10.1175/1520-0493(1997)125<2662:TGOHGT>2.0.CO;2.

Black, P., L. Harrison, M. Beaubien, R. Bluth, R. Woods, A. Penny, R. W. Smith, and J. D. Doyle, 2017: High-Definition Sounding System (HDSS) for atmospheric profiling. *J. Atmos. Oceanic Technol.*, **34**, 777–796, doi: 10.1175/JTECH-D-14-00210.1.

Brand, S., 1972: Very large and very small typhoons of the western North Pacific Ocean. *J. Meteor. Soc. Japan*, **50**, 332–341.

Bryan, G. H., and J. M. Fritsch, 2002: A benchmark simulation for moist nonhydrostatic numerical models. *Mon. Wea. Rev.*, **130**, 2917–2928, doi: 10.1175/1520-0493(2002)130<2917:ABSFMN>2.0.CO;2.

Bryan, G. H., and H. Morrison, 2012: Sensitivity of a simulated squall line to horizontal resolution and parameterization of microphysics. *Mon. Wea. Rev.*, **140**, 202–225, doi: 10.1175/MWR-D-11-00046.1.

Bryan, H. G., R. P. Worsnop, J. K. Lundquist, and J. A. Zhang, 2017: A simple method for simulating wind profiles in the boundary layer of tropical cyclones. *Bound.-Layer Meteor*, **162**, 475–502, doi: 10.1007/s10546-016-0207-0.

Bu, Y. P., R. G. Fovell, and K. L. Corbosiero, 2014: Influence of cloud–radiative forcing on tropical cyclone structure. *J. Atmos. Sci.*, **71**, 1644–1662, doi: 10.1175/JAS-D-13-0265.1.

Cai, H., W.-C. Lee, M. M. Bell, C. A. Wolff, X. Tang, and F. Roux, 2018: A generalized navigation correction method for airborne Doppler radar data. *J. Atmos. Oceanic Technol.*, doi: 10.1175/JTECH-D-18-0028.1.

Carrasco, C. A., C. W. Landsea, and Y.-H. Lin, 2014: The influence of tropical cyclone size on its intensification. *Wea. Forecasting*, **29**, 582–590, doi: 10.1175/WAF-D-13-00092.1.

Chan, K. T. F., and J. C. L. Chan, 2012: Size and strength of tropical cyclones as inferred from QuikSCAT data. *Mon. Wea. Rev.*, **140**, 811–824, doi: 10.1175/MWR-D-10-05062.1.

Chan, K. T. F., and J. C. L. Chan, 2014: Impacts of initial vortex size and planetary vorticity on tropical cyclone size. *Quart. J. Roy. Meteor. Soc.*, **140**, 2235–2248, doi: 10.1002/qj.2292.

Chan, K. T. F., and J. C. L. Chan, 2015: Impacts of vortex intensity and outer winds on tropical cyclone size. *Quart. J. Roy. Meteor. Soc.*, **141**, 525–537, doi: 10.1002/qj.2374.

Chang, M., C.-H. Ho, M.-S. Park, J. Kim, and M.-H. Ahn, 2017: Multiday evolution of convective bursts during western north pacific tropical cyclone development and nondevelopment using geostationary satellite measurements. *JGR*, **122**, 1635–1649, doi: 10.1002/2016JD025535.

Chavas, D. R., and K. A. Emanuel, 2010: A QuickSCAT climatology of tropical cyclone size. *Geophys. Res. Lett.*, **37**, L18 816, doi: 10.1029/2010GL044558.

Chen, B.-F., C. A. Davis, and Y.-H. Kuo, 2018: Effects of low-level flow orientation and vertical shear on the structure and intensity of tropical cyclones. *Mon. Wea. Rev.*, **146**, 2447–2467, doi: 10.1175/MWR-D-17-0379.1.

Chen, B.-F., C. A. Davis, and Y.-H. Kuo, 2019: An idealized numerical study of shear-relative low-level mean flow on tropical cyclone intensity and size. *J. Atmos. Sci.*, **76**, 2309–2334, doi: 10.1175/JAS-D-18-0315.1.

Cruz-Cano, R., and E. L. Mead, 2019: Causes of excess deaths in Puerto Rico after Hurricane Maria: A time-series estimation. *American Journal of Public Health*, **109**, 1050–1052, doi: 10.2105/AJPH.2019.305015.

Dai, A., 2006: Recent climatology, variability, and trends in global surface humidity. *J. Climate*, **19 (15)**, 3589–3606, doi: 10.1175/JCLI3816.1.

Davis, C. A., and D. A. Ahijevych, 2013: Thermodynamic environments of deep convection in Atlantic tropical disturbances. *J. Atmos. Sci.*, **70**, 1912–1928, doi: 10.1175/JAS-D-12-0278.1.

Davis, C. A., and T. J. Galarneau, Jr., 2009: The vertical structure of mesoscale convective vortices. *J. Atmos. Sci.*, **66**, 686–704, doi: 10.1175/2008JAS2819.1.

DeMaria, M., M. Mainelli, L. K. Shay, J. A. Knaff, and J. Kaplan, 2005: Further improvements to the Statistical Hurricane Intensity Prediction Scheme (SHIPS). *Wea. Forecasting*, **20**, 531–543, doi: 10.1175/WAF862.1.

Doyle, J. D., and Coauthors, 2017: A view of tropical cyclones from above: The Tropical Cyclone Intensity (TCI) Experiment. *Bull. Amer. Meteor. Soc.*, doi: 10.1175/BAMS-D-16-0055.1.

Dunion, J. P., 2011: Rewriting the climatology of the tropical North Atlantic and Caribbean Sea atmosphere. *J. Climate*, **24**, 893–908, doi: 10.1175/2010JCLI3496.1.

Dunnavan, G. M., and J. W. Diercks, 1980: An analysis of Super Typhoon Tip (October 1979). *Mon. Wea. Rev.*, **108**, 1915–1923, doi: 10.1175/1520-0493(1980)108<1915:AAOSTT>2.0.CO;2.

Eastin, M. D., P. G. Black, and W. M. Gray, 2002: Flight level thermodynamic instrument wetting errors in hurricanes. Part I: Observations. *Mon. Wea. Rev.*, **130**, 825–841, doi: 10.1175/1520-0493(2002)130<0825:FLTIWE>2.0.CO;2.

Eliassen, E., 1951: Slow thermally or frictionally controlled meridional circulation in a circular vortex. *Astrophys. Norv.*, **5**, 19–60.

Ertel, H., 1942: Ein neuer hydrodynamischer erhaltungssatz. *Naturwissenschaften*, **30**, 543–544.

Foerster, A. M., and M. M. Bell, 2017: Thermodynamic retrieval in rapidly rotating vortices from multiple-Doppler radar data. *J. Atmos. Oceanic Technol.*, **34**, 2353–2374, doi: 10.1175/JTECH-D-17-0073.1.

Foerster, A. M., M. M. Bell, P. A. Harr, and S. C. Jones, 2014: Observations of the eyewall structure of Typhoon Sinlaku (2008) during the transformation stage of extratropical transition. *Mon. Wea. Rev.*, **142**, 3372–3392, doi: 10.1175/MWR-D-13-00313.1.

Fovell, R. G., Y. P. Bu, K. L. Corbosiero, W. Tung, Y. Cao, H. Kuo, L. Hsu, and H. Su, 2016: Influence of cloud microphysics and radiation on tropical cyclone structure and motion. *Meteorological Monographs*, **56**, 11.1–11.27, doi: 10.1175/AMSMONOGRAPHS-D-15-0006.1.

Franklin, J. L., S. J. Lord, and F. D. Marks, Jr., 1988: Dropwindsonde and radar observations of the eye of Hurricane Gloria (1985). *Mon. Wea. Rev.*, **116**, 1237–1244, doi: 10.1175/1520-0493(1988)116<1237:DAROOT>2.0.CO;2.

Gray, W. H., 1968: Global view of the origin of tropical disturbances and storms. *Mon. Wea. Rev.*, **96**, 669–700.

Gray, W. M., 1998: The formation of tropical cyclones. *Meteor. Atmos. Phys.*, **67**, 37–69.

Guinn, T. A., and W. H. Schubert, 1993: Hurricane spiral bands. *J. Atmos. Sci.*, **50**, 3380–3403, doi: 10.1175/1520-0469(1993)050<3380:HSB>2.0.CO;2.

Hack, J. J., and W. H. Schubert, 1986: Nonlinear response of atmospheric vortices to heating by organized cumulus convection. *J. Atmos. Sci.*, **43**, 1559–1573, doi: 10.1175/1520-0469(1986)043<1559:NROAVT>2.0.CO;2.

Harr, P. A., M. S. Kalafsky, and R. L. Elsberry, 1996: Environmental conditions prior to formation of a midget tropical cyclone during TCM-93. *Mon. Wea. Rev.*, **116**, 1693–1710, doi: 10.1175/1520-0493(1996)124<1693:ECPTFO>2.0.CO;2.

Hausman, S. A., V. K. Ooyama, and W. H. Schubert, 2006: Potential vorticity structure of simulated hurricanes. *J. Atmos. Sci.*, **63**, 87–108, doi: 10.1175/JAS3601.1.

Hawkins, H. F., and S. M. Imbembo, 1976: The structure of a small, intense hurricane–Inez 1966. *Mon. Wea. Rev.*, **104**, 418–442, doi: 10.1175/1520-0493(1976)104<0418:TSOASI>2.0.CO;2.

Hawkins, H. F., and D. T. Rubsam, 1967: Hurricane Inez - A classic "micro-hurricane". *Mar. Wea. Log.*, **11**, 157–160.

Haynes, P. H., and M. E. McIntyre, 1987: On the evolution of vorticity and potential vorticity in the presence of diabatic heating and frictional or other forces. *J. Atmos. Sci.*, **44**, 828–841, doi: 10.1175/1520-0469(1987)044<0828:OTEOVA>2.0.CO;2.

Haynes, P. H., and M. E. McIntyre, 1990: On the conservation and impermeability theorems for potential vorticity. *J. Atmos. Sci.*, **47**, 2021–2031, doi: 10.1175/1520-0469(1990)047<2021:OTCAIT>2.0.CO;2.

Hence, D. A., and R. A. Houze, Jr., 2012: Vertical structure of tropical cyclone rainbands as seen by the TRMM precipitation radar. *J. Atmos. Sci.*, **69**, 2644–2661, doi: 10.1175/JAS-D-11-0323.1.

Hendricks, E. A., M. S. Peng, B. Fu, and T. Li, 2010: Quantifying environmental control on tropical cyclone intensity change. *Mon. Wea. Rev.*, **138**, 3243–3271, doi: 10.1175/2010MWR3185.1.

Hendricks, E. A., and W. H. Schubert, 2010: Adiabatic rearrangement of hollow PV towers. *J. Adv. Model. Earth. Syst.*, **2**, Art 8, 19 pp., doi: 10.3894/JAMES.2010.2.2.

Hendricks, E. A., W. H. Schubert, Y.-H. Chen, H.-C. Kuo, and M. S. Peng, 2014: Hurricane eyewall evolution in a forced shallow-water model. *J. Atmos. Sci.*, **71**, 1623–1643, doi: 10.1175/JAS-D-13-0303.1.

Hendricks, E. A., W. H. Schubert, R. K. Taft, H. Wang, and J. P. Kossin, 2009: Life cycles of hurricane-like vorticity rings. *J. Atmos. Sci.*, **66**, 705–722, doi: 10.1175/2008JAS2820.1.

Hendricks, E. H., M. T. Montgomery, and C. A. Davis, 2004: The role of "vortical" hot towers in the formation of Tropical Cyclone Diana (1984). *J. Atmos. Sci.*, **61**, 1209–1232, doi: 10.1175/1520-0469(2004)061<1209:TROVHT>2.0.CO;2.

Hill, K. A., and G. M. Lackmann, 2009: Influence of environmental humidity on tropical cyclone size. *Mon. Wea. Rev.*, **137**, 3294–3315, doi: 10.1175/2009MWR2679.1.

Hitchman, M. H., and S. M. Rowe, 2019: On the structure and formation of UTLS PV dipole/jetlets in tropical cyclones by convective momentum surges. *Mon. Wea. Rev.*, **147**, 4107–4125, doi: 10.1175/MWR-D-18-0232.1.

Holloway, C. E., and J. D. Neelin, 2009: Moisture vertical structure, column water vapor, and tropical deep convection. *JAS*, **66**, 1665–1683, doi: 10.1175/2008JAS2806.1.

Hoskins, B. J., M. E. McIntyre, and A. W. Robertson, 1985: On the use and significance of isentropic potential vorticity maps. *Quart. J. Roy. Meteor. Soc.*, **111**, 877–946, doi: 10.1002/qj.49711147002.

Houze, R. A., S. S. Chen, B. F. Smull, W.-C. Lee, and M. M. Bell, 2007: Hurricane intensity and eyewall replacement. *Nature*, **315**, 1235–1239, doi: 10.1126/science.1135650.

Houze, R. A., Jr., 2010: Clouds in tropical cyclones. *Mon. Wea. Rev.*, **138**, 293–344, doi: 10.1175/2009MWR2989.1.

Jordan, C. L., 1961: Marked changes in the characteristics of the eye of intense typhoons between the deepening and filling stages. *J. Meteor*, **18**, 779–789, doi: 10.1175/1520-0469(1961)018<0779:MCITCO>2.0.CO;2.

Judt, F., and S. S. Chen, 2016: Predictability and dynamics of tropical cyclone rapid intensification deduced from high-resolution stochastic ensembles. *Mon. Wea. Rev.*, **144**, 4395–4420, doi: 10.1175/MWR-D-15-0413.1.

Kaplan, J., M. DeMaria, and J. A. Knaff, 2010: A revised tropical cyclone rapid intensification index for the Atlantic and eastern North Pacific basins. *Wea. Forecasting*, **25**, 220–241, doi: 10.1175/2009WAF2222280.1.

Kaplan, J., and Coauthors, 2015: Evaluating environmental impacts on tropical cyclone rapid intensification predictability utilizing statistical models. *Wea. Forecasting*, **30**, 1374–1396, doi:

10.1175/WAF-D-15-0032.1.

Kepert, J. D., 2012: Choosing a boundary layer parameterization for tropical cyclone modeling. *Mon. Wea. Rev.*, **140**, 1427–1445, doi: 10.1175/MWR-D-11-00217.1.

Kieu, C. Q., and D.-L. Zhang, 2010: A piecewise potential vorticity inversion algorithm and its application to hurricane inner-core anomalies. *J. Atmos. Sci.*, **67**, 2616–2131, doi: 10.1175/2010JAS3421.1.

Kilroy, G., and R. K. Smith, 2017: The effects of initial vortex size on tropical cyclogenesis and intensification. *Quart. J. Roy. Meteor. Soc.*, doi: 10.1002/qj.3134.

Kimball, S. K., and M. S. Mulekar, 2004: A 15-year climatology of North Atlantic tropical cyclones. Part I: Size parameters. *J. Climate*, **17**, 3555–3575, doi: 10.1175/1520-0442(2004)017<3555:AYCONA>2.0.CO;2.

Kimberlain, T. B., E. S. Blake, and J. P. Canigialosi, 2016: Hurricane Patricia. National Hurricane Center Tropical Cyclone Report.

Kishore, N. K., and Coauthors, 2018: Mortality in Puerto Rico after Hurricane Maria. *New England Journal of Medicine*, **379**, 162–170, doi: 10.1056/NEJMsa1803972.

Klotzbach, P. J., M. M. Bell, S. G. Bowen, and E. J. Gibney, 2020: Surface pressure a more skillful predictor of normalized hurricane damage than maximum sustained wind. *Bull. Amer. Meteor. Soc.*, doi: 10.1175/BAMS-D-19-0062.1.

Klotzbach, P. J., S. G. Bowen, R. A. Pielke, Jr., and M. M. Bell, 2018: Continental U.S. hurricane landfall frequency and associated damage: Observations and future risks. *Bull. Amer. Meteor. Soc.*, **99**, 1359–1376, doi: 10.1175/BAMS-D-17-0184.1.

Knaff, J. A., S. P. Longmore, and D. A. Molenar, 2014: An objective satellite-based tropical cyclone size climatology. *J. Climate*, **27**, 455–476, doi: 10.1175/JCLI-D-13-00096.1.

Knaff, J. A., C. R. Sampson, and G. Chirokova, 2017: A global statistical–dynamical tropical cyclone wind radii forecast scheme. *Wea. Forecasting*, **32**, 629–644, doi: 10.1175/WAF-D-16-0168.1.

Knutson, T. R., J. J. Sirutis, M. Zhao, R. E. Tuleya, M. Bender, G. A. Vecchi, G. Villarini, and D. Chavas, 2015: Global projections of intense tropical cyclone activity for the late twenty-first century from dynamical downscaling of CMIP5/RCP4.5 scenarios. *J. Climate*, **28**, 7203–7224, doi: 10.1175/JCLI-D-15-0129.1.

Komaromi, W. A., 2013: An investigation of composite dropsonde profiles for developing and nondeveloping tropical waves during the 2010 PREDICT field campaign. *J. Atmos. Sci.*, **70**, 542–558, doi: 10.1175/JAS-D-12-052.1.

Kossin, J. P., and M. D. Eastin, 2001: Two distinct regimes in the kinematic and thermodynamic structure of the hurricane eye and eyewall. *J. Atmos. Sci.*, **58**, 1079–1090, doi: 10.1175/1520-0469(2001)058<1079:TDRITK>2.0.CO;2.

Kossin, J. P., and W. H. Schubert, 2001: Mesovortices, polygonal flow patterns, and rapid pressure falls in hurricane-like vortices. *J. Atmos. Sci.*, **58**, 2196–2209, doi: 10.1175/1520-0469(2001)058<2196:MPFPAR>2.0.CO;2.

Lee, W.-C., and F. D. Marks, Jr., 2000: Tropical cyclone kinematic structure retrieved from single-Doppler radar observations: Part II: The GBVTD-simplex center finding algorithm. *Mon. Wea. Rev.*, **128**, 1925–1936, doi: 10.1175/1520-0493(2000)128<1925:TCKSRF>2.0.CO;2.

Liu, K. S., and J. C. L. Chan, 2002: Synoptic flow patterns associated with small and large tropical cyclones over the western North Pacific. *Mon. Wea. Rev.*, **130**, 2134–2142, doi: 10.1175/1520-0493(2002)130<2134:SFPAWS>2.0.CO;2.

Louis, J. F., 1979: A parametric model of vertical eddy fluxes in the atmosphere. *Bound.-Layer Meteor.*, **17**, 187–202, doi: 10.1007/BF00117978.

Mallen, K. J., M. T. Montgomery, and B. Wang, 2005: Reexamining the near-core radial structure of the tropical cyclone primary circulation: Implications for vortex resiliency. *J. Atmos. Sci.*, **62**, 408–425, doi: 10.1175/JAS-3377.1.

Marks, F. D., Jr., R. A. Houze Jr., and J. Gamache, 1992: Dual-aircraft investigation of the inner core of Hurricane Norbert. Part I: Kinematic structure. *J. Atmos. Sci.*, **49**, 919–942, doi: 10.1175/1520-0469(1992)049<0919:DAIOTI>2.0.CO;2.

Marks, F. D., Jr., N. Kurkowski, M. DeMaria, and M. Brennan, 2019: National Oceanic Atmospheric Administration Hurricane Forecast Improvement Project Years Ten to Fifteen Strategic Plan. 83 pp., http://www.hfip.org/documents/HFIP_Strategic_Plan_20190625.pdf.

Martinez, J., M. M. Bell, R. F. Rogers, and D. J. Doyle, 2019: Axisymmetric potential vorticity evolution of Hurricane Patricia (2015). *J. Atmos. Sci.*, **76**, 2043–2063, doi: 10.1175/JAS-D-18-0373.1.

Martinez, J., M. M. Bell, J. L. Vigh, and R. F. Rogers, 2017: Examining tropical cyclone structure and intensification with the FLIGHT+ Dataset from 1999–2012. *Mon. Wea. Rev.*, **145**, 4401–4421, doi: 10.1175/MWR-D-17-0011.1.

McBride, J. L., and R. Zehr, 1981: Observational analysis of tropical cyclone formation. Part II: Comparison of non-developing versus developing systems. *J. Atmos. Sci.*, 1132–1151, doi: 10.1175/1520-0469(1981)038<1132:OAOTCF>2.0.CO;2.

McTaggart-Cowan, R., G. D. Deane, L. F. Bosart, C. A. Davis, and T. J. Galarneau, Jr., 2008: Climatology of tropical cyclogenesis in the North Atlantic (1948–2004). *Mon. Wea. Rev.*, **136**, 1284–1304, doi: 10.1175/2007MWR2245.1.

McTaggart-Cowan, R., T. J. Galarneau, L. F. Bosart, R. W. Moore, and O. Martius, 2013: A global climatology of baroclinically influenced tropical cyclogenesis. *Mon. Wea. Rev.*, **141**, 1963–1989, doi: 10.1175/MWR-D-12-00186.1.

Merrill, R. T., 1984: A comparison of large and small tropical cyclones. *Mon. Wea. Rev.*, **112**, 1408–1418, doi: 10.1175/1520-0493(1984)112<1408:ACOLAS>2.0.CO;2.

Miyamoto, Y., and D. S. Nolan, 2018: Structural changes preceding rapid intensification in tropical cyclones as shown in a large ensemble of idealized simulations. *J. Atmos. Sci.*, **75**, 555–569, doi: 10.1175/JAS-D-17-0177.1.

Miyamoto, Y., and T. Takemi, 2013: A transition mechanism for the spontaneous axisymmetric intensification of tropical cyclones. *J. Atmos. Sci.*, **70**, 112–128, doi: 10.1175/JAS-D-11-0285.1.

Mogensen, and Coauthors, 2020: JuliaNLSolvers/Optim.jl: v0.21.0. *Zenodo*, doi: doi:10.5281/zenodo.3778625.

Möller, J. D., and M. T. Montgomery, 1999: Vortex Rossby waves and hurricane intensification in a barotropic model. *J. Atmos. Sci.*, **56**, 1674–1687, doi: 10.1175/1520-0469(1999)056<1674:VRWAHI>2.0.CO;2.

Möller, J. D., and M. T. Montgomery, 2000: Tropical cyclone evolution via potential vorticity anomalies in a three-dimensional balance model. *J. Atmos. Sci.*, **57**, 3366–3387, doi: 10.1175/1520-0469(2000)057<3366:TCEVPV>2.0.CO;2.

Möller, J. D., and R. K. Smith, 1994: The development of potential vorticity in a hurricane like vortex. *Quart. J. Roy. Meteor. Soc.*, **120**, 1255–1265, doi: 10.1002/qj.49712051907.

Montgomery, M. T., and R. J. Kallenbach, 1997: A theory for vortex Rossby-waves and its application to spiral bands and intensity changes in hurricanes. *Quart. J. Roy. Meteor. Soc.*, **123**, 435–465, doi: 10.1002/qj.49712353810.

Montgomery, M. T., M. E. Nicholls, T. A. Cram, and A. B. Saunders, 2006: A vortical hot tower route to tropical cyclogenesis. *J. Atmos. Sci.*, **63**, 355–386, doi: 10.1175/JAS3604.1.

Montgomery, M. T., and L. J. Shapiro, 1995: Generalized Charney-Stern and Fjortoft theorems for rapidly rotating vortices. *J. Atmos. Sci.*, **52**, 1828–1833, doi: 10.1175/1520-0469(1995)052<1829:GCAFTF>2.0.CO;2.

Musgrave, K. D., J. L. Taft, R. K. Vigh, B. D. McNoldy, and W. H. Schubert, 2012: Time evolution of the intensity and size of tropical cyclones. *J. Adv. Model. Earth Syst.*, **4**, M08 001, doi: 10.1029/2011MS000104.

Nguyen, L. T., J. Molinari, and D. Thomas, 2014: Evaluation of tropical cyclone center identification methods in numerical models. *Mon. Wea. Rev.*, **142**, 4326–4339, doi:

10.1175/MWR-D-14-00044.1.

Nguyen, V. S., R. K. Smith, and M. T. Montgomery, 2008: Tropical-cyclone intensification and predictability in three dimensions. *Quart. J. Roy. Meteor. Soc.*, **134**, 563–582, doi: 10.1002/qj.235.

NOAA, 2018: National Centers for Environmental Information, State of the Climate: Hurricanes and Tropical Storms for Annual 2017. Retrieved on January 5, 2020, https://www.ncdc.noaa.gov/sotc/tropical-cyclones/201713.

Nolan, D. S., 2007: What is the trigger for tropical cyclogenesis? *Aust. Meteor. Mag.*, **56**, 241–266.

Nolan, D. S., and L. D. Grasso, 2003: Nonhydrostatic, three-dimensional perturbations to balanced, hurricane-like vortices. Part II: Symmetric response and nonlinear simulations. *JAS*, **60**, 2717–2745, doi: 10.1175/1520-0469(2003)060<2717:NTPTBH>2.0.CO;2.

Nolan, D. S., and M. T. Montgomery, 2002: Nonhydrostatic, three-dimensional perturbations to balanced, hurricane-like vortices. Part I: Linearized formulation, stability, and evolution. *J. Atmos. Sci.*, **59**, 2989–3020, doi: 10.1175/1520-0469(2002)059<2989:NTDPTB>2.0.CO;2.

Nolan, D. S., Y. Moon, and D. P. Stern, 2007: Tropical cyclone intensification from asymmetric convection: energetics and efficiency. *J. Atmos. Sci.*, **64**, 3377–3405, doi: 10.1175/JAS3988.1.

Onderlinde, M. J., and D. S. Nolan, 2017: The tropical cyclone response to changing wind shear using the method of time-varying point-downscaling. *J. Adv. Model. Earth Syst.*, **9**, 908–931, doi: 10.1002/2016MS000796.

Ooyama, K. V., 2002: The cubic-spline transform method: Basic definitions and tests in a 1D single domain. *Mon. Wea. Rev.*, **130**, 2392–2415, doi: 10.1175/1520-0493(2002)130<2392:TCSTMB>2.0.CO;2.

Pendergrass, A. G., and H. E. Willoughby, 2009: Diabatically induced secondary flows in tropical cyclones. Part I: Quasi-steady forcing. *Mon. Wea. Rev.*, **137**, 805–821, doi: 10.1175/2008MWR2657.1.

Persing, J., M. T. Montgomery, J. C. McWilliams, and R. K. Smith, 2013: Asymmetric and axisymmetric dynamics of tropical cyclone intensification. *Atmos. Chem. Phys.*, **13**, 12 299–12 341, doi: 10.5194/acp-13-12299-2013.

Pielke, R. A., Jr., J. Gratz, C. W. Landsea, D. Collins, M. A. Saunders, and R. Musulin, 2008: Normalized hurricane damage in the United States: 1900–2005. *Nat. Hazards Rev.*, **9**, 29–42, doi: 10.1061/(ASCE)1527-6988(2008)9:1(29).

Purser, R. J., W.-S. Wu, D. F. Parrish, and N. M. Roberts, 2003: Numerical aspects of the application of recursive filters to variational statistical analysis. Part I: Spatially homogeneous

and isotropic Gaussian covariances. *Mon. Wea. Rev.*, **131**, 1524–1535, doi: 10.1175//1520-0493(2003)131<1524:NAOTAO>2.0.CO;2.

Rappaport, E. N., and B. W. Blanchard, 2016: Fatalities in the United States indirectly associated with Atlantic tropical cyclones. *Bull. Amer. Meteor. Soc.*, **97**, 1139–1148, doi: 10.1175/BAMS-D-15-00042.1.

Raymond, D. J., S. Gjorgjievska, S. Sessions, and Z. Fuchs, 2014: Tropical cyclogenesis and mid-level vorticity. *Aust. Meteor. Oceanogr. J.*, **64**, 11–25.

Raymond, D. J., and H. Jiang, 1990: A theory for long-lived mesoscale convective systems. *J. Atmos. Sci.*, **47**, 3067–3077, doi: 10.1175/1520-0469(1990)047<3067:ATFLLM>2.0.CO;2.

Raymond, D. J., S. L. Sessions, and C. L. Carrillo, 2011: Thermodynamics of tropical cyclogenesis in the northwest Pacific. *J. Geophys. Res.*, **116**, D18 101, doi: 10.1029/2011JD015624.

Reasor, P. D., M. D. Eastin, and J. F. Gamache, 2009: Rapidly intensifying Hurricane Guillermo (1997). Part I: Low-wavenumber structure and evolution. *Mon. Wea. Rev.*, **137**, 603–631, doi: 10.1175/2008MWR2487.1.

Rios-Berrios, R., C. A. Davis, and R. D. Torn, 2018: A hypothesis for the intensification of tropical cyclones under moderate vertical wind shear. *J. Atmos. Sci.*, **75**, 4149–4173, doi: 10.1175/JAS-D-18-0070.1.

Rios-Berrios, R., R. D. Torn, and C. A. Davis, 2016: An ensemble approach to investigate tropical cyclone intensification in sheared environments. Part I: Katia (2011). *J. Atmos. Sci.*, **73**, 71–93, doi: 10.1175/JAS-D-15-0052.1.

Ritchie, E. A., and G. J. Holland, 1999: Large-scale patterns associated with tropical cyclogenesis in the Western Pacific. *Mon. Wea. Rev.*, **127**, 2027–2043, doi: 10.1175/1520-0493(1999)127<2027:LSPAWT>2.0.CO;2.

Rogers, R., P. Reasor, and S. Lorsolo, 2013a: Airborne doppler observations of the inner-core structural differences between intensifying and steady state tropical cyclones. *Mon. Wea. Rev.*, **141**, 2970–2991, doi: 10.1175/MWR-D-12-00357.1.

Rogers, R. F., P. D. Reasor, and J. A. Zhang, 2015: Multiscale structure and evolution of Hurricane Earl (2010) during rapid intensification. *Mon. Wea. Rev.*, **143**, 536–562, doi: 10.1175/MWR-D-14-00175.1.

Rogers, R. F., and Coauthors, 2006: The Intensity Forecasting Experiment (IFEX): A NOAA multi-year field program for improving tropical cyclone intensity forecasts. *Bull. Amer. Meteor. Soc.*, **87**, 1523–1537, doi: 10.1175/BAMS-87-11-1523.

Rogers, R. F., and Coauthors, 2013b: NOAA's Hurricane Intensity Forecasting Experiment: A progress report. *Bull. Amer. Meteor. Soc.*, **94**, 859–882, doi: 10.1175/BAMS-D-12-00089.1.

Rogers, R. F., and Coauthors, 2017: Re-writing the tropical record books: The extraordinary intensification of Hurricane Patricia (2015). *Bull. Amer. Meteor. Soc.*, doi: 10.1175/BAMS-D-16-0039.1.

Rotunno, R., and K. A. Emanuel, 1987: An air-sea interaction theory for tropical cyclones. Part II: Evolutionary study using a nonhydrostatic axisymmetric numerical model. *J. Atmos. Sci.*, **44**, 542–561, doi: 10.1175/1520-0469(1987)044<0542:AAITFT>2.0.CO;2.

Roux, F., V. Marécal, and D. Hauser, 1993: The 12/13 January 1988 narrow cold-frontal rainband observed during MFDP/FRONTS 87. Part I: Kinematics and thermodynamics. *J. Atmos. Sci.*, **50**, 951–974, doi: 10.1175/1520-0469(1993)050<0951:TJNCFR>2.0.CO;2.

Rozoff, C. M., J. P. Kossin, W. H. Schubert, and P. J. Mulero, 2009: Internal control of hurricane intensity variability: The dual nature of potential vorticity mixing. *J. Atmos. Sci.*, **66**, 133–147, doi: 10.1175/2008JAS2717.1.

Rozoff, C. M., C. S. Velden, J. Kaplan, J. P. Kossin, and A. J. Wimmers, 2015: Improvements in the probabilistic prediction of tropical cyclone rapid intensification with passive microwave observations. *WF*, **30**, 1016–1038, doi: 10.1175/WAF-D-14-00109.1.

Santos-Burgoa, C., and Coauthors, 2018: Differential and persistent risk of excess mortality from Hurricane Maria in Puerto Rico: A time-series analysis. *Lancet Planet Health*, **2**, e478–e488, doi: 10.1016/S2542-5196(18)30209-2.

Santos-Lozada, A. R., and J. T. Howard, 2018: Use of death counts from vital statistics to calculate excess deaths in Puerto Rico following Hurricane Maria. *Journal of the American Medical Association*, **320**, 1491–1493, doi: 10.1001/jama.2018.10929.

Schenkel, B. A., N. Lin, D. Chavas, G. A. Vecchi, M. Oppenheimer, and A. Brammer, 2018a: Lifetime evolution of outer tropical cyclone size and structure as diagnosed from reanalysis and climate model data. *J. Climate*, **31**, 7985–8004, doi: 10.1175/JCLI-D-17-0630.1.

Schenkel, B. A., N. Lin, D. R. Chavas, G. A. Vecchi, T. R. Knutson, and M. Oppenheimer, 2018b: Will outer tropical cyclone size change due to anthropogenic warming? *33rd Conference on Hurricanes and Tropical Meteorology*, Jacksonville, FL, Amer. Meteor. Soc., https://ams.confex.com/ams/33HURRICANE/webprogram/Paper339539.html.

Schubert, W. H., 2004: A generalization of Ertel's potential vorticity to a cloudy, precipitating atmosphere. *Meteorol. Z.*, **13**, 465–471, doi: 10.1127/0941-2948/2004/0013-0465.

Schubert, W. H., and B. T. Alworth, 1987: Evolution of potential vorticity in tropical cyclones. *Quart. J. Roy. Meteor. Soc.*, **113**, 147–162, doi: 10.1002/qj.49711347509.

Schubert, W. H., and J. J. Hack, 1982: Inertial stability and tropical cyclone development. *J. Atmos. Sci.*, **39**, 1687–1697, doi: 10.1175/1520-0469(1982)039<1687:ISATCD>2.0.CO;2.

Schubert, W. H., and J. J. Hack, 1983: Transformed Eliassen balanced vortex model. *J. Atmos. Sci.*, **40**, 1571–1583, doi: 10.1175/1520-0469(1983)040<1571:TEBVM>2.0.CO;2.

Schubert, W. H., S. A. Hausman, M. Garcia, K. V. Ooyama, and H.-C. Kuo, 2001: Potential vorticity in a moist atmosphere. *J. Atmos. Sci.*, **58**, 3148–3157, doi: 10.1175/1520-0469(2001)058<3148:PVIAMA>2.0.CO;2.

Schubert, W. H., and B. D. McNoldy, 2010: Application of the concepts of Rossby length and Rossby depth to tropical cyclone dynamics. *J. Adv. Model. Earth Syst.*, **2**, 13, doi: 10.3894/JAMES.2010.2.7.

Schubert, W. H., M. T. Montgomery, R. K. Taft, T. A. Guinn, S. R. Fulton, J. Kossin, and J. P. Edwards, 1999: Polygonal eyewalls, asymmetric eye contraction, and potential vorticity mixing in hurricanes. *J. Atmos. Sci.*, **56**, 1197–1223, doi: 10.1175/1520-0469(1999)056<1197:PEAECA>2.0.CO;2.

Shapiro, L. J., 1996: The motion of Hurricane Gloria: A potential vorticity diagnosis. *Mon. Wea. Rev.*, **124**, 2497–2508, doi: 10.1175/1520-0493(1996)124<2497:TMOHGA>2.0.CO;2.

Shapiro, L. J., and J. L. Franklin, 1995: Potential vorticity in Hurricane Gloria. *Mon. Wea. Rev.*, **123**, 1465–1475, doi: 10.1175/1520-0493(1995)123<1465:PVIHG>2.0.CO;2.

Smith, R. K., 2006: Accurate determination of a balanced axisymmetric vortex in a compressible atmosphere. *Tellus*, **58A**, 98–103.

Smith, R. K., and M. T. Montgomery, 2016: The efficiency of diabatic heating and tropical cyclone intensification. *Quart. J. Roy. Meteor. Soc.*, **142**, 2081–2086, doi: 10.1002/qj.2804.

Smith, R. K., M. T. Montgomery, and H. Bui, 2018: Axisymmetric balance dynamics of tropical cyclone intensification and its breakdown revisited. *J. Atmos. Sci.*, **75**, 3169–3189, doi: 10.1175/JAS-D-17-0179.1.

Stern, D. P., J. R. Brisbois, and D. S. Nolan, 2014: An expanded dataset of hurricane eyewall sizes and slopes. *J. Atmos. Sci.*, **71**, 2747–2762, doi: 10.1175/JAS-D-13-0302.1.

Stern, D. P., and D. S. Nolan, 2009: Reexamining the vertical structure of tangential winds in tropical cyclones: Observations and theory. *J. Atmos. Sci.*, **66**, 3579–3600, doi: 10.1175/2009JAS2916.1.

Stern, D. P., and F. Zhang, 2013: How does the eye warm? Part I: A potential temperature budget analysis of an idealized tropical cyclone. *J. Atmos. Sci.*, **70**, 73–90, doi: 10.1175/JAS-D-11-0329.1.

Sumwalt, R. L., C. A. Hart, E. F. Weener, and T. B. Dinh-Zahr, 2017: Safety recommendation report: Tropical cyclone information for mariners. National Transportation Saftey Board Tech. Rep. MSR-17/02. 21 pp.,

https://www.ntsb.gov/investigations/AccidentReports/Reports/MSR1702.pdf.

Tao, D., M. Bell, R. Rotunno, and P. J. van Leeuwen, 2020: Why do the maximum intensities in modeled tropical cyclones vary under the same environmental conditions? *Geophys. Res. Lett.*, **47 (3)**, e2019GL085 980, doi: 10.1029/2019GL085980.

Tao, D., and F. Zhang, 2014: Effect of environmental shear, sea-surface temperature, and ambient moisture on the formation and predictability of tropical cyclones: An ensemble-mean perspective. *J. Adv. Model. Earth Syst.*, **6**, 384–404, doi: 10.1002/2014MS000314.

Tory, K. J., J. D. Kepert, J. A. Sippel, and C. M. Nguyen, 2012: On the use of potential vorticity tendency equations for diagnosing atmospheric dynamics in numerical models. *J. Atmos. Sci.*, **69**, 942–960, doi: 10.1175/JAS-D-10-05005.1.

Tsujino, S., and H. Kuo, 2020: Potential vorticity mixing and rapid intensification in the numerically simulated Supertyphoon Haiyan (2013). *J. Atmos. Sci.*, doi: 10.1175/JAS-D-19-0219.1.

Velden, C., and Coauthors, 2005: Recent innovations in deriving tropospheric winds from meteorological satellites. *Bull. Amer. Meteor. Soc.*, **86**, 205–223, doi: 10.1175/BAMS-86-2-205.

Velden, C. S., C. M. Hayden, S. Nieman, W. P. Menzel, and J. Goerss, 1997: Upper-tropospheric winds derived from geostationary satellite water vapor observations. *Bull. Amer. Meteor. Soc.*, **78**, 173–195, doi: 10.1175/1520-0477(1997)078<0173:UTWDFG>2.0.CO;2.

Vigh, J. L., and W. H. Schubert, 2009: Rapid development of the tropical cyclone warm core. *J. Atmos. Sci.*, **66**, 3335–3350, doi: 10.1175/2009JAS3092.1.

Weatherford, C. L., and W. M. Gray, 1988: Typhoon structure as revealed by aircraft reconnaissance. Part II: Structural variability. *Mon. Wea. Rev.*, **116**, 1044–1056, doi: 10.1175/1520-0493(1988)116<1044:TSARBA>2.0.CO;2.

Willoughby, H. E., 1998: Tropical cyclone eye thermodynamics. *Mon. Wea. Rev.*, **126**, 3053–3067, doi: 10.1175/1520-0493(1998)126<3053:TCET>2.0.CO;2.

Xu, J., and Y. Wang, 2010: Sensitivity of the simulated tropical cyclone inner-core size to the initial vortex size. *Mon. Wea. Rev.*, **138**, 4135–4157, doi: 10.1175/2010MWR3335.1.

Xu, J., and Y. Wang, 2018: Effect of the initial vortex structure on intensification of a numerically simulated tropical cyclone. *J. Meteor. Soc. Japan*, **96**, 111–126, doi: 10.2151/jmsj.2018-014.

Zhai, A. R., and H. J. Jiang, 2014: Dependence of US hurricane economic loss on maximum wind speed and storm size. *Environ. Res. Lett.*, **9**, 064 019, doi: 10.1088/1748-9326/9/6/064019.

Zhang, D.-L., Y. Liu, and M. K. Yau, 2002: A multiscale numerical study of Hurricane Andrew (1992). Part V: Inner-core thermodynamics. *Mon. Wea. Rev.*, **130**, 2745–2763, doi: 10.1175/1520-0493(2002)130<2745:AMNSOH>2.0.CO;2.

Zipser, E. J., R. J. Meitin, and M. A. LeMone, 1981: Mesoscale motion fields associated with slowly moving gate convective band. *J. Atmos. Sci.*, **38**, 1725–1750, doi: 10.1175/1520-0469(1981)038<1725:MMFAWA>2.0.CO;2.